IntechOpen

Fractal Analysis

Applications in Health Sciences and Social Sciences

Edited by Fernando Brambila

FRACTAL ANALYSIS - APPLICATIONS IN HEALTH SCIENCES AND SOCIAL SCIENCES

Edited by **Fernando Brambila**

Fractal Analysis - Applications in Health Sciences and Social Sciences
http://dx.doi.org/10.5772/intechopen.68898
Edited by Fernando Brambila

Contributors

Vasileios Drakopoulos, Sean Dillon, Filipe Leoncio Braga, Alexandre Barbosa de Souza, Maricel Agop, Stefan Andrei Irimiciuc, Daniel Timofte, Decebal Vasnicu, Simona Bacaita, Andrei Agop, Yan-Guang Chen, José Luis Carrillo-Estrada, José Roberto Nicolás-Carlock, Victor Dossetti, Walter Edgardo Legnani, Ricardo L. Armentano, Leandro Cymberknop, Dmitrii Tayurskii, Inna Rusanova, Sergio Castiñeira-Ibañez, Daniel Tarrazó, Fuster José Miguel, Pilar Candelas, Constanza Rubio, Sabrina Farías, Fernando Lopez Aguilar

Notice

First published in Croatia, 2017 by INTECH d.o.o.
eBook (PDF) Published by IN TECH d.o.o.
Place and year of publication of eBook (PDF): Rijeka, 2019.
IntechOpen is the global imprint of IN TECH d.o.o.
Printed in Croatia

Legal deposit, Croatia: National and University Library in Zagreb

Additional hard and PDF copies can be obtained from orders@intechopen.com

Fractal Analysis - Applications in Health Sciences and Social Sciences
Edited by Fernando Brambila

p. cm.

Print ISBN 978-953-51-3213-4

Online ISBN 978-953-51-3214-1

eBook (PDF) ISBN 978-953-51-4721-3

Meet the editor

Fernando Brambila holds a PhD degree from UNAM, Mexico. His thesis on scattering theory was directed by Gunther Uhlmann at MIT. He obtained a postdoctoral position at ICTP, Italy, and has a diploma in Senior Technology Innovation Management at IPADE, Harvard. His research areas are mathematical analysis, partial differential equations, vectorial tomography, and hydraulic engineering. More recently, he has done research on fractional calculus and fractal geometry and applications with his collaborators K. Oleschko (UNAM), C. Fuentes (IMTA), and C. Chavez (UAQ). He is a full-time professor at the Mathematics Department of the School of Science at the National Autonomous University of Mexico, UNAM. He is a doctoral thesis advisor of F. Aceff, R. Mercado, J. Rico, B. Martinez, and C. Torres. Also, he is the former president of the Mexican Mathematical Society, and he is currently the president of AMITE (Mexican Association for Innovation in Educational Technology).

Contents

Preface

Fractal analysis has entered a new era. It is no longer just creating nice images, nor is it a branch of mathematics with little interaction with the other areas.

In this book, mathematical models and actual applications to health sciences and social sciences and humanities are presented.

Benoit Mandelbrot, creator of fractal geometry, would have been surprised by the use of fractal analysis presented in this book. It has been applied to such areas as anthropology, study of cultures, languages, cardiology, cancer prevention, medical image analysis, focusing sound, etc. If Mandelbrot had known that the answer to the 300-year-old mathematical problem of giving physical interpretation to fractional derivatives was in the fractal dimension of the domain of function, he would have surely been quite happy.

In the history of fractal geometry, important contributions were made toward seeing nature as it is, rather than as an approximation to classical geometry.

With the mathematics deduced from classical geometry, we could only model approximations of nature. Part of the history of fractal geometry was using them to create images of nature on a computer. For example, in 1978, Loren Carpenter achieved unprecedented images of mountains by using fractals, for a Boeing aircraft commercial. Carpenter based his work on the book *Fractals*: *Form, Chance and Dimension*, by Benoit Mandelbrot. And so begins the era of fractal images. Consider, for example, the lava scene from the movie Star Trek III —a masterpiece of fractal use.

This story takes us to 1999—the use of fractal antennas for cell phones. Cohen constructed the first fractal antenna for personal use; then, R. Hohlfeld and N. Cohen published an article in which they proved mathematically that in order to receive many frequencies it is necessary to have fractal antennas.

More recently, while analyzing heart rate charts at Harvard, H. Goldberger realized that fractal analysis of these graphs allowed him to distinguish between a heart in good health and one that is not in good health.

It has also helped us detect changes and abnormalities in blood flow, which allows us to determine whether an organ, such as a kidney, has or will have cancerous tumors, early cancer detection by the use of fractal analysis, basically.

Power laws in nature can be deduced from fractal dimension.

Fractals also allow us to know about the health of a forest. When we see a tree, we realize that a similar pattern is repeated all throughout the forest itself.

Now we enter the modern part of fractal geometry. We begin with the mathematical modeling that already uses the relation of fractional calculus and fractal geometry, which allows us to model phenomena with great precision.

The concept of fractal dimension classification cultures, the fractal concept of ramifications of populations, languages, and so on—the possibilities are endless! It is even used in cardiology, prevention of cancer, medical images, etc. Most applications we present are basically modern fractal analysis.

In this book, we present the use of fractal geometry, in particular, fractal analysis in two sciences: health sciences and social sciences and humanities.

Part 1 is Health Science. In it, we present the latest advances in cardiovascular signs, kidney images to determine cancer growth, EEG signals, magnetoencephalography signals, and photosensitive epilepsy. We show how it is possible to produce ultrasonic lenses or even sound focusing.

In Part 2, we present the use of fractal analysis in social sciences and humanities. It includes anthropology, hierarchical scaling, human settlements, language, fractal dimension of different cultures, cultural traits, and Mesoamerican complexity.

And in Part 3, we present a few useful tools for fractal analysis, such as graphs and correlation, self-affine and self-similar graphs, and correlation function.

It is impossible to picture today's research without fractal geometry.

Prof. Fernando Brambila
Mathematics Department
School of Sciences
National Autonomous University of Mexico
Mexico

Applications - Cardiovascular, Cancer, Images, Lenses, Nature

Chapter 1

Fractal Analysis of Cardiovascular Signals Empowering the Bioengineering Knowledge

Ricardo L. Armentano, Walter Legnani and
Leandro J. Cymberknop

Additional information is available at the end of the chapter

http://dx.doi.org/10.5772/67784

Abstract

The cardiovascular system is composed of a complex network of vessels, where highly uniform hierarchical branching structures are regulated by the anatomy and local flow requirements. Arteries bifurcate many times before they become capillaries where the scaling factor of vessel length, diameter and angle between two children branches is established at each level of recurrence. This behaviour can be easily described using a *fractal* scaling principle. Moreover, it was observed that the basic pattern of blood distribution is also fractal, imposed both by the anatomy of the vascular tree and the local regulation of vascular tone. In this chapter, arterial physiology was analysed, where waveform complexity of arterial pressure time series was related to arterial stiffness changes, pulse pressure variations and the presence wave reflection. Fractal dimension was used as a nonlinear measure, giving place to a 'holistic approach of fractal dimension variations throughout the arterial network', both in health and disease.

Keywords: fractal dimension, cardiovascular disease, arterial blood pressure

1. Introduction

1.1. The arterial function

Major arteries play two primary functions: to carry blood (they act as conduits) and to reduce its pulsatility (they act as dampers). Consequently, pathologies and systemic complications related to the myocardium will be mainly mechanical, including ruptures, clogs and pumping failures [1]. Along with the blood transport function, the damping function of arteries is responsible for supplying blood to body organs under a stabilized arterial

pressure regime, under laminar flow conditions. Otherwise, in the course of time, tissues would suffer pulsatility-derived degradation [2]. Thus, the response from the arterial tree in terms of intermittent excitement can be described as a mechanical filtering mechanism (removal of sudden variations) of high frequencies or pulsatile phenomena [3]. Cardiovascular pathologies such as arteriosclerosis and its most common form, atherosclerosis, drastically affect the blood transport and arterial damping functions. Atherosclerosis, in particular, is an example of a disease that affects the conductive aspects of flow, thus contributing to luminal obstruction through the formation of atheromatous plaque. Therefore, certain organs (such as the heart) may be progressively and inevitably unable to receive blood flow under normal conditions (ischemic process). It is evident, then, that atherosclerosis is focal, acting at the level of the tunica intima and in a clearly occlusive form [1]. Alternatively, the damping function is affected by arteriosclerosis, mainly through an increase in arterial stiffening (AS) without affecting the transport function. For this reason, arteriosclerosis acts diffusely at the level of the arterial tunica media and with dilation consequences [1].

Although AS increases irreversibly with age, it is important to differentiate the processes altering or accelerating its normal development [4]. With age, systemic arteries' walls undergo histological changes at the level of the tunica intima and tunica media. The presence of factors such as arterial hypertension (HBP), diabetes mellitus (DM), chronic kidney failure, or dyslipidaemia (alteration in the concentration of lipids) is directly responsible for the anticipated increase in the loss of arterial blood vessel distensibility [5]. This is due to the fact that significant changes in AS are used as early markers of vascular disease clinical signs. In this sense, a biological marker is defined as a characteristic that can be measured and evaluated objectively and that constitutes an indicator of normal biological processes, pathogenic processes or pharmacological responses. Age, gender, blood pressure, cholesterol, and diabetes are considered representative markers of cardiovascular risk (CVR) since they can help to predict the occurrence or development of CVDs [6]. More specifically, arterial biomarkers include AS, central blood pressure (CBP, measured in the aorta, at the output of left ventricle), the pulse wave velocity (PWV), the ankle-brachial index (ABI), endothelial dysfunction (ED), intima-media thickness (IMT) and coronary artery calcium (CAC). Currently, the inclusion of arterial biomarkers in the calculations of CVR prediction statistical models such as Framingham, European SCORE and Reynolds is unquestionable [6].

1.2. Arterial viscoelasticity

If a material experiences a reversible deformation when stress is applied on it (recovering its original shape when excitement ceases), it is assumed that it has a mechanical property called elasticity. The relationship between the applied stress and the experienced deformation (stress-strain curve, SSC) determines the type of elasticity of the material. Elasticity can be linear, where the SSC is represented by a straight line passing through the origin of the coordinates, in which case it is called Hookean. However, biological materials usually exhibit SSCs with convexity, a behaviour described as non-linear. In addition, vascular walls have viscosity (a characteristic of the fluids determined by their opposition

to tangential deformations) and must therefore be considered viscoelastic materials. The presence of viscosity in a material generates a delay in its deformation when a sudden stress is applied [7]. It is well known that the viscoelastic properties of the wall are linked to their constituent elements (elastin, collagen and smooth muscle fibres), and each of these elements is associated with a specific stiffness module [6]. Viscoelasticity can be evaluated by analysing the loop that describes the relation between arterial pressure (AP) and the resulting distension of the arterial diameter (AD). When creating the graph, where the abscissae correspond to AD and the ordinates correspond to AP, a hysteresis loop can be observed (after a cardiac cycle has elapsed). As a result of ventricular ejection, artery dilation describes a trajectory in the graph (systolic phase) which does not repeat during the emptying phase (diastolic phase). This means that the expansion and relaxation trajectories are dissimilar [8]. The elimination of the viscous behaviour would result in a strictly elastic pressure versus diameter relationship where both trajectories would be coincident (**Figure 1**).

1.3. Arterial stiffness assessment: clinical implications

Arterial wall stiffness can be quantified through non-invasive methodologies with direct applicability on human beings. In this sense, indexes accounting for the presence of vascular pathologies, related to AS variations, have been developed. The proper implementation of the analysis methodology as well as its reliability is permanently subjected to global consensus because of the high variability observed in *in vivo* experiments. In

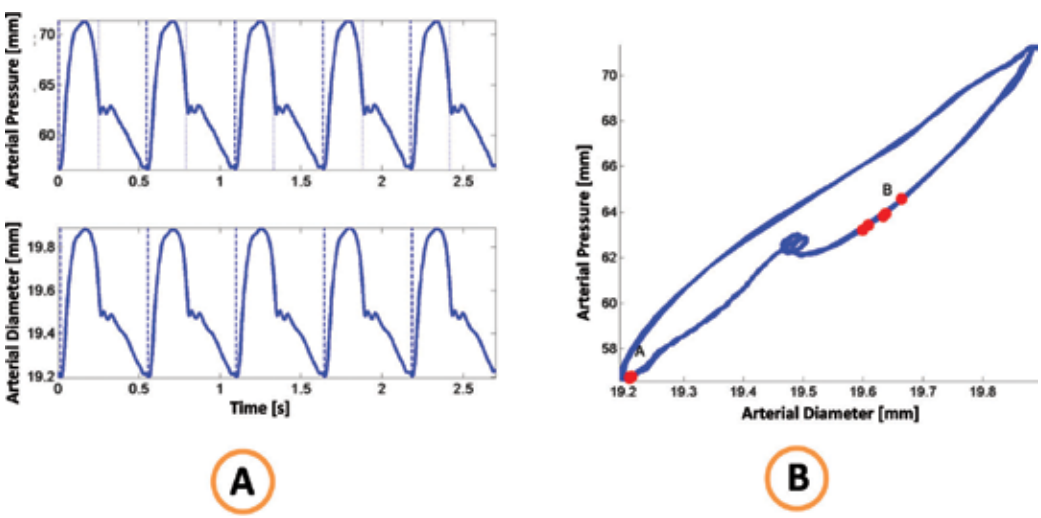

Figure 1. (A) Time series of arterial pressure (top panel) and diameter (bottom panel) obtained for a segment of an aortic conduit. Dashed lines: beginning of systolic phase. Dotted line: beginning of diastolic phase. (B) Hysteresis loop formed by the pressure-diameter relationship. Trajectory AB (clockwise direction) represents the cardiac systole while trajectory BA (same direction) represents the diastole. As can be observed, both trajectories differ because of the presence of viscous phenomena in the wall.

general terms, AS variation can be obtained at a systemic, regional or local level. At the systemic level, it reflects the joint opposition of the major arteries to the pulsatile effects of ventricular ejection [9]. At a regional level, it is often quantified in arterial sites of physiological relevance, such as the aorta (due to the prevalence of the damping function) or specific limbs like the arm. At the local level, it provides information related to the level of arterial wall distensibility [9]. Consequently, it is essential to properly identify the scope and functionality of the indexes used to characterize AS, essentially due to anatomic dependences and excitement conditions, which need to be considered in order to determine it.

There are many elasticity studies where measures are limited to the circumferential effect and to limited regions of the stress-strain curve, which are considered linear. An example is the estimation of the SSC slope, called the deformation modulus or Young's modulus (E), during the interval defined by the diastolic phase, where only elastic behaviours of the arterial walls intervene. This magnitude provides information on structural stiffness, and its determination requires knowing the values of AP, AD, and parietal thickness (h), which are characteristic of the vascular structure under study. However, the evaluation of the functional stiffness is based merely on the change of AD of its diastolic value due to a relative change of AP. This second magnitude, called Peterson modulus (EP), is of greater interest since it provides information on the reserve function of the major arteries [10]. It is used assuming a linear relationship between pressure and deformation, so that its determination is based on the use of systo-diastolic values corresponding to AP and AD, thus providing information at the local level. Pulse pressure (PP) is determined by the difference between the systolic and diastolic values of AP. It is one of the most useful parameters (clinically speaking), representative of AS. This index depends on systolic unloading, AS and the reflections generated in the periphery of the arterial tree. It increases with age (a result of an increase in systolic pressure), and it is influenced by the amplification factor (AF) of the arterial pressure wave (which becomes less pronounced with age). As a result of the above, special attention should be paid when using the PP value obtained through measurements on the brachial artery as a substitute of central PP (aortic and carotid). In this regard, the Framingham study has shown the applicability of PP in the prediction of cardiovascular events in people over 50 years old, rather than individual values of SBP or DBP [11, 12]. It was also mentioned that the SSC is clearly non-linear. An interesting aspect is that it can be adjusted to an exponential curve (through the AP vs. AD relation). As a consequence, the stiffness index can be defined [13]. Likewise, the pressure waves are subjected to amplitude changes along their path as a result of blood viscosity, the distribution of arterial branches and the variations of distensibilities throughout the circulatory system. Modifications in the arterial wall, such as the rupture of the elastic sheet, collagen deposits and calcium deposits, have a direct effect on AS [6]. As a consequence, arterial pulse wave velocity (PWV) is considered the most simple, robust, non-invasive and reproducible method to evaluate AS. The methodology to obtain it consists in measuring the phase difference (temporal displacement) of the AP wave when evaluated in two remote sites of the vascular network (often superficial arteries), whose distance is

known with precision. An example is the circulation line between the carotid artery, which is anatomically located in the neck, and the femoral artery, located in the upper thigh. Finally, changes in wall stiffness can be also estimated assuming that the arterial wall is an isotropic homogeneous elastic material, so that the linear elastic theory is able to be applied considering the first derivative of AP with respect to the strain, giving rise to the 'pressure-strain elastic modulus' (EPS) [8].

1.4. Arterial pressure waveform: morphologic evaluation

In general terms, AP is often defined as an oscillating magnitude that propagates from the cardiac muscle to the peripheral arteries. Like a mechanical wave (such the acoustic wave), it can be reflected and amplified [14]. As such, it has amplitude and frequency and can be analysed both in the temporal domain as well as in terms of its frequency content. It was assumed that variations in AS (dependent upon the anatomic disposition of the vascular conduit), the structural changes shown by the branching process and the eventual presence of obstructions, generate reflections of the mechanical magnitudes that propagate through the arterial network. Consequently, the AP wave increases in amplitude (scaling phenomenon, called amplification factor, AF) together with a level of non-linear deformation because its frequency components are not affected with the same intensity [14].

1.4.1. Augmentation index (AIX): assessment of wave reflection

The augmentation index quantifies the difference between the first and second systolic peaks (referring to PP) providing an indirect measure of the arrival time of the waves reflected from the arterial tree periphery. It is associated with the arterial mechanical properties through PWV because an increase in the latter (produced by a variation in AS) induces an early return of such peripheral reflections. At the aortic level, the reflected AP wave combines with the incident magnitude during systole, an interval in which the left ventricle is still ejecting blood. As a result, an increase in PP is observed called augmentation pressure (AuP), and thus extra work must be performed by the left ventricle to overcome such conditions [5]. In relation to the above, AIX can be determined as AuP divided by PP × 100 to give a percentage [15]. In clinical terms, AIX increases with age and in the presence of HBP, DM and hypercholesterolemia, among other pathologies. It can further be associated with the presence of ED, as a consequence of its close link with AS.

The evaluation of early descriptors or markers of pathologies on time domain signals is based on the analysis of representative parameters of the AP wave because its morphology is determined by the ventricular ejection pattern and the elasticity of the arterial tree [14]. Systolic, diastolic and mean pressures, the time occurrence of the dicrotic notch, PP and AIX provide relevant information on the waveform and suffer alterations with age and the onset of vascular pathologies (**Figure 2**). Likewise, signal morphology associated with vascular mechanics shows a marked irregularity. Unlike sinusoidal waveforms, they cannot be represented analytically through a deterministic function [16].

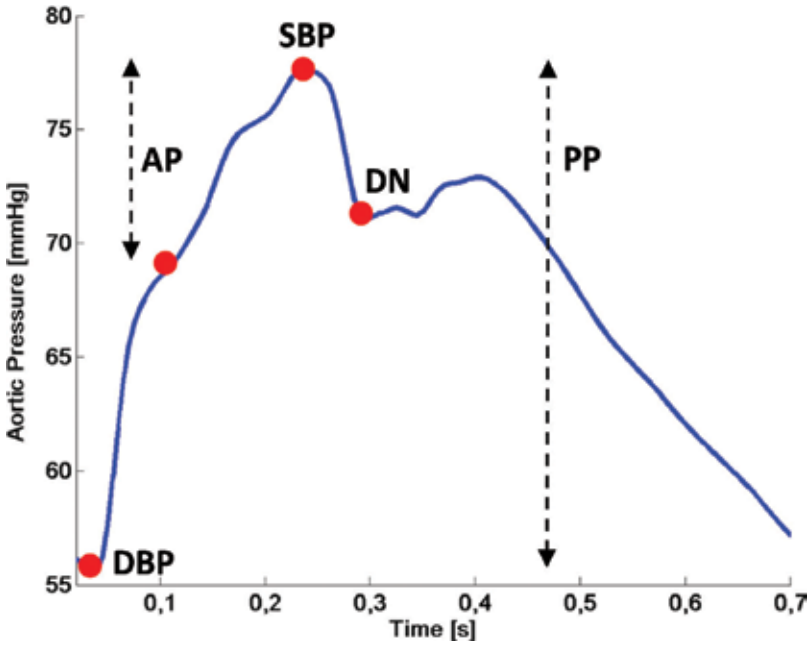

Figure 2. Analysis of a pulse wave for an arterial pressure signal. Diastolic blood pressure (DBP), systolic blood pressure (SBP), pulse pressure (PP), dicrotic notch (DN), augmentation pressure (AP).

2. Fractal analysis

2.1. The concept of 'dimension'

Before defining the concept of fractality, it is indispensable to introduce the concept of *dimension*. Formally speaking, it can be defined as the quantification of space occupied by a set near each of its points [17]. Furthermore, the traditional Euclidian approach argues that a curve is a uni-dimensional object, a surface is a two-dimensional object, and a volume is a tri-dimensional object. In such a statement, the dimension can be quantified in topological terms (TD), using whole numbers. Therefore, the object can be assumed to be embedded in a line (TD = 1), in a plane (TD = 2) or in the space (TD = 3). More precisely, the intuitive notion of dimension associates the space that the object occupies (V_O) with a linear unit of measure (e), using a power law, so that [18]

$$V_O \approx e^D \tag{1}$$

where V_O can be considered a distance, a surface or a volume. It can be inferred then that the area of a plane grows quadratically in relation to e and thus D = TD = 2. A similar situation is observed in curves and volumes, where the dimension acquires values corresponding to 1 and 3, respectively. This is the reason why the objects generated by means of Euclidian geometry acquire whole dimensional values. However, it is perfectly possible to conceive structures whose dimension differs from the established values so that they occupy greater or less

space than a traditional object [17]. The Euclidean geometric shapes go from one dimension to the other without generating detail in relation to its borders. However, there are natural and geometric processes which, through explicit rules, can generate structures that resemble each other when analysed at different scales of magnification. The development of 'self-similar processes' (among other qualities that will be analysed later) cannot be characterized under whole dimensional values, and thus the dimension becomes inevitably fractional. Therefore, objects occupying a metric space that fracture the TD value in which they are embedded are called fractals. As a result, the introduction of the concept of fractality leads to consider continuous dimension variations, unlike the Euclidian approach, which only admits discrete values. The fraction obtained describes the existence of a highly detailed structure whose representation is wholly ignored by the traditional perspective [19]. In mathematical terms, the measure of the dimension is found by means of the conceptualization proposed by Hausdorff (Hausdorff dimension, HD). Assuming that a disk is a set of points at a distance r of a centre, it can be inferred that for TD of value 1, the disks are segments; for TD of value 2, they are circles; and for TD of value 3, they are spheres [20]. Such disks having a radius *r*, whose dimension coincides with TD, are used to cover the object whose dimension needs to be known so that each point of the object is included at least in one of them, minimizing the number of elements used.

2.2. Fractality and time series behaviour

In general terms, fractal signals are those that show detail or structure when they are processed through all their timescales [21]. Formally, a fractal structure is an irregular geometric object that has self-similarity. It is composed of sub-units replicated iteratively so that under any scale of observation (considering ideal conditions), a structure similar to the whole set can be observed. Geometrically, it is possible to generate a fractal object from an initiating element, a morphogenesis rule (called generator) and a scaling interval. The latter determines the number of scales during which the above-mentioned rule must be applied. A traditional example is the Weierstrass curve [22] (**Figure 3**), whose iterative construction (defined as an infinite sum of cosine functions) gives rise to a fractal, continuous everywhere but differentiable nowhere time series.

Since this type of objects is characterized by a fractional dimension, it is called fractal dimension (FD). Conceptually, the FD can also be considered an irregularity measure. As the latter increases, the dimension increases its value as well, and thus it can be used a roughness or variation measure [23]. Natural structures are typically fractal. Their high irregularity can be observed in the contour of rock formations or in the structure of tree leaves. The intense manifestation of deformations and holes places such objects in non-integer intermediate dimensions. As a consequence, Euclidean geometry is unable to quantify the space occupied by a naturally generated object [17, 24]. Although it may be evident, clouds are not spheres, mountains are not cones and lightning bolts are not lines [25]. In physiological terms, fractal structures can be observed, for example, in arterial and venous branches, cardiopulmonary structures and bile ducts [26]. In the cardiovascular system, in particular, the recognition and quantification of this type of manifestations can only be performed through indexes such as

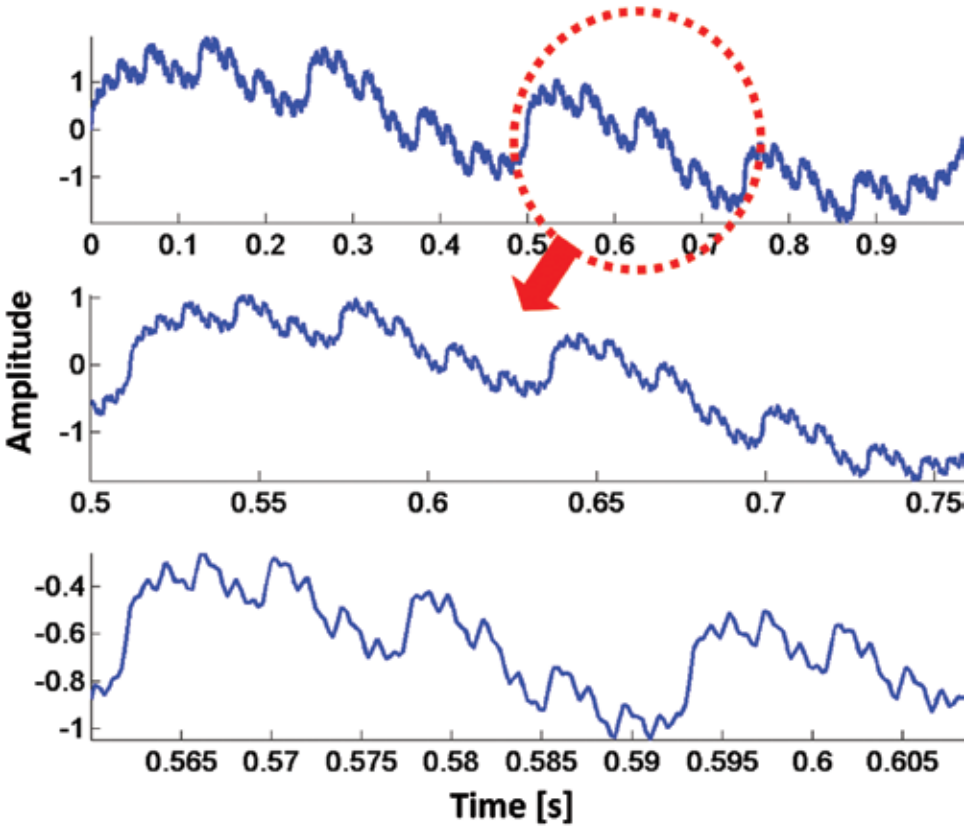

Figure 3. Self-similar Weierstrass time series, generated by a recursive procedure. Its fractal nature is revealed at different timescales.

FD [27]. In this regard, one of the excluding aspects that differentiate natural from geometric fractality is that, in natural fractals, the scale invariance is appreciated only within certain limits [28]. In addition, the presence of self-similarity does not convert a geometric object into a fractal. Although this is a necessary condition, it needs additional contributions for the consolidation of the concept. To such effect, a fractal object is characterized by the following conditions [17]: it has self-similarity; it has a fine structure (detail is observed irrespective of the scale); it is too irregular to be described by traditional geometry; usually, its Hausdorff dimension exceeds its topological dimension; and, in some cases, it can be defined through recursive procedures.

A classic example describing a non-fractal structure is the real line. Although it is self-similar (composed by reproductions of itself at different scales), the remaining imposed conditions cannot be attributed to it [17]. Therefore, finding the characteristics of fractal objects in time series does not necessarily mean that they may be considered fractal. However, having those characteristics would make them possible candidates for such behaviour and then a deeper

analysis would be required. To do this, it is necessary to have tools that can provide quantitative measures, such as FD [29].

Those fractals whose components are exact replicates of the initiator are called exact and present a self-similar dimension (SSD), which is exact as well. Alternatively, there are situations in which, when there are changes in the scale, similarity is not observed at structural levels but rather at statistical levels. A magnified vision of a shoreline may not reproduce the general vision with precision, but it shows the same qualitative appearance [18]. As a result, the fractal is considered statistical. Basically, the value acquired by HD is a real number, which characterizes the richness of geometric structures of limited sets. Since it is complex to calculate and although the information provided by HD is better than other types of measures, it is not used for practical purposes [24]. The approach closest to this concept is the capacity dimension (CD). The procedure required for its determination is similar to the one used for HD but the difference lies in the fact that minimal elements are counted, $N(r)$, required to cover the whole set. The operation is performed for diverse r values, so as to obtain the change in $N(r)$ as r decreases to 0 [20]. Consequently, DC is expressed as follows:

$$C_D = \lim_{r \to 0} \frac{\log N(r)}{\log\left(\frac{1}{r}\right)} \tag{2}$$

When disks do not overlap, and boxes are implemented in the form of grids, the procedure gives rise to the box counting dimension (BCD). In addition, and considering that natural fractals show self-similarity only in a limited number of scales, the SSD estimation is usually made using DC (and its simplest implementation, BCD), particularly in the presence of real, inaccurate and statistical fractal structures [30]. The methodologies proposed by [31–33] can be used to estimate BCD, among others in the existing literature. According to several authors [34–37], the Higuchi's method [32] can be highlighted as one of the most applied, owing to its well performance in FD estimation under different types of fractal time series. For this reason, any reference to the FD value in this chapter will be assumed to be the quantification of BCD. Finally, and unlike auto-similarity, the concept of self-affinity is applied to objects for which scaling is anisotropic. For these objects, the proportions between scales differ according to the direction of scaling. This situation is representative of the physiological time series, where amplitude has different units from those of time [30]. Therefore, it is more appropriate to use the auto-affinity concept (as will be done hereinafter) in relation to the morphological analysis of time variables related to cardiovascular mechanics.

3. Applications of fractal analysis to arterial pressure

Studies on the existence of hidden information in physiological time series have gained considerable popularity over the last few years. This has resulted in the application of techniques and concepts from statistical physics and chaos theory to biomedical issues [28]. Physiological parameters such breathing, heart rate (HR) and even AP itself do not show stationarity, and they are governed by non-periodic temporal fluctuations [30]. Thus, they should be characterized as non-stationary processes, whose analysis and processing require the application of mathematical

tools that can adapt to such behaviour. In this sense, the analysis provided by fractal geometry is among those which best describes the physiological phenomena observed [30].

3.1. Mapping the fractal dimension of the arterial tree

The fundamental goal of the systemic arterial network is to reach certain organs (or specific areas) in order to supply them with the correct amount of blood flow [38]. This network consists of a series of vascular conduits which recursively bifurcate in a dichotomic fashion (a parent branch, two child branches) until they reach the arteriole level. At this last level, the process no longer continues in a dichotomic fashion; the number of branches generated multiplies considerably [20]. Each bifurcation generated within the network implies the creation of a new scale or level. In particular, what makes the arterial tree different from other vascular structures (such as those observed in pulmonary cavities, the tracheobronchial tract, the His-Purkinje system or the kidneys) is the fact that the distribution of its branches and sub-branches is considerably uniform [38]. The presence of repetitive patterns at different scales can be observed, for example, in the relationship that exists between the length of the generating artery and the diameter of the generated one. This relation keeps constant if quantified using a double logarithmic scale, thus indicating the presence of a power law. As stated in other works, this mechanism is consistent with a fractal recursive rule [20]. As a result, the spatial fractal properties of the arterial tree can be assessed in terms of the FD. Together with the structural aspects of the relationship among its ramifications, the dimension has been also related to the flow rate value (or its velocity) in relation to the level of diversification reached [38]. There is previous evidence that the dimensional value acquired (between 1.2 and 1.4) results from the metabolic dependence of the tissue to be perfused and not from the tree structure itself [39]. The determination of the generation parameters, which defines the degree of symmetry of the branching angles and the value of the derived diameters, makes it possible to conceive differentiated structures which have either a blood supply function or a blood distribution function [38]. The structures mentioned are related to the heterogeneous distribution of flow, as established by the perfusion target site [20]. However, as branching progresses, instantaneous variations in symmetry rules are still not clear as a whole [38].

3.1.1. A conceptual model based on experimental measures

In [40, 41], continuous AP measurements were obtained in the following sites: left ventricle and descending thoracic aorta (five animals, instrumented with solid-state implantable pressure sensors) and carotid and femoral arteries (five male middle-aged subjects, without cardiovascular risks factors, evaluated by applanation tonometry). Due to experimental limitations, invasive (in animals) and non-invasive (in humans) measuring methodologies were performed. Assessment of FD in AP time series waveforms was developed by applying Higuchi's method where topological dimension was not considered in FD relative changes (ΔFD) calculation. Essentially, a significant increase in ΔFD was observed at the thoracic aorta (higher complexity) in respect to ventricular pressure FD values (+233.06 ± 75.34%). On the other hand, femoral artery AP manifested a decrease in ΔFD (lower complexity) in comparison to the carotid site (−56.51 ± 13.62%; **Figure 4A**).

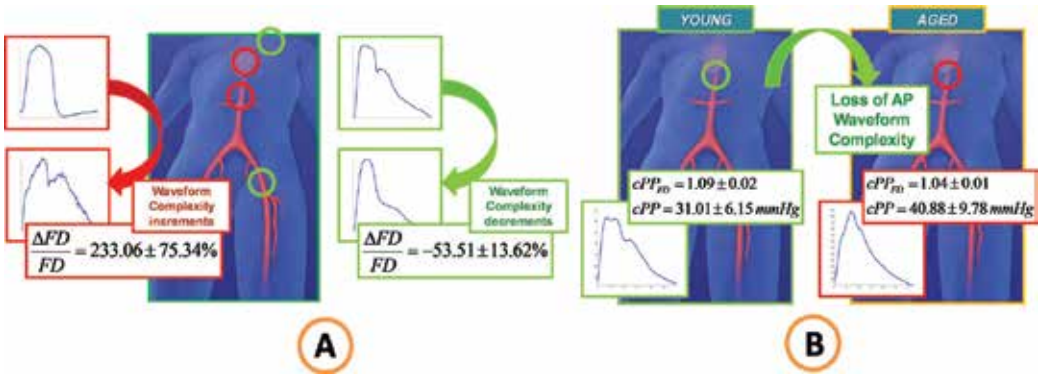

Figure 4. (A) Mapping the fractal dimension of arterial pressure along the arterial tree. (B) Changes of central pressure fractal dimension as a consequence of the ageing process.

From different experimental protocols that were carried out and assuming baseline states, a conceptual model of the morphological structure of AP waveform throughout the arterial network can be proposed. The ventricular pressure waveform, whose FD is minimal, is 'fractalized' during its path along the descending aorta, in addition to the effect caused by the arterial load. In particular, the latter is influenced by the general state of the vascular network, and it is affected by pathological states, which basically alter AS values (and thus PWV), in the same way as with wave reflection sites. As the mechanic wave propagates through the branches, the presence of a stiffness gradient and the vicinity of the periphery make its morphological structure less complex. For this reason, the loss of fractality in central pressure (as well as other CVR-related parameters) is relevant in terms of prevalence and development of CVDs.

3.2. Fractal dimension and ageing

Ageing is defined as the age-related decline in physiological function where arterial stiffening and hypertension constitute related disorders in the cardiovascular system [42]. Age can be considered one of the most powerful determinants of cardiovascular risk, usually regarded as a chronological, unmodifiable, and even untreatable factor [43]. Arterial mechanical properties of the small vessels are known to be altered with advancing age (dilating and stiffening), leading to a rise in PP [44, 45]. In this sense, central pulse pressure (cPP) has been more closely related to cardiovascular events than peripheral pulse pressure (pPP) where predictable changes occur in the arterial time series waveform whether recorded invasively or non-invasively [44, 46]. From the point of view of chaos theory, multiscale and non-linear complexity (structure and interactions of individual subsystems) appears to degrade with ageing and disease [47]. The structures and functions of the individual subsystems are not only affected by the process but also the interactions between them [48]. For this reason, the loss of complexity has even been hypothesized to be an indicator of the transition from normal ageing to frailty [49]. In [50], changes in the waveform complexity of cPP as a result of the ageing process were evaluated. A significant decrease in FD values was obtained in cPP waveform for aged subjects (−55.55%), concomitant to a cPP

increase (+31.87%). As a result, loss of waveform complexity was observed as a consequence of the ageing process in cPP (**Figure 4B**). Arterial structural changes were reflected in FD variations, independent of the AP calibration, due to the space filling property and the fine structure of the waveform were analysed. However, further studies are necessary in order to determine whether changes in waveform complexity can be utilized as a complementary factor of vascular ageing.

3.3. Fractal dimension, stiffness and wave reflection

The effect of arterial tree structure on arterial pressure fractal behaviour was assessed on laboratory animals in Refs. [51, 52]. Firstly, FD was applied, as a non-linear measure, in order to quantify waveform morphology complexity (or roughness) of aortic AP. Subsequently, aortic arterial wall stiffness was evaluated using the first derivative of the pressure-strain relationship, while the effect of wave reflection was estimated from AIX measurements. In order to eliminate peripheral wave reflections, a pneumatic cuff occluder made from silicon rubber was implanted around the descending thoracic aorta, proximally to the AP and AD transducers (piezo-resistive and ultrasonic, respectively). Aortic stiffness was studied by means of pressure-diameter loops both in basal and occlusion states (activation of the cuff and induction of total reflection). A biphasic model was adjusted, where the low pressure slope was related to the elastin elastic response, while the high pressure slope indicated the recruitment of collagen fibres.

As a result, a significant decrease in aortic pressure waveform complexity (pointed out by a FD diminution) was observed during the occlusion interval (−71.43%), concomitant to aortic stiffening (+155.71%) and an increase of AIX (+56.72%).This condition was also addressed in [53], during the evaluation the effect of arterial cross-clamping (a common strategy used in vascular surgery) on arterial stiffness, in humans. The Augmentation Index normalized to 75 beats-per-minute (AIx@75), and FD was calculated from radial arterial pressure tracings during surgery. In both aortic and iliofemoral interventions, after arterial clamping, median AIx@75 rose and FD dropped significantly; the opposite occurred after arterial unclamping.

4. Discussion

Along this chapter, a holistic evaluation of AP waveform complexity in the arterial network was performed, where its FD changes were related to the vascular site. While the ventricular pressure time series was observed to be 'fractalized' at the aortic level (due to the fact that the waveform is more exposed to the multiple wave reflections), AP showed a loss of complexity at distant sites from the cardiac muscle, as a consequence of AF. Concomitant changes in arterial stiffness (a rise of the elastic modulus towards periphery) jointly with the effects of wave reflection were particularly analysed.

4.1. The unwrinkling effect

The morphological changes observed in AP waveform during its propagation along the arterial tree can be summarized in an increase of amplitude combined with a loss of roughness.

This effect was first observed in the invasive experimental protocols implemented in the coronary network. The increase in vascular stiffness, induced by the smooth muscle activation of, was concomitant to an increase and loss of roughness in the time series structure [54]. A similar behaviour was observed in obstructive events of the descending aorta (absence of reflected peripheral waves) as well as in the pressure morphological variation analyses performed on the carotid and femoral arteries. The latter situation was associated with the effect produced by the arterial AF, whose activity has been described according to similar terms. Therefore, the scaling phenomenon with loss of complexity observed in mechanical waves in their path from the myocardium was conceptualized as a 'waveform unwrinkling', as shown in **Figure 5A**.

4.2. Structural fractality: the distributed model

The conception of the arterial system as a single, close-ended conduit, with constant or variable properties along its length, has generated acceptable results in relation to low-frequency perturbations [55]. However, in the case of high frequencies, the discrepancies are evident. The justification of this latter situation lies in the fact that although the arterial system is not a single conduit, it is made up of a set of tubular branches. In addition, the attenuation effect, produced by arterial wall viscosity, on the waves propagating through the network, must also be considered. One of the most relevant aspects is the inverse relationship that exists between frequency and wavelength since wavelengths corresponding to high frequencies will produce significant phase differences between the waves coming from different reflection sites. For this reason, the consideration of the stiffness gradient together with the distributed nature of the terminal branches significantly affects the overall behaviour of the arterial system [55].

In terms of non-linear processing, such behaviour may be expressed in multiple scales and thus evaluated through a fractal measure. The loss of high-frequency components is a typical feature of the loss of complexity, and it can be associated with the presence of diseases. In fact, this idea is part of the health/disease and FD conceptual framework, adopted in this chapter. In this sense, the transmission network models based on fractality have been consistently applied in the study of circulation [56]. In [57], arterial network simulations based on fractal

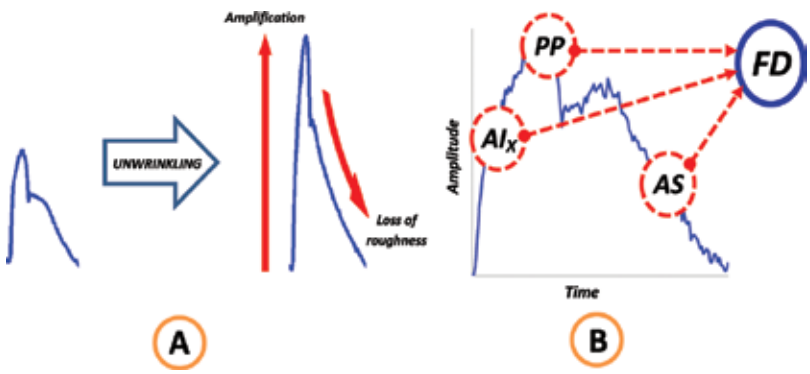

Figure 5. (A) Unwrinkling effect (stretching) evidenced by amplification and loss of roughness in the waveform. (B) Definition of the fractal dimension (FD) as a holistic indicator, which means that it may have variations in parameters related to wave pulsatility (pulse pressure, PP), arterial stiffness (AS) and wave reflection (augmentation index, AIX).

rules were developed, where Taylor's proposed premises were extended. One of the most relevant findings is that regardless of the dichotomic distribution of the branches and of the application of a power law to the relationship between their dimensions, the characteristic asymmetry of the bifurcations plays a fundamental role. This phenomenon is responsible for a marked reduction in the reflection coefficient and therefore affects the spectral oscillations in the input impedance.

Dispersion phenomena in physiological measurements are inevitable. The problem lies with the methodology used to quantify them, regardless of the size of the domain considered. Although a coincidence in the mean values is possible, this is not observed in the relative variance, since the latter depends on the measurement scale chosen to estimate the parameter. It is in these cases that the intervention of the concept of fractality cannot be disregarded [23]. This idea was first associated with physiological structures in [25]. In this work, explicit reference to the creation of vascular networks from fractal rules was made. As a result, an acceptably consistent hypothesis was posed: If the geometry of vascular beds has a fractal structure, isn't it expected that perfusion pressure and flow will be governed by such geometry? [23]. The impact of this structure on AP, its association with pathological states related to AS, and the presence of peripheral reflections constitute the great quest towards that direction.

The dichotomous branching of the arterial tree reflects its first fractal characteristic though in a more basic form. Indeed, the result is an open structure consisting of vascular segments and bifurcations, which constitute the universal block of the arterial network [58]. As stated above, the asymmetry present in each vascular division affects the magnitudes of the angles, lengths and diameters of the generated branches. Symmetrical bifurcations result in a rapidly progressing network, with a marked reduction in their diameters. This arterial structure has been observed at the coronary level in those vessels that enter the myocardium to reach the capillary bed, creating a blood supply pattern [39]. The opposite happens with highly asymmetric bifurcations. The parent branch maintains its structure since its reduction is minimal in each process. Again, in terms of coronary circulation, such structure corresponds to the major arteries surrounding the heart and has blood distribution patterns [39]. However, although the asymmetry factor is crucial in the formation of the structures mentioned, it shows variability in the vascular networks because it does not remain constant from one level to the other. Since there is no reason to consider this factor purely random, it may depend on the local anatomy or be the result of specific flow requirements [39].

In view of the foregoing, the fractal genesis of the arterial network is unquestionable. For this reason, the temporal behaviour of its hemodynamic variables was evaluated, using processing methodologies appropriate to such conception. However, although there are studies addressing the allocation of geometric parameters to each branch [58–60], no allocations related to intrinsic arterial wall features have been evaluated. As previously stated, the activity of the viscoelastic components of the arterial wall strongly determines arterial impedance. Therefore, the self-affine phenomenon observed in the AP time series can be modelled from the interaction of the reflected propagating components, whose distribution within the morphology is the result of local (or eventually systemic) biomechanical alterations of the arterial vascular structure.

http://dx.doi.org/10.5772/67784

4.3. Pressure waveform morphology: the influence of wave reflection

According to previous paragraphs, it may be inferred that exists an evident trend between the arterial network reflected waves and the morphology acquired by AP time series. Therefore, under total reflection (only carotid, subclavian and brachiocephalic branches remained without being occluded) aortic blood pressure unwrinkling (pulsatility increase in conjunction with a loss of roughness) is the consequence of the absence of the fractal nature, induced by the multiple branching of the arterial tree. It is noteworthy that FD analysis was performed over short-time intervals, no longer than two heartbeats. This consideration allowed the insolation of the intrinsic mechanical response, preventing the contribution of reflex regulation mechanisms (which take place around the fifth heartbeat after occlusion) whose intervention might contaminate the waveform structure. Additionally, the heart rate decrease, induced during the occlusion manoeuvre, constituted another intriguing result, which deserves further investigation. Fractal-based techniques have provided a nature-based approach, in order to identify the presence of multi-scale interactions, which are commonly generated by the characteristic of the physiological process [17]. In conclusion, arterial pressure fractality can be conceived as highly dependent on wave reflection.

In relation to this, a comparison of the structural complexity between a ventricular pressure wave and an aortic wave was presented above. Although the aortic wave is constrained in its frequency content (as a result of the buffer effect), it shows a marked irregularity in terms of morphology. The presence of wave reflections, coming from the multiple vascular branching sites, modifies its contour significantly. It was already stated that under pathological states, such as HBP, as represents a decrease in the system's global compliance. As a result, the elimination of high-frequency fluctuations is less efficient. In addition, the resulting increase in PWV generates an early return of the peripheral waves to the heart muscle, thus increasing the pressure in the abdominal aorta region [7]. In terms of fractal analysis, the processing of aortic pressure waveforms shows lower roughness values compared to normal states. Consequently, it may be inferred that the dispersion of reflections in relation to the structure plays a fundamental role. The early return of the reflected waves not only increases AP maximum values during its systolic excursion, but it also has an impact on the distribution of singularities that are part of heartbeat morphology. Such alterations are clearly differentiated by FD variation, which in fact presents the unwrinkling phenomenon.

4.4. Fractal dimension: a holistic index

The detection of a stretching in AP with a loss of complexity (unwrinkling) can be attributed to both an increase in AS (conductive factor) and to structural alterations typical of the arterial tree (obstructive factor). The loss of morphological roughness means that the AF has different impacts on pulsatility frequency components, making the waveform less complex and taking it to its pure oscillatory levels. This phenomenon may, in some aspects, be associated with the concept of oscillatory disease [26]. Consequently, proposing FD as a 'holistic index' is appropriate from more than one point of view. The holism concept entails the presence of non-linearity, where the whole is not the sum of the parts, thus not complying with the superposition principle. In addition, the FD has intrinsic behaviours based on multi-scale information, which are not specifically related to any particular magnitude or biological

system. Moreover, the calibration of the signal acquired in its determination is not required, and therefore, the measurement is independent of specific units. It should be stressed that the non-invasive determination of AP systo-diastolic variations (by means of the applanation tonometry technique) requires additional sphygmomanometric measurements, where the invariance of the mean and diastolic pressures throughout the vascular network are assumed. In this sense, the FD estimation may be affected by the values of such pressures.

The evolution of vascular diseases entails progressive changes, whose early stages are difficult to detect. Particularly in parietal alterations, they initially appear at a molecular level (e.g. excess of low density lipoproteins, nitric oxide deficiency), then at a cellular level (migration of smooth muscle cells, elastin fibre ruptures, leukocyte intervention), then at a local structural level (plaque formation, remodelling, vascular weakening) and finally at a global structural level (generalized disease with systemic consequences). In all these stages, the loss of complexity of the variables involved in the processes should become evident and, probably, a non-linear measure provided by the FD would be capable of identifying such abnormality. For this reason, the possible association between the multi-scale analysis of hemodynamic variables in the time domain and similar spatial behaviours, the latter representative of the different components present in the vascular structure has been proposed as a topic for future studies.

In conclusion, the various analyses performed indicated the presence of morphological variations in hemodynamic variables of the vascular mechanics, induced by the presence of pathological states. Such variations were quantified through non-linear processing based on fractal geometry. The main finding shows a decreased FD, concomitant to both the changes in AS and the absence of wave reflections. As a result, it may be inferred that the information provided by the measurement is systemic since it is influenced by both factors simultaneously. The FD observational analysis, associated with a potential marker, is significantly consistent in terms of health and disease. Through the adoption of this conceptual framework, it was possible to use the quantification of fractal complexity to detect underlying pathological states, associated with descriptive parameters of cardiovascular mechanics (**Figure 5B**).

Author details

Ricardo L. Armentano[1], Walter Legnani[2]* and Leandro J. Cymberknop[1]

*Address all correspondence to: walterlegnani@gmail.com

1 Group of Research and Development in Bioengineering, National Technological University, Buenos Aires, Argentina

2 Center of Signals and Images Processing, National Technological University, Buenos Aires, Argentina

References

[1] O'Rourke M. Mechanical principles in arterial disease. Hypertension. 1995; 26(1):2–9.

[2] Pessana F, Bia D, Pérez Campos H, Craiem D, Graf S, Zocalo Y, Risk M and Armentano R L. Dynamics of cryopreserved human carotid arteries. Annual International Conference of the IEEE Engineering in Medicine and Biology Society. 2004; 1:730–733.

[3] Armentano R L, Barra J G, Pessana F M, Craiem D, Graf S, Bia D, Sanchez R. Smart smooth muscle spring-dampers. IEEE Engineering in Medicine and Biology Magazine. 2007; 26: 62–70.

[4] Bia D, Zócalo Y, Pessana F, Armentano R L, Pérez H, Cabrera Fischer E I, Saldías M and Álvarez I. Acoplamiento viscoelástico y funcional entre arterias femorales nativas y homoinjertos arteriales y venosos, frescos y criopreservados. Revista Española de Cardiologia . 2006; 59(7): 679–687.

[5] Nichols W W. Clinical measurement of arterial stiffness obtained from noninvasive pressure waveforms. American Journal of Hypertension. 2005; 18(1): 3S–10S.

[6] Nichols W W, O'Rourke M F and Vlachopoulus C. McDonald's Blood Flow in Arteries: Theoretical, Experimental and Clinical Principles. 6th ed. A Hodder Arnold Publication;London; UK; 2011.

[7] Westerhof N, Stergiopulos N and Noble M I M. Snapshots of Hemodynamics: An Aid for Clinical Research and Graduate Education. 2nd ed. Springer; US; 2010.

[8] Armentano R L, Cabrera Fischer E I, Barra J G, Levenson J A, Simon A C and Pichel R H. Single beat evaluation of circumferential aortic elastin elastic modulus in conscious dogs: Potential application in non-invasive measurements. Medical Progress Through Technology. 1994; 20(1–2): 91–99.

[9] Pannier B M, Avolio A, Hoeks A, Mancia G, Takazawa K. Methods and devices for measuring arterial compliance in humans. American Journal of Hypertension. 2002; 15:743–753.

[10] Greenwald S E. Pulse pressure and arterial elasticity. Quarterly Journal of Medicine. 2002; 95(2): 107–112.

[11] Safar M E. Pulse pressure, arterial stiffness, and cardiovascular risk. Current Opinion in Cardiology. 2000;15(4): 258–263.

[12] Mendis S. The contribution of the Framingham Heart Study to the prevention of cardiovascular disease: a global perspective. Progress in Cardiovascular Disease. 2010; 53:10–4.

[13] Hirai T, Sasayama S, Kawasaki T and Yagi S. Stiffness of systemic arteries in patients with myocardial infarction. A noninvasive method to predict severity of coronary atherosclerosis. Circulation. 1989; 80(1): 78–86.

[14] Avolio A P, Van Bortel L M, Boutouyrie P, Cockcroft J R, McEniery C M, Protogerou A D, Roman M J, Safar M E, Segers P and Smulyan H. Role of pulse pressure amplification in arterial hypertension: experts' opinion and review of the data. Hypertension. 2009; 54(2):375–383.

[15] Laurent S, Cockcroft J, Van Bortel L, Boutouyrie P, Giannattasio C, Hayoz D, Pannier B, Vlachopoulos C, Wilkinson I and Struijker-Boudier H. Expert consensus document on

arterial stiffness: methodological issues and clinical applications. European Heart Journal. 2006; 27(21): 2588–2605.

[16] Zamir M. The Physics of Coronary Blood Flow. 1st ed. Springer; US; 2010.

[17] Falconer K. Fractal Geometry: Mathematical Foundations and Applications. 2nd ed. Wiley; London; UK;2003.

[18] Theiler J. Estimating the fractal dimension of chaotic time series. The Lincoln Laboratory Journal. 1990; 3(1):63–86.

[19] Sharma V. Deterministic chaos and fractal complexity in the dynamics of cardiovascular behavior: Perspectives on a new frontier. Open Cardiovascular Medicine Journal. 2009; 3: 110–123.

[20] Bassingthwaighte J B, Liebovitch L S and West B J. Fractal physiology. Published for the American Physiological Society by Oxford University Press.; New York; US; 1994.

[21] Madisetti V. The Digital Signal Processing Handbook. 2nd ed. Boca Raton FL: CRC; 2009.

[22] Weierstrass K. On continuous functions of a real argument that do not have a well-defined differential quotient. Classics on Fractals, Edgar GA ed. Basic Books; New York; US; 1993.

[23] Bassingthwaighte J B. Physiological heterogeneity: fractals link determinism and randomness in structures and functions. News in Physiological Science. 1988; 3(1): 5–10.

[24] Barnsley M F. Fractals Everywhere. 2nd ed. Morgan Kaufmann; California; US; 2000.

[25] Mandelbrot B. The Fractal Geometry of Nature. New York: Freeman; 1983.

[26] Goldberger A L, West B J. Fractals in physiology and medicine. The Yale Journal of Biology and Medicine. 1987; 60(5): 421–435.

[27] Cerutti S, Signorini M G. Nonlinear advanced methods for biological signal analysis. In IEEE; 20022; 4(1):23.

[28] Goldberger A L, Peng C K and Lipsitz L A. What is physiologic complexity and how does it change with aging and disease? Neurobiology of Aging. 2002; 23: 23–26.

[29] Cymberknop L J, Legnani W, Pessana F, Bia D, Zócalo Y and Armentano R L. Stiffness indices and fractal dimension relationship in arterial pressure and diameter time series *in-vitro*. Journal of Physics: Conference Series. 2011; 332: 012024.

[30] Eke A, Herman P, Kocsis L and Kozak L R. Fractal characterization of complexity in temporal physiological signals. Physiological Measurement. 2002; 23: R1–R38.

[31] Katz M. Fractals and the analysis of waveforms. Computers in Biology and Medicine. 1988; 18: 145–156.

[32] Higuchi T. Approach to an irregular time series on the basis of the fractal theory. Physica D. 1988; 31: 277–283.

[33] Sevcik C. On fractal dimension of waveforms. Chaos Solitons & Fractals. 2006; 28: 579–580.

[34] Esteller R, Vachtsevanos G, Echauz J and Litt B. A comparison of waveform fractal dimension algorithms. IEEE Transactions on Circuits and Systems I: Fundamental Theory and Applications. 2001; 48: 177–183.

[35] Girault J M, Kouame D and Patat F. Mean fractal dimension» of blood ultrasonic Doppler signals. Engineering in Medicine and Biology Society, Proceedings of the 23rd Annual International Conference of the IEEE. 2001; 2:1577–1580.

[36] D'Addio G, Corbi G, Accardo A, Russo G, Ferrara N, Mazzoleni M C, Princi T. Fractal behaviour of heart rate variability reflects severity in stroke patients. Studies in Health Technology and Informatics. 2009; 150: 794–798.

[37] Khoa T Q D and Nakagawa M. Recognizing brain activities by functional near-infrared spectroscope signal analysis. Nonlinear Biomedical Physics. 2008; 2:3.

[38] Zamir M. Arterial branching within the confines of fractal L-system formalism. The Journal of General Physiology. 2001; 118(3): 267–276.

[39] Karch R, Neumann F, Podesser B K, Neumann M, Szawlowski P, and Schreiner W. Fractal properties of perfusion heterogeneity in optimized arterial trees. The Journal of General Physiology. 2003; 122(3): 307–322.

[40] Armentano R L, Cymberknop L J, Legnani W, Pessana F M, Barra J G and Simon A. Arterial blood pressure complexity provides insightful information about arterial system dynamics. 34nd Annual International Conference of the IEEE Engineering in Medicine and Biology Society. 2012.

[41] Cymberknop L J, Armentano R L, Legnani W, Alfonso M and Pessana F M. Mapping the fractal dimension of arterial pressure. world congress on medical physics and biomedical engineering (IUPESM'15). 2015.

[42] Sun, Z. Aging, arterial stiffness, and hypertension. Hypertension. 2015; 65(2), 252–256.

[43] Najjar S S, Scuteri A and Lakatta E G. Arterial aging: is it an immutable cardiovascular risk factor?. Hypertension. 2005; 46(3): 454–462.

[44] McVeigh G E. Bratteli C W, Morgan D J, Alinder C M, Glasser S P, Finkelstein S M and Cohn J N. Age-related abnormalities in arterial compliance identified by pressure pulse contour analysis: aging and arterial compliance. Hypertension. 1999; 33(6): 1392–1398.

[45] McEniery C M, Wallace S, Mackenzie I S, McDonnell B, Yasmin Newby D E, and Wilkinson, I B. Endothelial function is associated with pulse pressure, pulse wave velocity, and augmentation index in healthy humans. Hypertension. 2006. 48(4): 602–608.

[46] Cecelja M, Jiang B, Spector T D, and Chowienczyk P. Progression of central pulse pressure over 1 decade of aging and its reversal by nitroglycerin a twin study. Journal of the American College of Cardiology. 2012; 59(5): 475–483.

[47] Goldberger A L. Fractal dynamics in physiology: Alterations with disease and aging. Proceedings of the National Academy of Sciences. 2002; 99: 2466–2472.

[48] Sleimen-Malkoun R, Temprado J J and Hong S L. Aging induced loss of complexity and dedifferentiation: consequences for coordination dynamics within and between brain, muscular and behavioral levels. Frontiers in Aging Neuroscience. 2014; 6(140): 1–17

[49] Lipsitz L A. Physiological complexity, aging, and the path to frailty. Science of Aging Knowledge Environment: SAGE KE. 2004; (16): pe16.

[50] Armentano R L, Cymberknop L J, Legnani W, Alfonso M and Pessana F M. Aging process: central pressure waveform loss of complexity. World Congress on Medical Physics and Biomedical Engineering (IUPESM'15). 2015.

[51] Armentano R L, Cymberknop L J, Legnani W, Pessana F M, Craiem D, Graf S and Barra J G. Arterial pressure fractality is highly dependent on wave reflection. 35nd Annual International Conference of the IEEE Engineering in Medicine and Biology Society; 2013.

[52] Cymberknop L J, Armentano R L, Legnani W, Pessana F M, Craiem D, Graf S and Barra J G. Contribution of arterial tree structure to the arterial pressure fractal behaviour. Journal of Physics: Conference Series. 2013; 477 012030. doi:10.1088/1742-6596/477/1/012030

[53] Politi M T, Wray S, Fernández J, Gaudric J, Ghigo A, Lagrée P-Y, Capurro C, Fullana J M and Armentano R. Impact of arterial cross-clamping during vascular surgery on arterial stiffness measured by the augmentation index and fractal dimension of arterial pressure. Health and technology. 2016; 6(3): 229–237.

[54] Cymberknop L J, Legnani W, Pessana F M, Crottogini A and Armentano R L. Coronary arterial stiffness is related with a loss of fractal complexity in the aortic pressure. 34nd Annual International Conference of the IEEE Engineering in Medicine and Biology Society. 2012; 4200–03.

[55] Taylor M G. The input impedance of an assembly of randomly branching elastic tubes. Biophysical Journal. 1966; 6(1): 29–51.

[56] Milnor W R. Hemodynamics. 2nd ed. Williams & Wilkins; Philadelphia; US; 1989.

[57] Brown D J. Input impedance and reflection coefficient in fractal-like models of asymmetrically branching compliant tubes. IEEE Transactions on Biomedical Engineering. 1996; 43(7): 715–722.

[58] Zamir M. On fractal properties of arterial trees. Journal of Theoretical Biology. 1999;197: 517–526.

[59] Murray C D. The physiological principle of minimum work applied to the angle of branching of arteries. Journal of General Physiology. 1926; 9:835–841.

[60] Pollanen M S. Dimensional optimization at different levels of the arterial hierarchy. Journal of Theoretical Biology. 1992; 159:267–270.

Chapter 2

Complex Systems with Self-Elimination of Dissipation with Implication in Bio-Structural Behavior Via Nondifferentiability

Maricel Agop, Decebal Vasincu, Daniel Timofte,
Elena Simona Bacaita, Andrei Agop and
Stefan Andrei Irimiciuc

Additional information is available at the end of the chapter

http://dx.doi.org/10.5772/67939

Abstract

In the present chapter, we show that the use of the nondifferentiable mathematical procedures, developed in the Scale Relativity Theory with constant arbitrary fractal dimension, simplifies very much the dynamics analyses in the case of complex systems. By applying such a procedure to various complex systems dynamics (biological structures, ablation or discharge plasmas, etc.), we are able to observe that it starts from a steady (oscillating state) and as the external factor is varied the system undergoes significant changes. The systems evolve asymptotically through various transition, toward a chaotic regime (like bifurcations or intermittencies), but never reaching it. Another important reveal from the study of the system's dynamics was the presence of various steady states depending on the resolution scale at which the theoretical investigations are performed.

Keywords: complex systems, fractal model, chaos, biological systems

1. Introduction

Complex systems, encountered in human societies, neural networks, the Internet, ecosystems, biological evolution, stock markets, economies, and many others, represent interdisciplinary research topics that have been studied by means of some fundamental theories, especially from physics and computer simulation. These systems are composed of a high number of individual components and their evolution cannot be predicted simply by analyzing the individual behavior of their elements or by adding their behavior. Their global evolution is decisively influenced by the manner in which the elements relate to each other,

leading to emergence, self-organization, and adaptability [1–3]. Correspondingly, the theoretical models corresponding to the complex systems dynamics become sophisticated [2, 3].

The models can be strongly simplified by taking into account that the complexity of interaction process imposes various temporal resolution scales, and the pattern evolution imposes different degrees of freedom [4]. Thus, new theoretical models can be developed by admitting that the complex systems that display chaotic behavior are recognized to acquire self-similarity in association with strong fluctuations at all possible space-time scales [5, 6]. Then, for large temporal scales compared to the inverse of the highest Lyapunov exponent [7–10], instead of deterministic trajectories we will work with a collection of potential trajectories and instead of definite positions with probability density. One interesting example is the case of collisions in complex system, where the dynamics of the particles can be described by nondifferentiable curves.

Therefore, in order to build a theoretical model for the evolution of complex systems, the fundaments of a nondifferentiable physics must be defined. For this, the system complexity is substituted with the nondifferentiable character of physical quantities, idea that lies at the base of Scale Relativity Theory (SRT) [11, 12] and of the nonstandard Scale Relativity Theory (NSRT), a particular case of the first one for a fractal dimension arbitrary constant [13]. In the framework of the above two theories, assuming that the individual components of the complex system move on continuous, but nondifferentiable curves, named fractal curves, the evolution of complex systems can be described by physical quantities depending both on the well-known space-time coordinates and, besides that, on the space-time scales resolution; thus, it can be considered fractal functions [11, 13]. Moreover, the complex system will act as a "fluid" without interactions because its individual components are reduced to and identified with their own trajectories, named geodesics.

Further, we show that the dynamics "control" of various complex systems (biological structures, ablation, discharge plasmas, etc.) can be realized by means of fractality.

2. Complex systems: mathematical model

Taking into consideration the above, the following consequences emerge regarding the complex systems dynamics [11–13]:

i. any trajectory of the individual components (fractal fluid line) is explicitly dependent on scale resolution δt;

ii. applying the substitution principle, $\delta t \equiv dt$, the scale resolution can be considered as an independent variable. We reserve the notation dt for the usual time as in the Hamiltonian complex system dynamics;

iii. the variables that appear in the dynamics of complex system are fractal, i.e., are functions that depends both on the space-time coordinates and on the scale resolution. Then, in any point of the fractal curve, two derivatives of the variable field $M(t, dt)$ as explicit functions of the two variables t and dt, can be defined:

http://dx.doi.org/10.5772/67939

$$\frac{d_+M(t,dt)}{dt} = \lim_{\Delta t\to 0_+}\frac{M(t+\Delta t,\Delta t)-M(t,\Delta t)}{\Delta t}$$
$$\frac{d_-M(t,dt)}{dt} = \lim_{\Delta t\to 0_-}\frac{M(t,\Delta t)-M(t-\Delta t,\Delta t)}{\Delta t} \quad (1)$$

The "+" sign indicates forward processes and the "–"sign to the backwards ones;

iv. the differential of the spatial coordinate field $dX^i(t,dt)$ is expressed as:

$$d_\pm X^i(t,dt) = d_\pm x^i(t) + d_\pm \xi^i(t,dt) \quad (2)$$

where $d_\pm x^i(t)$ is the "classical part" (differentiable, scale resolution independent) and $d_\pm \xi^i(t,dt)$ is the "fractal part" (nondifferentiable, scale resolution dependent);

v. the nondifferentiable part of the spatial coordinate field, by means of which we can describe the complex system dynamics, satisfies the fractal equation [5]:

$$d_\pm \xi^i = \lambda_\pm^i (dt)^{1/D_F} \quad (3)$$

where $\lambda_\pm^i$ are constant coefficients through which the fractalization type describing the complex system dynamics is specified and D_F defines the fractal dimension of the motion non-differentiable curve.

In our opinion, the complex system processes imply a dynamics on geodesics with various fractal dimensions. The variety of these fractal dimensions of the complex system geodesics comes as a result of complex system structure. Precisely, for $D_F = 2$, quantum type processes are generated in the complex system, for $D_F < 2$ correlative type processes are induced and for $D_F > 2$ noncorrelative type ones can be found (for details, see [8, 14]);

vi. the differential time reflection invariance of any dynamical variable of the complex system is recovered by combining the derivatives d_+/dt and d_-/dt in the nondifferentiable operator

$$\frac{\hat{\partial}}{\partial t} = \frac{1}{2}\left(\frac{d_+ + d_-}{dt}\right) - \frac{i}{2}\left(\frac{d_+ - d_-}{dt}\right) \quad (4)$$

This is a natural result of the complex prolongation procedure applied to complex system dynamics [13, 15]. Applying now the nondifferentiable operator to the spatial coordinate field, by means of which we can describe the fractal fluid dynamics, yields the complex velocity field of the fractal fluid:

$$\hat{V}^i = \frac{\hat{d}\mathbf{X}^i}{dt} = \mathbf{V}_D^i - V_F^i \quad (5)$$

with:

$$V_D^i = \frac{1}{2}\left(\frac{d_+X^i + d_-X^i}{dt}\right)$$
$$V_F^i = \frac{1}{2}\left(\frac{d_+X^i - d_-X^i}{dt}\right) \tag{6}$$

The real part, V_D^i, represents the "classical velocity" (differentiable, i.e., scale resolution independent), while the imaginary part, V_F^i, is the "fractal velocity" (nondifferentiable, i.e., scale resolution dependent), induced by fractality;

vii. any external constraint is equivalent with a selection of fractal fluid geodesics, whose nondifferentiability, together with the two values of the derivative imply a generalized statistical fluid-like description. Then, the average of $d_\pm X^i$ is:

$$\langle d_\pm X^i \rangle = d_\pm x^i \tag{7}$$

with

$$\langle d_\pm \xi^i \rangle = 0 \tag{8}$$

The previous relation (8) means that the average of the fractal fluctuations is null;

viii. in order to determine the scale covariant derivative, which describes the fractal fluid dynamics, we will consider that the individual components of the complex fluid move in a three-dimensional space and that X^i are the spatial coordinates of a point on their nondifferentiable curves. The second-order Taylor expansion for a variable field $M(X^i, t)$ is:

$$d_\pm M(X^i, t) = \partial_t M dt + \partial_i M \cdot d_\pm X^i + \frac{1}{2}\partial_l \partial_k M \cdot d_\pm X^l d_\pm X^k \tag{9}$$

These relations are valid in any point and more for the points X^i on the nondifferentiable curve which we have selected in Eq. (9). From here, forward and backward values for fractal fluid variables from Eq. (9) become:

$$\langle d_\pm M \rangle = \langle \partial_t M dt \rangle + \langle \partial_i M \cdot d_\pm X^i \rangle + \frac{1}{2}\langle \partial_l \partial_k M \cdot d_\pm X^l d_\pm X^k \rangle \tag{10}$$

Assuming that the differentials $d_\pm X^i$, dt are independent and the mediated values of all variables and their derivatives coincide with themselves, relation (10) becomes:

$$d_\pm M = \partial_t M dt + \partial_i M \cdot \langle d_\pm X^i \rangle + \frac{1}{2}\partial_l \partial_k M \cdot \langle d_\pm X^l d_\pm X^k \rangle \tag{11}$$

Using Eq. (3), for $i \neq j$ we can write:

http://dx.doi.org/10.5772/67939

$$\langle d_{\pm}\xi^{l} d_{\pm}\xi^{k}\rangle = \pm\lambda_{\pm}^{l}\lambda_{\pm}^{k}(dt)^{(2/D_F)-1}dt \tag{12}$$

where the signs "+" and "−" have the same significance as in relation (1).

Then, Eq. (11) takes the form:

$$d_{\pm}M = \partial_t M dt + \partial_i M \cdot \langle d_{\pm}\mathbf{X}^{i}\rangle + \frac{1}{2}\partial_l\partial_k M \cdot d_{\pm}x^{l} d_{\pm}x^{k} + \frac{1}{2}\partial_l\partial_k M[\lambda_{\pm}^{l}\lambda_{\pm}^{k}(dt)^{(2/D_F)-1}dt] \tag{13}$$

Using the method from [11–13], which involves dividing by dt and neglecting the terms with differential factors, we obtain:

$$\frac{d_{\pm}M}{dt} = \partial_t M + v_{\pm}^{i}\cdot\partial_i M + \frac{1}{2}\lambda_{\pm}^{l}\lambda_{\pm}^{k}(dt)^{(2/D_F)-1}\partial_l\partial_k M \tag{14}$$

with

$$v_{\pm}^{i} = \frac{d_{\pm}x^{i}}{dt}$$

These relations also allow us to define the operator:

$$\frac{d_{\pm}}{dt} = \partial_t + v_{\pm}^{i}\cdot\partial_i + \frac{1}{2}\lambda_{\pm}^{l}\lambda_{\pm}^{k}(dt)^{(2/D_F)-1}\partial_l\partial_k \tag{15}$$

Considering Eqs. (4), (5), and (15), it results:

$$\frac{\hat{d}M}{dt} = \partial_t M + \hat{V}^{i}\cdot\partial_i M + \frac{1}{4}(dt)^{(2/D_F)-1}D^{lk}\partial_l\partial_k M \tag{16}$$

where

$$\begin{aligned} &D^{lk} = d^{lk} - i\bar{d}^{lk} \\ &d^{lk} = \lambda_{+}^{l}\lambda_{+}^{k} - \lambda_{-}^{l}\lambda_{-}^{k},\ \bar{d}^{lk} = \lambda_{+}^{l}\lambda_{+}^{k} + \lambda_{-}^{l}\lambda_{-}^{k} \end{aligned} \tag{17}$$

Using Eq. (16), the scale covariant derivative in the fractal fluid dynamics is defined as:

$$\frac{\hat{d}}{dt} = \partial_t + \hat{V}^{i}\cdot\partial_i + \frac{1}{4}(dt)^{(2/D_F)-1}D^{lk}\partial_l\partial_k \tag{18}$$

3. Fractal fluid geodesics

Based on the scale covariance principle (physics laws are invariant in respect to all scale transformations), we will consider that the transition from classical to nondifferentiable physics is equivalent with the replacement of standard derivative d/dt with the nondifferentiable operator $\hat{d}/dt$. In consequence, it will act as scale covariant derivative, applied for writing the equations of fractal fluid dynamics in similar forms to those from the classical (differentiable)

physics. Thus, the operator (18) applied to the complex velocity (5), with no external constraint, implies the geodesics in the following form:

$$\frac{\hat{d}\hat{V^i}}{dt} = \partial_t \hat{V^i} + \hat{V^l} \cdot \partial_l \hat{V^i} + \frac{1}{4}(dt)^{(2/D_F)-1} D^{lk} \partial_l \partial_k \hat{V^i} = 0 \tag{19}$$

This means that the local acceleration $\partial_t \hat{V^i}$, the convection $\hat{V^l} \cdot \partial_l \hat{V^i}$, and the dissipation $D^{lk}\partial_l \partial_k \hat{V^i}$ make their balance in any point of the nondifferentiable curve. Moreover, the presence of the complex coefficient, $4^{-1}(dt)^{(2/D_F)-1} D^{lk}$, indicates that the fractal fluid has rheological properties, such as memory, determined by its internal structure.

Considering that the fractalization is induced by Markov-type stochastic processes, with individual components displacements of Lévy type [16, 17], then:

$$\lambda_+^i \lambda_+^l = \lambda_-^i \lambda_-^l = 2\lambda \delta^{il} \tag{20}$$

where δ^{il} is the Kronecker's pseudo-tensor.

In these conditions, Eq. (19) becomes:

$$\frac{\hat{d}\hat{V^i}}{dt} = \partial_t \hat{V^i} + \hat{V^l} \cdot \partial_l \hat{V^i} - i\lambda(dt)^{(2/D_F)-1} \partial^l \partial_l \hat{V^i} = 0 \tag{21}$$

Separating the individual components movements on differential and fractal scale resolutions, Eq. (21) becomes equivalent with the equations set:

$$\begin{aligned} \frac{\hat{d}V_D^i}{dt} &= \partial_t V_D^i + V_D^l \cdot \partial_l V_D^i - [V_F^l - \lambda(dt)^{(2/D_F)-1} \partial^l] \partial_l V_F^i = 0 \\ \frac{\hat{d}V_F^i}{dt} &= \partial_t V_F^i + V_D^l \cdot \partial_l V_F^i - [V_F^l - \lambda(dt)^{(2/D_F)-1} \partial^l] \partial_l V_D^i = 0 \end{aligned} \tag{22}$$

4. Geodesics in the Schrödinger-type representation

For irrotational motions, the complex velocity satisfies the condition:

$$\varepsilon_{ikl} \partial^k \hat{V^l} = 0 \tag{23}$$

where ε_{ikl} is the Levi-Civita pseudo-tensor. Then, the complex velocity field becomes:

$$\hat{V^i} = -2i\lambda(dt)^{(2/D_F)-1} \partial^i \ln \Psi \tag{24}$$

where for the moment, $\ln\Psi$ defines the scalar potential of the complex velocity field. Substituting Eq. (24) in Eq. (22), it results:

http://dx.doi.org/10.5772/67939

$$\frac{\hat{d}\hat{V}^i}{dt} = -2i\lambda(dt)^{(2/D_F)-1}\{\partial_t\partial^i \ln\Psi - i[2\lambda(dt)^{(2/D_F)-1}(\partial^j \ln\Psi\partial_j)\partial^i \ln\Psi + \lambda(dt)^{(2/D_F)-1}\partial^j\partial_j\partial^i \ln\Psi]\} = 0 \tag{25}$$

or using the identities:

$$\begin{aligned} &\partial^j\partial_j \ln\Psi + \partial_i \ln\Psi\partial^i \ln\Psi = \frac{\partial_l\partial^j\Psi}{\Psi} \\ &\partial^i\left(\frac{\partial_l\partial^j\Psi}{\Psi}\right) = 2(\partial^j \ln\Psi\partial_l)\partial^i \ln\Psi + \partial^j\partial_l\partial^i \ln\Psi \end{aligned} \tag{26}$$

the equation:

$$\frac{\hat{d}\hat{V}^i}{dt} = -2i\lambda(dt)^{(2/D_F)-1}\partial^i\left[\partial_t \ln\Psi - 2i\lambda(dt)^{(2/D_F)-1}\frac{\partial^j\partial_j \ln\Psi}{\Psi}\right] = 0 \tag{27}$$

By integration up to an arbitrary factor, set to zero by a suitable choice of Ψ phase, from Eq. (27) it results:

$$\lambda^2(dt)^{(4/D_F)-2}\partial^j\partial_j\Psi + i\lambda(dt)^{(2/D_F)-1}\partial_t\Psi = 0 \tag{28}$$

This is an equation of Schrödinger type, describing geodesics in the Schrödinger representation. It is reduced to the usual Schrödinger equation for motions on Peano-type curves, $D_F = 2$ [12–14], at Compton scale, $\lambda = \hbar/2m_0$, where $\hbar$ is the reduced Planck's constant and m_0 the rest mass of the particle. In the presence of an external constrain, defined by a scalar potential U, Eq. (28) can be written in the form:

$$\lambda^2(dt)^{(4/D_F)-2}\partial^j\partial_j\Psi + i\lambda(dt)^{(2/D_F)-1}\partial_t\Psi - \frac{U}{2}\Psi = 0 \tag{29}$$

The relation (29) corresponds to the equation of motion for the "one body problem" in the Schrödinger-type representation of the nondifferentiable model.

The standard equation of motion for the "one body problem" in the Scale Relativity Theory [12–14]:

$$D^2\partial^j\partial_j\Psi + iD\partial_t\Psi - \frac{U}{2}\Psi = 0 \tag{30}$$

results from Eq. (29) for movements of the complex system particles on Peano-type curves, i.e., $D_F = 2$ and the correspondence $\lambda \equiv D$, where D is the coefficient of the fractal-nonfractal transition from Scale Relativity Theory [12–14].

From such a view, in order to obtain the equations of motion for the "two-body problem" in the Schrödinger-type representation of the nondifferentiable model, we will apply a procedure which involves the next steps:

i. the equations of motion for the "two-body problem" are written in the complex momentum representation:

$$\frac{\hat{d}\hat{P_1^l}}{dt} = \partial_1^l \Phi, \frac{\hat{d}\hat{P_2^l}}{dt} = -\partial_2^l \Phi \tag{31}$$

where

$$\hat{P_1^l} = m_1 \hat{V_1^l}, \hat{P_2^l} = m_2 \hat{V_2^l} \tag{32}$$

are the complex momenta, $\hat{V_1^l}$ and $\hat{V_2^l}$ are the complex velocities, m_1 and m_2 are the rest masses of the "bodies" and Φ is the scalar potential of the interaction forces.

ii. let's consider that the motions are irrotational, i.e.,

$$\hat{V_1^l} = -2i\lambda_1 (dt)^{(2/D_F)-1} \partial_1^l \ln\Psi_1, \qquad \hat{V_2^l} = -2i\lambda_2 (dt)^{(2/D_F)-1} \partial_2^l \ln\Psi_2 \tag{33}$$

where $\ln\Psi_1$ and $\ln\Psi_2$ are the scalar potentials of the complex velocities associated to the physical objects.

iii. substituting Eq. (33) in Eq. (31) and following the method described above, the equations of motions of the "bodies" in the absence of direct contact are obtained in the form:

$$\begin{aligned} 2m_1\lambda_1 (dt)^{(2/D_F)-1} \partial_t \Psi_1 &= [-2m_1\lambda_1^2 (dt)^{(4/D_F)-2} \partial^{1l}\partial_{1l} + \Phi]\Psi_1 \\ 2m_2\lambda_2 (dt)^{(2/D_F)-1} \partial_t \Psi_2 &= [-2m_2\lambda_2^2 (dt)^{(4/D_F)-2} \partial^{2l}\partial_{2l} - \Phi]\Psi_2 \end{aligned} \tag{34}$$

In the presence of the direct contact, these equations become:

$$\begin{aligned} 2m_1\lambda_1 (dt)^{(2/D_F)-1} \partial_t \Psi_1 &= [-2m_1\lambda_1^2 (dt)^{(4/D_F)-2} \partial^{1l}\partial_{1l} + \Phi]\Psi_1 + \Gamma_{12}\Psi_2 \\ 2m_2\lambda_2 (dt)^{(2/D_F)-1} \partial_t \Psi_2 &= [-2m_2\lambda_2^2 (dt)^{(4/D_F)-2} \partial^{2l}\partial_{2l} - \Phi]\Psi_2 + \Gamma_{21}\Psi_1 \end{aligned} \tag{35}$$

where Γ_{12} and Γ_{21} are the coupling coefficients of the "bodies."

Since Ψ_1 and Ψ_2 have a direct physical significations only through as $|\Psi_1|^2$ and $|\Psi_2|^2$ probability densities, the deterministic trajectories are replaced by a collection of "potential routes." In its turn, the concept of "definite position" is replaced by that of probability density. Moreover, the complex fluid particles may be reduced to and identified with their own trajectories (i.e., their geodesics) so that complex fluid should behave as a special "fluid" free of interactions—a fractal fluid. In such a conjecture, quantum-type effects (tunneling effect, entanglement effect, etc.) can be extended to the macroscopic complex fluid.

5. Geodesics in the hydrodynamic-type representation

If $\Psi = \sqrt{\rho}e^{iS}$, with $\sqrt{\rho}$ the amplitude and S the phase of Ψ, the complex velocity (24) takes the forms:

http://dx.doi.org/10.5772/67939

$$\begin{aligned} \hat{V_D^i} &= 2i\lambda(dt)^{(2/D_F)-1}\partial^i S \\ \hat{V_F^i} &= 2i\lambda(dt)^{(2/D_F)-1}\partial^i \ln\rho \end{aligned} \tag{36}$$

Substituting Eq. (36) into Eq. (21) in the presence of an external potential and separating the real and imaginary parts, up to an arbitrary factor, set to zero by a suitable choice of Ψ phase, we obtain:

$$\partial_t V_D^i + (\hat{V_D^l}\partial_l)\hat{V_D^i} = -\partial^l(Q+U) \tag{37}$$

$$\partial_t \rho + \partial^i(\rho \hat{V_D^l}) = 0 \tag{38}$$

with Q, the specific nondifferentiable potential:

$$Q = -2\lambda^2(dt)^{(4/D_F)-2}\frac{\partial^l\partial_l\sqrt{\rho}}{\sqrt{\rho}} = \frac{V_F^l V_{Fl}}{2} + \lambda(dt)^{(2/D_F)-1}\partial_i V_F^i \tag{39}$$

Eq. (37) represents the specific momentum conservation law, while Eq. (38) represents the states density conservation law. Eqs. (37)–(39) define the fractal hydrodynamic model and imply the following:

i. any individual component is in permanent interaction with the surrounding fractal medium;

ii. the fractal medium can be identified with a nondifferentiable fluid, described by Eqs. (37)–(39);

iii. even if the fractal velocity $\hat{V_F^i}$ does not reflect a real motion, it influence the specific momentum and energy transfer (confirmed by the its absence from the conservation law of states density); and

iv. most part of the energy is the form of kinetic and potential energy, other parts in other forms, but the overall energy is constant; the energy and the specific momentum conservation is the one that ensures reversibility and the presence of eigenstates, but does not confirm a Levy type motion in an external field.

6. Fractal behaviors

Since, in our model, the fractality plays an essential role in the dynamics of the "complex fluid," next we will expand the model, admitting the following equations:

$$(V_F^i - \lambda(dt)^{(2/D_F)-1}\partial^l)\partial_l V_F^i = 0 \tag{40}$$

$$\partial_l V_F^l = 0 \tag{41}$$

The first equation presents the fact that "the fractal force" is null, while the second one presents the property of incompressibility of the fractal fluid.

6.1. Fractal laminar flow

To find the solutions for these equations can be a relatively difficult, due to the fact that this equation system is a nonlinear one [18–20]. However, there is an analytical solution of this system, in the particular case of a stationary flow in a plane symmetry (x, y). In these circumstances, Eqs. (40) and (41), with $V_F^i = V^i$, take the form:

$$V_x \frac{\partial V_x}{\partial x} + V_y \frac{\partial V_x}{\partial x} = \lambda (dt)^{(2/D_F)-1} \frac{\partial^2 V_x}{\partial y^2} \tag{42}$$

$$\frac{\partial V_x}{\partial x} + \frac{\partial V_y}{\partial y} = 0 \tag{43}$$

where $V_x = V_x(x, y)$ is the velocity along axis Ox, $V_y = V_y(x, y)$ is the velocity along axis Oy. The boundary conditions of the flow are:

$$\lim_{y \to 0} V_y(x, y) = 0, \qquad \lim_{y \to 0} \frac{\partial V_x}{\partial y} = 0, \qquad \lim_{y \to \infty} V_x(x, y) = 0 \tag{44}$$

and the flux momentum per length unit is constant:

$$\Theta = \rho \int_{-\infty}^{+\infty} V_x^2 dy = const. \tag{45}$$

Using the method from [18–20] for resolving Eqs. (42) and (43), with the limit conditions (44) and (45), the following solutions result:

$$V_x = \frac{\left[1.5\left(\frac{\Theta}{6\rho}\right)^{2/3}\right]}{\left[\lambda (dt)^{(2/D_F)-1} x\right]^{1/3}} \cdot \sec h^2 \frac{\left[(0.5y)\left(\frac{\Theta}{6\rho}\right)^{1/3}\right]}{\left[\lambda (dt)^{(2/D_F)-1} x\right]^{2/3}} \tag{46}$$

$$V_y = \frac{\left[4.5\left(\frac{\Theta}{6\rho}\right)^{2/3}\right]}{\left[3\lambda (dt)^{(2/D_F)-1} x\right]^{1/3}} \cdot \left[\frac{\left[y\left(\frac{\Theta}{6\rho}\right)^{1/3}\right]}{\left[\lambda (dt)^{(2/D_F)-1} x\right]^{2/3}} \cdot \sec h^2 \frac{\left[(0.5y)\left(\frac{\Theta}{6\rho}\right)^{1/3}\right]}{\left[\lambda (dt)^{(2/D_F)-1} x\right]^{2/3}} - \tanh \frac{\left[(0.5y)\left(\frac{\Theta}{6\rho}\right)^{1/3}\right]}{\left[\lambda (dt)^{(2/D_F)-1} x\right]^{2/3}} \right] \tag{47}$$

Relations (46) and (47) suggest that the fractal fluid velocity field is highly nonlinear by means of soliton and soliton-kink-type solutions. Given the structural complexity of the fluid (given by its various structural units, that retains their own velocity field), an accurate way of writing relations (46) and (47) will be the one in which we assign indexes for each component.

For $y = 0$, we obtain in relation (46) the critical velocity of the flow in the form:

http://dx.doi.org/10.5772/67939

$$V_x(x, y=0) = V_c = \frac{\left[1.5\left(\frac{\Theta}{6\rho}\right)^{2/3}\right]}{[\lambda(dt)^{(2/D_F)-1}x]^{1/3}} \tag{48}$$

while relation (45), taking into account Eq. (48), becomes:

$$\Theta = \rho \int_{-\infty}^{+\infty} V_x^2(x, y)dy = \int_{-d_c}^{+d_c} V_c^2(x, 0)dy \tag{49}$$

so that the critical cross section of the strain line tube is given by:

$$d_c(x, y=0) = \frac{\Theta}{2\rho V_c^2} = 2.42\left[[\lambda(dt)^{(2/D_F)-1}x]^{2/3}\right]\left(\frac{\rho}{\Theta}\right)^{1/3} \tag{50}$$

Relations (46) and (47) can be strongly simplified if we introduce the normalized quantities:

$$\xi = \frac{x}{x_0}, \quad \eta = \frac{y}{y_0}, \quad u = \frac{V_x}{w_0}, \quad v = \frac{V_y}{w_0}, \quad \Omega = \frac{\left(\frac{\Theta}{6\rho}\right)^{2/3}}{w_0[\lambda(dt)^{(2/D_F)-1}x_0]^{1/3}}, \quad \omega = \frac{\left(\frac{\Theta}{6\rho}\right)^{1/3}y_0}{[\lambda(dt)^{(2/D_F)-1}x_0]^{2/3}} \tag{51}$$

where x_0, y_0, w_0 are the specific lengths and the specific velocity, respectively, of the laminar flow of the fractal fluid. It results that

$$u(\xi, \eta) = \frac{1.5\Omega}{\xi^{1/3}} \sec h^2\left(\frac{0.5\Omega\omega\eta}{\xi^{2/3}}\right) \tag{52}$$

$$v(\xi, \eta) = \frac{4.5^{2/3}}{3^{1/3}}\frac{\Omega}{\xi^{1/3}}\left[\frac{\omega\eta}{\xi^{2/3}} \sec h^2\left(\frac{0.5\Omega\omega\eta}{\xi^{2/3}}\right) - \tanh\left(\frac{0.5\Omega\omega\eta}{\xi^{2/3}}\right)\right] \tag{53}$$

We present in **Figures 1(a, b)–4(a, b)** the dependence of the normalized velocity field u on the normalized spatial coordinates ξ, η for various nonlinearity degrees ($\omega = 0.1,\ 0.2,\ 0.5,\ 5$). The results show that the velocity field on the flow direction (ξ) is affected in a weak manner by the nonlinearity degree (the velocity always decreases on the flow axes regardless of the nonlinearity degree). On the other hand, the flow direction (η) is strongly affected. The flow starts from constant values on the η axis, and with the increase of ω, preferential flow direction can be identified.

Figures 5(a, b)–8(a, b) represent the dependence of the normalized velocity field v on the normalized spatial coordinates ξ, η for various nonlinearity degrees ($\omega = 0.1,\ 0.2,\ 0.5,\ 5$). For small nonlinearity degrees, the variations (increase/decrease) of the velocity field have similar behaviors on both directions (ξ, η), while for higher values of the nonlinearity degree, these variations are only focused on a single direction (ξ).

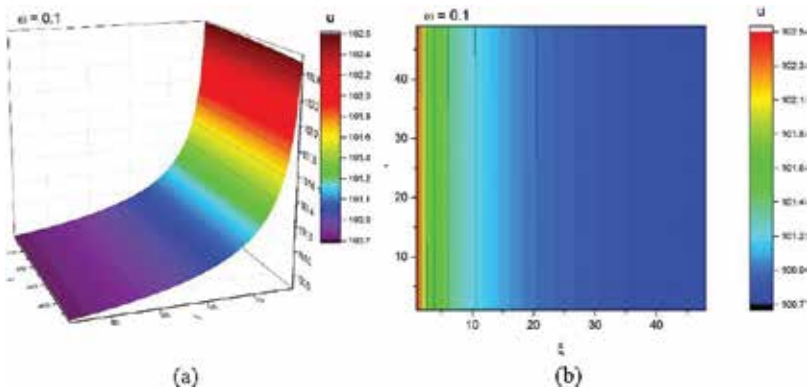

Figure 1. The dependence of the normalized velocity field u on the normalized spatial coordinates ξ, η for the nonlinearity degree $\omega = 0.1$: 3D representation (a), the contour plot (b).

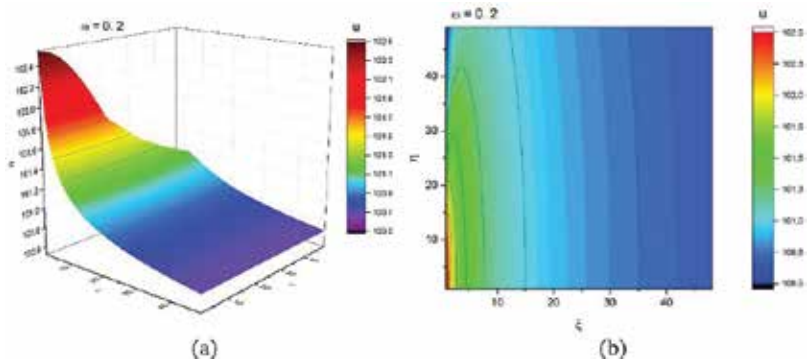

Figure 2. The dependence of the normalized velocity field u on the normalized spatial coordinates ξ, η for the nonlinearity degree $\omega = 0.2$: 3D representation (a), the contour plot (b).

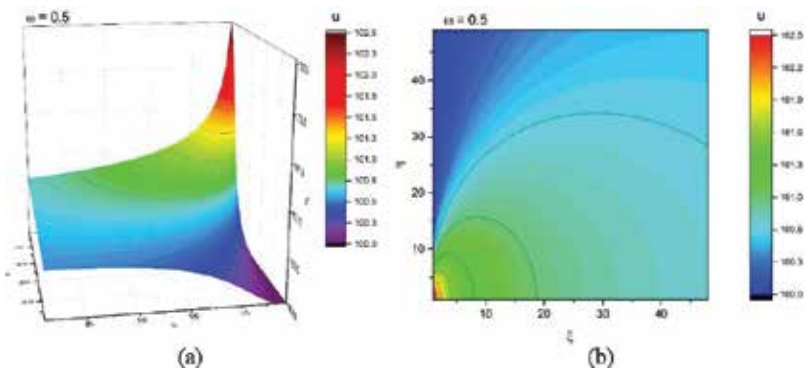

Figure 3. The dependence of the normalized velocity field u on the normalized spatial coordinates ξ, η for the nonlinearity degree $\omega = 0.5$: 3D representation (a), the contour plot (b).

http://dx.doi.org/10.5772/67939

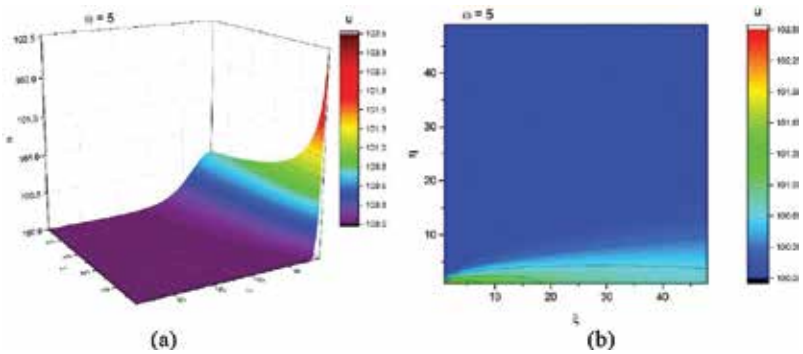

Figure 4. The dependence of the normalized velocity field u on the normalized spatial coordinates ξ, η for the nonlinearity degree $\omega = 5$: 3D representation (a), the contour plot (b).

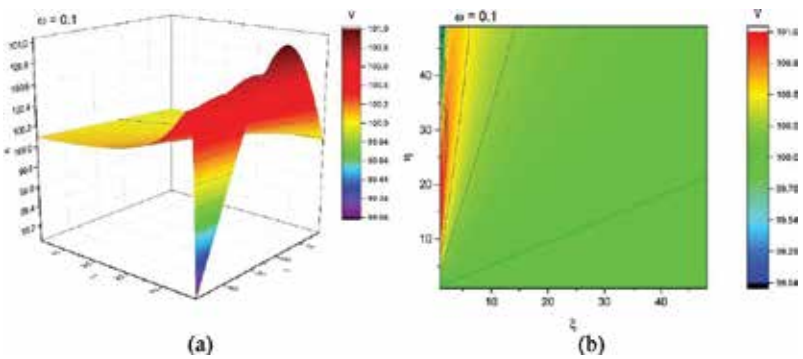

Figure 5. The dependence of the normalized velocity field v on the normalized spatial coordinates ξ, η for the nonlinearity degree $\omega = 0.1$: 3D representation (a), the contour plot (b).

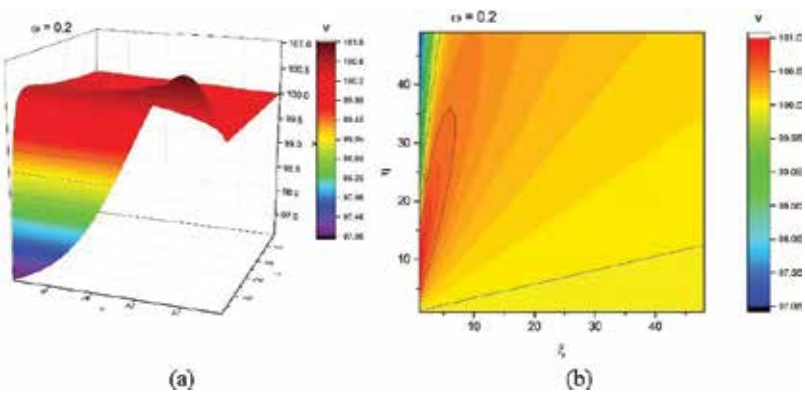

Figure 6. The dependence of the normalized velocity field v on the normalized spatial coordinates ξ, η for the nonlinearity degree $\omega = 0.2$: 3D representation (a), the contour plot (b).

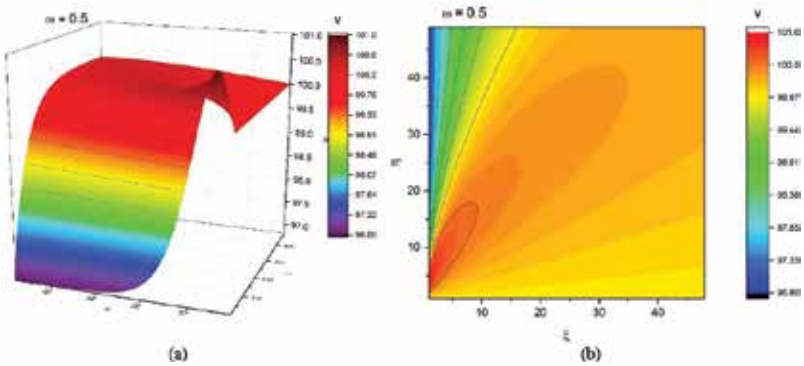

Figure 7. The dependence of the normalized velocity field v on the normalized spatial coordinates ξ, η for the nonlinearity degree $\omega = 0.5$: 3D representation (a), the contour plot (b).

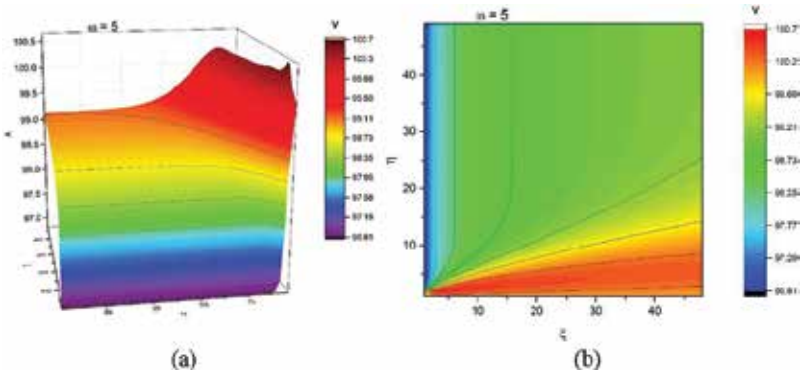

Figure 8. The dependence of the normalized velocity field v on the normalized spatial coordinates ξ, η for the nonlinearity degree $\omega = 5$: 3D representation (a), the contour plot (b).

6.2. Dynamics of laser ablation plasma assimilated as a fractal fluid

Due to the complexity of the interactions between the particles inside the plume as well as to those between the expanding plume and the background gas, it remains difficult to connect the laser-matter interactions with the plume expansion as well with the interactions between the plume and the laser beam, and the buffer gas. In the case of short laser wavelength, the ablation process can be generally divided in several stages [21]. In the first stages, laser-target interactions, such as laser absorption by the target, target heating, occur. If the laser fluency surpasses the ablation threshold of the target, the laser beam evaporates and ionizes material, generating a plasma plume above the material surface. First, the ejected particles undertake strong collisions in a high-density area near the target creating the Knudsen layer [22]. This leads to a directional evolution, orthogonal to the target surface. After the pulse ends, no more particles are ejected from the target surface. An adiabatic expansion of the plasma happens where the temperatures can be related to the dimensions of the plasma; the thermal energy is

http://dx.doi.org/10.5772/67939

then converted into kinetic energy, with the plasma reaching very high expansion velocities [23, 24]. During the initial stages of plasma expansion, defined by high densities, the mean-free path of the particles is short and the plasma dynamic can be considered as one of a continuum fluid. As the plasma expands, the thermal energy decreases at a quick rate; however, the drop diminishes over time since the energy is recovered in the processes of ions recombination. Once the ambient pressure increases, the plume evolution is determined by the interactions of the laser plasma and ambient gas [25].

Given the complexity of the elementary processes involved in the particle removal and plasma expansion presented above, the dynamic of the laser ablation plasmas can be considered a particular case for the fractal fluid previous presented. An exhaustive model is presented in [26, 27]. In such a conjecture, the evolution of the plasma plume can be seen as series of successive dynamics at various resolutions scales, described by a constant particle density. **Figures 9(a, b)–10(a, b)** present the flow of a fractal fluid at two simultaneously different resolution scales. We observed that the field velocity u depends on both expansion direction

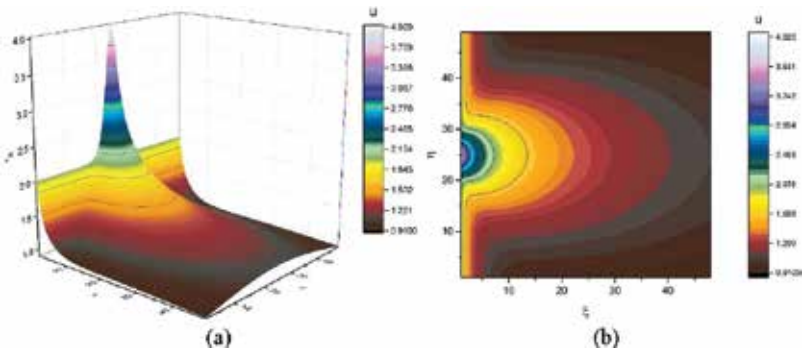

Figure 9. The dependence of the normalized velocity field u on the normalized spatial coordinates ξ, η for two simultaneously resolution scales: 3D representation (a), the contour plot (b).

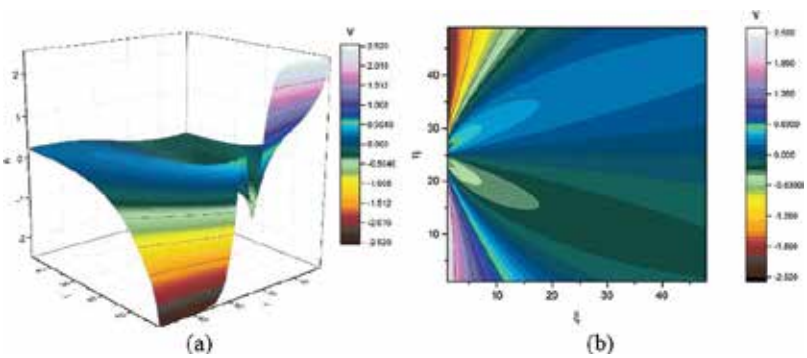

Figure 10. The dependence of the normalized velocity field v on the normalized spatial coordinates ξ, η for two simultaneously resolution scales: 3D representation (a), the contour plot (b).

and its values decrease exponentially. In **Figure 9(a, b)**, it is observed a single maximum, generally attributed to specific plasma structure. The field velocity v presents a similar evolution on the ξ axis while on the η direction we observe a split, described by two maxima, attributed to the splitting process often observed for laser-produced plasmas [26, 27].

6.3. Blood flow dynamics through fractal fluid approach

Blood is a physical fluid that carries both substances needed by cells for body functioning and, also, metabolic waste products from cells. It consists of 45% blood cells (red and white globules, platelets) and 55% plasma (92% water and various substances in dissipated forms, i.e., protein, glucose, ions, minerals, hormones, carbon dioxide, and cholesterol). Among blood cells, most numerous are red globules containing hemoglobin, a protein with iron in its structure, which facilitates the transport of oxygen by creating ionic bonds with it. In contrast, carbon dioxide is mostly transported extracellular as bicarbonate ion transported in plasma.

Blood is kept in continuous motion in the blood vessels by the heart, through its muscle contraction. Oxygen is transported by the arterial blood to all body cells, from where the waste product, carbon dioxide, is taken by the venous blood and carried to the lungs to be exhaled.

From a physical-chemical point of view, the blood is a suspension, a mixture of liquids, gases, and solids (cells).

In terms of anatomy and histology, blood is considered a specialized form of connective tissue, given its origin in the bones and the presence of potential molecular fibers in the form of fibrinogen.

Since the circulatory system has a fractal structure, it is expected like its functionality to be also fractal. This allows us to assimilate the dynamics of the blood flow with the one of the fractal fluid. In this context, although the velocity fields will remain the same as the one presented in **Figures 1–8**, it is of great importance for the understanding of arterial occlusion and other circulatory system diseases, the force that the fluid will exercise to the walls of the flow vessels.

In our case, the normalized force is given by the relation:

$$F = \partial_\eta u - \partial_\xi v = -\frac{1.5\Omega \sec h^2\left(\frac{0.5\omega\eta}{\xi^{2/3}}\right)\tanh\left(\frac{0.5\omega\eta}{\xi^{2/3}}\right)}{\xi} - \frac{1}{\xi^{1/3}}\left(0.9\Omega\left(-\frac{2}{3}\frac{\omega\eta \sec h^2\left(\frac{0.5\omega\eta}{\xi^{2/3}}\right)}{\xi^{5/3}} + \frac{0.66\omega^2\eta^2 \sec h^2\left(\frac{0.5\omega\eta}{\xi^{2/3}}\right)\tanh\left(\frac{0.5\omega\eta}{\xi^{2/3}}\right)}{\xi^{7/3}} + \frac{0.33\left[\left(1-\tanh^2\left(\frac{0.5\omega\eta}{\xi^{2/3}}\right)\right)\omega\eta\right]}{\xi^{5/3}}\right)3^{\frac{3}{2}}\right)$$
$$+ \frac{0.3\Omega\left(\frac{\omega\eta \sec h^2\left(\frac{0.5\omega\eta}{\xi^{2/3}}\right)}{\xi^{2/3}} - \tanh\left(\frac{0.5\omega\eta}{\xi^{2/3}}\right)\right)3^{\frac{3}{2}}}{\xi^{4/3}} \tag{54}$$

In **Figures 11(a, b)–14(a, b)**, it is represented the normalized force field evolution on the two flow direction (ξ, η) for various nonlinear degrees. It results that with the increase of the

http://dx.doi.org/10.5772/67939

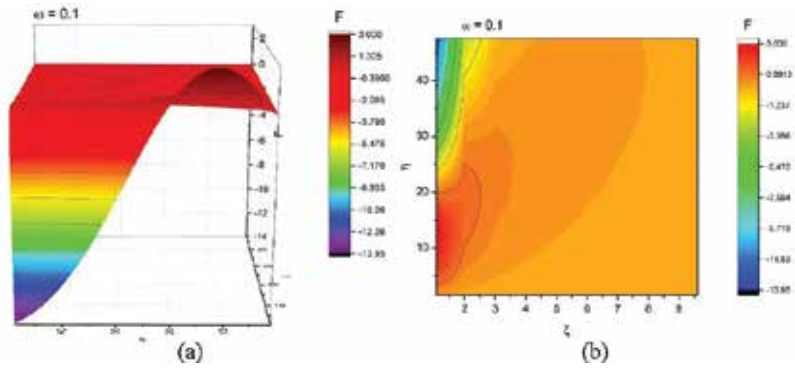

Figure 11. The dependence of the normalized force field F on the normalized spatial coordinates ξ, η for the nonlinearity degree $\omega = 0.1$: 3D representation (a), the contour plot (b).

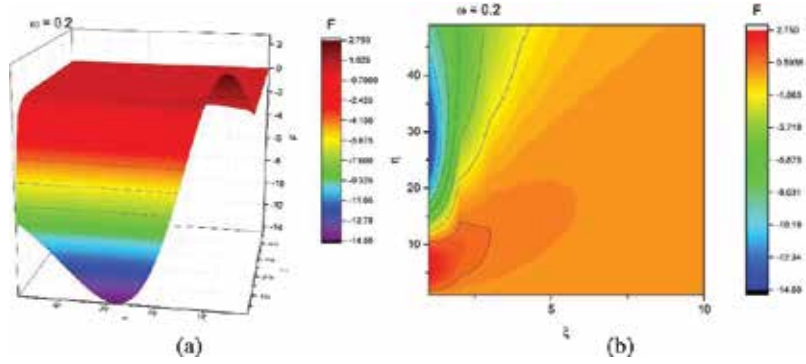

Figure 12. The dependence of the normalized force field F on the normalized spatial coordinates ξ, η for the nonlinearity degree $\omega = 0.2$: 3D representation (a), the contour plot (b).

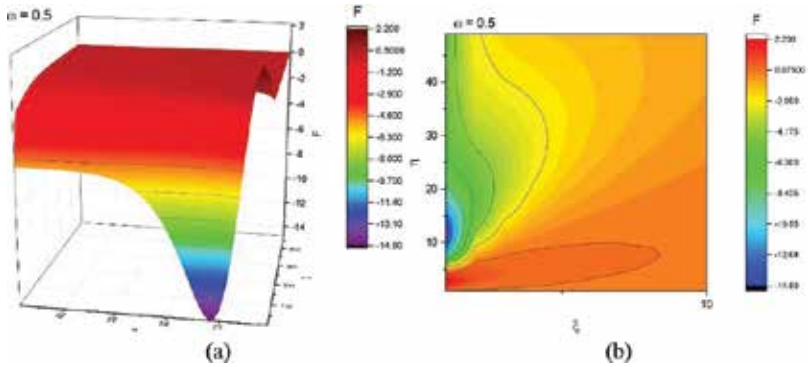

Figure 13. The dependence of the normalized force field F on the normalized spatial coordinates ξ, η for the nonlinearity degree $\omega = 0.5$: 3D representation (a), the contour plot (b).

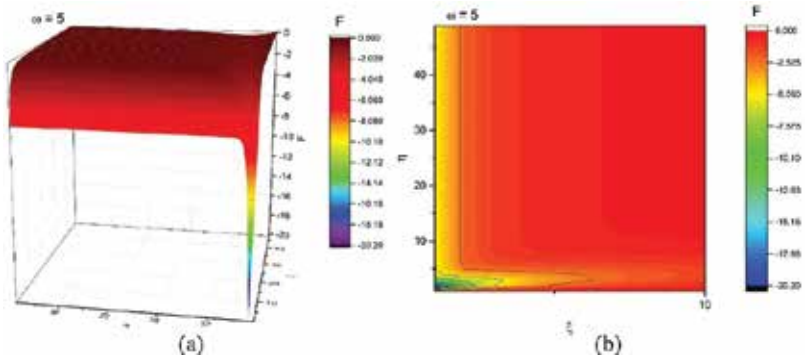

Figure 14. The dependence of the normalized force field F on the normalized spatial coordinates ξ, η for the nonlinearity degree $\omega = 5$: 3D representation (a), the contour plot (b).

nonlinearity of the fluid the force toward the walls increases. This can be a starting point for understanding the complexity of the mechanisms involved in the arterial occlusion.

The proposed theory has the advantage that it explains from a fractal point of view the atherogenesis process [28], basically "molding" to the classical anatomical and histopathological descriptions, completely respecting the process postulated by them. Thus, the fractal physics model represents a dynamic and novel argument for sustaining already accumulated morphopathological information and research. The electronic and optical microscopy images (**Figure 15**) describe the spatiotemporal hologram of the phenomenon; we can thus talk about the nonfractal-fractal and microscopic-macroscopic translation through holographically reproducible autosimilarity [28]. We can thus say that fractality represents the mathematical and semantic quintessence for defining atherogenesis, a process that can be physically characterized perfectly by fractal physics, physics becoming in this situation more of a component rather than an explanation for the complex biological system represented by the atheroma plaque [28].

Regarding the recovery of such biological diseases, there are a vast number of techniques. We remind that external electrical stimulation can cause changes in the blood vessels. Although

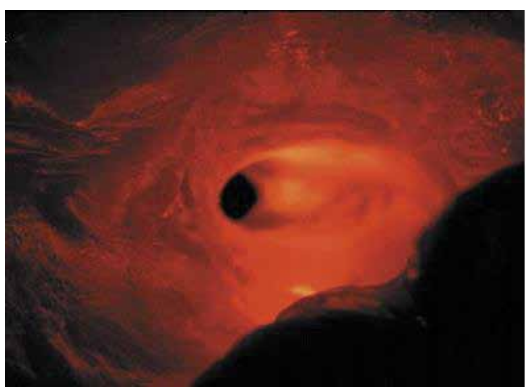

Figure 15. Endoluminal view—significant atherosclerotic plaque with thrombus (optical microscopy).

http://dx.doi.org/10.5772/67939

atherosclerosis cause vasodilatation in the affected area and blood flow remains unchanged for an extended period of time, the vascular wall stiffness will increase the pulse pressure [29]. Tracy et al. developed, in 1950, a study whose purpose was to measure the effects of electrical stimulation (ES) on blood flow and blood pressure. All subjects received electrical stimulation at intensity sufficient to produce torque equal to 15% of the predetermined maximal voluntary contraction of their right quadriceps femoral muscle. The conclusions were that the increase in blood flow occurred within 5 min after the onset of ES and dropped to resting levels within 1 min after a 10-min period of ES [30].

Kinesiotherapy or kinesitherapy or kinesiatrics is the therapeutic treatment of disease by passive and active muscular movements (as by massage and by exercise) [31].

From the physiotherapeutic point of view, the treatment is directed toward improving blood flow and toward decreasing the disparity between the demand for blood and its supply [32].

An effective vascular rehabilitation training program for improving walking efficiency and vascular remodeling in patients with diabetic atherosclerosis suffering from intermittent claudicating could be a supervised treadmill walking exercise combined with Allen-Burger exercises [33].

7. Complex system with the self-elimination of dissipation

If the fractalization is achieved by Markov-type stochastic processes, the scale covariant derivative (18) takes the form:

$$\frac{\hat{d}}{dt} = \partial_t + \hat{V}^l \cdot \partial_l \pm i\lambda(dt)^{(2/D_F)-1}\partial^l\partial_l \tag{55}$$

Postulating now the scale covariance principle the states density conservation laws become:

$$\frac{\hat{d\rho}}{dt} = \partial_t\rho + \hat{V}^l \cdot \partial_l\rho \pm i\lambda(dt)^{(2/D_F)-1}\partial^l\partial_l\rho \tag{56}$$

or more, separating the movement on the scale resolution:

$$\partial_t\rho + V^l\partial_l\rho = 0 \tag{57}$$

for the differentiable scale resolution and:

$$-V_F^l\partial_l\rho \pm \lambda(dt)^{(2/D_F)-1}\partial^l\partial_l\rho = 0 \tag{58}$$

for the nondifferentiable scale resolution. From such a perspective, the fractal-nonfractal dynamic transition of the state density can be obtained by summing Eqs. (57) and (58), taking the form:

$$\partial_t\rho + (V_D^l - V_F^l)\cdot\partial_l\rho \pm \lambda(dt)^{(2/D_F)-1}\partial^l\partial_l\rho = 0 \tag{59}$$

From here, by identifying the movements at the two resolution scales $V_D^l = V_F^l$, the fractal-type diffusion equations become:

$$\partial_t \rho \pm \lambda (dt)^{(2/D_F)-1} \partial^l \partial_l \rho = 0 \tag{60}$$

Let us now use Eq. (60) to analyze the dynamic of an electron beam accelerated in a strong electric field which impinges onto a neutral medium. As a result of these interactions, ionizations are produced by: (i) the primary electrons (from the fascicle), which are accelerated by an external electrical field, $-\alpha j$, where α is the primary ionization coefficient and j is the fascicle current density and by (ii) secondary electrons which results from the direct ionization process, $-\beta j \rho_e$, with $-\beta$ the secondary ionization coefficient and ρ_e the electron density. In this circumstance, we will further focus on the study of the dynamics induced only by the electronic branch through Eq. (60) written in the following form:

$$\partial_t \rho_e + \lambda (dt)^{(2/D_F)-1} \partial^l \partial_l \rho_e = -\alpha j - \beta j \rho_e \tag{61}$$

Since the previous dynamics implies a dimensional symmetry, Eq. (61) by means of substitutions:

$$\tau = \frac{x}{v} - t, \quad M = \frac{\Lambda}{\beta j v^2} \lambda (dt)^{(2/D_F)-1}, \quad 2R = -\frac{\Lambda}{\beta j}, \quad K = \Lambda, \quad \alpha j + \beta j \rho_e = \Lambda q \tag{62}$$

becomes a damped oscillator-type equation:

$$M\ddot{q} + 2R\dot{q} + Kq = 0 \tag{63}$$

Rewritten as:

$$\dot{p} = -2\frac{R}{M} p - \frac{K}{M} q, \quad q = p \tag{64}$$

Eq. (63) induces a two-dimensional manifold of phase space type (p, q) in which p would correspond to a momentum-type variable and q to a "position" type. Then, the parameters M, R, and K can have the following significance:

i. M characterizes the "inertial" type effect through the connection with ionization processes (global ionization described by $\alpha j + \beta j$ and the local ones described by βj) as well as in respect with the fractal diffusion ($\lambda (dt)^{(2/D_F)-1}$). All these are done with respect to a traveling wave-type movement based on the self-similar dynamic solutions ($\tau = \frac{x}{v} - t$);

ii. R represents the "dissipative" type effects through the connection with the ionization processes, the same as above;

iii. K represents the structural type efforts in connection with the ionization processes, consisting, in this case, only from global ionization effects $\alpha j + \beta j$.

The second equation from Eq. (64) corresponds to the momentum definition. Eq. (64) is not a Hamiltonian system, because the matrix traces are not null, and, as consequence, the associated matrix is not an involution. The observation becomes more obvious if we write it in matrix form:

http://dx.doi.org/10.5772/67939

$$\begin{pmatrix} \dot{p} \\ \dot{q} \end{pmatrix} = \begin{pmatrix} -2\dfrac{R}{M} & -\dfrac{K}{M} \\ 1 & 0 \end{pmatrix} \cdot \begin{pmatrix} p \\ q \end{pmatrix} \tag{65}$$

With M, R, K constant values, this matrix equation, written in an equivalent form, evidences the position of the energy, i.e., of the Hamiltonian. From Eq. (64) we can write:

$$\frac{1}{2}M(p\dot{q} - q\dot{p}) = \frac{1}{2}(Mp^2 + 2Rpq + Kq^2) \tag{66}$$

which proves that the energy in its quadratic form, i.e., the right-hand side of Eq. (66) is the variation rate of the physical action represented by the elementary area from the phase space. We would like to show here that the energy does not have to satisfy the conservation laws in order to act like a variation rate for the action. Another issue is the form of the conservation law, if it exists. For this, Eq. (66) will be written as a Riccati-type differential equation:

$$\dot{w} + w^2 + 2\mu w + \omega_0^2 = 0, \quad w = \frac{p}{q}, \quad \mu = \frac{R}{M}, \quad \omega_0^2 = \frac{K}{M} \tag{67}$$

The Riccati-type equation (67) represents always a Hamiltonian system that describes a dynamic of harmonic oscillating type:

$$\begin{pmatrix} \dot{p} \\ \dot{q} \end{pmatrix} = \begin{pmatrix} -\dfrac{R}{M} & -\dfrac{K}{M} \\ 1 & \dfrac{R}{M} \end{pmatrix} \cdot \begin{pmatrix} p \\ q \end{pmatrix} \tag{68}$$

This is a general characteristic of the Riccati-type equations and of the Hamiltonian's dynamic [34]. The 1-differential form for the elementary area from the phase space, obtained from Eq. (68), is identical with Eq. (60). Considering that the energy does not conserve anymore, but another, more complicated, dynamics variable is conserved, Eq. (65), by integration becomes [35]:

$$\frac{1}{2}(Mp^2 + 2Rpq + Kq^2) \cdot \exp\left\{\frac{2R}{\sqrt{MK - R^2}}\arctan\left(\frac{Mp + Rq}{q\sqrt{MK - R^2}}\right)\right\} = const \tag{69}$$

The energy conservation, in the classical meaning, occurs if either R is null, either the movement in the phase space takes place on a line though origin, with the slope R/M.

Moreover, by comparison with the case of the thermal radiation, regarding the distribution function of a preestablished ensemble [36]:

$$P(r, w) = \frac{1}{1 + 2rw + w^2}\exp\left[\frac{2r}{(1 - r^2)^{1/2}}\arctan\frac{w(1 - r^2)^{1/2}}{1 - rw}\right] \tag{70}$$

with r the correlation coefficient and $w^2 = \varepsilon_0/u$ the ratio between the quanta of thermal energy and the reference energy u, relation (69) becomes:

$$\frac{Kq^2}{2} = \frac{const}{1+2rw+w^2} \exp\left[2\frac{r}{(1-r^2)^{1/2}} \arctan\frac{w(1-r^2)^{1/2}}{1-rw}\right], \quad w^2 = \frac{Mp^2}{kq^2}, \quad r^2 = \frac{R}{k} \tag{71}$$

From here we can emphasize the statistic character of energy: the potential energy is constructed as a functional of a specific statistical variable, given by the ratio between the kinetic energy and the potential one of a local oscillator.

Through the correlation of all the oscillator-type ensembles, a "quantization" procedure can be established, by using the condition:

$$P(r,1) = e^{-\frac{\varepsilon_0}{kT}} = \frac{1}{2(1+r)} \exp\left[2\frac{r}{(1-r^2)^{1/2}} \arctan\left(\frac{1+r}{1-r}\right)^{1/2}\right]$$

where k is the Boltzmann constant and T the characteristic temperature of the thermal radiation (for details, see [37]). **Figure 16(a, b)** presents the **"**quantization" procedure through correlation of all statistical ensembles associated with "local oscillators."

It shows explicitly the connection between the "quanta" and the statistical correlation of the process represented by the thermal radiation. Moreover, it also specifies the expression of the "quanta" in the small correlation limit, i.e., for $r \to 0$, as $\varepsilon_0 \to kT\ln 2$.

Thus, in such limit, the quanta and, implicitly, the frequency υ (through $\varepsilon_0 = h\upsilon$, where h is the Plank constant) are proportional with the "color" temperature.

Since we are focused on identifying these dissipative forces, we will try and present a physical significance for the Riccati equation (67) and of the associated Hamiltonian (68). For this, we observe that Eq. (63) is the expression of a variation principle:

$$\delta\int_{t_0}^{t_1} Ldt = 0 \tag{72}$$

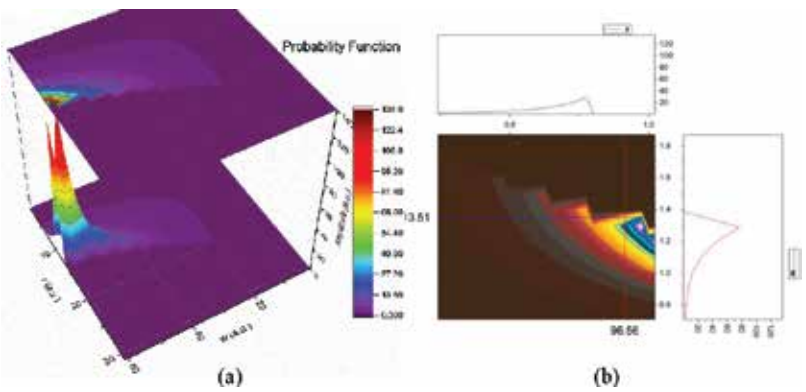

Figure 16. The probability function: in (r, w) space (a), and in the contour plot representation (b).

http://dx.doi.org/10.5772/67939

regarding the Lagrangian:

$$L(q,\dot{q},t)=\frac{1}{2}(M\dot{q}^2-Kq^2)\cdot e^{2\frac{R}{M}t} \tag{73}$$

This represents the Lagrangian form of a harmonic oscillator with explicit time-dependent parameters. The Lagrangian integral defined on a finite interval $[t_0, t_1]$ is the physical action of an oscillator on that specific time interval, describing the difference between the kinetic energy and the potential one. In order to obtain Eq. (63), it is necessary to consider the variation of this action under explicit conditions in such way that the variance of the coordinate at the interval extremes is null:

$$\delta q|t_0=\delta q|t_1=0 \tag{74}$$

In order to obtain a closed trajectory, a supplementary condition must be imposed; for example, that the coordinates values at the interval extremes are identical:

$$q(t_0)=q(t_1) \tag{75}$$

Moreover, if this trajectory is closed in the phase space, the same condition results also for velocities.

Let us focus now on the movement principle. The Lagrangian is defined until an additive function which needs to be derivative in respect with the time of another function. The procedure is largely used in theoretical physics by defining the gauge transformation. In our case we define a gauge transformation in which the Lagrangian is a perfect square. This is known and explored in the control theory [34]. The procedure consists in adding to the Lagrangian the following term:

$$\frac{1}{2}\frac{d}{dt}\left(we^{2\frac{R}{M}t}\cdot q^2\right) \tag{76}$$

where w is a continuous function in time, so that the Lagrangian is a perfect square. The function variation is null, only due to the conditions presented in Eq. (75) and, therefore, the motion equation does not change. The new Lagrangian, written in relevant coordinates, takes the form:

$$L(q,\dot{q},t)=\frac{1}{2}M\cdot e^{2\frac{R}{M}t}\left(\dot{q}+\frac{w}{M}q\right)^2 \tag{77}$$

with the condition that w satisfies the following Riccati-type equation:

$$\dot{w}-\frac{1}{M}w^2+2\frac{R}{M}w-K=0 \tag{78}$$

The Lagrangian from Eq. (77) can be considered here as representing the whole system energy. As before, there is a relationship between the Riccati equation (78) and the Hamiltonian dynamic. Henceforth, we will find a similar relation to the one presented in Eq. (68):

$$\begin{pmatrix} \dot{\eta} \\ \dot{\xi} \end{pmatrix} = \begin{pmatrix} -\frac{R}{M} & -\frac{K}{M} \\ 1 & \frac{R}{M} \end{pmatrix} \cdot \begin{pmatrix} \eta \\ \xi \end{pmatrix}, \quad w = \frac{\eta}{\xi} \tag{79}$$

In this case, our system is obviously a Hamiltonian one. Thus, we can identify the w factors with the phase space coordinates. Eq. (78) specifies the fact that w is a dissipation factor (a mass variation rate, for the variable mass case). It is important to find the most general solution of this equation. Carena and Ramos presented a modern approach to integrate a Ricccati equation [38]. Applied to our case, it is enough to note the complex numbers as:

$$w_0 \equiv R + iM\Omega, \quad w_0^* \equiv R - iM\Omega, \quad \Omega^2 = \frac{K}{M} - \left(\frac{R}{M}\right)^2 \tag{80}$$

The roots of the quadratic polynomial from the right-hand part of Eq. (78) are two constant solution of the equation. Being constant, their derivative is null; thus, the polynomial is also null. In order to avoid this situation, we first perform the homographic transformation:

$$z = \frac{w - w_0}{w - w_0^*} \tag{81}$$

In these circumstances, it results that through direct determination, z is a solution of a linear and homogeneous first-order equation:

$$\dot{z} = 2i\Omega \cdot z \therefore z(t) = z(0)e^{2i\Omega \cdot t} \tag{82}$$

Hence, if we express the initial condition $z(0)$ in a right manner, we can obtain the general solution of Eq. (78) by applying an inverse transformation to Eq. (81). We find:

$$w = \frac{w_0 + re^{2i\Omega(t-t_r)}w_0^*}{1 + re^{2i\Omega(t-t_r)}} \tag{83}$$

where r and t_r are two real constants which are characterizing the solution. Using Eq. (78) we can write the same solution in real terms:

$$z = R + M\Omega \cdot \left(\frac{2r\sin[2\Omega(t-t_r)]}{1 + r^2 + 2r\cos[2\Omega(t-t_r)]} + i\frac{1 - r^2}{1 + r^2 + 2r\cos[2\Omega(t-t_r)]}\right) \tag{84}$$

This relation shows frequency modulation through a Stoler transformation [39], which leads to the complex representation of this parameter.

The theoretical model proposed here analyzes the dynamic of charged particles in a plasma discharge where there is a strong flux of electrons from one plasma structure to another. Basically, the electrons dynamics are described using a forced damped oscillating system, with the aim to investigate the response of the global discharge current to different changes in resolution scale, oscillation frequency and dapping coefficient. Since our mathematical approach is sensitive to the changes in the resolution scales, we plotted in **Figure 17(a–f)** the 3D maps and the

http://dx.doi.org/10.5772/67939

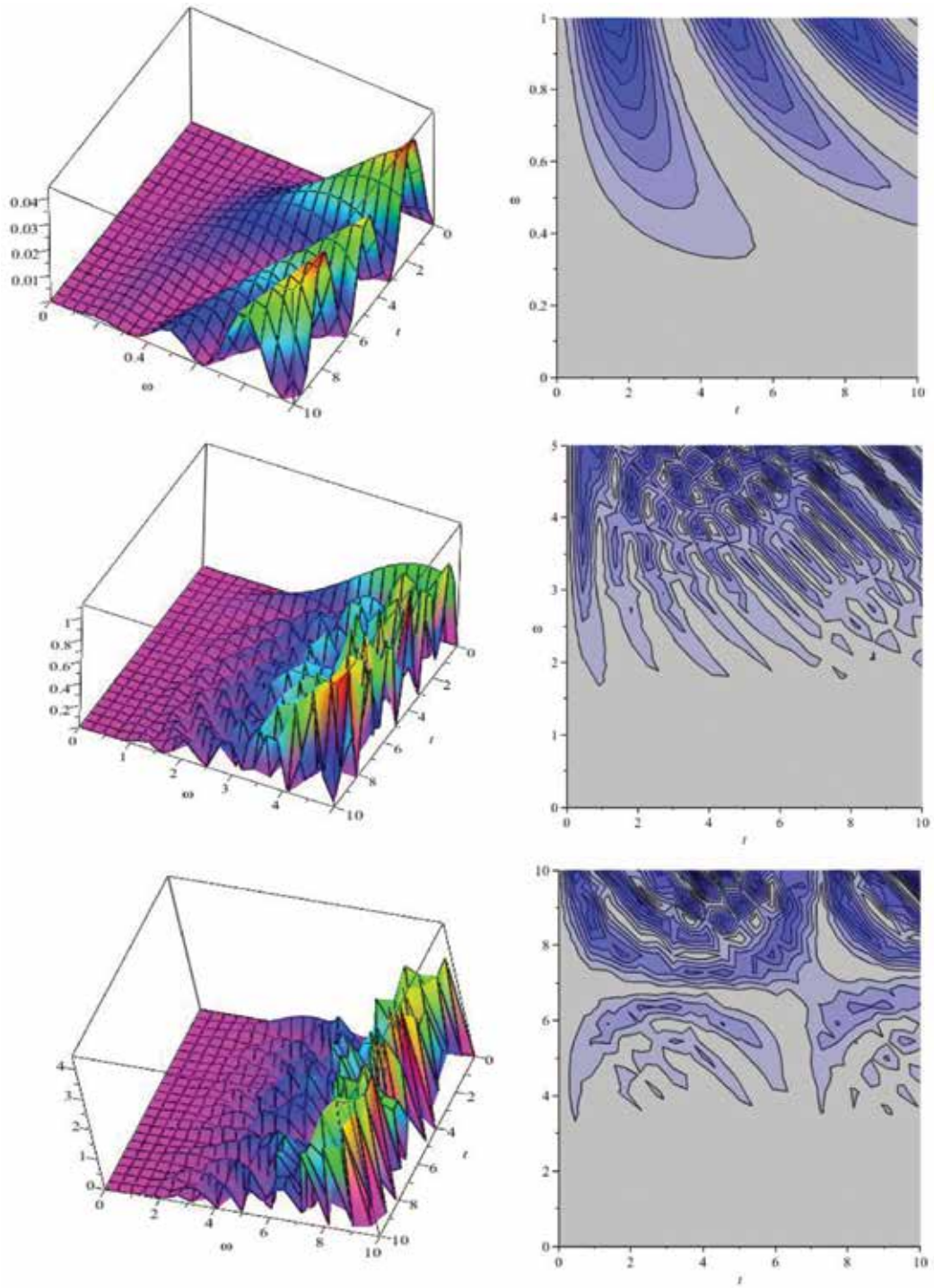

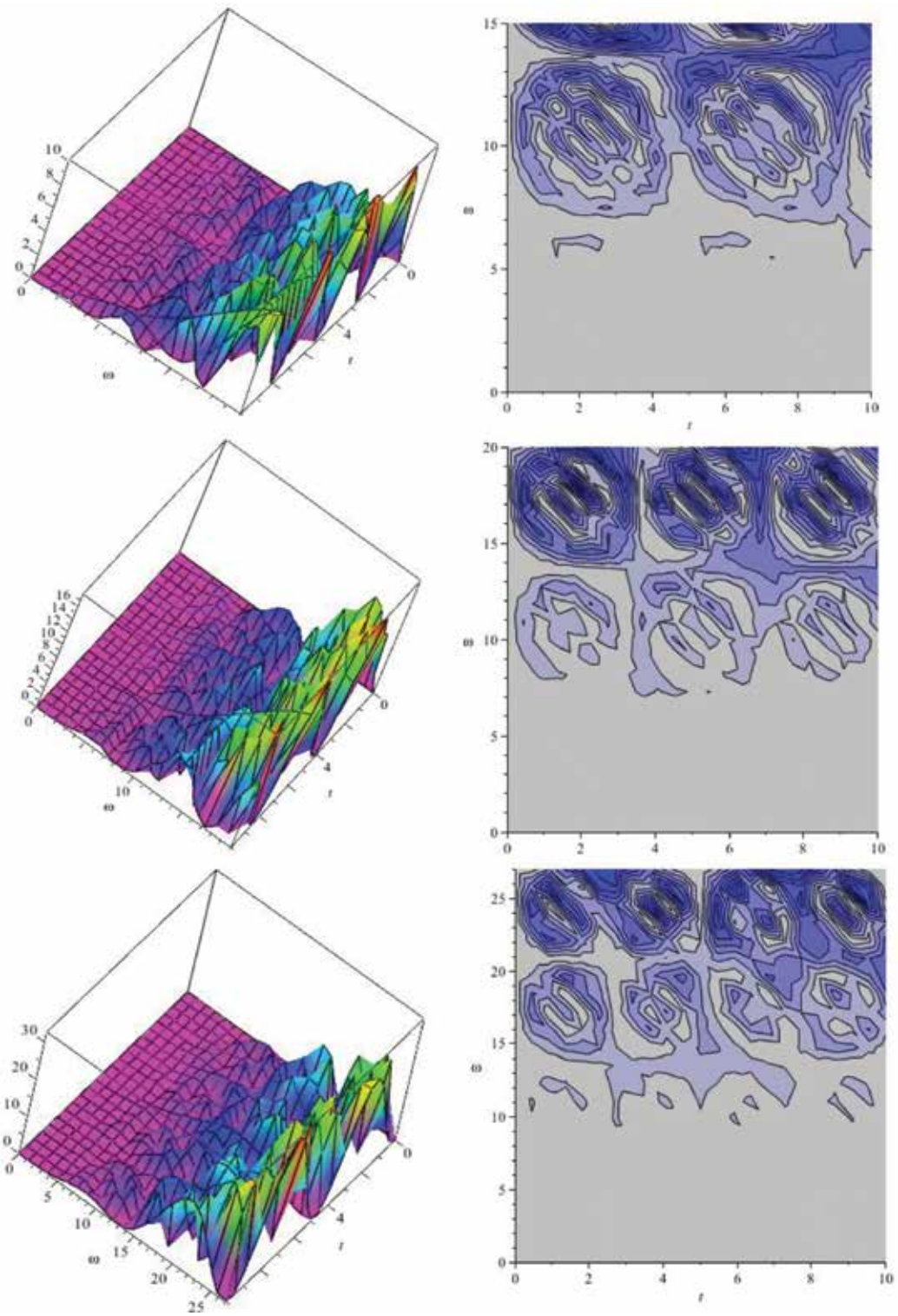
ω
t
ω
t
ω
t

http://dx.doi.org/10.5772/67939

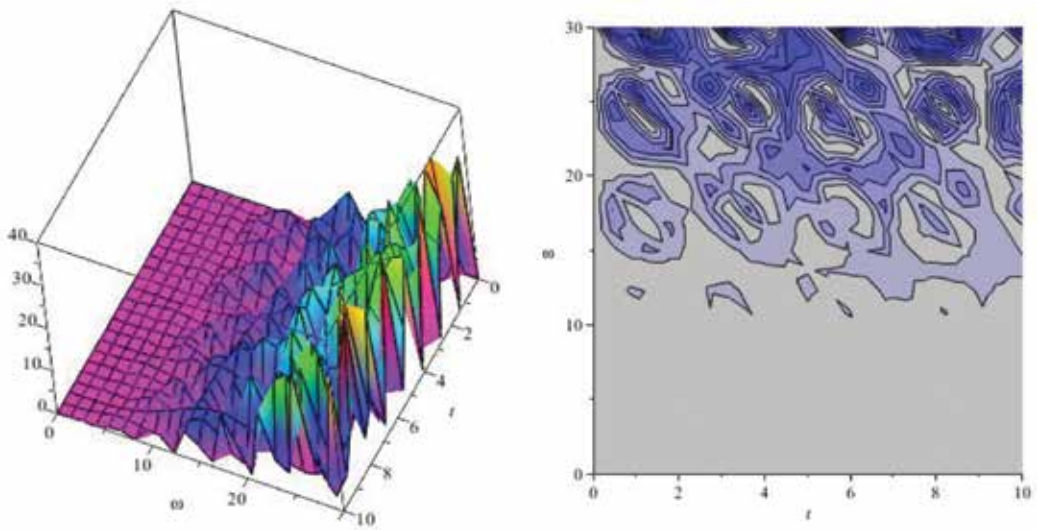

Figure 17. 3D representation of the discharge current for different resolution scales: 0–1 (a), 0–10 (b), 0–15 (c), 0–20 (d), 0–25 (e), 0–30 (f) with respect to the oscillation frequency and the corresponding contour plot representations.

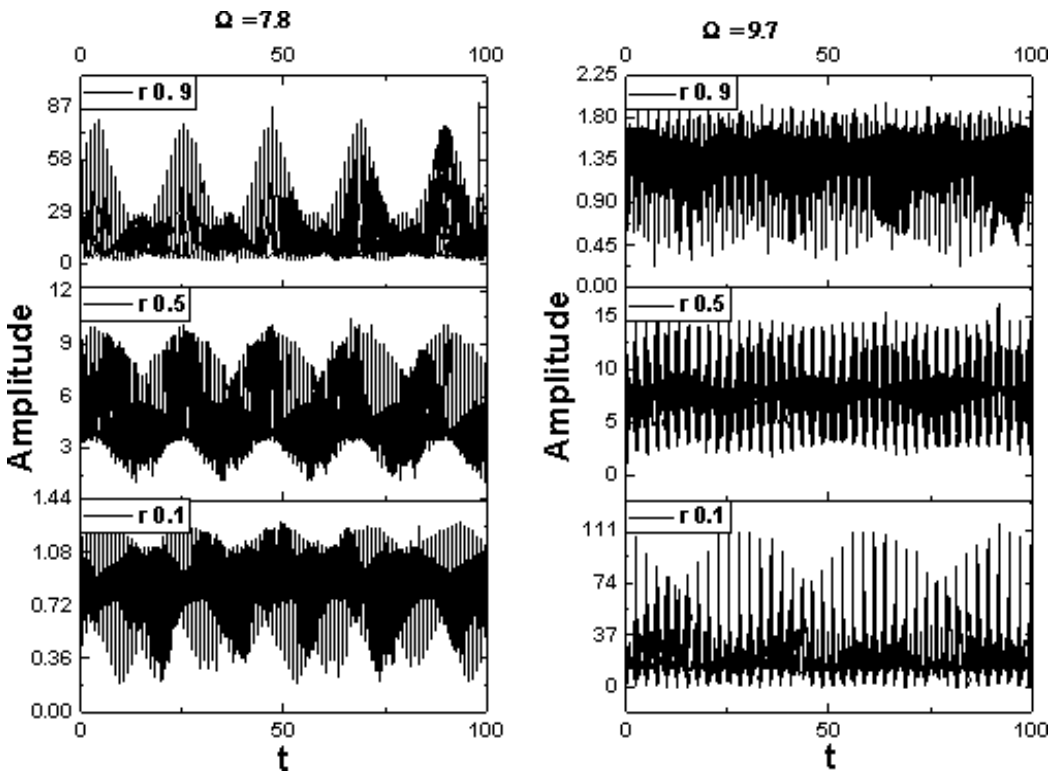

Figure 18. (a and b) Discharge current temporal traces for various values of the damping coefficient extracted for two different frequencies scales.

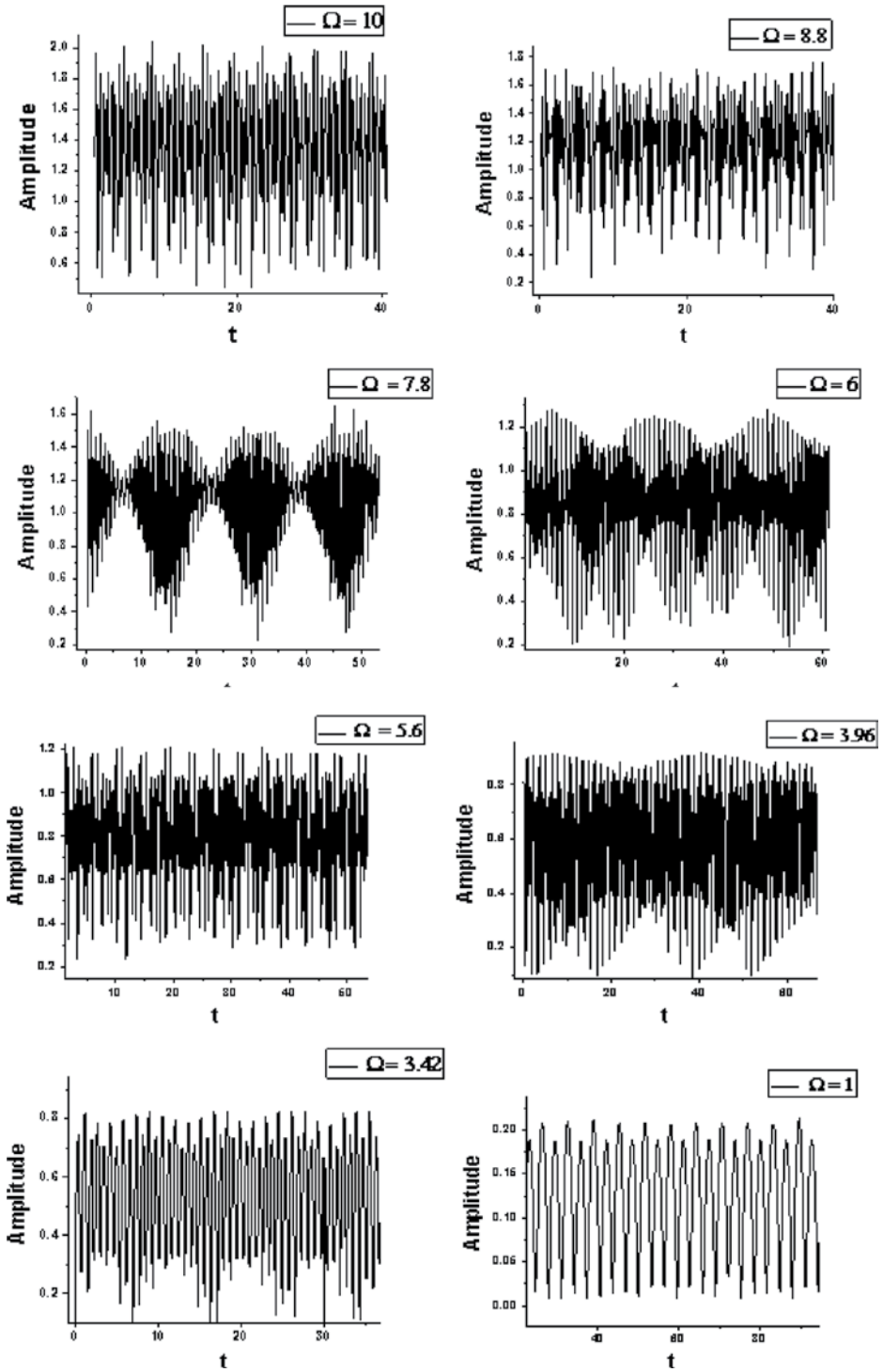

Figure 19. Discharge current temporal traces for different values of the oscillation frequency at a constant damping coefficient ($r = 0.1$).

http://dx.doi.org/10.5772/67939

corresponding contour plot representations of the discharge current as functions of time and oscillation frequency, for a fixed value of the damping constant: 0,1. We observe that, for small resolutions, the current is described by a simple oscillatory regime, and, as the frequency resolution scale increases, we notice the appearance of some patterns. The patterns become denser and are foreshadowing the presence of some modulation in the oscillating frequency.

The damping of the oscillatory state describes the losses through dissipative mechanisms. In order to study the effects induced by these mechanisms on the global current, we pointed two different oscillation frequencies, and observe the temporal response at different values of the damping coefficient. The results can be seen in **Figure 18(a, b)**.

We can identify competing oscillatory behaviors, described by two oscillation frequencies with comparable amplitudes. As the damping increases, the ratio between the two changes oscillation frequencies, and in the end the system oscillates on a single frequency.

The effect of the forced oscillations, which can be attributed to one of the plasma structures, is presented in **Figure 19**, where the discharge current for a fixed value of the damping coefficient and various values of the forced oscillations is represented. The systems seemingly start from a state described by period doubling, and goes through frequency modulation as the values increase. The important aspect is that the oscillation frequencies found for the current are not the ones induced through forced oscillatory system. This means that the system although forced to get on a specific state, it will define its own dynamic influenced, but not determined, by the external parameters.

Finally, we investigated the evolution of our system with the increase of the control parameter ω. We investigate for a large range of values the evolution of the system and we observe (**Figure 20a**) that the system starts from double period state (see **Figure 19**), which arises periodically as the values of the control parameter increases. Also, the amplitude of such oscillations increases of about 10 times. In **Figure 20(b)**, the bifurcation map is presented, where we observe that our system starts from steady state (double period state) and passes toward a chaotic one ($\omega = 7, 22, 44$), but never reaches it.

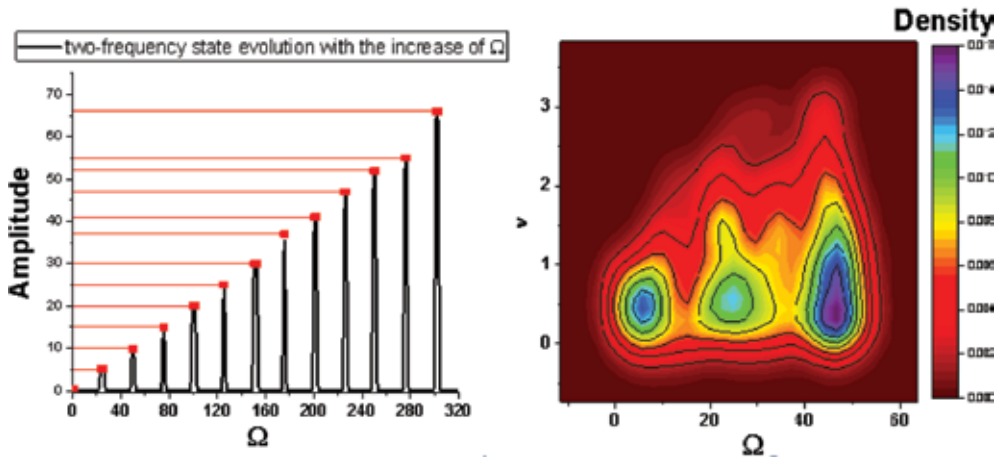

Figure 20. The evolution of the double-period state (a) and the characteristic bifurcation map (b) with relation to the control parameter ω.

Thus, the evolution of complex system, in our case a plasma, not only intends to reach a chaotic state, but each transition back to the steady state leads to an increase in the system energy, which can be seen in the increase of the amplitude.

8. Conclusions

This chapter proposes a new approach for the analysis of dynamics in complex systems based on fractal models, based on the assumption that the "individual components" motion takes place on continuous, but nondifferentiable curves. Consequently, the standard and the "exotic" properties of complex system flow at meso and nano scale can be highlighted.

In this framework, we analyze possible implications of complex fluids in blood flow dynamics. We can affirm that the fractal physics can explain the initiation phase of arteriosclerosis, overcoming the common expression found in classical medicine, "at a certain moment," which lacks a precise temporal-spatial definition. Moreover, our model imposes redefinition of "good" and "bad" cholesterol, traditionally associated with HDL, respectively LDL. Instead, they should be replaced by the following notions: specific cholesterol entities, associated with a certain nondifferentiable curve, that have a major endothelial impact, i.e., HDL, and specific cholesterol particles which have no or low endothelial impact, i.e., LDL.

We consider that our complex system flow model could also be used for the further development of the study of other complex systems dynamics, such as pulmonary and metabolic diseases or environmental systems.

The evolution of a complex system (plasma discharge or biological systems) was discussed as nonconservative and presented in a simpler way (i.e., through a forced damped oscillating system). Here, the driving force is used to simulate the response of the immune system, while the damping covers the energy loses during the evolution of the tumor cells. Once such a system is chosen, by simply investigating its dynamics, we were able to observe that the systems start from a steady (oscillating state), and as the external factor is varied, the system undergoes significant changes. The system evolves asymptotically through various transition, toward a chaotic regime (like bifurcations or intermittencies), but never reaching it. Another important reveal from the study of the system's dynamics, was the presence of various steady states depending on the resolution scale at which the theoretical investigations are performed.

Our study not only shows the chaotic evolution tendencies of the complex system, but also reveals that there is a high probability for the presence of steady states. These states arise during the system's evolution toward chaos, and could be related to dormant stages of the disease and the transitions toward chaos correspond to the uncontrollable growth. The fact that the system would still reach a healthy (steady) state followed by a chaotic evolution couple with an increase in energy would connect to some rebound of cancer in some cases.

http://dx.doi.org/10.5772/67939

Author details

Maricel Agop[1,2]*, Decebal Vasincu[3], Daniel Timofte[4], Elena Simona Bacaita[1], Andrei Agop[5] and Stefan Andrei Irimiciuc[6]

*Address all correspondence to: m.agop@yahoo.com

1 Department of Physics, "Gheorghe Asachi" Technical University of, Iasi, Romania

2 Academy of Romanian Scientist, Bucuresti, Romania

3 Department of Biophysics, "Grigore T. Popa" University of Medicine and Pharmacy, Iasi, Romania

4 Department of Surgery, "Grigore T. Popa" University of Medicine and Pharmacy, Iasi, Romania

5 Faculty of Engineering and Material Science, "Gheorghe Asachi" Technical University of, Iasi, Romania

6 Faculty of Physics, "Alexandru Ioan Cuza" University of Iasi, Iasi, Romania

References

[1] Mitchell M. Complexity: A Guided Tour, Oxford University Press, New York; 2009.

[2] Thomas Y. H. Multi-scale Phenomena in Complex Fluids: Modeling, Analysis and Numerical Simulations, World Scientific Publishing Company, Singapore; 2009.

[3] Michel O. D., Thomas B. G. Mathematical Modeling for Complex Fluids and Flows, Springer, New York; 2012.

[4] Badii R., Politi A. Complexity: Hierarchical Structure and Scaline in Physics, Cambridge University Press, Cambridge; 1997.

[5] Mandelbrot B. B. The Fractal Geometry of Nature (Updated and augm. ed.). W. H. Freeman, New York; 1983.

[6] Winfree A.T. The Geometry of Biological Time, 2nd edition, Springer New York; 2000.

[7] Weibel P., Ord G., Rosler O. E. Space Time Physics and Fractility, Springer, New York; 2005.

[8] El Naschie M. S., Rossler O. E. Prigogine I., Quantum Mechanics, Diffusion and Chaotic Fractals, Elsevier, Oxford; 1995.

[9] Cristescu C. P. Non-Linear Dinamics and Chaos. Theoretical Fundaments and Applications (in Romanian), Romanian Academy Publishing House, Bucharest; 2008.

[10] Federer J., Aharoner A. Fractals in Physics, North Holland, Amsterdam; 1990.

[11] Nottale L. Scale Relativity and Fractal Space-Time. A New Approach to Unifying Relativity and Quantum Mechanics, Imperial College Press, London; 2011.

[12] Nottale L. Fractal Space-Time and Microphysics: Towards a Theory of Scale Relativity, World Scientific, Singapore; 1993.

[13] Merches I., Agop M. Differentiability and Fractality in Dynamics of Physical Systems, World Scientific, Singapore; 2016.

[14] Nottale L. Fractals and the quantum theory of space-time. International Journal of Modern Physics A. 1989; **4**: 5047–5117. DOI: 10.1142/S0217751X89002156

[15] Cresson J. Non-differentiable deformations of $\mathbb{R}^n$**.** International Journal of Geometrical Methods in Modern Physics. 2006; **3**: 1395–1415. DOI: 10.1142/S0219887806001752

[16] Stauffer D., Stanley H. E. From Newton to Mandelbrot: A Primer in Theoretical Physics with Fractals for the Personal Computer, 2nd edition, Springer, New York; 1995.

[17] Gouyet J. F. Physique et Structures Fractales, Masson, Paris; 1992.

[18] Solovastru L. G., Ghizdovat V., Nedeff V., Lazar G., Eva L., Ochiuz L., Agop M., Popa R. F. Non-linear effects at differentiable-non-differentiable scale transition in complex fluids. Journal of Computational Theoretical Nanoscience. 2016; **13**: 1–6. DOI: 10.1166/jctn.2016.4099

[19] Batchelor G. K. An Introduction to Fluid Dynamics, Cambridge University Press, Cambridge; 2000.

[20] Landau L.D., Lifshitz E.M. Fluid Mechanics, 2nd edition, Butterworth Heinemann, Oxford; 1987.

[21] Miller J. C. Laser Ablation. Principle and Applications, Springer-Verlag, Berlin Heidelberg; 1994.

[22] Anisimov S. I., Bauerle D., Luk'yanchuk B. S. Gas dynamics and film profiles in pulsed-laser deposition of materials. Physical Review B. 1993; **48**: 12076. DOI: 10.1103/PhysRevB.48.12076

[23] Miotello A., Kelly R. On the origin of the different velocity peaks of particles sputtered from surfaces by laser pulses or charged-particle beams. Applied Surface Science. 1999; **138–139**: 44–51.

[24] Anisimov S. I., Luk'yanchuk B. S., Luches A. An analytical model for three-dimensional laser plume expansion into vacuum in hydrodynamic regime. Applied Surface Science. 1996; **96–98**: 24–32. DOI: 10.1016/0169-4332(95)00373-8

[25] Miloshevsky A., Harilal S. S., Miloshevsky G., Hassanein A. Dynamics of plasma expansion and shockwave formation in femtosecond laser-ablated aluminum plumes in argon

gas at atmospheric pressures. Physics of Plasmas. 2014; **21**: 043111. DOI: 10.1063/1.4873701

[26] Nica P., Agop M., Gurlui S., Focsa C. Oscillatory Langmuir probe ion current in laser produced plasma expansion. Europhysics Letters. 2010; **89**: 6500. DOI: 10.1209/0295-5075/89/65001

[27] Gurlui S., Agop M., Nica P., Ziskind M., Focsa C. Experimental and theoretical investigations of transitory phenomena in high-fluence laser ablation plasma. Physical Review E. 2008; **78**: 026405.

[28] Tesloianu N. D., Ghizdovat V., Agop M. Flow Dynamics via Non-Differentiability and Cardiovascular Diseases. A Proposal for an Interdisciplinary Approach between Non-Differentiable Physics and Cardiovascular Morphopatology, Scholars' Press, Saarbrucken; 2015.

[29] Singh R. B., Mengi S. A., Xu Y.-J., Arneja A. S., Dhalla N. S. Pathogenesis of atherosclerosis: A multifactorial process. Experimental & Clinical Cardiology. 2002; **7**(1): 40–53.

[30] Tracy J. E., Currier D. P., Threlkeld A. J. Comparison of selected pulse frequencies from two different electrical stimulators on blood flow in healthy subjects. Physical Therapy. 1988; **68**: 1526–1532.

[31] Wedlick L. T. Recent advances in medical electricity. The Australian Journal of Physiotherapy. 1955; **1**: 152–157.

[32] Casely E. Atherosclerosis obliterans. The Australian Journal of Physiotherapy. 1958; **4**: 19–22.

[33] Hassan S., Mehani M. Comparison between two vascular rehabilitation training programs for patients with intermittent claudication as a result of diabetic atherosclerosis. Bulletin of Faculty of Pharmacy, Cairo University. 2012; **17**: 7–16.

[34] Zelkin M. I. Control Theory and Optimization I. Encyclopaedia of Mathematical Sciences, Vol. 86, Springer-Verlag, Berlin Heidelberg; 2000.

[35] Denman H. H. Time-translation invariance for certain dissipative classical systems. American Journal of Physics. 1968; **36**: 516–519.

[36] Planck M. Plancks Original Papers in Quantum Physics. Wiley and Sons, New York; 1972.

[37] Mazilu N., Porumbreanu M. The Becoming of Quantum Mechanics (in Romanian), Limes Publishing, Cluj -Napoca, Bucuresti; 2011.

[38] Cariñena J. F., Ramos A., Integrability of the Riccati equation from a group-theoretical viewpoint. International Journal of Modern Physics A. 1999; **14**: 1935–1951. DOI: 10.1142/S0217751X9900097X

[39] Stoler D. Equivalence classes of minimum uncertainty packets. Physical Review D. 1970; **1**: 3217–3219.

Chapter 3

The Fractal Analysis of the Images and Signals in Medical Diagnostics

Tayurskii Dmitrii Albertovich and
Rusanova Inna Aleksandrovna

Additional information is available at the end of the chapter

http://dx.doi.org/10.5772/intechopen.68167

Abstract

In the present chapter, we summarize our results concerning fractal analysis of some medical data. The aim of this study is to identify the inherent human body "chaotic" dynamics and insufficient disclosure of the physical essence of the processes observed, depending on the extent of developing a pathology that is characterized by a decrease or increase in the degree of complexity and as a consequence—randomness, for which, in some cases, hidden fractal. The proposed approach based on identifying the presence of the properties of self-similarity can be useful in preliminary clinical trials for the diagnosis of cancerous epithelial diseases, blood, and liver in the initial stage, the analysis of digital images, the structure of correlations biomedical parameters, as well as in the study of pathologies of the central nervous system—the neurological, neurodegenerative disorders, psychiatric disorders, and may be the basis for the development of the interface "brain-computer", on the basis of electroencephalography and magnetoencephalography. Additional measures are proposed to study the presence of self-similar properties in the form of self-similarity and magnitude SRGB ratio (area of a triangle in the coordinate system of the properties).

Keywords: fractal dimension, EEG signals, magnetoencephalography signals, photosensitive epilepsy, malignant tissue, leukemia, brain-computer

1. Introduction

Up to date, much attention is paid to study the problems of modern physics of complex systems related to identification and to quantitative description of their functioning, especially from the geometrical point of view. Fractal geometry is widely used for studies of the irreversible dynamics of natural objects, materials structure, and their properties. A common characteristic of

inhomogeneous structures is the spatial or spatiotemporal self-similarity, which means the invariance of basic geometric features at different scales. The quantitative measure of the self-similar structure is a fractal dimension, which allows one to study the structure of objects and the relationship between it and the processes occurring in such systems as the random polymers, colloidal aggregates, coarse and porous surfaces, branching structures of arteries, bone tissues, etc.

Fractal analysis methods are widely used in medical physics, in particular to find a scale invariance (scaling) and the self-similarity of digital images and signals. New promising diagnostic approaches now include not only noninvasive methods but also visual imaging methods avoiding any potentially damaging procedures.

In the present chapter, we summarize our last results concerning fractal analysis of some medical data. The aim of these studies is to identify the inherent to human body "chaotic" dynamics as well as a rather poorly understood physical nature of the observed processes in the dependence on the degree of developing pathology. Such dependence is characterized by the decrease or increase of complexity and therefore—the degree of chaos, behind which the fractality is hidden in some cases.

For the carefully collected sets of data (digital images of the main types of cancer epithelial diseases; parameters of the biochemical analysis of blood and ESR in acute leukemia compared with liver disease; magnetoencephalography signals (MEG) with photosensitive epilepsy (PSE) and a group of healthy subjects; electroencephalographic signals (EEG) form moving hands (legs), and their imagination in brain), the fractal analysis has been applied. Additional measures were proposed to study the presence of self-similar properties in the form of self-similarity and magnitude SRGB ratio (area of a triangle in the coordinate system of the properties).

It was revealed that the study of the color palette of the epithelium in a focal zone and near of near-focus area in the presence of self-similarity properties is rather effective for a differential diagnosis between malignant and benign tissues. It was shown that the fractal dimension of healthy epithelium was less than the fractal dimension of the damaged epithelium. It appeared that the SRGB method is more sensitive compared to the definition of fractal dimension and self-similarity coefficient.

Based on a complex mathematical apparatus (correlation (structural) analysis and fractal geometry), a study of the indicators of biochemical analysis of blood and ESR showed the patterns, similarities, and differences between the studied groups. It allowed to study the mechanisms, which determine the dynamics of the processes occurring in the blood at acute leukemia, in comparison with liver disease. Having these correlations, we could build the correlation pleiads and find some blocks of mutual dependence of the blood biochemical parameters.

Also, the fractal features of the neuromagnetic brain activity in PSE before and after exposure to light flickering stimulus of different color combinations (red–blue, red–green, blue, and green) have been investigated. The effect of self-similarity has been studied, and the areas of the cerebral cortex with the most significant change in the fractal structure of MEG signals in the case of PSE have been determined.

The provided fractal analysis of EEG signals of activity areas of the cerebral cortex for the cases where the subject is asked to perform movements left or right hand (foot), and then reproduce them mentally, has demonstrated clearly the sensitivity of this method to the presence in the EEG signals structure and the properties of spatiotemporal self-similarity. It was shown that the imaginary hand movements (toe) have the same effect on the activity of brain regions as real physical exercises. When one repeats a physical hand movement the localization of the excitation region of the cerebral cortex is observed in the right hemisphere. It was revealed that a clear decrease of the fractal dimension value during "back" movement of the hand, and it may indicate the inclusion of a "braking" effect. During the long-term random motion of the leg (right, left), a steady activity excitation of parietal brain and temporal regions, with a characteristic increase of the fractal dimension of the EEG signals from the frontal region and the decrease in the occipital, is observed. It gives some evidence on the localization of activity excitation of the cerebral cortex during this kind of movement.

It is interesting to increase the informational content of the investigations to be developed under the cancer influence changes in the epithelial structure. When texture images have the same color characteristics, almost visually undistinguishable, the fractal analysis can be exploited to reveal the texture features. We have found the sensitivity of developed method for the description of inhomogeneous structures of digital images of epithelial surfaces in the outbreak of the disease and in the perilesional area.

The identification in the statistical relationships of blood biochemical parameters of self-similar properties in acute leukemia and their absence in liver disease might be useful to explain the mechanisms of disease development. It would be interesting to continue the work devoted to the finding the causal relationships of the obtained correlation parameters of the biochemical analysis of blood and ESR, the similarities and differences between the treatment groups, etc.

The presented results of fractal analysis of spontaneous and induced magnetoelectric activity of the human cerebral cortex may contribute to solving the problems of diagnosis of neurological diseases, such as photosensitive epilepsy.

Currently, one of the most promising approaches is to use interface "brain-computer" (IMC) on the basis of the EEG and the imagined movements. The study of EEG signals activity areas of the cerebral cortex when making movements of the left (right) hand (foot) and mental play, with the identification of self-similarity properties of presence, can be useful in the development of modern neurotechnological IMC interfaces.

The presence of self-similar properties indicates that the dynamics of above-mentioned processes is characterized by a certain space-time structure at each hierarchical level. This structure appears in accordance with the general principles and laws of the disease development.

The proposed approach based on the identifying the presence of self-similarity properties can be useful in preliminary clinical trials for the diagnosis of cancerous epithelial diseases, blood, and liver on the initial stage, the analysis of digital images, the structure of correlations of biomedical parameters, as well as in the study of pathologies of the central nervous system—the neurological, neurodegenerative disorders, psychiatric disorders, and may be the basis for

the development of the interface "brain-computer," on the basis of electroencephalography and magnetoencephalography.

2. Dynamic chaos and fractals

The change during recent decades in the scientific paradigm has changed the scientific world view. Today the world is seen as a chaotic world with the limited predictability, manifested itself in such a different phenomena as the gas turbulence and fluid kinetics of chemical reactions, geophysical and weather changes, physiological responses, epidemics, population dynamics, social events, etc. The vast area of interdisciplinary research, namely nonlinear science, is based on the nonlinear thermodynamics, the theory of dynamical chaos, catastrophe theory, and fractal geometry.

The isolated systems, due to the linear thermodynamic processes tend to evolve to a steady state of maximum entropy and disorder. Irreversible processes in open systems, are at the border of sustainability, generate high levels of organization, including dissipative structures. One can assume that dissipation forces a physical system to thermodynamic equilibrium steadily. However, the actual process may be much more complex what can be seen from the gas dynamics. In general, the behavior of rarefied gas is well described by the kinetic Boltzmann equation. The equations of gas dynamics are an example of the description of physical systems far from equilibrium, and allow to describe their behavior even at extreme conditions and in various geometries. For example, the hydrodynamics of superfluid helium in a highly disordered porous media or nanoporous media with fractal dimension gives an important information about dynamics of a Bose-Einstein condensate in a disordered potential with a complex fractal geometry. Taking into account nonadditive thermodynamics methods, it is possible to develop the models for small particle numbers or strongly correlated systems [1–3].

The chaotic dynamics is inherent not only to the continuous dynamic systems but to the discrete ones as well [4]. The state of the system far from equilibrium is evolved by means of nonlinear processes. The small external fluctuations may cause the unpredictable behavior of the system as a whole, and even to destroy it, to force the transition into a different state (catastrophe theory). The model of self-organized criticality [5] predicts that catastrophical behavior in complex systems can occur not only due to external reasons, but also due to the fact that small events inside a system can add up together, lead to a chain reaction and spontaneous evolution to a critical state (cascade of bifurcations, turbulent). Such physical systems being strongly nonequilibrium exhibit complex dynamic behavior with properties that cannot be reduced to the properties of the components (parts).

In the phase space of dissipative systems (the set of all possible states of a dynamic system), there appear the attracting sets with complex structure—strange chaotic attractors—that do not have a rigid periodic dynamics and possess a dimension different from the topological and therefore identified with fractals [6]. Systems with strange attractors can simulate a variety of phenomena—oscillating chemical reactions, population dynamics population, hydrodynamic

processes, and the processes in the economy [7–12]. Self-similarity of fractal structures allows to determine the link between short-range and long-range orders and to describe mathematically the extreme irregular structures and processes. Most natural fractals are multifractals (heterogeneous fractals), for the full description of which one needs a spectrum of fractal dimensions (for example, nonuniform distribution of star clusters, aggregation properties of blood cell elements, and the evolution of an ensemble of dislocations and metal fatigue fracture). The so-called Mandelbrot sets and Julia sets (**Figure 1**) despite their complex structure are formed by simple mathematical rules. Such a kind of set belongs to the group or algebraic fractals generated by the iterations of algebraic functions [13].

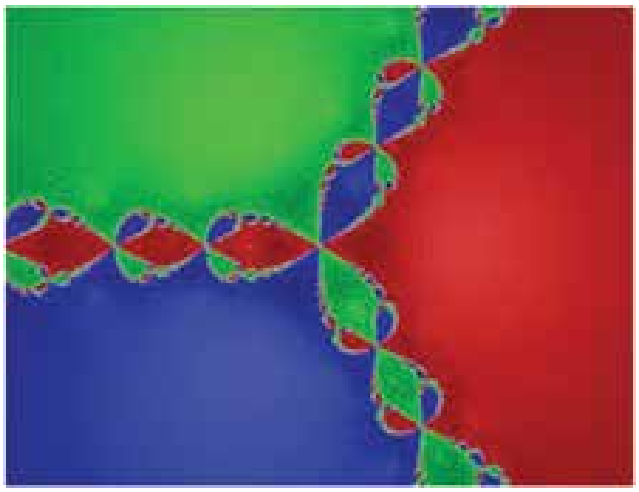

Figure 1. A classic example of an attractor—a comprehensive set of Julia.

Simple models of self-organizing systems are also cellular automata, which can describe the phase transition, the wave process, to generate oscillating and fixed local structures, including fractal ones. Thus, nonlinear dynamics and fractal geometry are closely related and their relationships are the subject of research in the various fields of knowledge.

3. The method of fractal description

In general, the fractal dimension of a geometry objects can be determined as

$$D = \frac{\log N}{\log\left(\frac{1}{R}\right)} = \frac{\log N(b)}{\log b}, \tag{1}$$

where b is the amount of identical parts and N is the number of identical units on a scale R. In order to cover the structure in the m, dimensional phase space, the number $N(b)$ of m,

dimensional cells with side b is calculated, so that the condition of Hausdorff dimension $N(b) \sim b^{-D}$, at $b \to 0$ has to be satisfied [14, 15].

Consider a partially ordered finite set $A(N^2)$, where N^2, is the number of elements $a_{i,j}$ in the set $a_{i,j} \in A(N^2)$, were $i, j = 1 \ldots N$. Let us assume that the partial order on the finite set is determined by the Hasse diagram (**Figure 2 I**), while the set elements are characterized by some properties $H_\xi(a)$ (dimension, color, volume, shape, etc.), inherent only elements in the given set $\forall a_{i,j}\left(a_{i,j} \in \{a|H_\xi(a)\}\right)$. If one considers few properties $\xi > 1$, then the set is described using a few fractal dimensions.

We represent the set $A(N^2)$ in the following form

$$A(N^2) = Q^{(1)}(n^2) \cup Q^{(2)}(n^2) \cup \ldots \cup Q^{(\alpha^2)}(n^2), \tag{2}$$

where $Q^{(k)}(n^2)$, disjoint subsets of the set $A(N^2)$, $\alpha = N/n$, α and n are integer. Then, α and n are the sets $\forall \alpha \in \{\alpha_\gamma\}$ and $\forall n \in \{n_\gamma\}$. For $N = 24$, we get $\{\alpha_\gamma\} = \{24, 12, 8, 6, 4, 3, 2, 1\}$ and $\{n_\gamma\} = \{1, 2, 3, 4, 6, 8, 12, 24\}$.

Suppose that there are upper and lower bounds of the set $A(N^2)$ for all properties $H_\xi(a)$: $G_\xi = \sup A(N^2)$ and $g_\xi(a) = \inf A(N^2)$, so that $G_\xi \in A(N^2)$ and $g_\xi \in A(N^2)$. Then, the scaling of the set $A(N^2)$ is possible at all properties. We associate with the upper G_ξ and lower g_ξ bounds of the set $A(N^2)$ the numbers R_ξ and r_ξ, respectively. Then, the whole set $A(N^2)$ may be covered by a cube with volume $V_\xi = (R_\xi - r_\xi)^3$ in the space of each property. Each element of the set $A(N^2)$ will be associated with a region in the space of properties with areas $s_\xi = (R_\xi - r_\xi)^2/N^2$. Accordingly, each subset $Q^{(k)}(n^2)$ can be covered by the cubes $v_\xi = V_\xi/\alpha^3$, and their number is determined by the size of $\sup Q^{(k)}(n^2) \in Q^{(k)}(n^2)$ in the input scale properties, the area occupied by a subset of the elements will $S_\xi(n^2) = s_\xi n^2$.

We define the fractal dimension D_ξ of the set $A(N^2)$ on the property $H_\xi(a)$ by the angular coefficient of the dependence of $\log \Gamma_\xi(n^2)$ on $\log s_\xi n^2$, where $\Gamma_\xi(n^2)$ is the number of noncontiguous surfaces of cubes, covering the subset $Q^{(k)}(n^2)$:

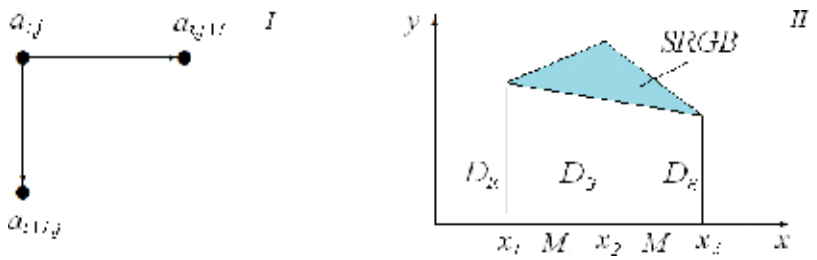

Figure 2. Presentation of experimental data: (I) diagram Hasse and (II) area of triangle in the property frame of references.

$$D_\xi = \sum_\gamma \frac{\log\Gamma_\xi(n^2_{\gamma+1}) - \log\Gamma_\xi(n^2_\gamma)}{abs\left(\log S_\xi(n^2_{\gamma+1})\right) - abs\left(\log S_\xi(n^2_\gamma)\right)}\left(\frac{\alpha_{\gamma+1} - \alpha_\gamma}{N-1}\right). \tag{3}$$

Self-similarity coefficient $-1 \le K_\xi \le 1$ can be defined as

$$K_\xi = \frac{D^0_\xi}{D_\xi}, \tag{4}$$

where D^0_ξ is fractal dimension of self-similar set:

$$D^0_\xi = \frac{\log\Gamma_\xi(N^2) - \log\Gamma_\xi(1)}{abs(\log S_\xi(N^2) - abs(\log S_\xi(1)))}. \tag{5}$$

For example, in the study of the fractal properties of the images the three colors can be selected as properties $H_\xi(a)$: red ($\xi = R$), green ($\xi = G$), and blue ($\xi = B$). Thus, the description of the image structure in this case is performed by three fractal dimensions D_R, D_G, and D_B, with which one can calculate a some value SRGB (area of triangle in the property frame of references) (**Figure 2 II**), which is highly sensitive to the changes in the structure of a color image [16]:

$$\text{SRGB} = \frac{1}{2}M[-2(D_R + D_B) + (D_B + D_G) + (D_G + D_R)]. \tag{6}$$

For a nonordered finite set $A(N)$, the description by means of fractal dimensions D_ξ on the property $H_\xi(a)$ will lead to $k = 1\ldots N!$ different dimensions $D^{(k)}_\xi$. If the set of properties of each element of the set $A(N)$ is the ordered finite set $H = \{H_\xi(a)\}$, then each element of the set $A(N)$ it can be characterized by the fractal dimension of this set of properties, where $k = 1\ldots N$.

4. The study of fractal structure of the image of the nail bed and periungual epithelium

Today the digital processing and image recognition in medical technology are one of the rapidly developing areas of research. In the process of image formation and image processing, the following characteristics of the surfaces of the studied objects are introduced—geometric features, characteristics of color, brightness settings, textural properties, and signs of movement. However, when the image textures have the same color characteristics, it is difficult to distinguish them visually. Their complex spatial organization can be characterized quantitatively using fractal dimension as a measure of the filling of the space (an index of the complexity of the spatial structure of the surface). It is interesting to study the possibility to increase the diagnostic informational content of the changes in the inhomogeneous structure of the epithelial surface (in the outbreak of the disease and in the perilesional area) under the influence of cancer at the early stages of manifestation of irreversible diffusion changes.

As the objects of study, the electronic images of the main types of cancer and diseases of the epithelium of the nail plate were examined (**Figure 3**, **I**). There were treated 50 electronic images of the main types of skin cancer, the nail bed, and periungual epithelium diseases. For a comparative analysis, the healthy epithelial tissue image surfaces and nail plates were included to the control group. In accordance with the color code of each pixel of the working surface, the weight contribution of the color code was converted into the height of the point. And the result is that, the three-dimensional (3D) volumetric object with corrugated inhomogeneous surface is obtained (**Figure 3**, **II**).

It was revealed that, despite on the difference in the apparent change of the inhomogeneous structure of the surface of the epithelium in the source zone, near and outside this region (**Figure 3a** and **b**), expressed in the form of seals (build-up) and in a different color palette, the general behavior of the characteristic changes is manifested by the presence of self-similarity and scaling properties, characterized by the value of the fractal dimension of the various sections of the test surface of the skin: $D_1 \approx D_2$, $D\{(\neq D_1 / \neq D_2)$, where D is fractal dimension of damaged epithelium, D_1 is fractal dimension of pathological focus, and D_2 is fractal dimension of near-focus area. It was demonstrated that the fractal dimension of healthy epithelium was less than the fractal dimension of the damaged epithelium.

Structures of nail bed and periungual epithelium have been considered for the patient data within eight groups of diseases (**Figure 3c** and **d**) and (**Figures 4**–**6**): (1) blue nails; (2) periungual moles; (3) koilonychia; (4) dyschromia; (5) nail dystrophy; (6) onychia; (7) acrolentiginosis (subungual melanoma); and (8) onychomycosis. In **Figure 4**, the values of fractal dimension for the affected and unaffected parts of the nail bed and periungual epithelium for different types of diseases are presented. One can see the existence of the general laws in the behavior of the fractal dimension D for groups of diseases: (1, 6, 8) and (2, 4, 5).

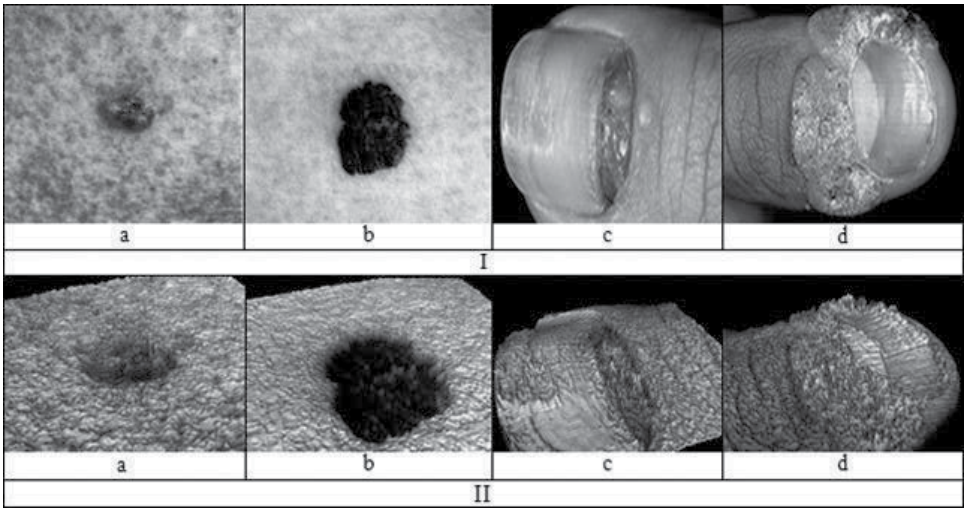

Figure 3. Epithelium surface images with pathological focus (a, b), nail bed and periungual epithelium images (c, d) for basic types of cancer and their 3D images: (a) skin basiloma; (b) skin malignant melanoma; (c) acrolentiginosis (subungual) melanoma; and (d) periungual moles.

http://dx.doi.org/10.5772/intechopen.68167

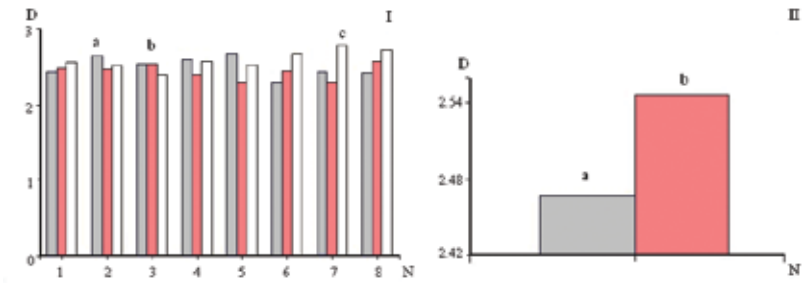

Figure 4. Dependence of mean fractal dimension D: (I) for eight groups of patient data: (a) damaged segment of nail bed, (b) nondamaged segment of nail bed, (c) periungual epithelium area; (II) control group: (a) healthy nail bed and (b) healthy periungual epithelium area.

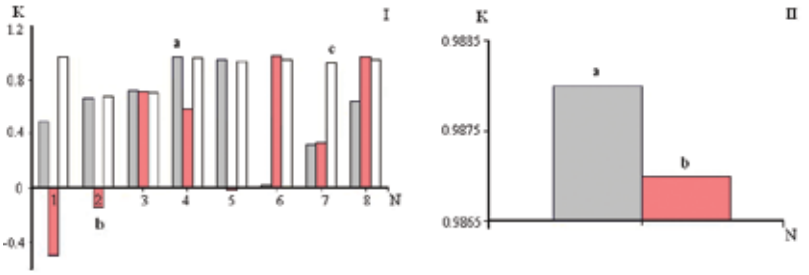

Figure 5. Dependence of mean self-similarity coefficient K: (I) eight groups of diseases: (a) damaged segment of nail bed, (b) nondamaged segment of nail bed, (c) periungual epithelium area; (II) control group: (a) healthy nail bed and (b) healthy periungual epithelium area.

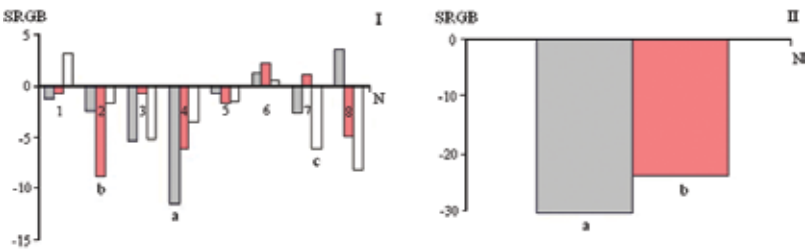

Figure 6. Dependence of mean value of SRGB: (I) eight groups of diseases: (a) damaged segment of nail bed, (b) nondamaged segment of nail bed, (c) periungual epithelium area; (II) control group: (a) healthy nail bed and (b) healthy periungual epithelium area.

The self-similarity coefficient $-1 \le K \le 1$ provides the geometrical evidence for the difference of tested object surface from the ideal fractal one in terms of color code. It was demonstrated that self-similarity coefficients in different areas of nail bed and periungual epithelium are different for eight groups of diseases (**Figure 5**). Mean values of SRGB for the tested segments (nail bed, pathological focus, periungual epithelium area) are different for the different diseases in most

cases; the majority of the mean values are negative and less than corresponding values for the control group (**Figure 6**). The mean values of SRGB for the healthy nail bed and periungual epithelium area are similar [16].

The found presence of self-similar properties of the structure of the epithelial surface in the outbreak of the disease and in the surrounding areas of the nail bed and periungual epithelium may indicate the existence of a specific algorithm, acting in accordance with the laws of development of the disease and performing at every stage of the status change. It allows to identify, to describe quantitatively, and to diagnose the disease at an early stage.

5. Structural and fractal analysis of the dynamics of pathological processes in cases of leukemia and liver diseases

According to classical ideas, the healthy systems are exposed to some self-regulation to reduce the volatility and to maintain the physiological constancy. Studies in this area show a large-scale nonlinear complexity of human physiological functions, which are simplified or complicated in certain "dynamic diseases," with impaired coordination and the control of a variety of other functions of the body. Such diseases include respiratory disorders, sleep and blood disorders, including the form of leukemia [17, 18]. Today the fractal properties of normal and malignant hematological cells are found and their potential as a tool to assess the clinical behavior of hematological diseases is shown [19]. The correlation was found between the fractal dimension of nuclear chromatin as a prognostic factor and clinical outcomes in patients with leukemia [20].

Measurement of the fractal dimension seems to be a sensitive method for assessing the hematological phenotype cells and determine the clinical group. This tool can be potentially useful. Modern methods of the treatment of acute lymphocytic leukemia can achieve the remission for 70–85% of patients [21]. The forecast for the cure of children is 50%, for adults it is not so favorable. The positive results of the treatment are the result of assessment of the nature of the disease with the use of modern methods of diagnostics of acute leukemia and consistently, methodically correct, and long-term treatment program. The liver plays a major role in maintaining the functioning of the blood and its diseases are equally disturbing. At present, the etiology of such diseases, including their mutual correlations, is the subject of the growing interest [22]. An analysis of biomedical information of the dynamics of change processes under study often reveals the changes in the strength of relationships between characteristics of groups of blood biochemical parameters. During the treatment, the strengthening or weakening of the correlation of certain physiological parameters can be seen. The study of the relationships between indicators characterizing the course of acute pathological process is the issue for healthcare professionals in different fields. In particular, the evaluation of correlations of physiological parameters can be used as a criterion for comparing groups of people in the process of adaptation or development of pathological process [23]. The study of the mechanism of the blood structure changes for leukemia is of a great interest. Here, one can look for availability of the properties of space-time self-similarity as one of the key factors for the description.

http://dx.doi.org/10.5772/intechopen.68167

In this section, we show how the regularities of the blood parameters changes in the treatment of acute leukemia can be set by the use of the correlation (structural) analysis and methods of fractal and how the properties of self-similar structure correlations of parameters of the biochemical analysis of blood and ESR can be revealed. As the subject of our research, we have to choose the average age group of men and women suffering from acute leukemia (30 patients observed permanently since the aggravation of the disease before the onset of remission and leaving the hospital). The control group consisted of their peers—30 people with liver disease (cirrhosis, hepatitis) [24].

The most important method of research, which allows to suggest, in some cases to diagnose acute leukemia is a common blood test. Biochemical analysis of blood contributes to the identification of characteristic changes caused by the underlying disease. To identify the mechanism of dynamics of structural indicators of blood tests for leukemia, hidden in the statistics of correlations, the data of biochemical analysis of blood and ESR were tested. These experimental and control groups were grouped by diagnosis procedure (15 tests) from the moment of admission to the day of discharge, at the same time intervals at delivery of analyzes. The correlation analysis of the ESR and biochemical analysis of blood parameters in leukemia indicates a significant adjustment in the relationship of the studied parameters of structural organization from the moment of aggravation to the state of remission. The dynamics of increasing structural correlations observed in both groups, but the greatest increase in recovery and correlations was observed in the experimental group with the disease of acute leukemia compared with liver patients. Correlation constellation constructed on the diagnostic data of patients with hepatic (**Figure 7b**, **III** and **IV**), is "broken" into three blocks, one of which includes parameters such as "aspartate," "total protein," and "ESR." Inside this "unit," the parameters show anticorrelative connection. The second "block" is formed by performance "alaninaminotransferaza," "urea," and "total protein" with strong correlations. The third block includes "creatinine," "direct bilirubin," "alkaline phosphatase," and "total bilirubin," with more or less strong correlations with a significance level of $p = 0.05$. Here, the parameters have low correlation interdependencies.

Much more complex structure of the parameters of the correlation observed in the constellation of the experimental group with leukemia (**Figure 7a**, **I** and **II**), although here as well as in the control group, the "Maclagan test" is excluded from the correlation relationships because it did not show significant correlations. A small number of significant correlation relationships are also observed in the parameters "ESR" and "total protein" at the time of an exacerbation of disease, which is restored by the time of remission and recovery. It is very interesting the presence of only one direct correlation interdependence in the parameter "alaninaminotransferaza" ($p = 0.05$) at the first diagnosis at the time of exacerbation. It detects the correlation with a parameter "alkalinephosphatase," and this interdependence is connected with inverse correlation parameters "total bilirubin" and "urea" ($p = 0.05$). This is important because accordingly to the statistical comparison of averages the parameter "alaninaminotransferaza" reveals significant differences with a significance level of $p = 0.001$.

To detect the presence of the fractal properties of the structure correlations in acute leukemia and liver diseases, we have transferred the weighted deposits of the spatial correlation

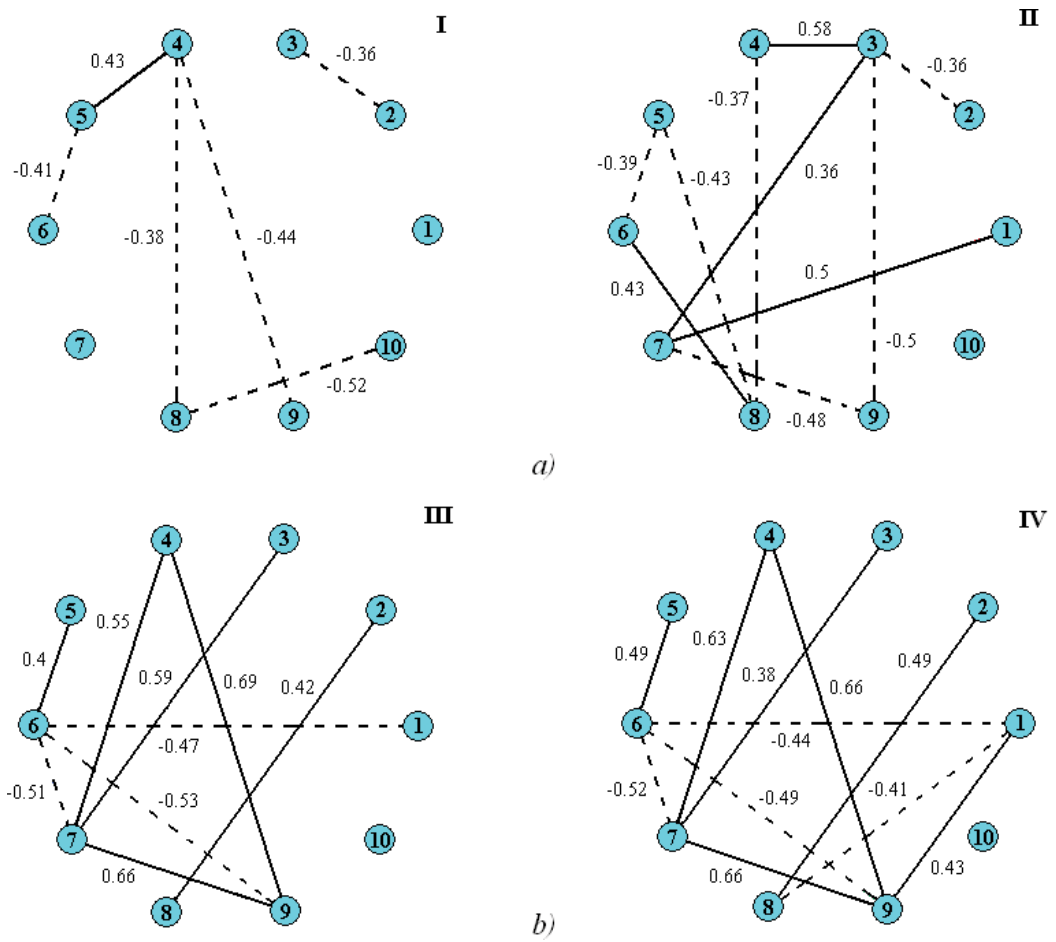

Figure 7. Correlation graphs for biochemical parameters and general blood tests: (a) leukemia, (b) liver disease: (I and III, the first diagnosis and II and IV, final diagnosis at discharge; 1, ESR; 2, creatinine; 3, direct bilirubin; 4, alaninamino-transferaza; 5, alkaline phosphatase; 6, aspartate; 7, the total protein; 8, total bilirubin; 9, urea; and 10, Maclagan test).

coefficients ρ_{jk} into the height of points. As the result, three-dimensional objects with non-uniform rugged surface have been obtained. The study of the correlation of distributions of blood parameters showed the presence of their fractal properties for the case of leukemia, with an average fractal dimension $2 < D < 3$ (**Figure 8a**, **1**)). This may indicate the existence of a certain space-time mechanism, functioning as a self-similar algorithm, in accordance with the laws of development of the disease and the onset of remission. For the group of patients with liver disease, the absence of the fractal properties of the structure correlations between blood parameters has been found (**Figure 8a**, **2**). Numerical calculations of self-similarity coefficient K showed the absence of abnormal changes in the structure of correlations of parameters of blood tests for both groups of diseases: $0 < K < 1$. It was revealed that in acute leukemia there is a characteristic change in the dynamics of self-similarity coefficient, which has an inverse relationship to the fractal dimension: the increase of fractal dimension is accompanied by a

http://dx.doi.org/10.5772/intechopen.68167

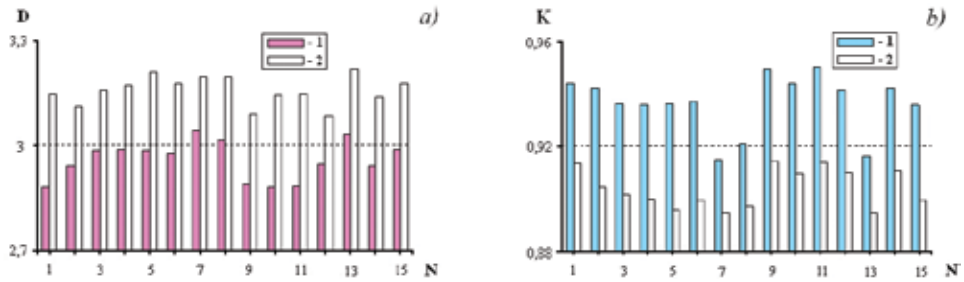

Figure 8. Histogram of the dynamics of the fractal dimension (a) and self-similarity coefficient *K* (b) the structure of correlations biochemical indices of blood tests and ESR (of N diagnostic test (1), acute leukemia and (2) liver disease).

decrease in the rate of self-similarity *K*, and vice versa, which, however, is not observed in the study group with liver disease (**Figure 8b**).

Identification of the statistical relationship of blood biochemical parameters of self-similar properties in acute leukemia and their absence in liver diseases at different time intervals can be helpful in explaining the mechanisms of disease development. It is important to continue the work for finding the causal structure of the obtained correlation parameters of the biochemical analysis of blood and ESR, the similarities and differences between the treatment groups, with the estimation of the influence of various external factors on the mechanism of disease development, etc.

6. Self-similar mechanism neuromagnetic dynamics of brain activity

The use of fractal geometry in the study of pathological activity of the human cerebral cortex has led to the substantial progress in the understanding of the physiological mechanisms of brain function disorders for various diseases, such as epilepsy. The study of self-similarity of rhythmic brain activity allows one to set the characteristics of preclinical and clinical stages of epileptogenesis to detect predictors for sufficiently large time intervals, up to 1 hour [25], as well as to identify the foci of excitation, leading to different types of epileptic seizures [26]. Besides using fractal analysis, wavelets reveal the markers of the formation of epileptic activity developing in various types of seizures [27]. It should be noted that in all these works as one of the forerunners of the attack appears the decrease of multiscale complexity of the background activity of the brain and the fractal dimension of the EEG (electroencephalogram) [28].

MEG signals represent the interest for the study of brain pathologies. In this section, we will show how the diagnostic signs of photosensitive epilepsy (PSE) can be found on the basis of the analysis of the self-similarity effects realized in MEG signals, in which attacks are provoked by flickering light. It is widely known that the disease received after cases of mass attacks in Japan during the demonstration of the animated series "Pokemon." Previously, the individual characteristics of the subjects' reactions have been identified based on the method of flicker-noise spectroscopy on a red-blue and red-green incentive, and set the degree of contribution of various types of irregularities in normal and pathological dynamics of brain activity signals [29].

Here, we examined the fractal characteristics neuromagnetic brain activity in photosensitive epilepsy (PSE) before and after exposure to light flickering stimuli of different color combinations (red-blue, red-green, blue-green). On the basis of the proposed approach one can investigate the fractal characteristics at different stages of development of the epileptic process.

6.1. Description of experimental data—registration of activity of human cerebral cortex

In the experiments [30], the registration of cortex neuromagnetic signals caused by the flickering stimuli was carried out using Neuromag-122 (Neuromag Ltd., Finland) with 61 SQUID (superconducting quantum interference device) sensors with a sampling frequency of 500 Hz. MEG signals were recorded in healthy control group (nine patients in the age of 22–27 years who do not have a hereditary predisposition to epilepsy) and the patient with PSE (teenager, 12 years). The incentives of different color combinations (red-blue, red-green, blue-green) were generated using the projector on a special screen for 2 seconds at intervals of 3 seconds. The experiment consisted of 80 episodes. After removing the artifacts, the results of all series were averaged. During the first 400 ms (200 points), the control signal was recorded when the screen is not fed flickering stimulus, during the next 1.78 s (201–1095 points) the stimulus is supplying. It have been demonstrated that the most significant pathological response in the patient's brain activity is observed with the PSE in case of a red and blue stimulus.

6.2. Fractal analysis of MEG-signals

Calculation of fractal dimension was carried out for MEG signals obtained in the natural state of patients as well as after a flickering stimulus. MEG signals $x(t)$ are dynamic variables $x(t) = x_i(t)$ at a certain value $i(1 \le i \le n)$. Let $\{x_i\}_{i=1,..,200}$ is the time series obtained by the MEG signal measurements before photostimulation, $\{x_i\}_{i=200,..,1095}$ - time series obtained by the MEG signal measurements during photostimulation, then the time series $\{x_i\}_{i=1,..,1095}$ is a "total" signal before and during application of photostimulation. The fractal dimension *D* is a measure of the spatial inhomogeneity of the signal.

The values of fractal dimension D for different combinations of the MEG signal of the patient with PSE and the average values of D for the control group of healthy subjects are shown in **Figure 9**. The primary impact of the stimulus leads to a further strengthening of "regulatory" brain possibilities.

The supply of red-green and blue-green stimulus does not lead to a significant change in the fractal dimension *D*. At all conditions of the registration the lower level of fractality is observed for the control group. For the patient with PSE a considerable variation in the value of *D* is revealed, and this variation is essential in the absence of a visual stimulus. Supplying of a light stimulus does not lead to noticeable changes in index *D* for healthy subjects. The criteria found allow one to carry out a preliminary diagnosis of photosensitive epilepsy: the intervals of fractal dimension for healthy group and the patient with PSE do not overlap. If the values of this parameter are in the range from 1.2 to 1.34, the preliminary diagnosis is negative, from 1.45 and up—positive.

http://dx.doi.org/10.5772/intechopen.68167

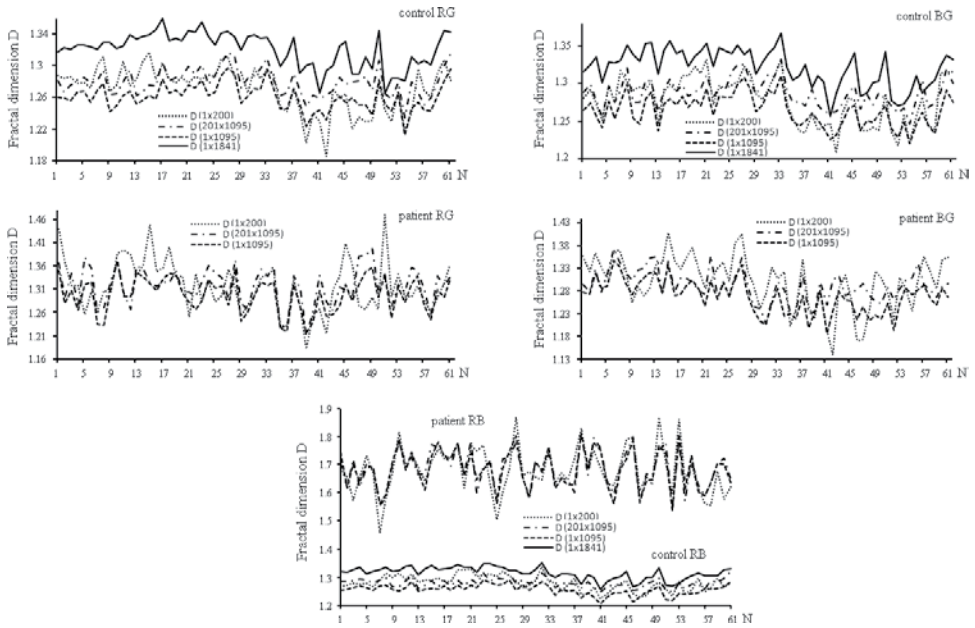

Figure 9. Fractality index values D of MEG signals (61 SQUID sensor) for the group of healthy subjects (mean values) and the PSE patients: before and after emission of a light stimulus and the entire signal.

Topographic map of the fractal dimension make it possible to trace the reaction of different brain regions to supplying the stimulus for healthy group (the average for the group) and patients with PSE (**Figures 10** and **11**), as well as allow to find the areas whose activities are broken at PSE. Before the switching of stimulus, the biggest differences are observed for the crown (most clearly), occipital, left temporal lobe of the cerebral cortex. Supplying the visual stimuli leads to a change in reactive centers—all frontal lobe, occipital (most clearly) and the left-parietal region are governed by the influence. The supply of red and blue stimulus RB (201–1095 points) is very interesting, because it leads to the formation of the specific localization of excitation zones in the form of a symmetrical "trefoil" in the parietal region for the representative from healthy group (**Figures 10** and **12**).

Spontaneous neuromagnetic activity substantially differs for healthy group and patients with PSE in the parietal, occipital, and left temporal lobes of the cerebral cortex, and the induced one in frontal, occipital, parietal, left. Supplying of flickering stimulus leads to substantial reaction of almost all areas of the brain for the representatives of the control group. At the same time for the patient with PSE only a few localized foci is observed. The occipital, temporal, and frontal lobe are most involved. It should be noted that the reaction of these areas is shown as an increase or decrease of fractal dimension *D*. The data of the patient demonstrate only a few pockets of susceptible reaction (parietal, occipital lobe, and temporal region), while in most parts a decrease of fractal dimension of MEG signals is recorded.

The presented diagnostic criteria reflect the effect of a defense mechanism, blocking the abnormal development of the collective activity of groups of neurons in response to dangerous

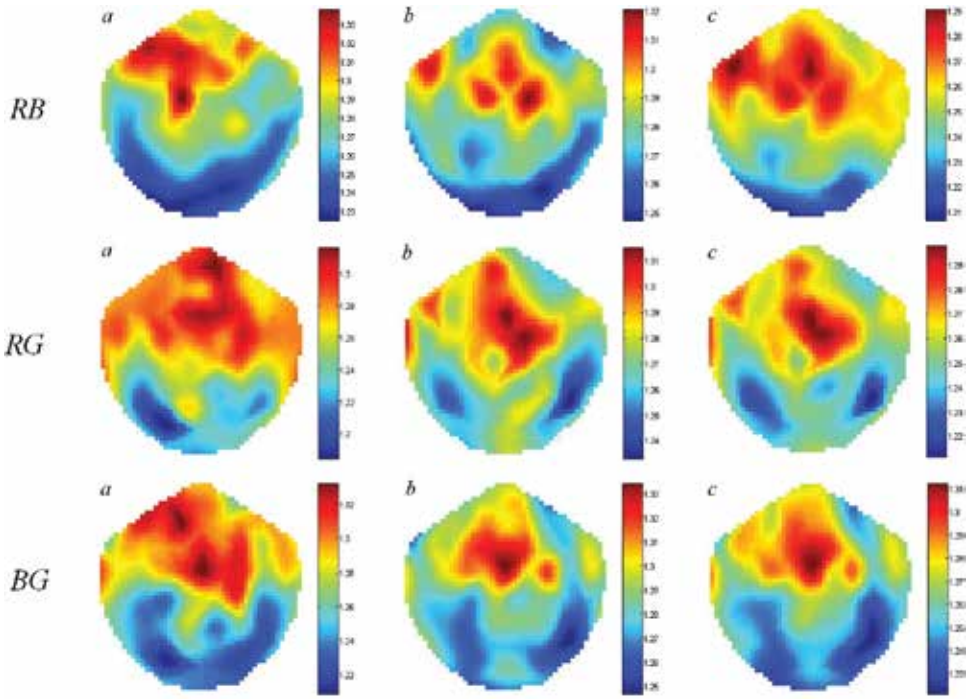

Figure 10. Topographic map of the fractal dimension when applying flickering stimuli (red-blue RB, red and green RG, blue-green BG) for MEG signals the control healthy group at time intervals: (a) 1–200, (b) 201–1095, and (c) 1–1095.

visual impact. This mechanism appears to change the structure of signals generated by the almost entire surface of the head, which is reflected in the values of the index of fractality *D*. In the case of photosensitive epilepsy the mechanism is broken or its action is inhibited [31].

Topographic map of self-similarity coefficient have a high sensitivity to detection of minimal deviations in the structure of the chaotic dynamics of the MEG signal from the ideal fractal. Impact of flickering stimuli on neuromagnetic activity of the cerebral cortex as a whole is characterized by negative values of self-similarity coefficient for the group of healthy subjects (mean value) and patients with PSE (**Figures 12** and **13**). However, the effect of the red-blue RB incentive for patients with PSE leads to abnormal changes in the chaotic dynamics of reactive centers on a given stimulus. Thus, the comparison of the coefficients of self-similarity on the impact stimulus time slots (or the entire period of observation) (**Figure 12**, RB, **a**, **b**) to an initial state neuroactive cortex (up stimulus exposure) shows the appearance of areas of brain activity ($-1 \le K \le 1$). This suggests that the smallest change in the reactive centers is subjected to the right parietal-occipital and left-field. The impact of all the combinations of stimuli is characterized by spatial localization of reactive centers.

The presented histogram of fractal dimension *D* for neuromagnetic activity of different lobes of the brain (**Figure 14**) after the red-green and blue-green incentives demonstrate that for the patient with PSE the largest decrease of fractal complexity of the background activity of the brain of the nonlinear dynamics of MEG signals is observed while for the healthy group

http://dx.doi.org/10.5772/intechopen.68167

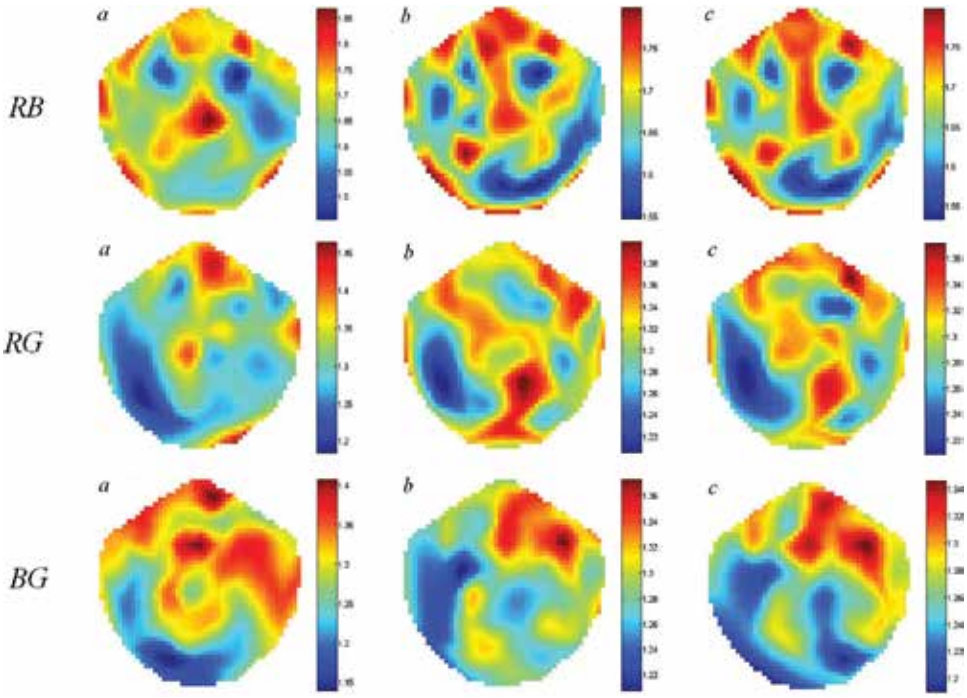

Figure 11. Topographic map of the fractal dimension when applying flickering stimuli (red-blue RB, red and green RG, blue-green BG) for a patient MEG signals with PSE at time intervals: (a) 1–200, (b) 201–1095, and (c) 1–1095.

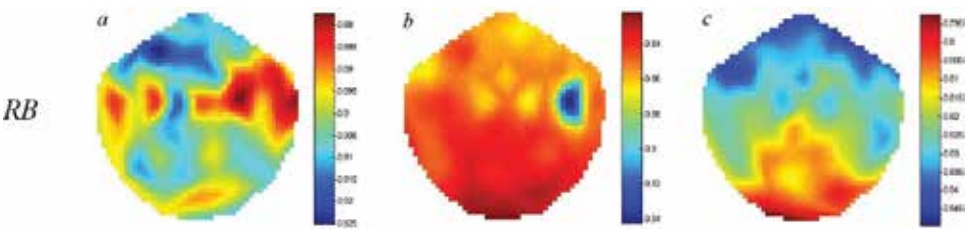

Figure 12. Topographic map of self-similarity factor when applying red and blue (RG) flickering stimulus for healthy group MEG signals at time intervals: (a) 1–200, (b) 201–1095, and (c) 1–1095.

the supplying of the given incentives leads to an increase of chaotic dynamics reacting centers. The opposite reaction of reactive centers is observed when applying red and blue stimulus RB: for the patient with PSE the majority of lobes exhibits the amplification of reaction centers in response to the impact of the stimulus, except left-temporal and occipital areas, whereas for the healthy group, a decrease of the complexity of chaotic dynamics is observed, except the right-parietal, right-temporal, and occipital regions.

Thus, the analysis of fractal characteristics of neuromagnetic activity of the cerebral cortex for healthy group and patients with photosensitive epilepsy (PSE) reveals the diagnostic features

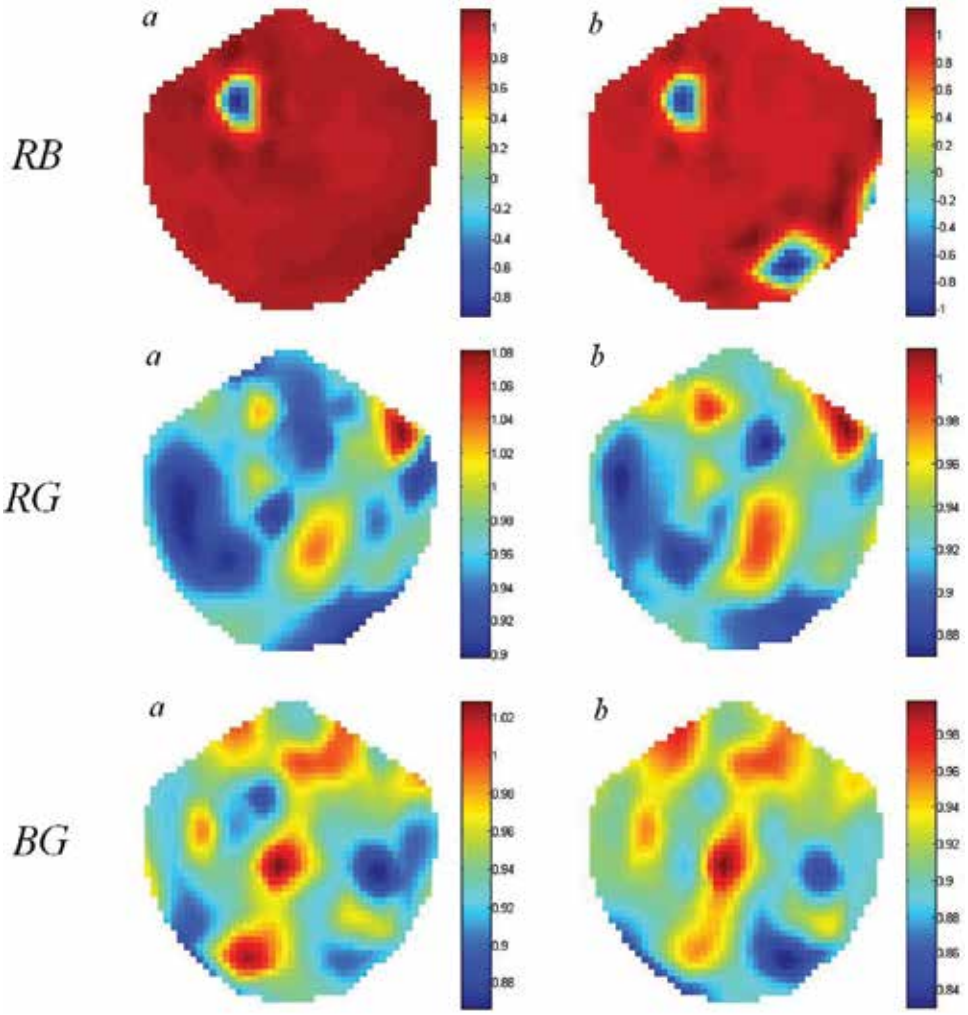

Figure 13. Topographical map of coefficients of self-similarity at different time intervals when applying flickering stimuli (red-blue RB, red and green RG, blue-green BG) for MEG signals from the patient's PSE: (a) (201–1095)/(1–200), (b) (1–1095)/(1–200).

of the disease. High fractal dimension of patient-feedback signals in combination with a smaller "reactionary" ability of different areas of the cerebral cortex to visual stimuli can be considered as diagnostic features of PSE. The most significant differences are revealed for the parietal, occipital, frontal, left parietal, and left temporal regions of the brain. Supplying of stimulus leads to the reaction of different cortex regions for the representatives of control group, while for the patient a localized response is observed only. The presented results of fractal analysis of spontaneous and induced magnetoelectric activity of the human cerebral cortex may contribute to solving the problems of diagnosis of neurological diseases, such as photosensitive epilepsy.

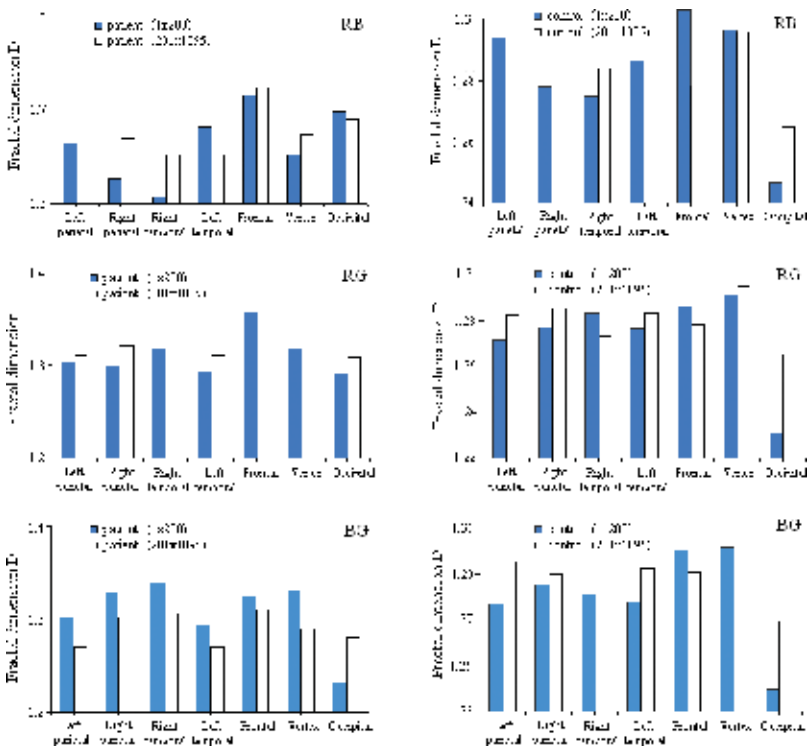

Figure 14. Histogram of the fractal dimension D before and after the red-blue stimulus (RB), red-green (RG), and the blue-green (BG) for the patient MEG signals from the PSE and a group of healthy subjects.

7. Fractal complexity of the chaotic rhythms of EEG signals of real and imagined movements of the hands (legs)

Currently, much attention is paid to the development and application in the field of modern neurotechnology "brain-computer" interfaces (BCI), capable for human to communicate with external electronic and electromechanical devices without the use of peripheral nerves and muscles, for example, by recording the electrical activity of the brain [32–35]. Developments of IBC interface based on EEG, magnetoencephalography, functional magnetic resonance imaging, electrocorticography, impulse activity of neurons, distribution and intensity of the blood flow in the brain and the likes are carried out by research groups around the world [36, 37]. However, none of the models of IMC has not been currently used in the clinics, where it is necessary to comply with the safety requirements of the patient (noninvasive), to provide the simplicity of the device, and to have the relative cheap technology. One promising approach in this case is the use of BCI based on the EEG and the imagined movements [38, 39]. The different approaches used today to the quantitative analysis of the EEG in BCI applications do not provide the necessary accuracy of the classification required for the creation of systems for comfortable use in everyday life. An important problem is the choice of the EEG signal

processing techniques to classify the EEG patterns of real and imagined movements of the hand (leg).

Numerous studies have demonstrated that the alpha rhythm dominating in the spectrum of EEG (the main component of the background electrical activity of the brain of a healthy person awake) has a fractal dimension [40, 41]. Also, all systems of a healthy brain, which are the sources of EEG signals, as well as the activity of individual neurons and neuronal networks normally exhibit chaotic behavior [42, 43]. Sensorimotor rhythms at rest are characterized by a high amplitude (beat sync). It is believed that the chaotic trajectory in phase space makes the neurons to be able to quickly switch between different states to ensure liability of the central nervous system and its resistance to external influences [44]. Neuroactive cortex inherent fractal chaotic dynamics of the EEG signal indicates its normal operation, while an excessively ordered mode indicates the presence of disease [18]. When moving or preparing to perform motor functions in, there was a decline in their intensity during activation of the corresponding motor or sensory areas of the cortex, which leads to the rhythm desynchronization [45]. The main objective of the BCI is the correct recognition of the state of desynchronization and the synchronization of rhythms.

Imaginary movements can slow or stop muscle atrophy because the mental muscle exercises affect the neuromuscular pathways what is important for the people with limited mobility. Visualization technique is also used by professional athletes to improve performance. Such BCI are needed for the rehabilitation of patients with disorders in the motor area, but can also be used by healthy people to control auxiliary devices: exoskeletons, prosthetic limbs, muscles electrical stimulator, etc. [46, 47].

It should be noted that currently a lot of attention to doctors, physiologists, biochemists, psychologists, and professionals involved in physical activity, is paid to a nonlinear dynamics, concerning the effects of exercise on changes in the complexity of the neural activity in the temporal region. Typically, these changes are associated with a decrease of fractal complexity chaotic rhythms in time and temporal region is involved in the regulation of the compensation with the monotonous physical stress. It has been suggested that in order to maintain physiological activity must be in contrast to the emphasis on the monotonous repetition of intense exercise, use positive specific effects that give qualitative and quantitative changes in the practical exercises [48].

7.1. Registration of the signals of electrical activity of the cerebral cortex

In the chapter,[1] the registration of signals of the cerebral cortex was carried out using 19 sensors with a sampling frequency of 500 Hz using Neurofax EEG System which uses a daisy chain montage. The data were exported with a common reference using Eemagine EEG. The order of electrodes FP1 FP2 F3 F4 C3 C4 P3 P4 O1 O2 F7 F8 T3 T4 T5 T6 FZ CZ PZ is shown in **Figure 15**, **IV**. EEG signals were recorded from a healthy subject (male, aged 21). During the removal of EEG test signals, the patient did not control his breathing or swallowing. Signal recording was performed with eyes closed. The transition from one type of movement to

[1]Brain Computer Interface research at NUST Pakistan, research carried out at National University of Sciences and Technology, Pakistan https://sites.google.com/site/projectbci/.

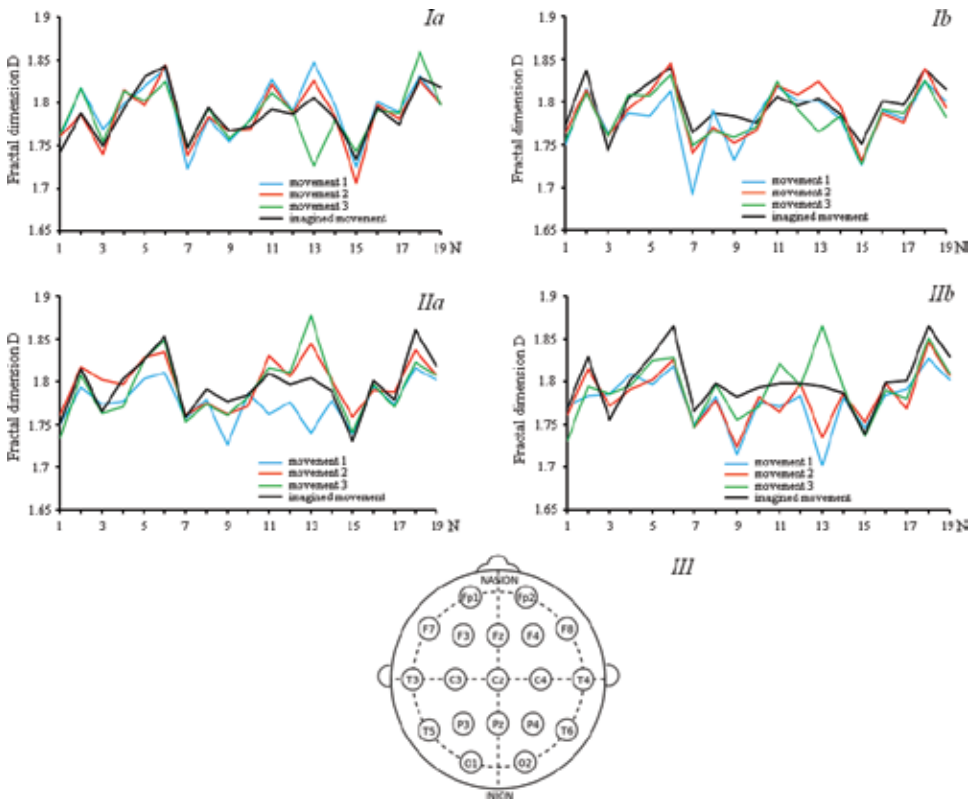

Figure 15. The fractal index D of EEG signals (19 sensors) when the right-handed subjects movements and mental play: (Ia) left hand back, (Ib) left hand forward, (IIa) right hand back, (IIb) right hand forward, (III) location of EEG sensors.

another occurs by the audio signal—"go." EEG signals $x(t)$ are dynamic variables $x(t) = x_i(t)$ at a certain value $i(1 \le i \le n)$. Let $\{x_i\}_{i=1,..,3008}$ is the time series obtained by the EEG signal measurements hand movement left (right) forward (backward), $\{x_i\}_{i=1,..,7040}$—time series obtained by the EEG signal measurements imaginary hand movements (left, right), $\{x_i\}_{i=1,..,64300}$—time series obtained by the EEG signal measurements random movements both, right (left) hands, then the time series $\{x_i\}_{i=1,..,10048}$ obtained by the EEG signal measurements random motion of leg (left, right).

7.2. Fractal analysis of signals EEG

Motor function of various organs creates different distribution activity of brain areas. Of particular interest is the identification of the activity of brain regions that are directly set with the motor command and precede its formation. For example, areas that meet the definition of executive selection, the direction of its operation directed to the target, and then manipulating the object recognition parameters.

Self-organization as the ability to create a variety of spatial and temporal patterns manifested in different ways when the motor functions arms (legs). In **Figure 15 (Ia, Ib)** shows the values

of fractal dimension *D* for EEG signals (horizontal sensor 19) when the three subjects aimed successive movements of the left (right) hand (back, forward). Implementation of the first movements of different "triggers" gain "control" brain possibilities in the selection of the executive arms in action, and directions for its operation. So, for the left hand is executed first movement "back" shows the highest fractal dimension for the whole crust, except the left and pravozatylochnoy areas, with a decrease in size by repeated movements, especially in the field of levovisochnoy. When the movement is "forward" with his left hand, the fractal dimension reaches the highest values in most areas of the brain during the execution of the second movement. It should be noted that in the area formed levovisochnoy spatiotemporal pattern, characterized by the lowest fractal dimension of the neural activity of the brain while driving with his left hand (back, forward), and the highest when the right hand movements. The fractal dimension of the neural activity of the cortex for the right hand (**Figure 15 IIa** and **IIb**) reaches its maximum value when performing the third directional movement as the back and forward in all areas, except the front part. Rerunning the real hand movements should gradually lead to some of the effects of inhibition of neuroactively most involved areas of the brain, but this effect was not shown to the right hand, which may be due to the fact that the subject is right-handed. At the same time, the implementation of imaginary movements of both hands (back, forward) has a general orientation corresponding activation of motor areas of the cortex, with a characteristic decrease in the fractal dimension *D* in the left and right temporal regions and growth in the frontal, parietal, and occipital regions. Fractal analysis of EEG signals revealed the presence of the same multiscale effect due to the fact that the imaginary hand movements activate the same areas of the brain, as well as actually performed movement. For random arm movements, both right and left formed like spatiotemporal pattern of neural activity of the brain, with the most significant increase in fractal dimension *D* for the right hand (**Figure 16b**).

Topographic map of the fractal dimension of EEG signals of three successive movements of the left hand (forward, backward) at different time intervals show different localization of the

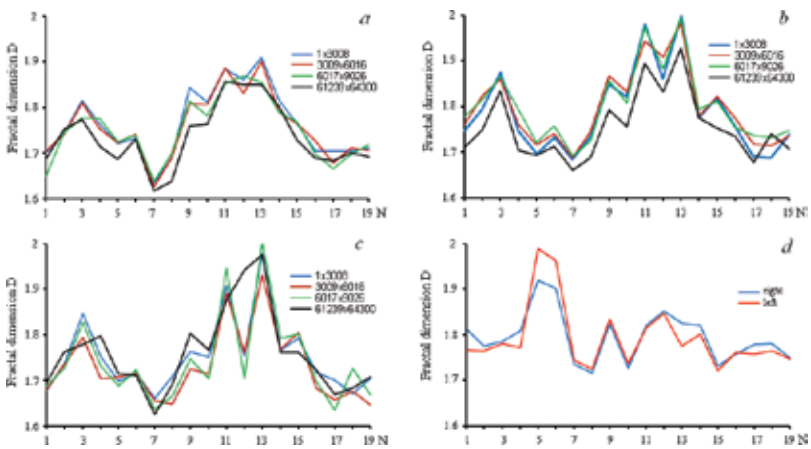

Figure 16. The fractal index *D* of EEG signals (19 sensors) when the right-handed subjects were random movements: (a) left hand, (b) right hand, (c) both hands, and (d) random movement foot (right, left).

http://dx.doi.org/10.5772/intechopen.68167

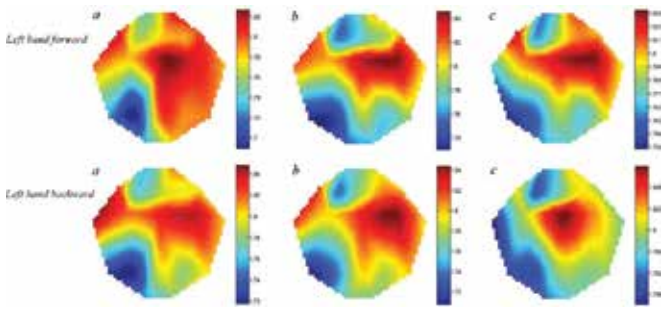

Figure 17. Topographical map of the fractal dimension for EEG signals of three successive movements of the left hand on the slots: (a) 1 × 3008, (b) 3009 × 6016, and (c) 6017 × 9024.

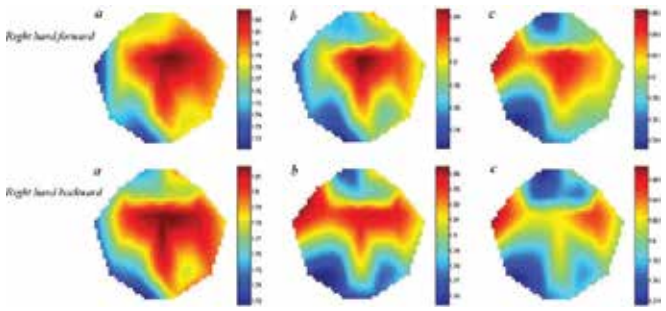

Figure 18. Topographic map of the fractal dimension for EEG signals of three successive movements of the right hand at the slots: (a) 1 × 3008, (b) 3009 × 6016, and (c) 6017 × 9024.

excitation region neural activity of the cerebral cortex in the parietal and right temporal regions of the third movement, with the largest decrease in the fractal dimension D of the motion "backward" (braking effect) (**Figure 17c**). **Figure 18** shows that when the repeated movements of the right hand moves "forward," observed the localization of excitation in the parietal region, whereas in repeated movements "backward" is formed by the reaction of a particular neural activity of the brain and is redistributed in the direction of the parietal region to the left and right temporal regions. The observed redistribution of zones of activity of brain areas with the spatial localization of the excitation region during repeated motoractions, demonstrates a decrease in the structural complexity of the background activity of brain regions with inherent fractal properties of space-time scale invariance and the formation of temporal patterns.

Topographic map of the fractal dimension of the EEG signals imaginary left movement (right) hands show the formation of the same space-time pattern for the forward movement (back), with the increase of fractal dimension with the largest imaginary movements of the right hand (**Figure 19**). As a control group of the learning process at different time stages of the EEG signals are presented randomly directed, uncontrolled movements of arms (both, left, right) (**Figure 20**). **Figure 21** presents topographical diagram of self-similarity coefficient K random arm movements (both, left, right), which can detect the minimum (abnormal), especially in the self-similar characteristics of the neuronal activity of the brain in the areas of self-organization

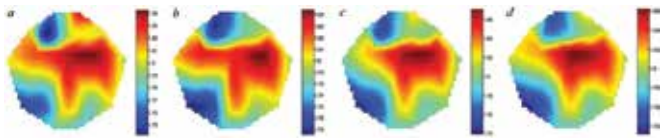

Figure 19. Topographic map of the fractal dimension of the EEG signals imaginary movement in the time interval (1 × 7040 points): (a) left hand forward; (b) left hand backward; (c) right hand forward, and (d) right hand backward.

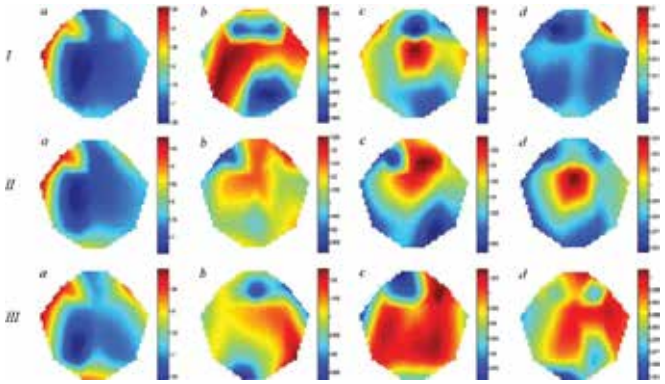

Figure 20. Topographic map of the fractal dimension *D* (a), and their relationship to the signals of EEG random movements of both (I), right (II) and left (III) hands: (a) (1 × 3008), (b) (3009 × 6016)/(1 × 3008), (c) (6017 × 9024)/(1 × 3008), and (d) (61293 × 64300)/(1 × 3008).

in comparison with the ideal (ordered) fractal. At different time intervals ratio of self-similarity coefficients revealed the formation of specific areas of brain activity fluctuations at different time intervals, wearing messy anomalous. Such processes do not always correspond to the criterion of the nonlinear chaos in which the effects of some "noise" is accompanied by an increase of order, followed by the effect of "inhibition" in long-term performance of similar movements.

The observed redistribution of zones of activity of brain areas with the spatial localization of the excitation region during repeated motor activity, demonstrates the reduction in the structural complexity of the background activity of brain regions with inherent fractal properties of space-time scale invariance. Thus, long-term random motion of leg (right, left) there is a steady activity excitation parietal and temporal regions of the brain (**Figure 21**), with a characteristic increase in the fractal dimension of the largest in the frontal region and the decrease in the occipital, which may indicate a localization of activity excitation of the cortex with this type of movement.

Chaotic dynamics inherent in neurons provides a quick transition between different states, including the brain resilience. Thus, long-term random motion of leg (right, left) there is a steady activity excitation in the left and right parietal and temporal regions of the brain (**Figure 22**), with a characteristic change in the fractal dimension of the largest in the frontal

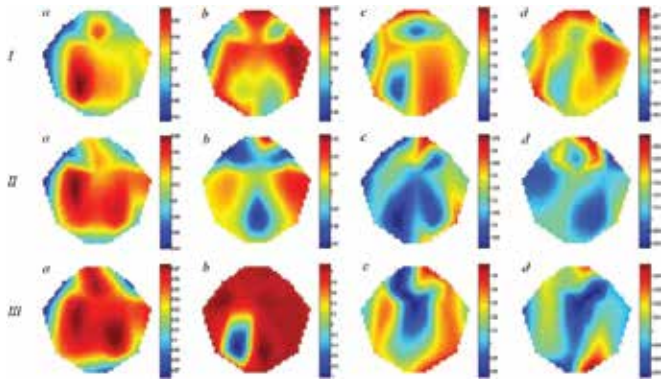

Figure 21. Topographic map of self-similarity coefficient K (a) and their relationship to the different time intervals for the EEG signals random movements both (I), right (II) and left (III) hand: (a) (1 × 3008), (b) (3009 × 6016)/(1 × 3008), (c) (6017 × 9024)/(1 × 3008), (d) (61293 × 64300)/(1 × 3008).

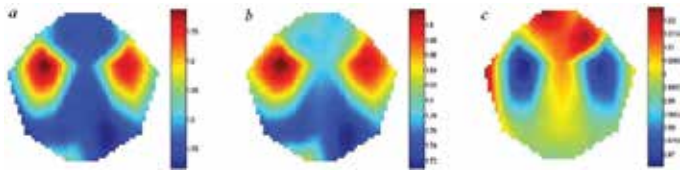

Figure 22. Topographic map of the fractal dimension of EEG signals consistent leg movements (1×10048): (a) left, (b) right, and (c) ratio of $D_{\text{right.}}/D_{\text{left}}$.

region and the decrease in the occipital, which may indicate the formation of a special spatio-temporal pattern of activity in the process of localization of the excitation of the cerebral cortex when driving leg (right, left).

This study is of particular interest, since it demonstrates the sensitivity of fractal geometry to an increase in neural activity in the initial stage of training, and then return to their previous level. This is due to the fact that occurs early in the search for new activity pattern and its location after sensorimotor rhythm activity decreases.

These results from the space-time dimension D fractal patterns allow a provisional diagnosis of functional activity of the musculoskeletal system and the neural activity of brain regions.

8. Conclusion

Many complex structures of living systems exhibit the property of self-similarity. Of particular interest is the question of nonlinearity of physiological functions and anatomical structures of the human. In accordance with the classical concepts of physiological monitoring, healthy self-regulation systems are susceptible to reduce volatility and maintain physiological constancy. However, a variety of events, such as, for example, a normal human heart, characterized by rather complex vibrations even at rest, with a chaotic pattern, bearing the signs of self-similarity.

Peculiar to these systems multifractal cascades in a wide range of time scales, suggest that the nonlinear regulatory systems are far from equilibrium, and that the continued persistence is not the purpose of physiological self-control. In contrast to systems with pathologies, characterized by fractal organization, with decreasing complexity and increasing frequency.

This chapter presents a study showing a large-scale nonlinear complexity of human physiological functions, which are simplified or complicated in certain diseases, the identification of the presence in their structure of the chaotic fractal properties. Our studies have shown that the effect of the disease state leads to a decrease of functional complexity of various processes occurring with the development of the observed frequency, only on a certain dominant time interval. The complexity of the processes, characterized by a detectable our inherent multifractal property may decrease under the influence of various factors such as the disease state of various complexity, immune deficiency, age, resulting in the development of the dynamics of adaptation to a different volume. These results show us that the human body to adapt the regulatory system, bearing linear, operates in conditions far from equilibrium. Chaotic processes in dynamic adaptation processes, whether they are a consequence of disease or training (combination of light flickering stimuli IMC), allow the body to include the self-organization of the system, adequately responding to the rapidly flowing and unpredictable changing circumstances [49]. Disease state, as well as the age factor, leads to a decrease of the fractal dimension, which characterizes the degree of randomness of the processes. However, as shown by our study, the presence of disease does not always lead to a decrease of fractal dimension and the growth of the periodicity (regularity). These results demonstrate the behavior of self-similarity coefficient formation at different time intervals characteristic of abnormal deviations in a self-organizing structure of the body, compared with an ordered (ideal) fractal. Such processes confirm that occurring for a long time processes do not always correspond to the criterion of the nonlinear chaos in which the effects of some "noise" is accompanied by an increase of order.

The fractal dimension characterizes the spatial and temporal invariance of time intervals in healthy individuals, which disappears in severe pathological diseases, causing disorders of motor functions, coordination and control of the executive body, as demonstrated by us in studies of "dynamic conditions" as leukemia and liver disease, as well as in the study-MEG signals the effects of different combinations of light flickering stimuli and EEG signals, when the motor functions in the learning process. The presence of self-similar properties indicates that the dynamics of the process, the result of which they are characterized by a certain space-time mechanism, acting in accordance with the general principles and laws of development of the disease, and functioning at each hierarchical level.

The use of computer technology and diagnostic equipment in the diagnosis considerably facilitates work of the doctor-diagnostician, reducing the influence of the human factor. In most cases, information is provided for diagnosis of the form of two-dimensional signals in a halftone image (tomogram, ultrasonic images, X-rays, etc.). When processing of digital images for diagnosis, to date, the great difficulty is the selection of small objects arranged randomly and having vague outlines. Our studies on the identification of sensitive fractal analysis to changes in the surface structure, and epithelial density in cancer, aimed at identifying the presence of atypical areas in the images and is an urgent task for the detection of pathological

changes in the early stages of the disease, characterized by changing the fractal characteristics (fractal dimension, SRBG method, the self-similarity ratio).

In the development of applications of nonlinear dynamics in human physiology and disease noninvasive diagnostic techniques, based on the application of fractal geometry, new approaches study demonstrating the need for and benefits of fractal analysis in medical diagnostics. It is expected that the results can be the basis of new methods of medical diagnosis and treatment of diseases of the human physiological functions. The proposed approaches based on identifying the presence of the properties of self-similarity may be useful to conduct preliminary clinical trials for the diagnosis of cancerous epithelial diseases, blood, and liver in the initial stages, the analysis of digital images, the structure of correlations of biomedical parameters, and EEG signals and magnetoencephalography in the study of pathologies the central nervous system—neurological, neurodegenerative disorders, psychiatric disorders, and may be the basis for the development of the interface "brain-computer." Our results can be used in the treatment of various pathological conditions.

Author details

Tayurskii Dmitrii Albertovich and Rusanova Inna Aleksandrovna*

*Address all correspondence to: irusanova@yandex.ru

Kazan Federal University, Kazan, Russia

References

[1] Tayurskii D, Lysogorskiy Yu. Superfluid hydrodynamic in fractal dimension space. Journal of Physics: Conference Series. 2012;**394**:012004.

[2] Tayurskii D, Lysogorskii Yu, Zvezdov D. Two-fluid hydrodynamic model for superfluids in fractal dimensions. Journal of Physics: Conference Series. 2009;**150**:032110(1–4).

[3] Tayurskii D, Mehaute A. Le Complex fractional differential operators, geometrical phase transition and Riemann conjecture. Fractional Differentiation and Its Applications. 2013;**6** (1):138–142.

[4] Crownover R. Fractals and Chaos in Dynamic Systems. Moscow: Postmarket; 2000. p. 352.

[5] Bak P, Chen K. Self-organized criticality. World of Science. 1991;**3**:16–24.

[6] Schroeder M. Fractals, Chaos, Power Laws: Minutes from an Infinite Paradise. New York: W.H. Freeman; 1991. p. 429.

[7] Avnir D, Gutfraind R, Farin D, Fractal Analysis in Heterogeneous Chemistry. In: Bunde A., Havlin S., (eds.). Fractals in Science, Berlin: Springer; 1994. p. 229–256.

[8] Newman T. Population dynamics with a refuge: Fractal basins and the suppression of chaos. Theoretical Population Biology. 2002;**62**:121–128.

[9] Dubovikov M, Starchenko N, Dubovikov M. Dimension of the minimal cover and fractal analysis of time series. Physica. 2004;**A339**:591–608.

[10] Wen F, Jun W. Statistical properties and multifractal behaviors of market returns by using dynamic systems. International Journal of Modern Physics C. 2012;**23**(3):1250023-1-1250023-14.

[11] Radu V, Bacaita S, Uliniuc A et al. Fractal hydrodynamic model for drug release processes from starch based hydrogels. Materiale Plastice. 2013;**50**(1):18–22.

[12] Mehaute A, Tayurskii D, Menezes R. Innovation management from fractal infinite paths integral point of view. Hyperion International Journal of Econophysics & New Economy. 2014;7(1):27–44.

[13] Welstead S. Fractal and Wavelet Image Compression Techniques. SPIE Press: USA; 1999. p. 259.

[14] Mandelbrot B. The Fractal Geometry of Nature. San Francisco: W.H. Freeman; 1982. p. 460.

[15] Feder J. Fractals. New York: Plenum Press; 1988. p. 260.

[16] Rusanova I. Study of fractal structure of images of nail bed and periungual epithelium. Biomedical Engineering. 2013;**47**(2):83–85.

[17] Goldberger A, Giles F. Filley lecture. Complex systems. Proceedings of the American ThoracicSociety. 2006;**3**:467–471.

[18] Goldberger A, Amaral L,Hausdorff J et al. Fractal dynamics in physiology: Alterations with disease and aging. Proceedings of the NationalAcademy of Sciences of the United States of America. 2002;**99**:2466–2472.

[19] Mashiah A, Wolach O, Sandbank J. Lymphoma and leukemia cells possess fractal dimensions that correlate with their biological features. Acta Haematologica. 2008;**119**: 142–150.

[20] Randall L, Rosana C, Fernanda G, et al. The fractal dimension of nuclear chromatin as a prognostic factor in acute precursor B lymphoblastic leukemia. Cellular Oncology. 2006;**28**: 55–59.

[21] Onischuk S, Suprunov V, Aslamazova G, Naida A. Hematologic aspects oncological diseases. Proceedings of the International Scientific Symposium. [Internet]. 2015. Science of the XXI century and the challenges of our time. Available from: http://sworld.com.ua/simpoz4/134.pdf

[22] Maiev I, Cucheravui Y, Morozov S, et al. Effect of ursodeoxycholic acid drugs on biochemical parameters of blood and elastography of the liver in patients with alcoholic cirrhosis. Clinical Prospects of Gastroenterology, Hepatology. 2010;**4**:43–48.

[23] Razzhevaikin V, Shpitonkov M, Gerasimov A. Application of correlation adaptometry in biomedical problems. Operations Research (Models, Systems, Solutions). Moscow: VTs RAN; 2002. pp. 51–55.

[24] Rusanova I. The structural analysis of processes dynamics, proceeding in blood. Medical Physics. 2013;**1**(57):59–64.

[25] Kugiumtzis D, Larsson P. Linear and nonlinear analysis of EEG for the prediction of epileptic seizures. Proceedings of the 1999 Workshop Chaos in Brain? Singapore: World Scientific; 2000. pp. 329–333.

[26] Osorio I, Frei M. Hurst parameter estimation for epileptic seizure detection. Communications in Information and Systems. 2007;7(2):167–176.

[27] Li X, Polygiannakis J, Kapiris P et al. Fractal spectral analysis of pre-epileptic seizures in terms of criticality. Journal of Neural Engineering. 2005;**2**:11–16.

[28] Hornero R, Abasolo D, Escudero J et al. Nonlinear analysis of electroencephalogram and magnetoencephalogram recordings in patients with Alzheimer's disease. Philosophical Transactions of Royal Society A. 2009;**367**(1887):317–336.

[29] Timashev S, Yulmetyev R, Demin S, Panischev O. Yu et al. Analysis of biomedical signals by flicker-noise spectroscopy: Identification of photosensitive epilepsy using magnetoencephalograms. Laser Physics. 2009;**19**:836–854.

[30] Bhattacharya J, Watanabe K, Shimojo S. Nonlinear dynamics of evoked neuromagnetic responses signifies potential defensive mechanisms against photosensitivity. International Journal of Bifurcation and Chaos. 2004;**14**:2701–2720.

[31] Panischev O, Demin S, Rusanova I. Studying properties of abnormal human brain activity in photosensitive epilepsy caused by light stimulation. Biomedical Engineering. 2015;**49**(4):236–239.

[32] Wolpaw J, Birbaumer N, McFarland D et al. Brain-computer interface for communication and control. Clinical Neurophysiology. 2002;**113**:767–791.

[33] Zander T, Kothe C. Towards passive brain–computer interfaces: Applying brain–computer interface technology to human–machine systems in general. Journal of Neural Engineering. 2011;**8**(2):025005.

[34] Khan M, Hong M, Hong K, Decoding of four movement directions using hybrid NIRS-EEG brain-computer interface. Frontiers in Human neuroscience. 2014;**8**:1–10. DOI:10.3389/fnhum.2014.00244

[35] Ma J, Zhang Y, Cichocki A, Matsuno F. A novel EOG/EEG hybrid human–machine interface adopting eye movements and ERPs: Application to robot control. In IEEE Transactions on Biomedical Engineering. 2015;**62**(3):876–889.

[36] Lotte F, Congedo M, Lecuyer A et al. Review of classification algorithms for EEG-based brain-computer interfaces. Journal of Neural Engineering. 2007;**4**:1–24.

[37] Blankertz B, Tangermann M, Vidaurre C et al. Berlin brain-computer interface: Non-medical uses of BCI technology. Frontiers in Neuroscience. 2010;**4**(198):17.

[38] Kaiser V, Kreilinger A, Muller-Putz G, Neuper Ch. First steps toward a motor imagery based stroke BCI: New strategy to set up a classifier. Frontiers in Neuroscience. 2011;**5** (86):10.

[39] Morash V, Bai O, Furlani S et al. Classifying EEG signals preceding right hand, left hand, tongue, and right foot movements and motor imageries. Clinical Neurophysiology. 2008;**119**:2570.

[40] Bass G. Nonlinear Man. Chaos, Fractal and Homeostatic Interplay in Human Physiology [Internet]. 1997. Available from: http://www.tonleenders.nl/Pdf/chaos_and_man.PDF

[41] Lehnertz K. Non-linear time series analysis of intracranial EEG recordings in patient with epilepsy—an overview. International Journal of Psychophysiology. 1999;**34**:45–52.

[42] Korn H, Faure P. Is there chaos in the brain? II. Experimental evidence and related models. Comptes Rendus Biologies. 2003;**326**(9):787–840.

[43] Izhikevich E. Dynamical Systems in Neuroscience. The Geometry of Excitability and Bursting. The MIT Press. Massachusetts: Cambridge; 2007. p. 210.

[44] Schiff S, Jerger K, Duong D et al. Controlling chaos in the brain. Nature. 1994;**370**(6491): 615–620.

[45] Dornhege G, Millan J, Hinterberger T. Toward brain-computer interfacing. A Bradford Book. The MIT Press. Massachusetts: Cambridge; 2007. p. 520.

[46] Sonkin K, Stankevich L, Khomenko Y et al. Classification of EEG patterns of imaginary and real movements of the fingers of one hand the method of support vector machines. Pacific Journal of Medicine. 2014;**2**:30–35.

[47] Sotnikov P. Review methods of EEG signal processing in the brain-computer interface. Electronic Scientific Engineering and Technical Journal Gazette. [Internet]. 2014;10. Available from: http://engbul.bmstu.ru/doc/739934.html

[48] Pakenas A, Souza J, Pereira B. Non-linear dynamics and physical exercise: Concepts and applications. Revista Brasiliera de Medicina do Esporte. 2007;**13**(5):299e–303e.

[49] Rusanova I. Structural analysis of age features adaptive reactions in tumor processes in the lung. Medical Physics. 2016;**3**(71):81–86.

Chapter 4

Polyadic Cantor Fractals: Characterization, Generation, and Application as Ultrasonic Lenses

Sergio Castiñeira-Ibañez, Daniel Tarrazó-Serrano,

José Miguel Fuster, Pilar Candelas and

Constanza Rubio

Additional information is available at the end of the chapter

http://dx.doi.org/10.5772/intechopen.68425

Abstract

The term fractal was coined in 1975 by Benoit Mandelbrot. Since then, fractal structures have been widely used by the international scientific community. Its range of applications includes multiple areas, such as optics, physics, cryptography, medicine, economics, and so on. The application of fractal structures to modulate light beams in the field of optics has been extensively studied, and it has been shown that in some cases these new fractal lenses improve the response of traditional lenses. Fractal lenses are able to provide beamforming capabilities, and allow the optimization of the optical beam according to the specific requirements. In some applications, it may be necessary to improve the focus in a certain area, while in others it may be critical to obtain a sharp attenuation by means of destructive interference. It may even be required a beam profile with multiple focus and a certain control over them. This work investigates the application of fractal structures based on Polyadic Cantor sets as ultrasonic lenses, analyzing how the relation between the different design parameters and the performance of the lens. It is shown that the working frequency becomes a precise control mechanism that can modify dynamically the focus position of the lens.

Keywords: fractal, polyadic Cantor sets, ultrasonic lenses, sound beam modulation, sound focusing

1. Introduction

Every structure with symmetry properties of scale invariance, even for a short range, is likely to possess fractal properties. These structures are characterized by a noninteger fractal dimension that can be sighted as a measure of their irregularity. It can be said that the whole structure resembles its internal parts [1], and it has been found that several natural phenomena follow these patterns, such as snowflakes or some tree leaves. Fractal structures have attracted great interest from the scientific community, having been applied in several areas of science and technology, such as optic engineering, medicine, or economy [2]. Furthermore, research into the properties of heterogeneous artificial materials has been very active throughout the last two decades.

Wave application of fractal structures in the optical field has received a lot of attention, and it has been shown that the use of fractal diffractive lenses improve focalization over traditional lenses. These new fractal lenses have an interesting property, that is, they can produce multiple focal points along the optical axis due to the fact of fractal self-similarity [3].

Among other wave applications of fractal structures, different studies related to the acoustic field have been performed. Petri et al. [4] analyzed the vibration properties of a hierarchic system consisting on a Cantor sequence of piezoelectric and resin elements. Sapoval et al. [5] numerically investigated the acoustic properties of irregular cavities described as fractals. They proved that the geometric irregularity improved the modal density at low frequencies, localizing many of the modes at the edge of the cavity and modifying its attenuation properties. Lubniewski and Stepnowski [6] developed a simple method to identify the seabed using elements of fractal analysis. Castiñeira-Ibáñez et al. [7, 8] presented an acoustic barrier to control the noise formed by rigid cylinders in the fractal geometry of a Sierpinski triangle. These structures are capable of producing sharp attenuation by means of destructive interference, as well as focalization through constructive interference. Gomez-Lozano et al. [9] studied the transmission response in perforated plates with subwavelength holes. The transmission spectrums showed that every iteration with the Sierpinski carpet has the characteristic peaks and dips associated with the lattice constant of each matrix pattern. In other branches of acoustics, other devices based on diffraction such as root primary gratings (RPGs) offer the possibility of modulating acoustic beams.

Since the wave theory of different areas of physics have great similarity, many concepts used in these areas related to guiding the waves using fractal structures have been translated to the acoustic area and a new approach for the construction of ultrasonic lenses based on fractal structures is proposed. These lenses are able to modulate the ultrasonic beam in a different way compared to conventional lenses, where its ability to focus and guide waves comes from the fact that they are built with refractive materials with curved surfaces. Among different fractal structures, we have focused our attention on polyadic Cantor sets (PCSs). This type of fractals is very easy to construct, being that the main reason why most man-made fractal creations are based on Cantor fractals [10–17]. Nevertheless, focalization in the ultrasonic range requires further attention. Therefore, the aim of this chapter is to present the generation

http://dx.doi.org/10.5772/intechopen.68425

and characterization of fractal structures based on PCS and analyze their application as ultrasonic lenses.

2. Fractals

2.1. Fractal geometry

As it has been mentioned in Section 1, several phenomena in nature such as tree leaves, clouds, mountains, and circulatory system, among others, present fractal geometry (see **Figure 1**). Typical properties of fractal geometries, such as self-similarity, can be observed in these examples. The self-similarity property describes those fractals that contain self-copies and can be defined recursively. Thus, an object is said to be self-similar if its parts have the same shape or structure as the whole, although they may occur on a different scale and may also be slightly deformed. It is observed that the self-similarity property in elements in nature usually disappears after some iterations, not being able to reach infinity. When generating fractal structures, the current iteration of the fractal is also known as the stage of the fractal.

2.1.1. Fractal dimension

If the analyzed object presents self-similar properties, it can be considered a fractal object and thus it can be characterized by a parameter known as the fractal dimension (D).

Fractal dimension is a generic concept that has its origin in mathematical metrics. Unlike topological dimensions, the fractal dimension can take noninteger values. The topological dimensions of lines, squares, and cubes are respectively one, two, and three. Mandelbrot's research, based on previous works of Hausdorff, introduced the possible existence of geometric objects of intermediate dimensions between those integer values, and thus, the concept of fractal dimension [1, 18]. It can also be understood as a measure of the space-filling capacity of a fractal pattern.

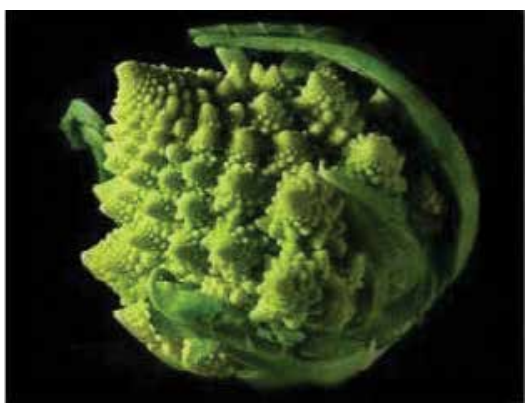

Figure 1. Example of fractal in nature (Public-Domain-Photos.com).

Fractals are generated from an initiator corresponding to step $s = 0$ (see **Figure 2**) and the fractal dimension can be calculated as,

$$D = -\frac{\ln N}{\ln r} \tag{1}$$

with N the number of self-copies of the initiator at stage 1 ($s = 1$), i.e., the generator and r the scale factor that rules the length shrinkage of the copy in each new stage.

This work focuses on a fractal structure based on the Cantor set. The original Cantor set is constructed, taking an initial unit segment at stage 0 ($s = 0$) and splitting it in three identical parts. Then, the middle segment is erased and the first stage ($s = 1$) is obtained. This procedure is repeated infinitely to obtain the Cantor set.

For the original Cantor set, the number of self-copies in stage $s = 1$ is $N = 2$, while the scaling factor becomes $r = 1/3$, resulting in a fractal dimension, which corresponds to a fractal dimension of $D = 0.6309$.

2.1.2. Lacunarity

In mathematics, symmetries are expressed as invariances, i.e., lack of change, under different operations such as a spatial translation. The concept of lacunarity was first used by Mandelbrot [1]. The lacunarity parameter was introduced to describe the degree of translational invariance or homogeneity of a fractal. It is a measure of how fractal patterns fill space. Patterns that present larger holes or show a lower translational invariance are generally said to have a high lacunarity. In contrast, fractals that are more homogeneous or approach translational invariance have low lacunarity. Thus, two fractals that are constructed with a similar procedure, and even have the same fractal dimension, may present a different lacunarity, depending on their degree of heterogeneity. It can be said that the lacunarity parameter, therefore, describes the texture of the fractal pattern and makes it possible to distinguish sets that have the same fractal dimension, but different textures [19].

Many methods have been proposed to quantify this fractal parameter, some of which involve calculating the first- and second-order moments of the fractal mass distribution. One of the best known methods is the gliding box algorithm that has been used in the present work.

Figure 2. Building of the Cantor set. Stages $s = 0$, 1, 2, and 3 are shown.

http://dx.doi.org/10.5772/intechopen.68425

2.1.3. Prefractal

As it has been explained in Section 2.1.1, fractals are generated from an initiator corresponding to step $s = 0$. In the next step ($s = 1$), the initiator is replaced by a number or scaled copies of itself. This procedure is repeated over and over in the following stages. Strictly speaking, a fractal is reached when the number of stages tends to infinity. When this whole process is truncated, prefractal structures are obtained instead.

However, throughout the chapter, the term fractal is used instead of the term prefractal as it has become a standard in engineering applications. However, this whole work refers to fractal structures with a finite stage of growth, i.e., prefractals.

2.2. Generalized polyadic Cantor sets

If the same construction procedure of the original Cantor set is replicated, but substituting the ratio $r = 1/3$ by an arbitrary ratio between 0 and 1/2, fractal sets with the same nature but with a different fractal dimension (D) are obtained. The fractal dimension has always a value between 0 and 1. These sets are known as generalized polyadic Cantor sets (GPCSs) and are characterized by the same parameters as the original Cantor set as shown in the **Figure 3** (s denotes the prefractal current stage; N, the number of scaled self-copies of the initiator at stage $s = 1$; D, the fractal dimension and, r, the scale factor with which each new copy is shrinked at the next stage). A new parameter ε represents the width lateral gaps generated at stage $s = 1$. This new parameter characterizes the distribution of the gaps inside the polyadic Cantor set and becomes a new design parameter, which enhances the control flexibility of these fractal structures in new applications. This ε parameter has also been widely accepted as an indication of the lacunarity parameter in the literature [15].

The size of all segments, which belong to the same stage (s) is identical and its value is ruled by the expression:

$$W_S = Lr^S \tag{2}$$

with L the length of the initial segment, i.e., the initiator.

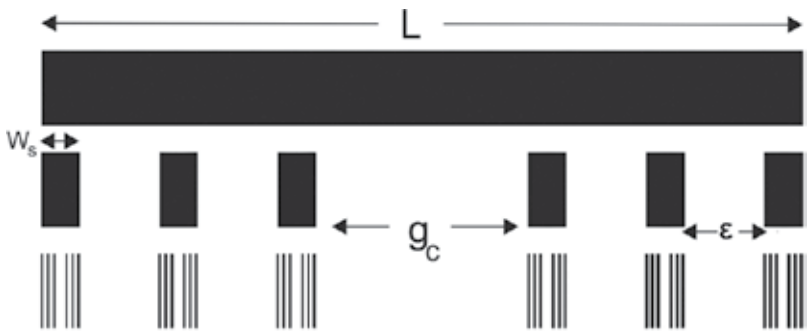

Figure 3. Generalized polyadic Cantor sets (GPCSs) main parameters.

Eq. (1), which calculates the fractal dimension, can be also expressed as a function of the number of gaps in stage 1 (n_{gaps}). Thus, the fractal dimension is rewritten as:

$$D = -\frac{\ln(n_{gaps} + 1)}{\ln r} \tag{3}$$

If the number of elements, N, is fixed, the scaling factor, r, must be modified to obtain a different fractal dimension, D. Thus, the fractal descriptor, D, becomes a direct measure of the transparency of the generated prefractal. If a prefractal presents a higher D parameter, it will be more opaque, i.e., filled with matter, whereas a lower D parameter results in a more transparent prefractal structure.

Generalized polyadic Cantor sets (**Figure 4**) can have either even or odd order. In the first stage ($s = 1$), the even-order sets have a central gap and an even number of gaps on both sides (lateral gaps). In contrast, those of odd order do not have a central gap, but two gaps or identical size next to the central segment. These two gaps closer to the center (adjacent gaps) are equivalent to the central gap in an even-order set. The rest of the gaps (lateral gaps) are identical among them and distributed as in the even-order case, but have a different size to the adjacent gaps.

The width of the central gap is denoted by g_C. In the even-order set the central gap has a width equal to $h\ g_C$, while in the odd-order case the two adjacent gaps have a width equal to $g_C/2$. The width of the lateral gaps for both the even case and the odd case is denoted by ε.

One can discuss which cases present minimal or maximum lacunarity. Thus, when all the gaps at the first stage, including the central or the adjacent gaps, are of equal width, the lacunarity is said to be minimal (homogeneous case). The value of this gap width, which produces this minimal lacunarity turns out to be:

$$\varepsilon_{min\_lacunarity} = \frac{1 - N\,r}{N - 1} \tag{4}$$

As it can be observed in **Figure 5**, all of the gaps in stage $s = 1$ present the same width. This case is an even-order set with $N = 6$ and achieves minimum lacunarity since the distribution of gaps is homogeneous.

On the other hand, maximum lacunarity is achieved when the lateral gaps are removed ($\varepsilon_{max\_lacunarity} = 0$). Thus, for an even-order Cantor set, a central gap remains in the middle of the set and two identical segments without gaps are placed at both sides of that central gap, as shown in **Figure 6**. For an odd-order cantor set, there is a segment in the center with two identical adjacent gaps. Then, two identical segments without lateral gaps are found at both sides of the set as in the even-order case.

Lacunarity may also be increased going in the opposite direction. The central gap may be shrinked instead of augmented. In this direction, the higher lacunarity is obtained when the central gap disappears and the whole gap space is split among the lateral gaps, as shown in **Figure 7**.

http://dx.doi.org/10.5772/intechopen.68425

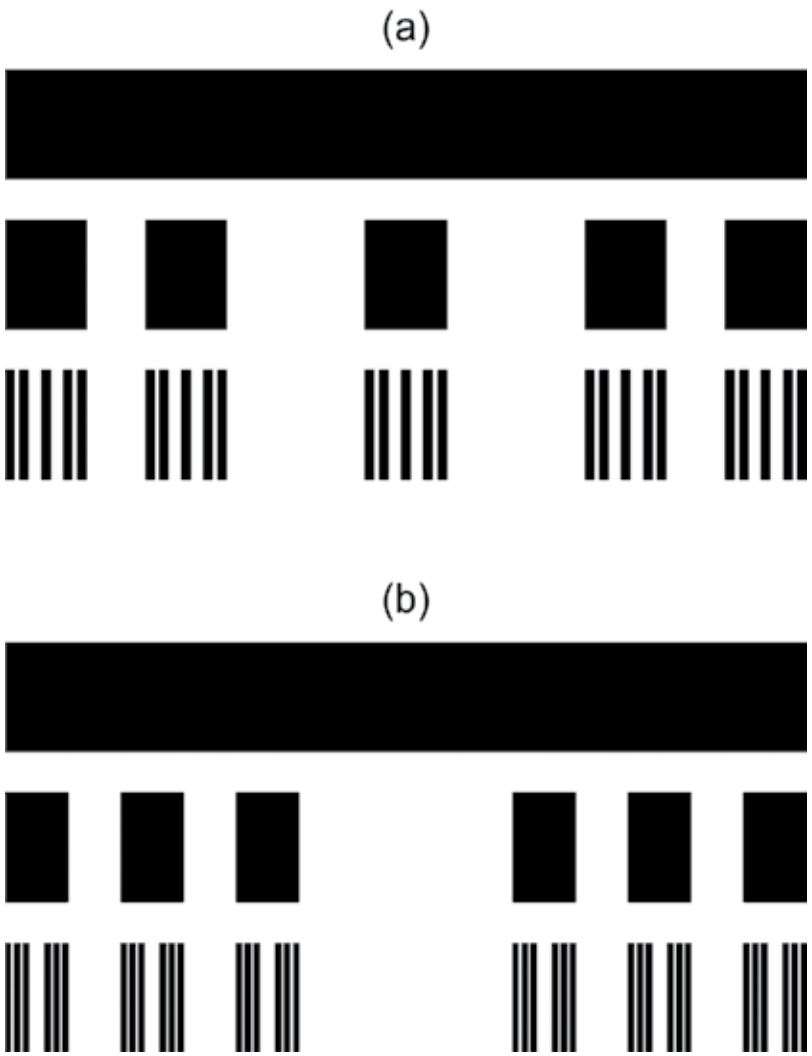

Figure 4. Generalized polyadic Cantor sets. (a) Odd order ($N = 5$) and (b) even order ($N = 6$).

This case corresponds to an ε value given by:

$$\varepsilon_0 = \frac{1 - N\,r}{N - 2} \text{ if } N \text{ is even} \tag{5}$$

$$\varepsilon_0 = \frac{1 - N\,r}{N - 3} \text{ if } N \text{ is odd} \tag{6}$$

The general expressions for the ε parameter, for any lacunarity value, are given by,

$$\varepsilon = \frac{1 - N\,r - g_C}{N - 2} \ (N \geq 4) \text{ if } N \text{ is even} \tag{7}$$

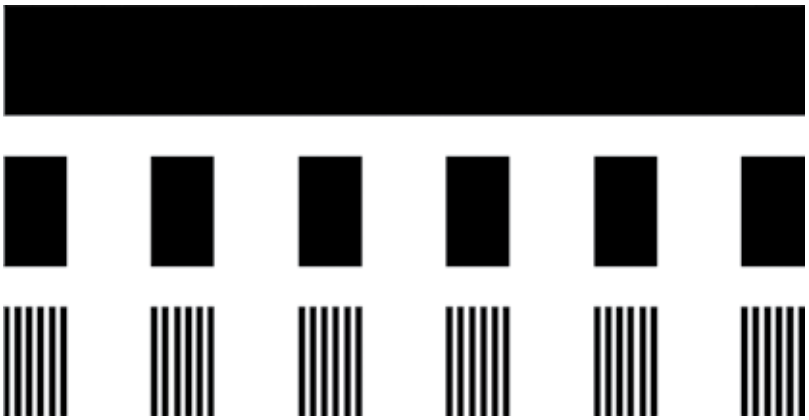

Figure 5. Generalized polyadic Cantor set ($N = 6$) with minimum lacunarity.

Figure 6. Generalized polyadic Cantor set ($N = 6$) with maximum lacunarity.

$$\varepsilon = \frac{1 - N\,r - g_C}{N - 3} \ (N \geq 5) \text{ if } N \text{ is odd} \tag{8}$$

Another very useful parameter is the central gap fraction (f_{gc}). This parameter conveys the same information as the ε parameter, but it is a more intuitive parameter easier to visualize. The central gap fraction represents the ratio between the width of the central gap and the total width of the combination of the gaps of the PCS. The central gap fraction can be expressed as,

$$f_{gc} = \frac{g_C}{1 - Nr} \ (N \geq 4) \tag{9}$$

And the relationship between the f_{gc} and the ε parameters is given by,

$$f_{gc} = \frac{1 - Nr - (N-2)\varepsilon}{1 - Nr} \text{ if } N \text{ is even} \tag{10}$$

http://dx.doi.org/10.5772/intechopen.68425

Figure 7. Generalized polyadic Cantor set ($N = 5$) with high lacunarity.

$$f_{gc} = \frac{1 - Nr - (N-3)\varepsilon}{1 - Nr} \text{ if } N \text{ is odd} \tag{11}$$

3. Numerical models and lens design

The interaction of acoustic waves with matter is well explained by means of theoretical models. The development of these accurate models has allowed, to a large degree, the development of acoustics in the last decades. These models are numerically programmed, providing an intake to understand the underlying physics in new systems and devices. Thus, numerical modeling is a very useful tool to enhance the design of polyadic Cantor fractal lenses (PCFLs) before fabricating them.

In our work, numerical modeling has been split into two separate procedures. First, polyadic Cantor sets and their corresponding ultrasonic lenses are designed using the Matlab software, and then, their acoustic behavior has been analyzed using the finite element method (FEM).

The main parameters used for the design of the PFCL are the following: fractal dimension (D), stage (s), number of self-copies of the generator (N), central gap fraction (f_{gc}), scale ratio (r), central gap width (g_C), and lateral gap width (ε). Additionally, there are other parameters that also affect the behavior of the lens and have to be considered, such as the working frequency (f) or the size of the lens characterized by its radius (R).

The scale ratio can be easily obtained from Eq. (1) and is given by,

$$r = N^{-1/D} \tag{12}$$

And the central gap width can be calculated from,

$$g_C = (1 - rN) f_{gc} \tag{13}$$

The following equations show the theoretical formulas to calculate the position of the Cantor bars in a polyadic Cantor set. These equations are implemented recursively. The first stage is

calculated using Eq. (14) and has a different implementation depending on the order (even or odd) of the PCS. The rest of the stages are computed recursively from stage $s = 1$ using Eq. (15).

$b_{(i,1)}$ indicates the start and end of each of the Cantor bars in stage $s = 1$, where i is an integer index that ranges from 1 to $2N$.

$$b_{(i,1)}\begin{cases} \text{int}\left(\frac{i}{2}\right)\cdot r + \text{int}\left(\frac{i-1}{2}\right)\cdot \varepsilon + \text{true}(i > N)(g_C - \varepsilon) \text{ even } N \\ \text{int}\left(\frac{i}{2}\right)\cdot r + \text{int}\left(\frac{i-1}{2}\right)\cdot \varepsilon + \text{true}\Big(i > (N-1)\Big)\Big(\frac{g_C}{2} - \varepsilon\Big) + \\ \qquad + \text{true}\Big(i > (N+1)\Big)\Big(\frac{g_C}{2} - \varepsilon\Big) \text{ odd } N \end{cases} \tag{14}$$

In Eq. (14), the function int(x) stands for the floor function that maps a real number to the largest previous integer and the function true(x) is the true function which returns the value 1 when the condition inside the brackets is fulfilled and 0 otherwise.

$b_{(i,s)}$ indicates the start and end of each of the Cantor bars in stage s, where i is an integer index that ranges from 1 to $2N^s$.

$$b_{(i,s)} = b\left(1 + 2\,\text{int}\left[\frac{i-1}{2N^{s-1}}\right], 1\right) + r\cdot b(1 + \text{mod}[i-1, 2N^{s-1}],\ s-1) \tag{15}$$

The function mod(x,y) returns the reminder after division x by y.

Once the polyadic Cantor sets have been constructed, box counting methods have been used to verify the main fractal parameters, which are fractal dimension and lacunarity.

PCS have axial symmetry, and this symmetry is extended to the construction of its corresponding lens. The PCFL is constructed by rotating the PFS around its symmetry axis. When using the finite element method to simulate the PCFL acoustic behavior, this symmetry becomes a significant advantage as it reduces the computational time of the simulation.

Describing physical phenomena frequently leads to space and time-dependent problems, mathematically described by partial differential equations (PDEs). In the PFCL characterization, it is not possible to solve these equations analytically and a numerical approximation, typically, in terms of a certain discretization, is applied. FEM have been conceptually developed for the numerical discretization of problems with bounded domains and they are especially applicable for solving Helmholtz problems. A PCFL characterization problem in which the geometry, boundary conditions, and materials are symmetric with respect to an axis can be solved as an axisymmetric problem instead of as a three-dimensional problem.

The interaction of ultrasound waves with ultrasonic lenses is a very complex problem. The finite element method (FEM) seems to be an appropriate computational tool to determine the distribution of acoustic pressure and, therefore, the focal position and the size of the focal spot. To decrease the computational cost of the simulations, the geometrical properties of the model that has been implemented must be taken into account. Due to axial symmetry of these

http://dx.doi.org/10.5772/intechopen.68425

structures, numerical calculation was made by means or the 2D axisymmetric method. This model includes a piston source, which consists of an axially oscillating disk of dimensions equal to the axisymmetric lens. A plane wave with amplitude P_0 impinges the axisymmetric lenses upward along the y-direction.

For this purpose, it is necessary to solve the Helmholtz equation given by

$$\nabla\left(-\frac{1}{\rho}\nabla p\right) = \frac{\omega^2}{\rho c^2} p \tag{16}$$

where ρ ($\rho = 1000$ kg/m^3) is the medium density, c ($c = 1500$ m/s) is the ultrasound velocity, ω is the angular frequency, and p is the acoustic pressure. The assumptions made in the simulations are the following: (1) the wavelength of the incident plane wave (IPW) is large compared to the thickness of the lens, (2) the lens is considered to be acoustically rigid, therefore, the Neumann boundary condition (zero sound velocity) is applied, and (3) the plane wave radiation condition is applied to the boundaries of the domain to simulate free space and emulate the Sommerfeld condition in the numerical solution of the wave problem as shown in **Figure 8**.

Due to the characteristics of the system that is being modeled, where small time-dependent pressure variations values are assumed, the so-called background pressure field is considered.

To quantify the acoustic field, the sound pressure level is calculated in each point of the domain, and then the acoustic gain is calculated using the expression

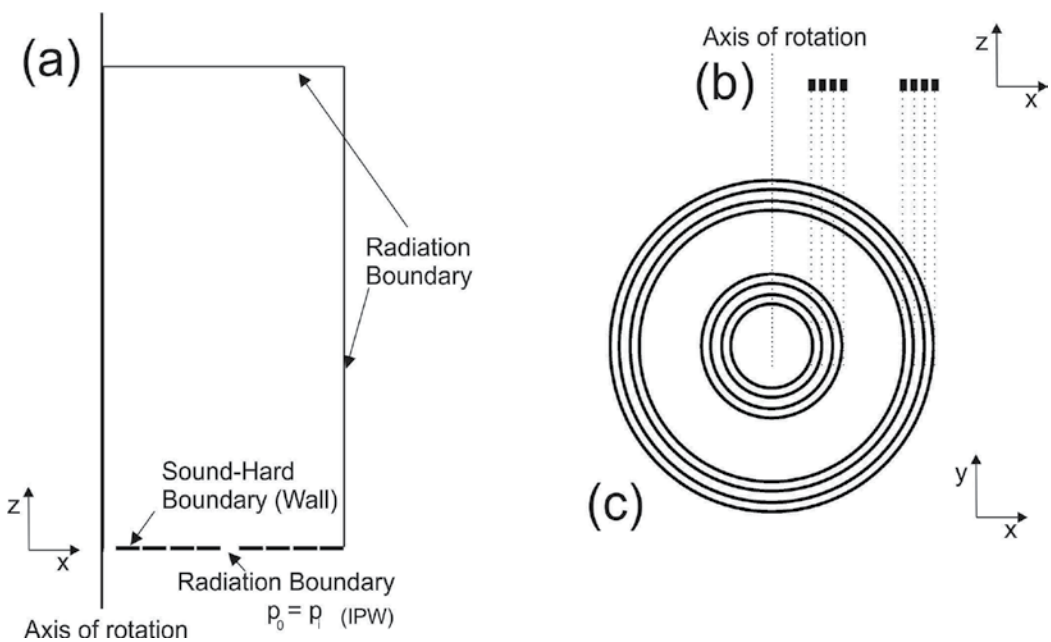

Figure 8. (a) Schematic diagram of the configuration simulated in the numerical domain where the solutions are obtained. (b) *XZ*-plane view of the PCFL. (c) *XY*-plane view of the PCFL.

$$G_{\text{focus}} = 20 \cdot \log_{10}\left|\frac{p}{p_{\text{incident}}}\right| \tag{17}$$

where p is the sound pressure at an arbitrary point, and p_{incident} is incident pressure at the lens.

4. Characterization of polyadic Cantor fractal lenses

Once the design parameters of the polyadic Cantor fractal lenses (PCFLs) have been presented, the influence of these parameters onto the modulation of sound beams is analyzed using the numerical method described in the previous section. All this work is applied to design acoustic lenses with beamforming and focal energy control mechanisms.

As it can be observed from **Figure 9**, a source emits waves of a certain frequency generating an incident plane wavefront (IPW) traveling in the direction of the *Z*-axis. The lens is oriented parallel to the *XY* plane ($Z = 0$), and is intercepted by this IPW. The PCFL has several rings that, due to diffraction phenomena, produce an infinite number of in-phase emission points, which generate a certain beamforming of the sound beam. In particular, much of the energy is concentrated at a point known as the focal lens (FL), because of constructive interferences. These types of lenses may generate more than one focus along the *Z*-axis, depending on the selected parameter values, and that can become an advantage in certain applications.

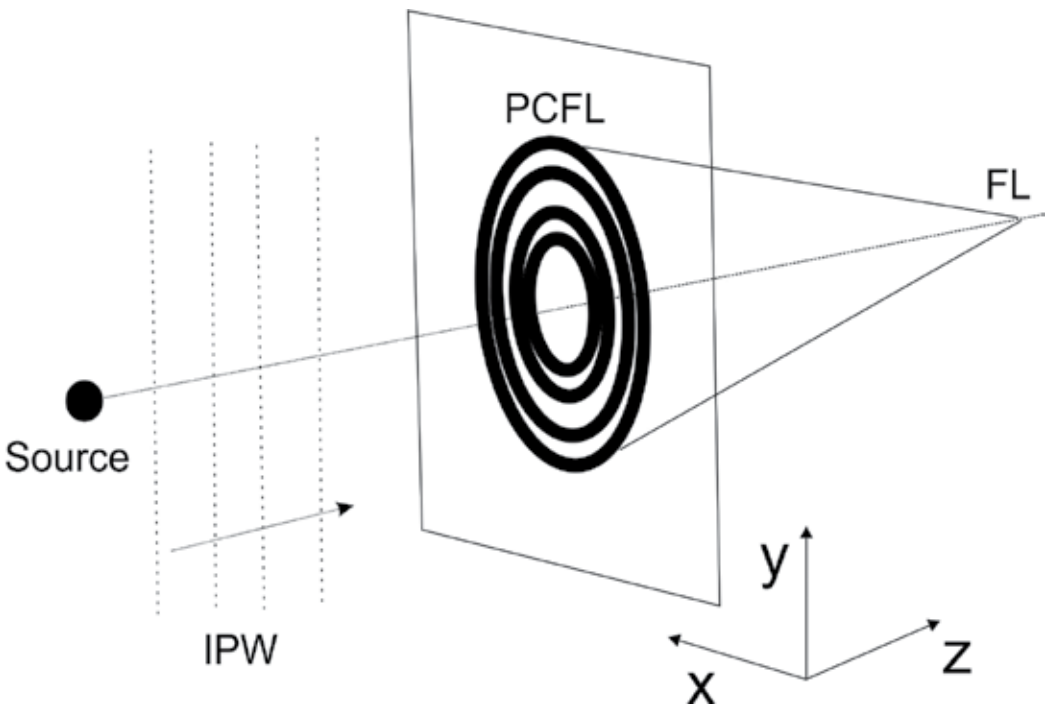

Figure 9. Numerical set-up. The IPW and FL are in *Z*-axis direction and the PCFL is placed in the *XY*-plane.

The final objective of this work is two-fold. On the one hand, the design of fractal lenses, which are capable of modulating the acoustic beam, is pursued. On the other hand, once a specific lens has been designed, it is desirable to find a dynamic parameter, such as the working frequency, that allows a certain control on the beamforming capabilities of the lenses.

For this purpose, a lens of R = 12.5 cm and negligible thickness, compared to the working wavelength, is selected. The design parameters are initially set to the following values: D = 0.6, N = 5, f_{gc} = 0.4. The working frequency is set to f = 100 kHz. For practical reasons, the PCFL stage will remain constant with value s = 2.

Throughout this section, each of the design parameters (f, D, f_{gc}, and N) will be shifted to different values, one parameter at a time, keeping the remaining parameters to their initial values. With this procedure, the influence of each parameter onto the acoustic response of the designed PCFL can be analyzed independently. Likewise, a similar study is carried out to establish the effect of the working frequency on the beamforming capability of the PCFL.

4.1. Focal distance variation with frequency

Using the design parameters values given above (D = 0.6, N = 5, f_{gc} = 0.4, s = 2, and R = 12.5 cm), a PCFL has been simulated using to the numerical methods discussed in Section 3. A flat acoustic wavefront reaches the lens. The frequency of this wavefront is shifted to values between 50 and 400 kHz. The effect of the frequency shift onto the acoustic transmission variation and beamforming modulation is then analyzed. The PCFL in the XZ-plane view is shown in **Figure 10**. **Figure 11** shows the pressure maps (gains in dB) at the XZ-plane, perpendicular to the wave propagation direction, for frequencies of 50, 100, 200, 300, and 400 kHz.

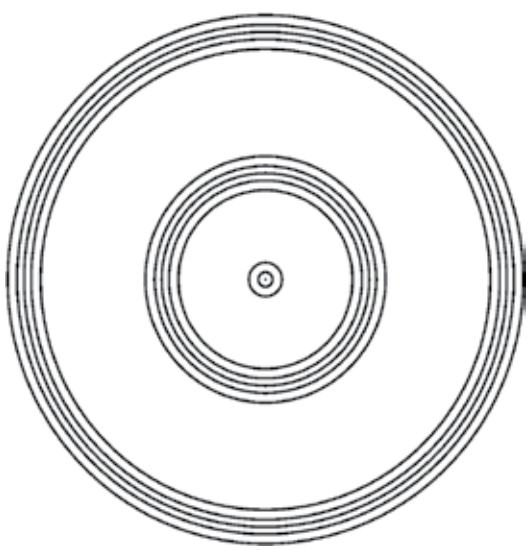

Figure 10. XY-plane view of the PCFL with D = 0.6, N = 5, f_{gc} = 0.4, s = 2, and R = 12.5 cm.

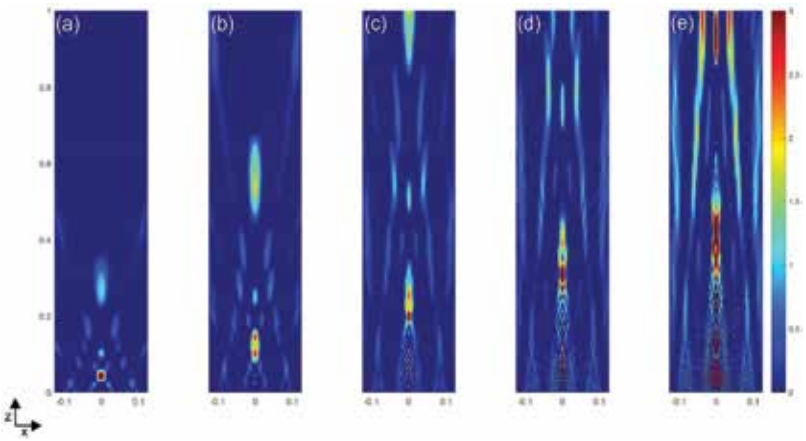

Figure 11. Two-dimensional spatial distribution of the acoustic gain (in dB) in the *XZ*-plane for the PCFL with $D = 0.6$, $N = 5$, $f_{gc} = 0.4$, $s = 2$, and $R = 12.5$ cm, for (a) 50 kHz, (b) 100 kHz, (c) 200 kHz, (d) 300 kHz, and (e) 400 kHz.

Analyzing the variation with the *X*-axis, direction parallel to the lens, a focalization in the central region ($x = 0$) may be observed. This focalization is constant and independent of the working frequency. However, the variation with the *Z*-axis, direction perpendicular to the lens, is a different subject. It can be observed that the position of the focalization area shifts with the working frequency. Moreover, the focalization area width and the focal gain also increase with the working frequency. From the simulation, a linear relationship can be established between the PCFL focal length and the working frequency given by:

$$d_f = d_{50}\frac{f}{50} = kf \tag{18}$$

being d_{50} the distance from the closest focus to the lens at a frequency of 50 kHz, which has been considered as the reference frequency, in *m*, f is the current working frequency in kHz, and d_f is the focal distance for the current working frequency in m. The k factor is defined to simplify the expression as the ratio between the focal distance at the reference frequency and the value of that reference frequency in kHz. This constant has been defined in m/kHz units.

This result is very significant, since it allows a very precise control of the lens focus location in a dynamic way, without requiring the modification of the lens design. In medical applications where focal location control is critical, such as thermal, these types of lenses have a great potential. They can be combined with high-intensity focus ultrasound (HIFU) to design treatment planning and targeting before applying an ablative level of ultrasound energy.

4.2. Variation of the fractal dimension *D*

In order to analyze the influence of the fractal dimension on the PCFL design, the design parameters are reboot to the initial values that have been previously selected ($N = 5$, $f_{gc} = 0.4$, $s = 2$, $R = 12.5$ cm) and the working frequency is set to $f = 100$ kHz. The *XZ*-view of the PCFLs for different values of *D*, (a) $D = 0.5$, (b) $D = 0.6$, (c) $D = 0.7$, and (d) $D = 0.8$, are shown in

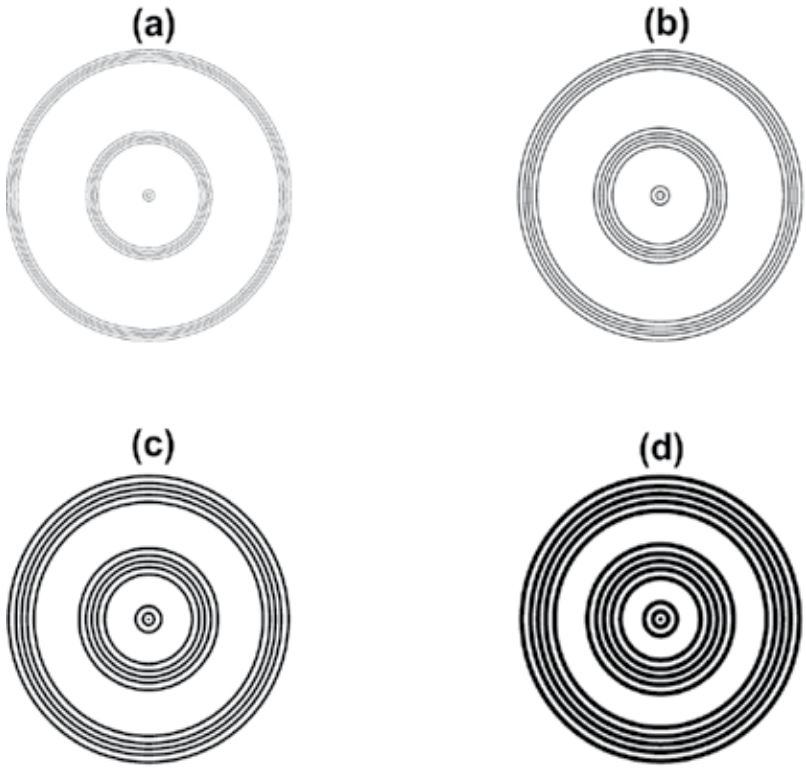

Figure 12. *XY*-plane view of the PCFL with $N = 5$, $f_{gc} = 0.4$, $s = 2$, and $R = 12.5$ cm and $f = 100$ kHz for: (a) $D = 0.5$, (b) $D = 0.6$, (c) $D = 0.7$, and (d) $D = 0.8$.

Figure 12. It can be observed how the lens becomes more opaque as D increases. **Figure 13** shows the pressure maps (gain in dBs) for fractal dimension values of $D = 0.5$, 0.6, 0.7, and 0.8.

Figure 13 shows that the focus position remains constant with the fractal dimension, and there is not any shift in either the *X*- or the *Z*-axis directions. However, the fractal dimension value has an influence on the focal gain of the PCFL. This effect is due to the diffraction mechanism. The raise on fractal dimension results in a more opaque lens, and the transmitted wave decreases, while the diffracted field increases, resulting in higher constructive interference at the lens focuses. The required focal gain will depend on the specific application and will define the fractal dimension for the PCFL design, as described in Section 4.1.

4.3. Variation of the central gap fraction (f_{gc})

In this section, the influence of the central gap fraction parameter (f_{gc}) on the PCFL beamforming capabilities is analyzed. The rest of the parameters are set again to their initial values ($f = 100$ kHz, $N = 5$, $s = 2$, $D = 0.6$, and $R = 12.5$ cm) as in the previous cases. From **Figure 14**, it can be noted how as the f_{gc} parameter increases the central gap width increases and then, the lateral gap width decreases. **Figure 15** shows the PCFL pressure maps (gain in dB) for f_{gc} values: (a) $f_{gc} = 0.2$, (b) $f_{gc} = 0.4$, (c) $f_{gc} = 0.6$, and (d) $f_{gc} = 0.8$.

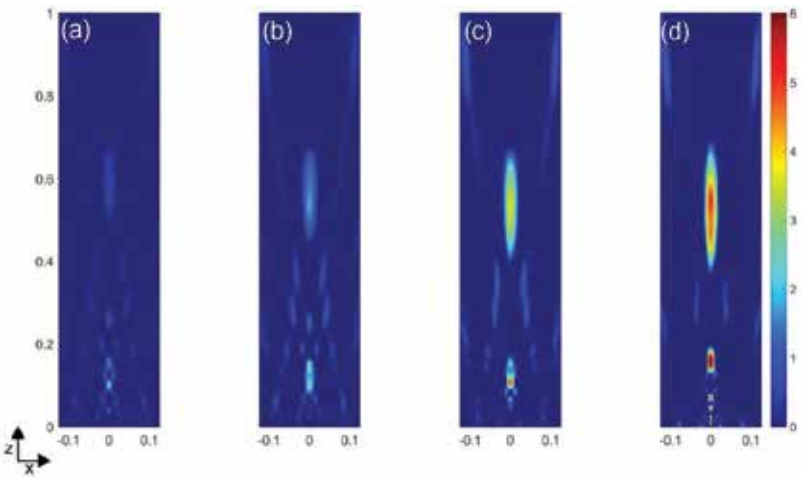

Figure 13. Two-dimensional spatial distribution of the acoustic gain (in dB) in the *XZ*-plane for the PCFL with $N = 5$, $f_{gc} = 0.4$, $s = 2$, and $R = 12.5$ cm and $f = 100$ kHz for: (a) $D = 0.5$, (b) $D = 0.6$, (c) $D = 0.7$, and (d) $D = 0.8$.

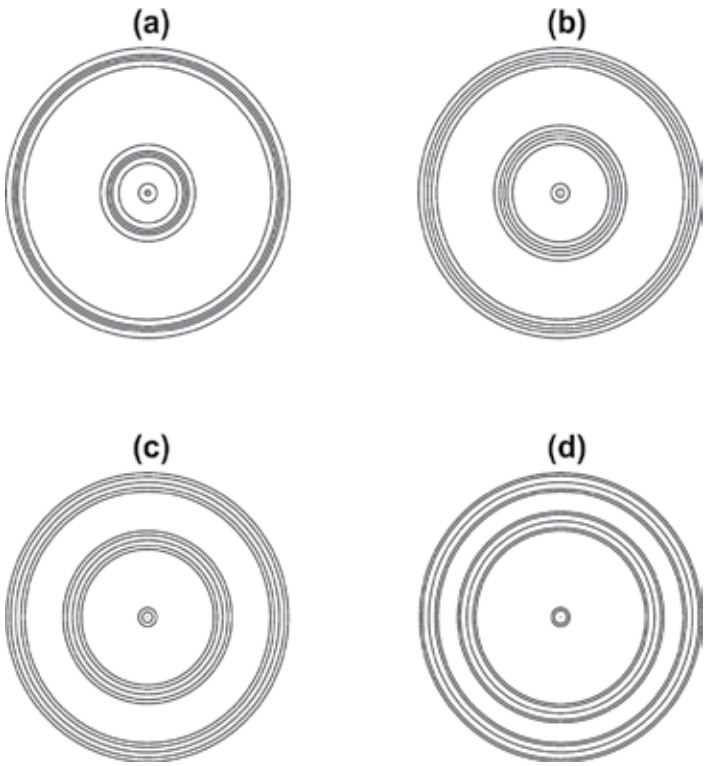

Figure 14. *XY*-plane view of the PCFL with $N = 5$, $D = 0.6$, $s = 2$, and $R = 12.5$ cm and $f = 100$ kHz for: (a) $f_{gc} = 0.2$, (b) $f_{gc} = 0.4$, (c) $f_{gc} = 0.6$, and (d) $f_{gc} = 0.8$.

The increase of the f_{gc} parameter results in a larger central gap, while the lateral gaps width (ε) becomes smaller, remaining constant the combination of the widths of all the gaps present in the PCFL. The ε parameter has been previously defined in Eqs. (7) and (8).

Figure 15 shows the influence of the central gap fraction on the modulation of the acoustic beam. It can be shown that the focal points remain at the same locations. At the further focus, approximately located at z = 0.55 m, the focal gain diminishes when the f_{gc} parameter is increased, while the closest foci increase their focal gain with the f_{gc} parameter. Therefore, the f_{gc} selection has a direct impact on the modulation of the acoustic beam and should be carefully considered when designing the PCFL.

4.4. Variation of the number of elements (*N*)

In this section, the influence of the N parameter on the pressure maps is considered. The rest of the parameters are set to their initial values as in the previous sections (f = 100 kHz, s = 2, D = 0.6, f_{gc} = 0.4 = 0.4, and R = 12.5 cm). **Figure 16** shows the XY-plane views of the PCFLs for different N values (N = 4, 5, 6, and 7) while **Figure 17** shows their corresponding pressure maps.

Table 1 shows the dependence of parameters r and g_C with N. Increasing N results in a decrease in r if fractal dimension is kept constant, as a result of the elements becoming smaller. However, this inverse relationship is not linear as can be observed in Eq. (1). Therefore, the opaque percentage of the PCFL diminishes when N is increased, and the central gap becomes higher. Thus, increasing the number of elements N makes the lens slightly more transparent without requiring the variation of the fractal dimension.

Figure 17 shows a similar behavior to that obtained in Section 4.3, reducing the focal gain of the further focus and increasing the focal gains of the closest foci when the number of elements is increased.

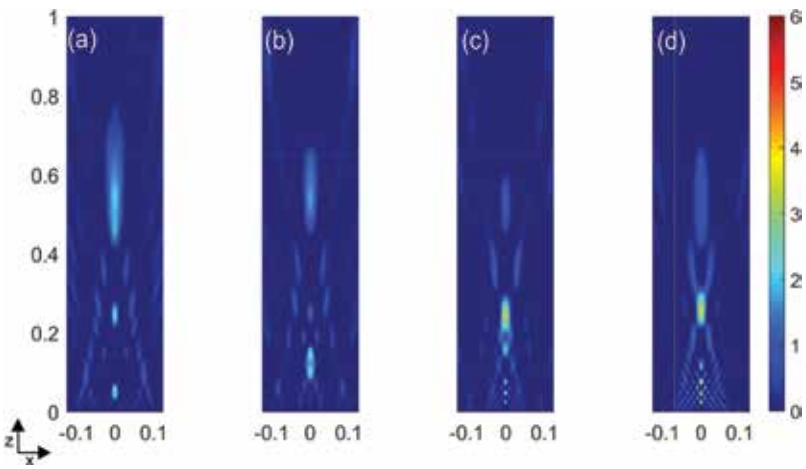

Figure 15. Two-dimensional spatial distribution of the acoustic gain (in dB) in the XZ-plane for the PCFL with N = 5, D = 0.6, s = 2, and R = 12.5 cm and f = 100 kHz for (a) f_{gc} = 0.2, (b) f_{gc} = 0.4, (c) f_{gc} = 0.6, and (d) f_{gc} = 0.8.

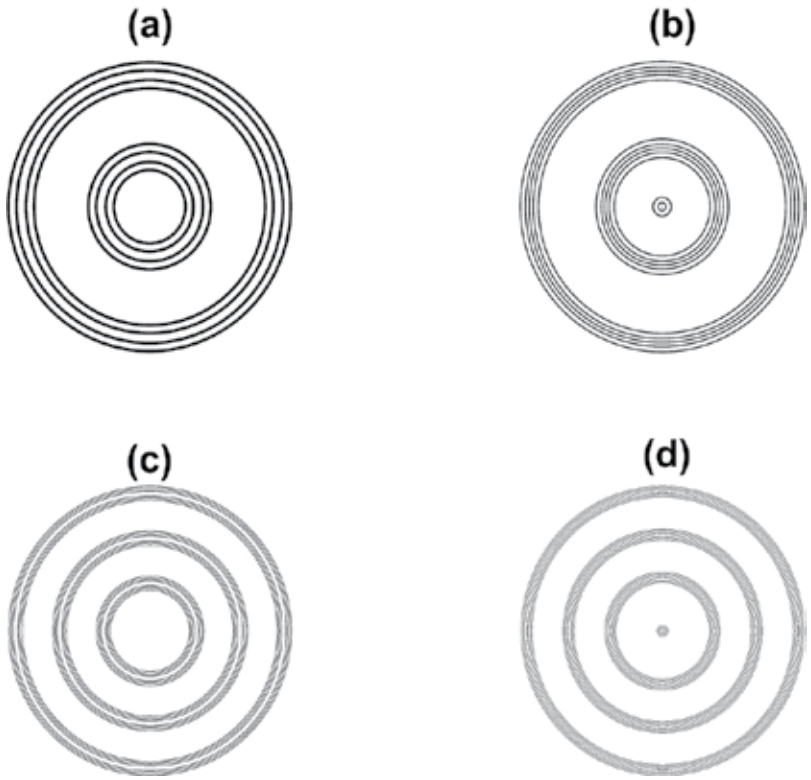

Figure 16. *XY*-plane view of the PCFL with f_{gc} = 0.4, D = 0.6, s = 2, and R = 12.5 cm and f = 100 kHz for (a) N = 4, (b) N = 5, (c) N = 6, and (d) N = 7.

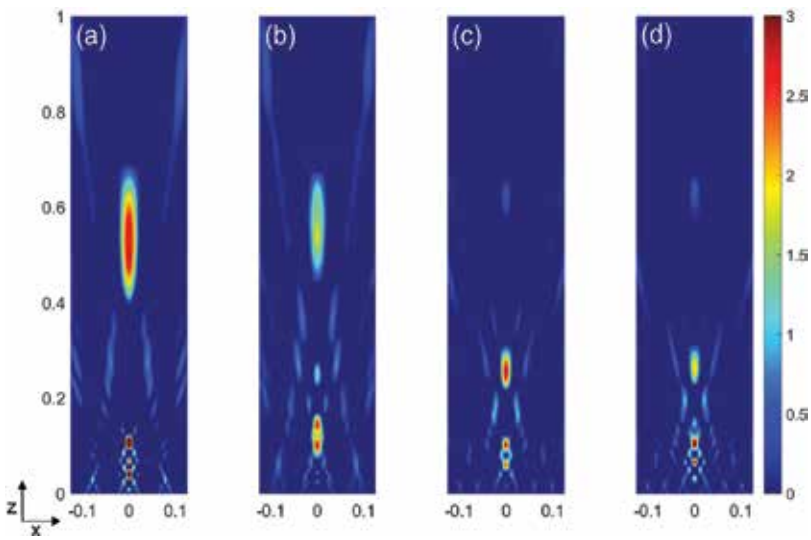

Figure 17. Two-dimensional spatial distribution of the acoustic gain (in dB) in the *XZ*-plane for the PCFL with f_{gc} = 0.4, D = 0.6, s = 2, and R = 12.5 cm parameters and working frequency of 100 kHz. The number of solid zones is: (a) N = 4, (b) N = 5, (c) N = 6, and (d) N = 7.

N	f_{gc}	r	$g_C/2R$	D
4	0.4	0.099	0.241	0.6
5	0.4	0.068	0.263	0.6
6	0.4	0.050	0.278	0.6
7	0.4	0.039	0.291	0.6

Table 1. Numerical results for variations of N.

4.5. Scalability of the lens

It this section the scalability of the lens is verified. This means that the same modulation of the acoustic beam is obtained, although at a different scale, when the size of the lens is reduced and the working frequency is increased in the same proportion. **Figure 18** shows the pressure in dBs along the Z-axis for four different lens sizes: (a) R = 12.5 cm, (b) R = 6.25 cm, (c) R = 3.125 cm, and (d) R = 1.5625 cm. The corresponding frequencies are: (a) 50, (b) 100, (c) 200, and (d) 400 kHz. As it can be observed from **Figure 18**, the pressure levels are equal for the different cases. The location of the focus area is scaled as expected. Notice that the horizontal axes in **Figure 14** show different scales. If the focus position is normalized with the size of the lens, the same results are obtained in all four cases.

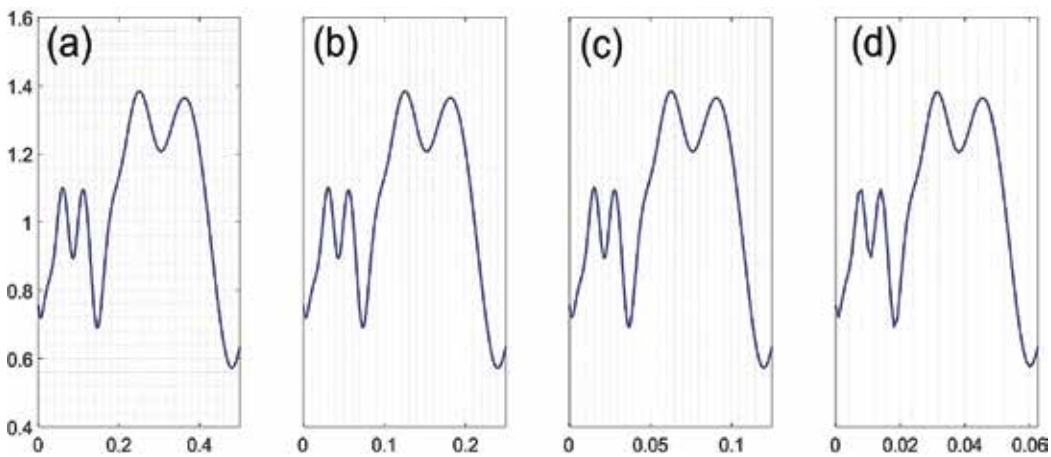

Figure 18. Spatial distribution of the acoustic pressure level (in dB) along the Z-axis or the PCFL with D = 0.6, N = 5, f_{gc} = 0.4, s = 2 for (a) R = 12.5 cm, (b) R = 6.25 cm, (c) R = 3.125 cm, and (d) R = 1.5625.

5. Conclusions

This work presents a comprehensive analysis of polyadic Cantor fractal lenses (PCFLs). It has been shown that the variation of the PCFL design parameters affect the modulation of the acoustic beam. Fractal dimension (D) affects the gain of the main focus of the pressure map. Varying the central gap fraction (f_{gc}) or the number of elements at stage s = 1 (N) results in a similar behavior, allowing to enhance the gain of further or closer foci, depending on the application requirements. Moreover, the numerical model shows that the PCFL is scalable.

Finally, once the PCFL is designed, a precise focus shifting along the Z-axis is achieved and controlled by slightly varying the working frequency. This gives the user a dynamic parameter to control the focus position without modifying the lens. This dynamic control is critical in certain medical applications where focusing of an ultrasonic beam allows tumors thermal ablation.

Acknowledgements

This work has been supported by Spanish MINECO (TEC2015-70939-R) and Generalitat Valenciana (AICO/2015/119).

Author details

Sergio Castiñeira-Ibañez[1], Daniel Tarrazó-Serrano[2], José Miguel Fuster[2], Pilar Candelas[2] and Constanza Rubio[2]*

*Address all correspondence to: crubiom@fis.upv.es

1 Electronic Engineering Department, University of Valencia, Burjassot, Valencia, Spain

2 Physical Technologies Center, Polytechnic University of Valencia, Valencia, Spain

References

[1] Mandelbrot BB. The Fractal Geometry of Nature. New York, USA: W.H. Freeman and Company; 1983. p. 468

[2] Takayasu H. Fractals in the Physical Sciences. Manchester, United Kingdom: Manchester University Press; 1990. p. 179

[3] Remón L, Calatayud A, Ferrando V, Giménez F, Furlan WD, Monsoriu JA. Fractal diffractive lenses. In: Shankar G. Pandalai, editors. Recent Research Developments in Optics. Vol. 8. Research Singpost; Kerala, India, 2013. pp. 31–71

[4] Petri A, Alippi A, Bettucci A, Cracium F, Farrelly F. Vibrational properties of a continuous self-similar structure. Physical Review B. 1994;49(21):15067–15075

[5] Sapoval B, Haeberlé O, Russ S. Acoustical properties of irregular and fractal cavities. Journal of the Acoustical Society of America. 1997;102(4):2014–2019. DOI: 10.1121/1.419653

[6] Lubniewski Z, Stepnowski A. Application of the fractal analysis in the sea bottom recognition. Archives of Acoustics. 1998; **23**(4):499–512

[7] Castiñeira-Ibáñez S, Romero-García V, Sánchez-Pérez JV, García-Raffi LM. Overlapping of acoustic bandgaps using fractal geometries. EPL. 2010;**92**:24007. DOI: 10.1209/0295-5075/92/24007

[8] Castiñeira-Ibáñez S, Rubio C, Romero-García V, Sánchez-Pérez JV, García-Raffi LM. Design, manufacture and characterization of an acoustic barrier made of multi-phenomena cylindrical scatterers arranged in a fractal-based geometry. Archives of Acoustics. 2012;**37**(4):455–462. DOI: 10.2478/v10168-012-0057-9

[9] Gomez-Lozano V, Uris A, Candelas P, Belmar F. Acoustic transmision through perforated plates with fractal subwavelength apertures. Solid State Communications. 2013;**165**:11–14. DOI: 10.1016/j.ssc.2013.04.012

[10] Saavedra G, Furlan WD, Monsoriu JA. Fractal zone plates. Optics Letters. 2003;**28**(12):971–973. DOI: 10.1364/OL.28.000971

[11] Monsoriu JA, Saavedra G, Furlan WD. Fractal zone plates with variable lacunarity. Optics Express. 2004;**12**(18):4227–4234. DOI: 10.1364/OPEX.12.004227

[12] Furlan WD, Saavedra G, Monsoriu JA. White-light imaging with fractal zone plates. Optics Letters. 2007;**32**(15):2109–2111. DOI: 10.1364/OL.32.002109

[13] Gimenez F, Monsoriu JA, Furlan WD, Pons A. Fractal photon sieve. Optics Express. 2006;**14**(25):11958–11963. DOI: 10.1364/OE.14.011958

[14] Monsoriu JA, Zapata-Rodriguez CJ, Furlan WD. Fractal axicons. Optics Communications. 2006;**263**(1):1–5. DOI: 10.1016/j.optcom.2006.01.020

[15] Jaggard AD, Jaggard DL. Scattering from fractal superlattices with variable lacunarity. Journal of the Optical Society of America A (Optics and Image Science). 1998;**15**(6):1626–1635. DOI: 10.1364/JOSAA.15.001626

[16] Aubert H, Jaggard DL. Wavelet analysis of transients in fractal superlattices. IEEE Transactions on Antennas and Propagation. 2002;**50**(3):338–345. DOI: 10.1109/8.999624

[17] Lehman M. Fractal diffraction grating built through rectangular domains. Optics Communications. 2001;**195**(1–4):11–26. DOI: 10.1016/S0030-4018(01)01285-8

[18] Mandelbrot BB. How long is the coast of Britain? Science. 1967;**156**:636–638

[19] Allain C, Cloitre M. Characterizing the lacunarity of random and deterministic fractal sets. Physical Review A. 1991;**44**:3552–3558. DOI: 10.1103/PhysRevA.44.3552

Chapter 5

Fractal to Non-Fractal Morphological Transitions in Stochastic Growth Processes

José Roberto Nicolás-Carlock, Víctor Dossetti and
José Luis Carrillo-Estrada

Additional information is available at the end of the chapter

http://dx.doi.org/10.5772/67941

Abstract

From the formation of lightning-paths to vascular networks, diverse nontrivial self-organizing and self-assembling processes of pattern formation give rise to intricate structures everywhere and at all scales in nature, often referred to as fractals. One striking feature of these disordered growth processes is the morphological transitions that they undergo as a result of the interplay of the entropic and energetic aspects of their growth dynamics that ultimately manifest in their structural geometry. Nonetheless, despite the complexity of these structures, great insights can be obtained into the fundamental elements of their dynamics from the powerful concepts of fractal geometry. In this chapter, we show how numerical and theoretical fractal analyses provide a universal description to the well observed fractal to nonfractal morphological transitions in particle aggregation phenomena.

Keywords: aggregation, entropic/energetic forces, fractal growth, morphological transitions, universality

1. Introduction

In nature, fractal structures emerge in a wide variety of systexms as a local optimization of diverse growth processes restricted to the entropic and energetic inputs from the environment. Even more, the fractality of these systems determines many of their physical, chemical, and/or biological properties. Thus, to comprehend the mechanisms that originate and control the fractality is highly relevant in many areas of science and technology [1–3].

One of the most successful approaches to this problem employs stochastic growth processes of particle aggregation. In general, aggregation phenomena are out-of-equilibrium processes of fractal pattern formation that are ubiquitous in nature [4]. As such, since the introduction of the diffusion-limited aggregation (DLA) and ballistic aggregation (BA) models, a plethora of studies has been developed trying to understand the ultimate aspects of the aggregation dynamics that give rise to *self-similar* or fractal clusters, the relationship of this *fractality* with their physical and chemical properties, and the most effective methods and techniques to control the fractal growth.

In particular, one striking feature of these systems is the morphological transition that they undergo as a result of the interplay of the entropic and energetic aspects of their growth dynamics that ultimately manifest themselves in the geometry of their structure [5]. It is here, where despite of their complexity, great insight can be obtained into the fundamental elements of their dynamics from the powerful concepts of fractal geometry [6, 7].

One example of this is the well-known dielectric breakdown model (DBM) or generalized Laplacian growth model, which has importantly contributed to our understanding of far-from-equilibrium growth phenomena, to such extent that seemingly unrelated patterns found in nature, as river networks or bacterial colonies, are understood in terms of a single framework of complex growth [8, 9]. However, we are still in need for a complete scaling theory of growth for systems far-from-equilibrium, as well as a comprehensive description of the fractality of systems that exhibits fractal to nonfractal morphological transitions [10].

In this chapter, starting from the mean-field result for the fractal dimension of Laplacian growth, we present a theoretical framework for the study of these transitions. Using a statistical approach to fundamental particle-cluster aggregation dynamics, under which it is possible to create four nontrivial fractal to nonfractal transitions that will capture all the main features of fractal growth, we show that, regardless of their space symmetry-breaking mechanism, they are well described by a universal dimensionality function, including the Laplacian one.

In order to show this, we consider the following: first, we introduce a general dimensionality function that is able to describe the measured fractal dimensions and scaling of clusters generated form particle aggregation. Second, we apply this equation to a set of fractal to nonfractal morphological transitions, created by identifying the fundamental dynamics that drive the fractal growth in particle aggregation and by combining three fundamental *off-lattice* particle-cluster aggregation models, the DLA, BA, and a recently introduced infinite-range mean-field (MF) attractive model [11, 12] under two different schemes. Afterwards, the scaling of the clusters along the transitions is measured for different values of their control parameters using two standard methods: the two-point density correlation function and the radius of gyration. Finally, we show how all measurements for the scaling of the DLA-MF, and BA-MF transitions collapse to a single universal curve valid for any embedding Euclidean space, under the appropriate variable transformations of the general dimensionality function.

http://dx.doi.org/10.5772/67941

2. Fundamental models

In the Laplacian theory of growth, the growth probability at a given point in space, μ, is given by the spatial variation of a scalar field, ϕ, i.e., $\mu \propto |\nabla \phi|$. An example of such processes is the paradigmatic DLA model, where particles randomly aggregate one-by-one to a seed particle to form a cluster [8–10] (**Figure 1**). It has been found that the structure that emerges from this process exhibits self-similar properties described by a fractal dimension, D, only dependent on the Euclidean dimension, d, of its embedding space [13, 14] given by,

$$D(d) = \frac{d^2 + 1}{d + 1}. \tag{1}$$

For $d = 2$, this expression predicts $D = 5/3 \approx 1.67$, different from the widely reported and numerically obtained value for off-lattice DLA, $D = 1.71$. Furthermore, it was found that D is highly dependent on the mean square displacement of the particles' trajectories, giving rise to a continuous screening-driven morphological transition that has been neatly described by extending the Laplacian theory to consider a general process where particles follow fractal

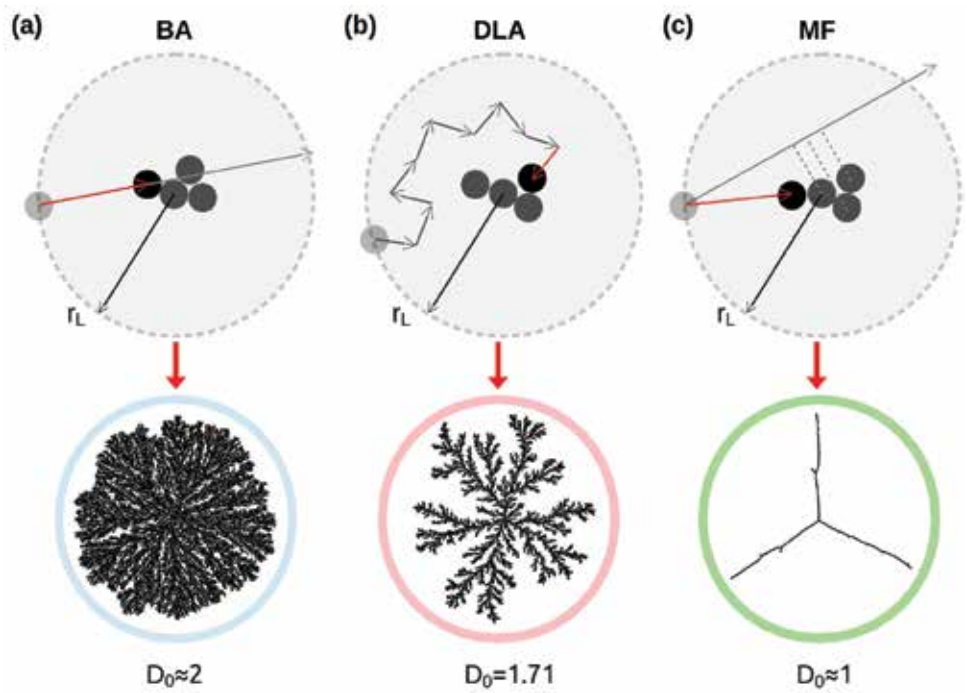

Figure 1. Schematic diagram of the fundamental aggregation models (top row) used in this work, where particles, that are launched one-by-one into the system from r_L with uniform probability in position and direction, (a) follow straight-line trajectories before aggregation in BA, (b) perform a random walk in DLA, and (c) get radially attached to the closest particle in the cluster as a result of an infinite-range radial interaction in MF. The morphology of MF emerges solely from its long-range interaction, as opposed to the stochastic BA and DLA. The corresponding characteristic cluster with its fractal dimension D_0 is shown in the bottom row.

trajectories [15]. It was found that D is related to the dimension of the walkers' trajectories, d_w, through the Honda-Toyoki-Matsushita (HTM) mean-field equation [16, 17]:

$$D(d, d_w) = \frac{d^2 + d_w - 1}{d + d_w - 1}. \tag{2}$$

Here, for $d_w = 1$ one gets $D = d$, as expected for ballistic-aggregation dynamics (see **Figure 1**), whereas for $d_w = 2$, the value $D = 5/3$ for DLA is recovered. This BA-DLA transition has been reproduced in diverse and equivalent aggregation schemes, e.g., of wandering particles under drift [18], or with variable random-walk step size [19], by imposing directional correlations [20, 21], and through probabilistically mixed aggregation dynamics [22].

However, one of the most challenging aspect of the theory comes when the growth is not purely limited by diffusion, e.g., when it takes place under the presence of long-range attractive interactions, where strong screening and anisotropic effects must be considered [1, 5, 7]. In this case, a clever generalization to the Laplacian growth process was proposed within the context of the DBM, assuming $\mu \propto |\nabla(\phi)|^{\eta}$, where η is a positive real number that keeps the information associated with all effects coming from screening and anisotropy [23, 24]. This process generates a characteristic fractal to nonfractal morphological transition from a compact structure with $D = d$ when $\eta = 0$, through DLA at $\eta = 1$, to a linear one with $D = 1$, as $\eta \to \infty$ [25, 26]. In this scenario, the generalized HTM equation [17, 27], given as,

$$D(d, d_w, \eta) = \frac{d^2 + \eta(d_w - 1)}{d + \eta(d_w - 1)}, \tag{3}$$

provides a good approximation to the dimensions of this transition but due to its mean-field limitations, it does not have a good correspondence with the numerical results [25, 26]. Nonetheless, as shown here, Eq. (3) is the starting point to clarify this aspect of the theory and, even, to establish a suitable and general framework to analyze more complex morphological transitions in stochastic growth processes.

This is done by considering that the fundamental dynamical elements of aggregation, which drive the fractal growth, are mainly two: a stochastic one, coming from the particles' trajectories randomness, and an energetic one, coming from attractive interactions. With regard to the latter, there are two physical mechanisms related to these interactions and two models that are able to reproduce their effects. First, the model we will refer to as λ-model [11], incorporates the screening effects associated to long-range attractive interactions (such as those coming from an attractive radial potential) by means of an effective interaction radius λ, as illustrated in **Figure 2a–c**. Second, the model referred here to as the p-model [12], incorporates anisotropy effects coming from surface-tension-like interactions by means of a Monte Carlo approach to aggregation using fundamental stochastic and energetic models as explained below and illustrated in **Figure 2d**. Therefore, by controlling the interplay of any of these two mechanisms with a pure stochastic model (in this case the DLA or BA models), one is able to generate fractal to nonfractal morphological transitions.

http://dx.doi.org/10.5772/67941

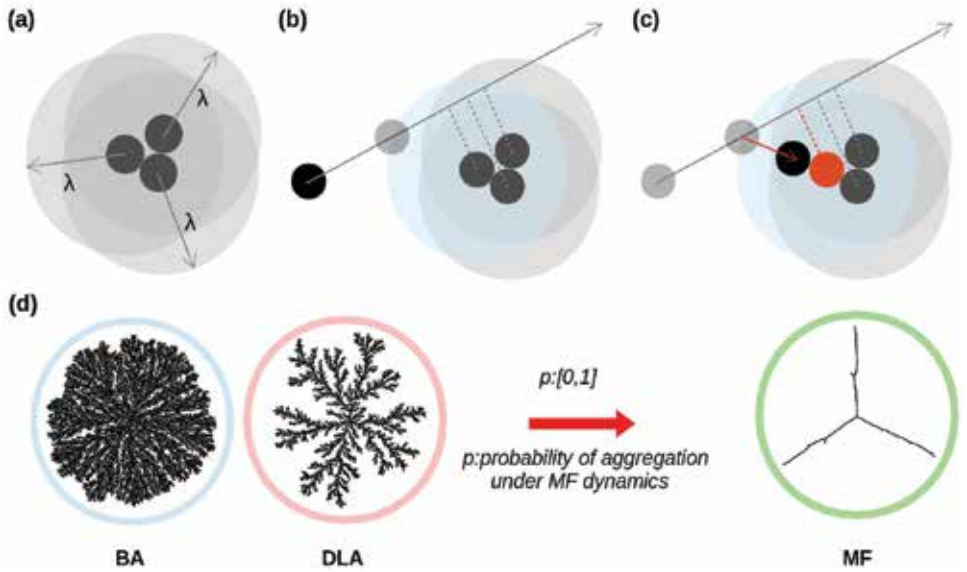

Figure 2. Schematic diagrams of the *energetic* aggregation schemes. For the λ-model: (a) every particle in the cluster is provided with an effective radius of aggregation λ. (b) A particle "collides" with the cluster when its trajectory intersects for the first time the interaction boundary of any aggregated particle. (c) The particle is aggregated to the closest particle along its direction of motion. This is determined by the position of the aggregated particles projected onto the direction of motion of the incoming particle. For the *p*-model: (d) a Monte Carlo approach to aggregation is established through the variable $p \in [0, 1]$, that controls the probability of aggregation under MF dynamics.

3. Methods

In the following and as explained below, all data for D were measured over a large ensemble of clusters (with $N = 1.5 \times 10^5$ particles) for each value of the control parameters of the models proposed, by means of two standard methods: the two-point density correlation function, $C(r) \propto r^{-\alpha}$, and the radius of gyration, $R_g(N) \propto N^{\beta}$, where the scaling exponents are related to D as $D_\alpha = d - \alpha$, and $D_\beta = 1/\beta$.

3.1. Aggregation dynamics

In all of the numerical calculations, we choose as a unit of distance, the particles' diameter here is set to one. For generating aggregates based on BA or MF (**Figure 1a** and **1c**), a standard procedure was used in which particles are launched at random, with equal probability in position and direction of motion, from a circumference of radius $r_L = 2r_{\max} + \delta$, where $r_{\max}$ is the distance of the farthest particle in the cluster with respect to the seed particle at the origin. As well, we used $\delta = 1000$ particle diameters to avoid undesirable screening effects. On the other hand, for the MF model, particles always aggregate to the closest particle in the cluster. This is determined by projecting the position of the aggregated particles along the direction of motion of the incoming particle (see **Figure 1c**). Finally, in the

case of aggregates generated using DLA dynamics (**Figure 1b**), particles were launched from a circumference of radius $r_L = r_{max} + \delta$ with $\delta = 100$, while their mean free path was set to one particle diameter in the beginning. Further on, as typically done, their mean free path is modified as the particles wander beyond a distance larger than r_L or in-between branches. As well, a killing radius is set at $r_K = 2r_L$ in order to speed up the aggregation process. For the special case of the λ-model, for aggregates generated with DLA dynamics, particles were launched from a circle of radius $L = r_{max} + \lambda + \delta$, with $\delta = 100$.

Regarding the p-model, in order to mix different aggregation dynamics, a Monte Carlo scheme of aggregation is implemented using the BA, DLA, and MF models. The combination between pairs of models results in the DLA-MF and BA-MF transitions by varying the mixing parameter $p \in [0, 1]$. This parameter is associated with the probability or fraction of particles aggregated under MF dynamics, $p = N_{MF}/N$, where N is total number of particles in the cluster. Therefore, as p varies from $p = 0$ (pure stochastic dynamics given by the BA or DLA dynamics) to $p = 1$ (purely energetic dynamics given by the MF model), it generates two transitions discussed below. The evaluation of the aggregation scheme to be used is only updated once and the particle has been successfully aggregated to the cluster under a given dynamics.

3.2. Fractal and scaling analysis

In all measurements, we performed an ensemble average over 128 clusters containing 1.5×10^5 particles each. In first place, we measured the fractal dimension from the two-point density correlation function,

$$C(r) = \langle\langle \rho(\mathbf{r}_0)\rho(\mathbf{r}_0 + \mathbf{r})\rangle\rangle_{|\mathbf{r}|=r}, \tag{4}$$

where the double bracket indicates an average over all possible origins r_0 and all possible orientations. Here, it is assumed that $C(r) \approx r^{-\alpha}$, where the fractal dimension is given by $D_\alpha = d - \alpha$ with d being the dimension of the embedding space. In second place, we also measured the radius of gyration given by

$$R_g^2 = \sum_{i=1}^{N} (r_i - r_{CM})^2, \tag{5}$$

where N is the number of particles, r_i is the position of the ith-particle in the cluster and, r_{CM} is the position of the center of mass. Here, it is assumed that $R_g(N) \approx N^\beta$, where the fractal dimension is given by $D_\beta = 1/\beta$. In this way, the fractal dimensions D_α and D_β are, respectively obtained from linear-fits to the corresponding functions $C(r)$ and $R_g(N)$ in log-log plots at different scales.

In particular, for the p-model, linear-fits at different scales were performed in order to capture the main local fractal features. In addition, we averaged the results of 10 linear fits, distributed over a given interval, in order to improve the precision of the measurements. In both transitions, DLA-MF and BA-MF, $D_\alpha(p)$ was measured at short length-scales (regions α_I in **Figure 6**) over the interval $r_i \in [1, 2]$ with fitting-length equal to 10, and $r_f \in [11, 12]$ (in

http://dx.doi.org/10.5772/67941

particle diameters units). At long length-scales (α_{II}), over $r_i \in [10, 11]$ with fitting-length equal to 40, and $r_f \in [50, 51]$. For $D_\beta(p)$, measurements at medium scales (β_I) were performed over the interval $r_i \in [10^2, 10^3]$ with fitting-length equal to 10^4, and $r_f \in [1.01 \times 10^4, 1.1 \times 10^4]$ (in particle number). Finally, at large scales (β_{II}), over the interval $r_i \in [10^3, 10^4]$ with fitting-length equal to 0.9×10^5, and $r_f \in [9.1 \times 10^4, 10^5]$.

4. Fractality prescriptions

Despite the complexity leading to morphological transitions, simple models can be established to describe their fractality or scaling as a function of the control parameter, in our case, the branching parameter ε for the λ-model (see below) or the mixing parameter p for the p-model. To do so, let us start by showing that Eq. (3) can in fact be recovered as the first-order approximation in $f(\eta)/d$ of a general exponential form,

$$D(d) = 1 + (d-1)e^{-f(\eta)/d}, \tag{6}$$

with $f(\eta) = \Lambda\eta(d_w - 1)$. It easily follows that,

$$D(d) \approx 1 + \frac{d-1}{1+f(\eta)/d} = \frac{d^2 + f(\eta)}{d + f(\eta)}. \tag{7}$$

In this form, by setting $\Lambda = 1$, Eq. (3) can be fully recovered. Therefore, it is clear that $f(\eta)$ in Eq. (6) keeps all the information associated with the structural symmetry-breaking of the clusters in the DBM. Under this formalism, let us introduce $f(p)$ with control parameter p, which takes a similar role as $f(\eta)$, i.e., it is associated with the net effect of all screening/anisotropy-driven forces of a more complex growth process, not necessarily corresponding to the DBM description. For simplicity, we propose $f(p) = \Lambda p^\chi$, where $p \in [0, 1]$ is the parameter that controls the transition, and where Λ and χ are two positive real numbers associated with the strength of screening/anisotropy-driven forces, that are to be determined either theoretically or phenomenologically according to the studied transition. This allows us to define a general dimensionality function, $D(p)$, that describes the fractal dimension of a structure collapsing toward $D = 1$ under the effects of $f(p)$ as,

$$D(p) = 1 + (D_0 - 1)e^{-f(p)/D_0}, \tag{8}$$

where D_0, with $d \geq D_0 > 1$, is the fractal dimension of the clusters for $p = 0$. This equation predicts an inflection point at p_i, given by $(\Lambda/D_0)p_i^\chi = (\chi - 1)/\chi$ which defines the change in dynamical growth regimes. Additionally, the first-order approximation of Eq. (8), is,

$$D(p)^{(1)} = \frac{D_0^2 + f(p)}{D_0 + f(p)}, \tag{9}$$

with p_i given now by $(\Lambda/D_0)p_i^{\chi} = (\chi - 1)/(\chi + 1)$. Eqs. (8) and (9) describe a continuous morphological transition from $D = D_0$ for $f(p) = 0$ (disordered/fractal states) toward $D = 1$ as $f(p) \to \infty$ (ordered states), with a well-defined change in growth dynamics at p_i.

Furthermore, let us introduce the reduced parameter, $q = p/p_i$. Analytically, substituting $q \in [0,\infty)$, back into Eq. (8) leads to,

$$D(q) = 1 + (D_0 - 1)e^{-\Phi(q)}, \tag{10}$$

where

$$\Phi(q) = q^{\chi}(\chi - 1)/\chi, \tag{11}$$

is an effective parameter associated to a generalized screening/anisotropy-driven force. Its first-order approximation is then,

$$D(q)^{(1)} = \frac{D_0 + \Phi(q)}{1 + \Phi(q)}, \tag{12}$$

where the effective parameter is now given as,

$$\Phi(q) = q^{\chi}(\chi - 1)/(\chi + 1). \tag{13}$$

With this prescription, the dynamical change in growth regime is now located at $q_i = 1$ for all transitions. Here, we can also include the DBM transition as well, for which $\Phi(q) = q(d_w - 1)/d$.

5. Morphological transitions

5.1. The λ-model: screening-driven transition

In the first approach to morphological transitions, we will consider the case when long-range attractive interactions are introduced in the growth dynamics. In this case, the way to obtain self-similar clusters, that is, clusters with a single fractal dimension, is to maintain a proper balance between the energetic and entropic contributions to the growth process. This can be done by considering an aggregation radius, λ, associated with the range of the interaction for each particle in the growing cluster.

For example, for $\lambda = 1$, or *direct-contact* interaction, the usual DLA or BA models are recovered (see **Figure 3a** and **4a**, respectively). When $\lambda > 1$, the attractive interactions modify the local morphology of the aggregates, leading to a more stringy structure. Two well defined features emerge due to the interplay of the long-range interactions and the way particles approach the cluster (in relation with their trajectories): a *multiscaling* branching growth and a crossover in fractality, from $D \to 1$ (as $\lambda \to \infty$) to $D = D_0$ (when $N \to \infty$), as shown in **Figures 3** and **4**.

It can be appreciated that this growth presents three well-defined stages as illustrated in **Figures 3d** and **4d**. In the first one, the growth is limited by the interactions and is

http://dx.doi.org/10.5772/67941

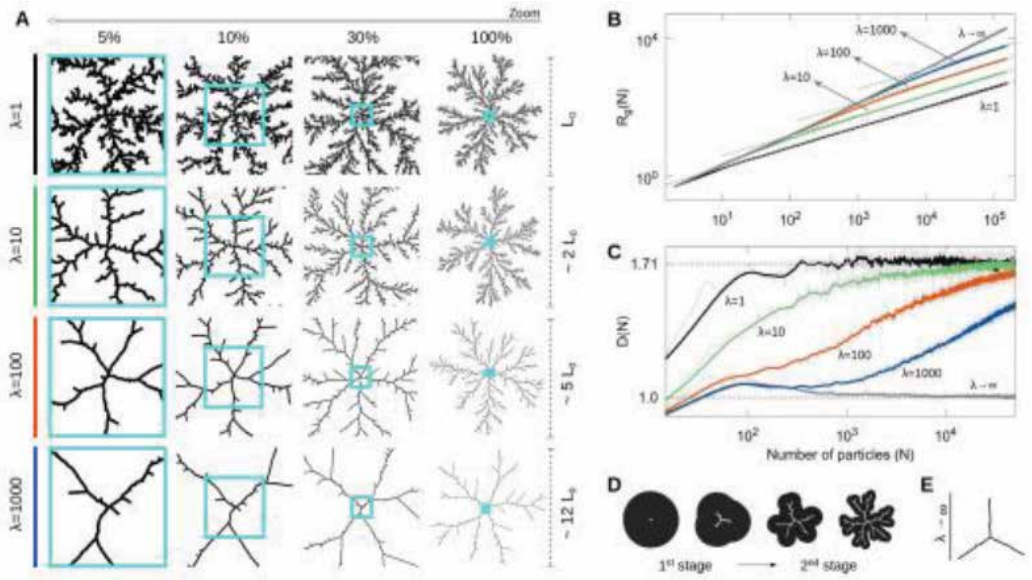

Figure 3. (a) Multiscaling aggregates based on DLA, containing $N = 150 \times 10^3$ particles each, for $\lambda = 1, 10, 100$ and 1000 units, visualized at 5, 10, 30 and 100% of their total size. The squares display the multiscaling evolution of the structure. (b) Radius of gyration, R_g, and (c) fractal dimension, D, versus the number of aggregated particles, N, in log-log and lin-log plots, respectively. Notice that, when $\lambda \to \infty$, the structure of the aggregates tends to MF ($D = 1$). (d) Evolution of the growing front for the first two stages of growth. (e) Typical structure of an MF aggregate.

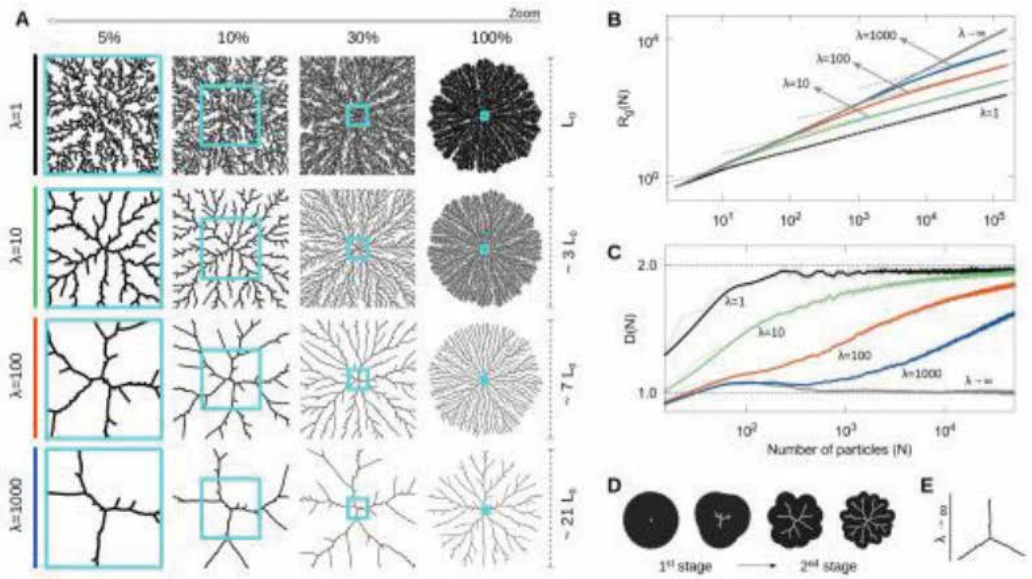

Figure 4. (a) Multiscaling aggregates based on BA, containing $N = 300 \times 10^3$ particles each, for $\lambda = 1, 10, 100$ and 1000 units, visualized at 5, 10, 30 and 100% of their total size. (b) Radius of gyration, R_g, and (c) fractal dimension, D, versus the number of aggregated particles, N, in log-log and lin-log plots, respectively. (d) Evolution of the growing front for the first two stages of growth. (e) Typical structure of an MF aggregate.

characterized by $D \to 1$ as $\lambda \to \infty$. This is due to the fact that the radial size of the cluster is small compared to λ. In consequence, the individual interaction regions of the aggregated particles are highly overlapped, forming an almost circular envelope or effective boundary of aggregation around the cluster. This makes the last aggregated particle the most probable aggregation point in the cluster for the next incoming particle. Because of this, there is a tendency for the clusters to develop three main arms or branches, clearly seen as $\lambda \to \infty$. This structural feature is reminiscent of a mean-field (MF) behavior. In the second stage, clusters exhibit a transition in growth dynamics. Here, the envelope starts to develop small deviations from its initial circular form, with typically three main elongations or growth instabilities associated with the main branches. When the distance between the tips of the two adjacent branches becomes of the order of λ, a bifurcation process begins, generating multiscaling growth. Then, when the interactive envelope develops a branched structure itself, particles are able to penetrate into the inner regions of the aggregate and another transition in growth dynamics takes place, from *interaction-limited* to *trajectory-limited*. In the third stage, when the distance among the tips of the main branches becomes much larger than λ, growth is limited by the mean squared displacement of the wandering particles. In this case, the asymptotic value $D = D_0$ and the main features in the global structure of the cluster are remarkably recovered as $N \to \infty$, inheriting the main characteristics of the entropic aggregation-model used, either DLA or BA. That is, even though interactions leave a strong imprint in the local structure and fractality of the clusters, the stochastic nature of the particle trajectories will ultimately determine their global characteristics.

However, taking into account that the spatial size of the clusters is proportional to the radius of gyration $R_g \propto N^{1/D}$, the desired balance between entropic and energetic forces, the latter related to the long-range attractive interaction and to the parameter λ, can be achieved by scaling the interaction range itself with the number of particles in the cluster through $\lambda(N) = \lambda_0 N^{\varepsilon}$, where λ_0 is fixed to one, while ε is the scaling parameter that takes values in [0, 1]; we will refer ε as the *branching* parameter. Given a fixed value of ε and this choice for $\lambda(N)$, every aggregate grown under these conditions has a precise and uniquely defined fractal dimension $D = D(\varepsilon)$. In fact, using $D(\varepsilon)$ for different values of ε, one can define the entropic and energetic ratios given by $f_S = (D(\varepsilon) - 1)/(D_0 - 1)$ and $f_E = 1 - f_S$, respectively, that quantify the specific entropic and energetic contribution to the fractal dimension of the clusters (see **Figure 5**). Here, one can clearly appreciate the transition in growth regimes from entropic, when $\varepsilon \to 0$, to energetic, as $\varepsilon \to 1$, and the nontrivial interplay between them to generate each cluster with a specific dimensionality.

Additionally, this model allows one to estimate $\varepsilon(D)$, in order to grow aggregates with any prescribed fractal dimension D in $[1, D_0]$, once the underlying entropic model, DLA or BA, is selected. As such, we are no longer restricted to the purely entropic models of fractal growth with a constant λ, as the energetic contribution of the long-range attractive interactions is maintained through the varying $\lambda(N)$, enabling one to explore in a continuous manner the full range of clusters with fractal dimensions in $[1, D_0]$. Nonetheless, the purely entropic contribution of the underlying models (DLA or BA) has two important contributions to the clusters' structure: first, they establish an upper limit to the fractal dimensionality (D_0), and second, they define a characteristic morphology to the clusters (that of DLA or BA). This kind of control over the

http://dx.doi.org/10.5772/67941

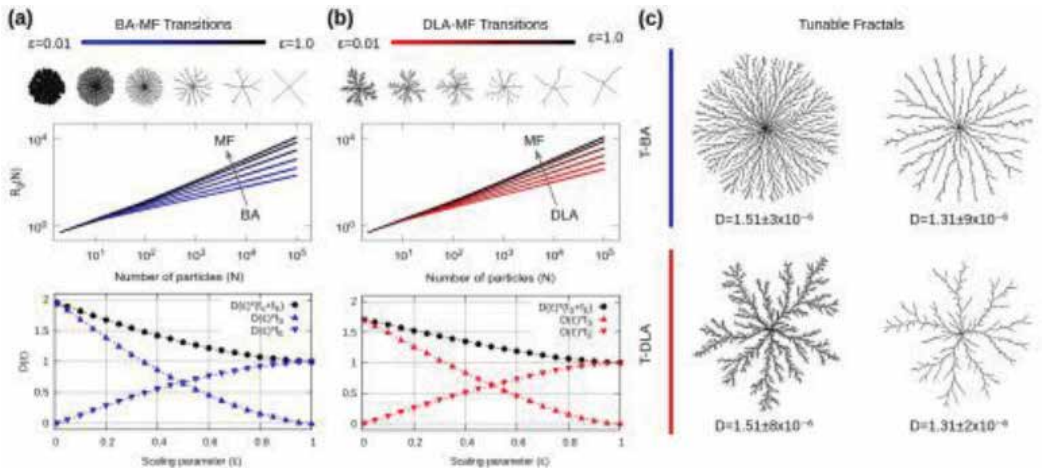

Figure 5. In (a) and (b), aggregates grown with specific values of ε in the interval $[0.01, 1]$ with the λ-model (top row) and log-log plots for R_g (middle row) for (a) BA and (b) DLA with $N = 10^5$ particles. One can appreciate the difference in the morphology of these monofractal-aggregates with respect to ε. Additionally, the specific entropic and energetic contributions to the clusters fractal dimension $D(\varepsilon)$ are shown in the bottom panes. (c) Clusters based in BA (left) and DLA (right) with the same fractal dimension, from top to bottom $D = 1.51$ and 1.31, grown with a very high precision around the desired value.

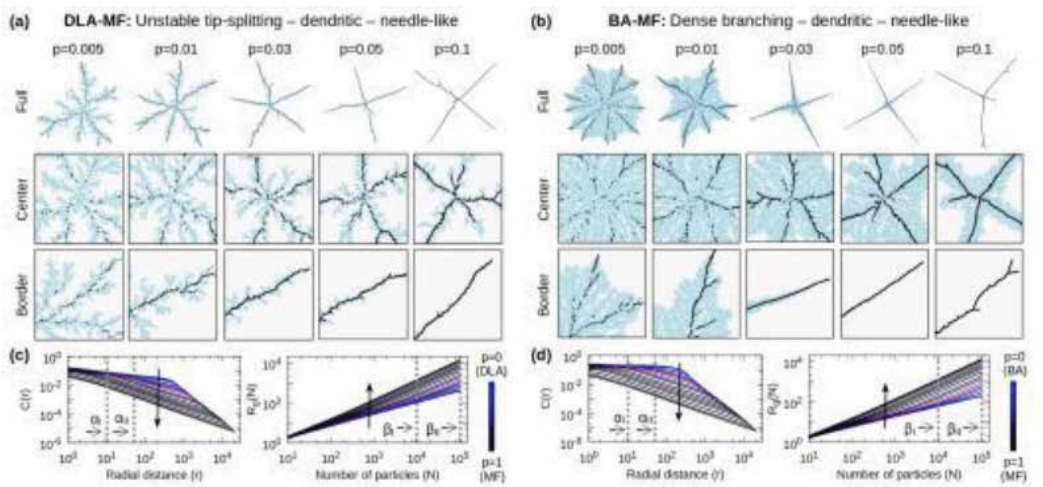

Figure 6. Clusters of 1.5×10^5 particles grown with the indicated values of p, are shown at different magnifications for the (a) DLA-MF and (b) BA-MF transitions. Particles aggregated under DLA/BA are colored in light-grey while those through MF in black. These transitions exhibit fast morphological transformations as p increases, from unstable tip-splitting (DLA) or dense branching (BA), through (inhomogeneous) dendritic, to needle-like growth (MF). (c-d) $C(r)$ and $R_g(N)$ display deviations from a well-defined linear behavior for different p, revealing the inhomogeneity or crossover effects in these clusters. Arrows indicate the direction of the transition as function of p:0→1. This is better seen at low scales, where the stochasticity of DLA or BA dominate the local growth, whereas MF tends to dominate the global morphology as $p \to 1$. In both cases, the dynamical growth-regime changes at $p \approx 0.1$. Labels α_I, α_{II}, β_I, and β_{II} indicate the scales used for the scaling analysis.

clusters' fractal dimension and the range it spans, as well as over the morphology of the clusters, has not been obtained before under any other related scheme of fractality tuning [11].

5.2. The *p*-model: anisotropy-driven transition

In the second approach, a general stochastic aggregation process can be model under a Monte Carlo scheme involving three fundamental and simple *off-lattice* models of particle-cluster aggregation. On one hand, the well-known BA and DLA models provide disordered/fractal structures through their stochastic (entropic) dynamics (**Figure 1a** and **1b**). On the other, we introduce a mean-field (MF) model of long-range interactive particle-cluster aggregation [11, 12] that provides the most energetic (and noiseless) aggregation dynamics that, simultaneously, acts as the main source of anisotropy. We must remark that this anisotropy is purely generated by the growth dynamics and not from lattice effects [28] (see **Figure 1c**). Then, the statistical combination of these models results in an off-lattice DLA-MF and BA-MF dynamics, whose morphological transitions can be controlled by the *mixing* parameter $p \in [0, 1]$, associated with the probability or fraction of particles aggregated under MF dynamics, $p = N_{\mathrm{MF}}/N$, where N is total number of particles in the cluster. Therefore, as p varies from $p = 0$ to $p = 1$, it generates two nontrivial transitions from fractals (DLA) or fat fractals (BA) with fractal dimension $D = D_0$, to nonfractal clusters with $D = 1$ (MF), that capture all the main morphologies of fractal growth [6] (see **Figure 6**).

6. Universal description

It is necessary to remark that the DLA-MF and BA-MF transitions in the p-model are characterized by inhomogeneous clusters, i.e., structures with nonconstant scaling as shown in **Figure 6c** and **d**, in contrast with the ones present in BA-DLA [15, 21] and the DBM [23, 25] characterized by monofractals. These multiscaling features reveal a crossover behavior that can be properly quantified by measuring a local or effective, $D(p)$, at different scales [7], as shown in **Figure 7a** (details for the values of the parameter used to produce **Figure 7** are presented in **Table 1**). Analytically, all measurements can be described by Eqs. (8) and (9), using Λ and χ as fitting parameters. Indeed, the data for $D(p)$ as obtained through to $C(r)$ are very well described by Eq. (8), whereas Eq. (9) better describes the results obtained through $R_g(N)$. In the case of the λ-model, the BA/DLA-MF transitions are governed by the branching parameter, ε, that is equivalent to the mixing parameter p of the p-model. Nonetheless, in the λ-model, the clusters exhibit a monofractal behavior all along the transition as measured by $R_{\mathrm{g}}(N)$. Thus, the data obtained are then described by Eq. (8) as a fitting function. This analysis is presented in **Figure 7d**.

By observing the description of the transitions based on the function $D(q)$ in **Figure 7**, one can clearly appreciate their continuous nature for both the λ- and p-models, as well as the fact that $q = 1$ defines a change in aggregation dynamics from purely entropy to highly energetic. In particular, the similarity between the transitions of BA-MF and those of the DBM is quite interesting, with results such as $D(q) \approx 1$ for $q = 4$ and $D(q) \approx 1.71$ for $q = 1$ in the BA-MF transitions, while $D(\eta) \approx 1$ for $\eta = 4$ and $D(\eta) \approx 1.71$ for $\eta = 1$ in the case of the DBM, even though the processes are different (see **Table 2**). Even more, by plotting all data as a function of $\Phi(q)$ itself, i.e., $D(\Phi)$, the DLA-MF, BA-MF,

http://dx.doi.org/10.5772/67941

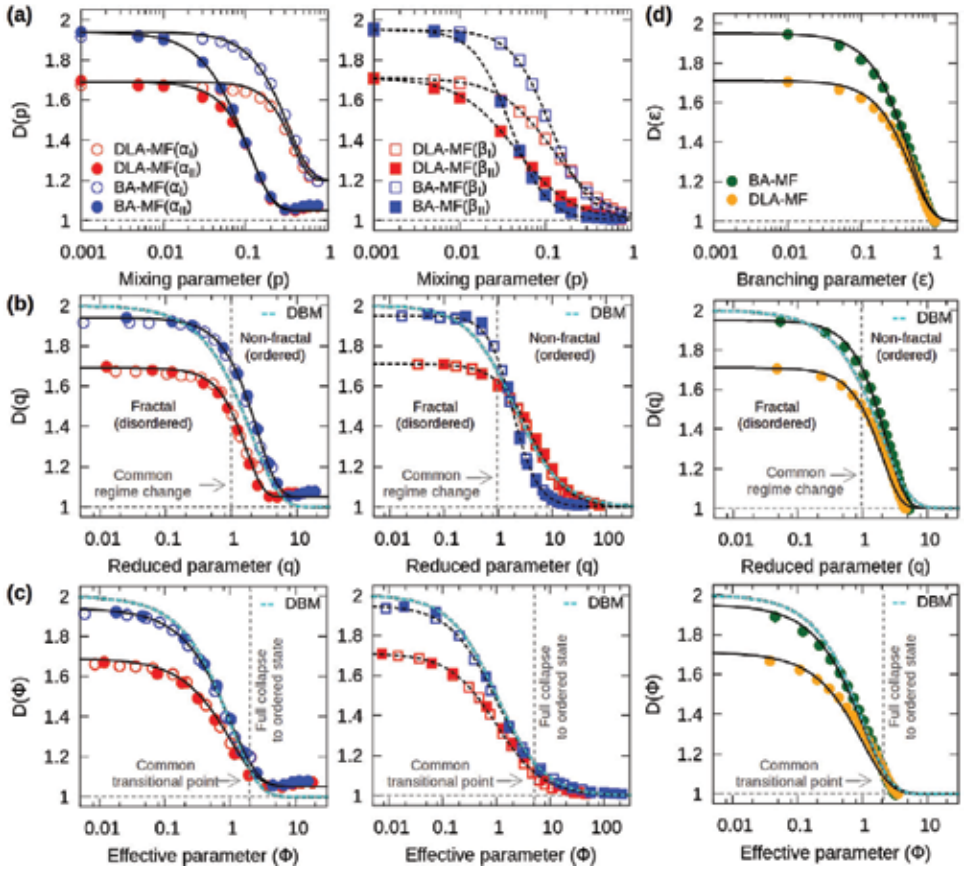

Figure 7. Scaling analysis for the p-model: (a) Plots of $D(p)$ for the DLA-MF and BA-MF transitions obtained from $C(r)$ (left), at small (α_I) and large (α_{II}) scales, and $R_g(N)$ (right), at medium (β_I) and large (β_{II}) scales, in correspondence to **Figures 6c** and **6d**, respectively. These results are described by the solid and dotted curves given by equations (8) and (9), respectively, for different values of the parameters Λ and χ. (b) By plotting D as a function of $q = p/p_i$ (where p_i is calculated for each curve), data collapses into single master curves, $D(q)$, according to Eqs. (10) and (12), respectively. Note the common point of regime change at $q_i = 1$, marked with the vertical dashed lines. The curves for the DBM given by Eqs. (6) and (7), respectively, with $\Lambda = 1$ and $d = d_w = 2$, are also included. (c) In the description with the function $D(\Phi)$, all of the morphological transitions approach common transitional points where clusters have fully collapsed to an ordered structure, independently of the stochastic model used. (d) The corresponding scaling analysis is performed for the BA- and DLA-MF transitions obtained by using the λ-model. In this case, Eqs. (8), (10) and the exponential form of (14), were used. For further details about the parameter values used, see **Table 1**.

and DBM transitions approach the highly anisotropic regime in an almost identical manner, departing from Eqs. (10) and (12). See, for example, **Figure 7c** and the bottom pane in **Figure 7d**.

A final important implication of the previous findings is that the DBM and BA-MF transitions (for both λ- and p-models), even though completely different in origin, could be treated as belonging to the same universality class. To understand this, we must recall that the DBM ($\eta = 1$) and viscous fingering phenomena are said to belong to the same universality class as DLA, because they are all characterized by $D = 1.71$ [10, 29]. Therefore, by extending this idea to the description

with the function $D(\Phi)$ of Eq. (10), the *universality* of these morphological transitions must be understood in the sense that they are described by the same scaling in their fractal dimension. In fact, by defining the reduced codimension, $D^* \in [0,1]$ as $D^* = (D-1)/(D_0-1)$, it is still possible

Model	Transition	Method	Scale	Λ	χ	D_0	p_i, q_i
p	DLA-MF	$C(r)$	α_I	15.4	2.24	1.67	0.29
			α_{II}	71.5	1.82		0.08
		$R_g(N)$	β_I	33.8	1.41	1.71	0.03
			β_{II}	101.6	1.32		0.01
	BA-MF	$C(r)$	α_I	11.6	1.61	1.94	0.18
			α_{II}	45.4	1.38		0.04
		$R_g(N)$	β_I	124.8	1.95	1.95	0.06
			β_{II}	1547.7	2.05		0.02
λ	DLA-MF	$R_g(N)$	10^3 to 10^5	6.10	1.52	1.70	0.21
	BA-MF	$R_g(N)$	10^3 to 10^5	6.35	1.43	1.95	0.19
p	DLA-MF	$C(r)$	–	–	1.69	1.67	1.0
		$R_g(N)$	–	–	1.34	1.71	1.0
	BA-MF	$C(r)$	–	–	1.39	1.94	1.0
		$R_g(N)$	–	–	1.88	1.95	1.0
λ	DLA-MF	$R_g(N)$	–	–	1.52	1.70	1.0
	BA-MF	$R_g(N)$	–	–	1.43	1.95	1.0

In the first block, we present the parameter values used to describe $D(p,\Lambda,\chi)$, using Eqs. (8) and (9). In the second block for Eqs. (10) and (12), used as fitting functions to the $D(q,\chi)$ data obtained through $C(r)$ and $R_g(N)$. In this prescription, χ is the only free parameter to be determined and, by construction, all the inflection points are located at $q = 1$. All of the fittings to the numerical data were performed using the *gnuplot* embedded algorithms.

Table 1. Parameters for the plots of $D(p)$ and $D(q)$ in **Figure 7**.

Model	Data	D_0	χ	$\Phi_t(v = 0.1)$	q_t	$\Phi_t(v = 0.05)$	q_t	$D(q = 1)$
p	BA-MF (α)	1.94	1.39	2.3	4.5	3.0	5.4	1.72
	DLA-MF (α)	1.67	1.69	2.3	2.8	3.0	3.2	1.46
	BA-MF (β)	1.95	1.88	9.0	6.0	19.0	9.0	1.73
	DLA-MF (β)	1.71	1.34	9.0	21.7	19.0	37.8	1.62
λ	BA-MF	1.95	1.43	2.3	4.2	3.0	5.0	1.70
	DLA-MF	1.71	1.52	2.3	3.5	3.0	4.2	1.50

The labels α and β indicate that these data were obtained through measurements of the fractal dimension using $C(r)$ and $R_g(N)$, respectively.

Table 2. Transitional points for which the reduced co-dimension $D^* \approx 0$ for the λ- and p-models studied in this work.

http://dx.doi.org/10.5772/67941

to define the ultimate representation for the scaling of the transitions through the reduced codimensionality functions. From Eqs. (10) and (12), these are, respectively given by,

$$D^*(\Phi) = e^{-\Phi}, \tag{14}$$

$$D^*(\Phi)^{(1)} = \frac{1}{1+\Phi}, \tag{15}$$

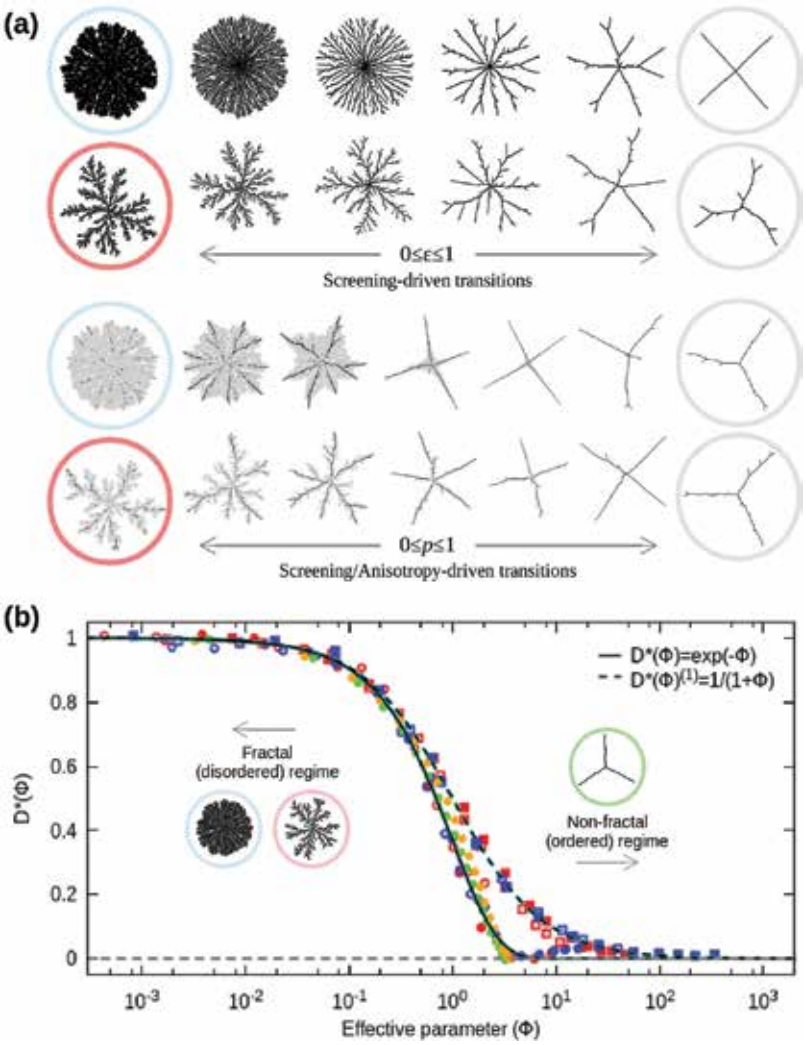

Figure 8. (a) Snapshots of typical clusters present in fractal to nonfractal morphological transitions obtained from the λ-model with the branching parameter ε as the control parameter, and the p-model with the mixing parameter p as the control parameter. (b) By plotting $D^*(\Phi)$ and $D^*(\Phi)^{(1)}$, the data for the morphological transitions DLA-MF, BA-MF, and DBM collapse to universal curves described by Eqs. (14) and (15). Under this prescription, these universal fractal to nonfractal morphological transitions are independent of the initial fractal dimension, D_0, the symmetry-breaking process that drives the transition, even crossover effects, and, quite remarkably, the Euclidean dimension, d, of its embedding space. All of the numerical data comes from **Figure 7**.

where the effective parameter Φ is, respectively, given by Eqs. (11) and (13) for each of the previous two equations. Notice that, since the morphological transitions presented in this work are independent of their symmetry-breaking processes, initial-configuration, and that D_0 is given by the HTM equation, we arrive to the important conclusion that, under the formalism based on Eqs. (14) and (15), fractal to nonfractal morphological transitions will follow the same curves independently of the Euclidean dimension of the embedding space, as shown in **Figure 8**. This finding makes it clear that it is possible to define *universal* transitional point, Φ_t, where the screening/anisotropy effects are dominant over the morphology of the cluster and $D \approx 1$. Starting with reduced codimension at Φ_t, i.e., $D_t^* = (D(\Phi_t) - 1)/(D_0 - 1) = \nu$, we can ask for the condition $\nu \ll 1$ to be fulfilled (see **Figure 8**). Then, the universal transitional points, Φ_t, must, respectively satisfy $\exp(-\Phi_t) = \nu$ and $\Phi_t = (1 - \nu)/\nu$ for the Eqs. (14) and (15). In order to recover the particular transitional points for Eqs. (10) and (12), we must recall that $\Phi_t = \Phi(q_t)$ and thus, one has to solve for q_t. Notice also that $q_t = q_t(\nu, \chi, D_0)$, therefore it gives different values for each transition (see **Table 2**).

7. Conclusion

It has been stated above that the entropic and energetic elements are the two aspects of the complex aggregation dynamics which in nature are strongly correlated. Nonetheless, this reductionist approach that essentially encapsulates the information of all the finer details of the dynamics into an effective interaction (in the λ-model, for example) or through a Monte Carlo approach to aggregation (as in the p-model) has proven to be quite rewarding, as one can appreciate the wide assortment of fractal morphologies that can be generated and the fine and easy control one can achieve by means of a single parameter. Here, we shall recall that in two-dimensional systems ($d = 2$), by changing the fractal dimension of the particle trajectories, d_w, from $d_w = 2$ (random) to 1 (ballistic), it is possible to generate a complete set of clusters with fractal dimension between $D = 1.71$ (DLA) to 2 (BA), corresponding to the stochastic (entropic) regime. However, by scaling the interaction range λ with N, or by gradually introducing an energetic element trough MF dynamics, we are no longer restricted to this range in D as we were. We can now explore the full set of fractals with D in $[1, D_0]$, where D_0 ranges from that value corresponding to DLA to that corresponding to BA, not necessarily bound to $d = 2$, since these approaches can be easily extended to higher dimensions [30].

Additionally, the descriptive framework for the scaling of fractal to nonfractal morphological transitions in stochastic growth processes, which includes the concept of an effective screening/anisotropy force and reduced codimensionality transformations, has revealed that the DLA-MF, BA-MF, and DBM transitions exhibit a well-defined universal scaling $D^*(\Phi)$, which is independent of the initial fractal configuration of the system, the dimensionality of the embedding space, crossover effects, and the anisotropy force acting upon them.

The results and models discussed in this chapter represent an important unifying step toward a complete scaling theory of fractal growth and far-from-equilibrium pattern formation. Additionally, the possibility of applying the dimensionality function to discuss complex structures in other research areas, ranging from biology [4, 1], intelligent materials engineering [31, 32] to medicine [33], seems to be in some cases straightforward.

Acknowledgements

The authors gratefully acknowledge the computing time granted on the supercomputers MIZTLI (DGTIC-UNAM) and THUBAT-KAAL (CNS-IPICyT) and on XIUHCOATL (CINVESTAV) through M.A. Rodriguez (ININ, Mexico). We acknowledge the partial financial support by CONACyT and VIEP-BUAP through the grants: 257352, DIRV-EXC16-I, and CAEJ-EXC16-G.

Author details

José Roberto Nicolás-Carlock[1], Víctor Dossetti[2] and José Luis Carrillo-Estrada[1]*

*Address all correspondence to: carrillo@ifuap.buap.mx

1 Physics Institute, Autonomous University of Puebla, México

2 CIDS-Instituto de Ciencias, Autonomous University of Puebla, Mexico

References

[1] Ben-Jacob E. From snowflake formation to growth of bacterial colonies. Part I. Diffusive patterning in azoic systems. Contemporary Physics. 1993; **34**:247–273. DOI: 10.1080/00107519308222085

[2] Ben-Jacob E. From snowflake formation to growth of bacterial colonies. Part II. Cooperative formation of complex colonial patterns. Contemporary Physics. 1997; **38**:205–241. DOI: 10.1080/001075197182405

[3] Ronellenfitsch H, Katifori E. Global optimization, local adaptation, and the role of growth in distribution networks. Physical Review Letters. 2016; **117**:138301. DOI: 10.1103/PhysRevLett.117.138301

[4] Vicsek T. Fluctuations and scaling in biology. Oxford University Press, New York, 2001.

[5] Ben-Jacob E, Garik P. The formation of patterns in nonequilibrium growth. Nature. 1990; **343**:523–530. DOI: 10.1038/343523a0

[6] Vicsek T. Fractal growth phenomena. World Scientific, Singapore, 1992.

[7] Meakin P. Fractals, scaling and growth far from equilibrium. Cambridge University Press, United Kingdom, 1998.

[8] Sander L M. Fractal growth processes. Nature. 1986; **322**:789–793. DOI: 10.1038/322789a0

[9] Sander L M. Diffusion-limited aggregation: A kinetic critical phenomenon? Contemporary Physics. 2000; **41**:203–218. DOI: 10.1080/001075100409698

[10] Sander L M. Fractal growth processes. In: Meyers R A, editor. Mathematics of complexity and dynamical systems. Springer, New York, 2011. 429 p. DOI: 10.1007/978-0-387-30440-3

[11] Nicolás-Carlock J R, Carrillo-Estrada J L, Dossetti V. Fractality à la carte: a general particle aggregation model. Scientific Reports. 2016; **6**:19505. DOI: 10.1038/srep19505

[12] Nicolás-Carlock J R, Carrillo-Estrada J L, Dossetti V. Universality of fractal to non-fractal morphological transitions in stochastic growth processes. Arxiv. [Preprint] 2016. Available from: https://arxiv.org/abs/1605.08967

[13] Muthukumar M. Mean-field theory for diffusion-limited cluster formation. Physical Review Letters. 1983; **50**:839. DOI: 10.1103/PhysRevLett.50.839

[14] Tokuyama M, Kawasaki K. Fractal dimensions for diffusion-limited aggregation. Physics Letters. 1984; **100A**:337. DOI: 10.1016/0375-9601(84)91083-1

[15] Meakin P. Cluster-particle aggregation with fractal (Levy flight) particle trajectories. Physical Review B. 1984; **29**:3722. DOI: 10.1103/PhysRevB.29.3722

[16] Honda K, Toyoki H, Matsushita M. A Theory of fractal dimensionality for generalized diffusion-limited aggregation. Journal of the Physical Society of Japan. 1986; **55**:707–710. DOI: 10.1143/JPSJ.55.707

[17] Matsushita M, Honda K, Toyoki H, Hayakawa Y, Kondo H. Generalization and the fractal dimensionality of diffusion-limited aggregation. Journal of the Physical Society of Japan. 1986; **55**:2618–2626. DOI: 10.1143/JPSJ.55.2618

[18] Meakin P. Effects of particle drift on diffusion-limited aggregation. Physical Review B. 1983; **28**:5221. DOI: 10.1103/PhysRevB.28.5221

[19] Huang Y-B, Somasundaran P. Effects of random-walk size on the structure of diffusion-limited aggregates. Physical Review A. 1987; **36**:4518–4521. DOI: 10.1103/PhysRevA.36.4518

[20] Huang S-Y, Zou X-W, Tan Z-J, Jin Z-Z. Particle-cluster aggregation by randomness and directive correlation of particle motion. Physics Letters A. 2001; **292**:141–145. DOI: 10.1016/S0375-9601(01)00761-7

[21] Ferreira Jr S C, Alves S G, Faissal B A, Moreira J G. Morphological transition between diffusion-limited and ballistic aggregation growth patterns. Physical Review E. 2005; **71**:051402. DOI: 10.1103/PhysRevE.71.051402

[22] Alves S G, Ferreira Jr S C. Aggregation in a mixture of Brownian and ballistic wandering particles. Physical Review E. 2006; **73**:051401. DOI: 10.1103/PhysRevE.73.051401

[23] Niemeyer L, Pietronero L, Wiesmann H J. Fractal dimension of dielectric breakdown. Physical Review Letters. 1984; **52**:1033. DOI: 10.1103/PhysRevLett.52.1033

[24] Pietronero L, Erzan A, Evertsz C. Theory of fractal growth. Physical Review Letters. 1988; **61**:861. DOI: 10.1103/PhysRevLett.61.861

[25] Sánchez A, et al. Growth and forms of Laplacian aggregates. Physical Review E. 1993; **48**:1296. DOI: 10.1103/PhysRevE.48.1296

[26] Hastings M B. Fractal to non-fractal phase transition in the dielectric breakdown model. Physical Review Letters. 2001; **87**:175502. DOI: 10.1103/PhysRevLett.87.175502

[27] Hayakawa Y, Kondo H, Matsushita M. Monte Carlo simulations of the generalized diffusion-limited aggregation. Journal of the Physical Society of Japan. 1986; **55**:2479–2482. DOI: 10.1143/JPSJ.55.2479

[28] Meakin P. Noise-reduced and anisotropy-enhanced Eden and screened-growth models. Physical Review A. 1988; **38**:418. DOI: 10.1103/PhysRevA.38.418

[29] Mathiesen J, Procaccia I, Swinney H L, Thrasher M. The universality class of diffusion-limited aggregation and viscous fingering. Europhysics Letters. 2006; **72**:257–263. DOI: 10.1209/epl/i2006-10246-x

[30] Tolman S, Meakin P. Off-lattice and hypercubic-lattice models for diffusion-limited aggregation in dimensionalities 2–8. Physical Review A. 1989; **40**:428–437. DOI: 10.1103/PhysRevA.40.428

[31] Lehn J-M. Toward self-organization and complex matter. Science. 2002; **295**:2400. DOI: 10.1126/science.1071063

[32] Whitesides G M, Grzybowski B. Self-assembly at all scales. Science. 2002; **295**:2418. DOI: 10.1126/science.1070821

[33] Sturmberg J P, West B J. Fractals in physiology and medicine. In: Sturmberg J P, Martin C M, editors. Handbook of systems and complexity in health. Springer, New York; 2013. 171 p. DOI: 10.1007/978-1-4614-4998-0

Section 2

Anthropology

Chapter 6

The *Altepetl*: Fractal Modeling of a Pre-Hispanic Human Agency

Fernando López Aguilar

Additional information is available at the end of the chapter

http://dx.doi.org/10.5772/intechopen.68190

Abstract

The *altepetl* is a category that describes the organizational structure of the territory and the social hierarchy of pre-Hispanic societies in Mesoamerica. This category is used to understand the basic generator of territorial and political complexity in pre-Hispanic times. It is proposed that the repetition of itself, its iteration, increases social complexity until reaching structures comparable to big cities and great empires. These complex cultural developments are self-similar to the basic structure that generates them, the *altepetl*. The modeling of the pre-Hispanic *altepetl* is based on contributions made by ethnohistory to a spatial and social organization of territory and on the characteristics of alliances and segregations. These constitute the mechanisms that can explain linearization, increasing complexity or collapse of societies. The interactions between the *altepetl* and its agency capability are studied from the perspective of complexity theories to understand the relationships between neighboring entities. The study seeks to demonstrate the fractal properties of the structure and dynamics of Mesoamerican groups, based on the iteration principle of the generator component: the *altepetl*.

Keywords: *altepetl*, agency, complex systems, interaction

1. Introduction

The historical reconstruction of pre-Hispanic civilizations of Mexico has been undertaken from a traditional point of view, building on the western concept of "City." Associated with this approach is a linear perspective of history that emphasizes the origin of civilization, its climax, and its collapse, forming a path that resembles a Gaussian function. Civilization and complex societies, the city that characterized them and their collapse have been considered as a unique historical event.

Pre-Hispanic history of Mesoamerica was characterized by the civilizing and cultural climax of the Classic Horizon, and its catastrophic collapse was an enigma that archaeology tried to solve. The terms "Maya collapse" or "end of the Classic Horizon" allude to the idea that for the whole of the cultural area, climax occurred between 400 and 800 AD and that the cultures that the Spanish conquerors observed 700 years later were the decadent remains of great civilizations (**Figure 1**).

The representation of this linear process does not allow to observe the fractal properties of the evolution of pre-Hispanic cultures; it is seen as having an integer dimension, and not a fractional one. However, for example, from an epigraphic and ethnohistorical exploration, Joyce Marcus has observed that this view was incorrect and that the pre-Hispanic history of the Mayas was characterized by permanent fluctuations; small and big collapses could be observed, some local and other of a regional scale. Her perspective was based on two processes: linearization and segregation, that is, the alliances and ruptures that characterized the social dynamics of the Maya [1].

López Aguilar and Bali analyzed the fluctuations and instabilities inherent to the evolution of pre-Hispanic societies. They included in their study three variables obtained from available archaeological information: maximum extent of the territory of a system, the size of the capital, and the hierarchical levels of the subordinated settlements. The hierarchical levels considered what some scholars have called *altepetl*, the City-State, as a minimum unit of analysis that generates increasing complexity by the reiteration of the hierarchical structure of Mesoamerican societies. This study identified three divergent and intertwined trajectories: stable, unstable, and semi-stable [2].

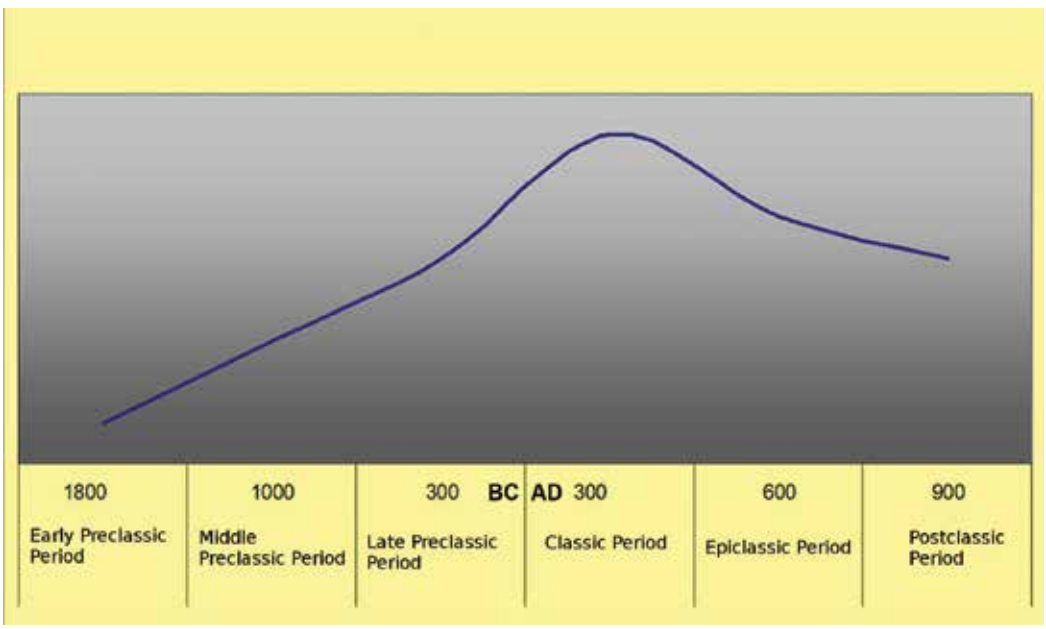

Figure 1. Traditional evolutionary path of Mesoamerican civilizations.

http://dx.doi.org/10.5772/intechopen.68190

Criss-cross oscillations of the three trajectories—between the lower limit defined by the structure of the *altepetl*, below which the Mesoamerican system would collapse, and the upper limit being the maximum structural complexity attained, over which the system would transform—characterize the fluctuating order of the Mesoamerican attractor with a history of 30 centuries, from its origin around 1500 BC to the sixteenth century AD. In **Figure 2**, the beginning of a "turbulence" lasting for 500 years can be observed. The turbulence was resolved by an increasing hierarchy (linearization) of the systems depicted in the Central and Southern trajectories.

The collapse of these two systems resulted in a small fluctuation that started around 650 AD and it gave place to a plateau-type stability phenomenon that collapsed with the expansion and linearization of the Central trajectory in the sixteenth century. The hypothesis that guided this research was that fluctuations of social systems of pre-Hispanic Mesoamerica had self-similar fractal properties based on the reiteration of a basic generating unit: the *altepetl*. The repetition of processes added or eliminated levels of hierarchical control in a non-lineal manner.

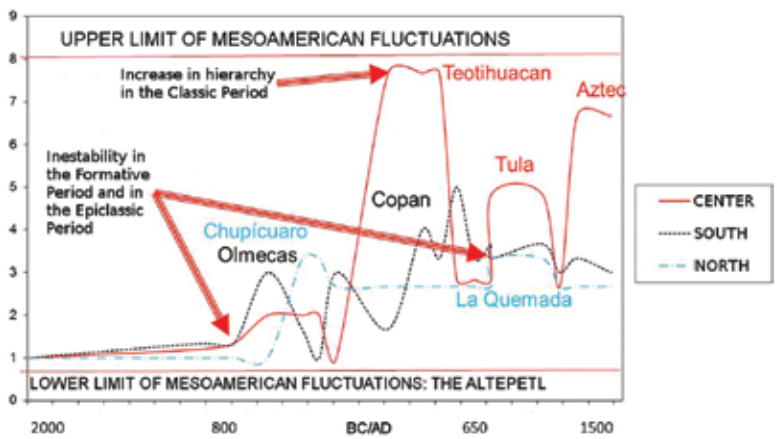

Figure 2. Mesoamerican trajectories.

2. The *altepetl*

Altepetl was the term with which the pre-Hispanic Mesoamerican groups referred to the people, their government, their space, their territory, and their time. The nahuatl term *in atl in tepetl* has equivalents in all the indigenous languages and can be translated as "in the water in the hill": the concept refers to a mountain located in a place where there is water, both with a sacred character. As a metaphor, the term includes territory, time, space, social organization, the form of government, the sacred, and the profane.

The discussion of the fruitfulness of this ethno-category for the comprehension of the Mesoamerican indigenous world is beyond the scope of this work. The intention here is to start a modeling process of Mesoamerican dynamics that builds on a symbiosis of the ethno-category with models, concepts, and metaphors taken from complexity sciences and fractals as families of models [3], inspired by auto-organized criticality research [4] and complex agents [5].

The *altepetl* has been studied by ethnohistorians for a number of years [6–9] and at present it is considered to have a greater explanatory potential than concepts developed elsewhere such as that of "City-State."

To date, the exact configuration of the structure of the *altepetl* is unknown. Based on anthropological models, Paul Kirchhoff noted that it could be a recursive system of a structure of hierarchical lineages that had called the attention of anthropologists for some time: the conical clan. In it, social hierarchy was based on the proximity by kinship to the common ancestor or the founder of the lineage, and its growth was nurtured by marriage alliances. In classic anthropology, the clan system corresponds to social hierarchization that precedes state structures [10, 11]. This type of social organization could have existed around 2000 BC in the Mesoamerican farming communities that gave place to the first *altepeme*[1] around the sixth century BC.

With time, the pre-Hispanic interaction system started a long and irreversible fragmentation process, indicating that the Mesoamerican attractor no longer existed. In the sixteenth century AD, with Spanish conquest and the insertion of America in the capitalist world-system, the long history of fluctuations of the indigenous social organization was shattered, which gave place to an a synchronic pulverization of the *altepeme* subsequent to the segregation of its structural components: lineages and the seminal structure of the conical clan [12, 13].

Gradually, the mechanisms of linearization and segregation were lost, the scope of action and control of indigenous rulers was reduced as a consequence of territorial conflicts generated by the Spanish and mestizo invasion of the space of the *altepetl* and by the emergence of new organizations of the Indian peoples and communities between the eighteenth and twentieth centuries structured along the lines of the Spanish model of town council (Cabildo).

However, the segregation and fragmentation of the territory of the *altepetl* of Ixmiquilpan, for example, show self-similar, recursive, and fractal processes: the number of segregated towns, the extension of their territories, the size of their borders, and the fractal dimension of the latter are a function of time. The process is isomorphic with respect to the reduction of the fractal dimension of the Sierpinsky carpet [14, p. 154].

Bounded in the time and space of the Mesoamerican attractor, the dynamics of growth and collapse of pre-Hispanic cultures was based on a system of alliances and conquests, of segregations and independences. Alliances permitted the aggregation of similar structures to the body of the *altepetl* until it reached the form of a great confederation, like the insights Lewis

[1] *Altepeme* is the plural of *altepetl*.

H. Morgan had since the nineteenth century of the Iroquois and Aztec confederations [15]. Alliances allowed the system to increase complexity and hierarchy within a structure that has been proposed as self-similar to the fundamental entity.

The reiteration of the *altepetl* on itself reached a complexity comparable to that of the great cities and empires. In ancient Mesoamerica, these had the ambiguous appellation of *huey altepetl*, the great *altepetl*. Equally, independence and segregation of components could take place, producing significant changes in the organizational structure of the *altepetl*. Fragmentation could even reach the level of the rudimentary generating unit.

The basic structure of government entailed at least three discernible hierarchical posts: the *tlatoani*, the *tecuhtli*, and the mayor, which were associated with the same number of hierarchical levels of settlements: the capital, the subordinated village, and the neighborhood or extended family house (*calli*). This arrangement is not necessarily linear. Joyce Marcus proposes four levels for Maya settlements, from first level villages to hamlets [1, p. 314], but it seems that at the base of this hierarchical, rotating, and non-linear system, a structure like the conical clan could be found in the hamlets.

In the conical clan, social organization and economy were beyond the level of an equalitarian community. Even if production was based on domestic units, the population had to collaborate in the construction of extensive works, like temples or palaces, and products and services were exacted for the purposes of the clan, the deities or for the hierarchy of the rulers [11, pp. 45–46]. This system was repeated in the neighborhoods, the hamlets, the capital, in the *altepetl*, in the *huey altepetl*, increasing the number of participants and the structure of the organization.

This basic structure repeated itself by means of alliances of different types, especially through marriage bonds (a higher level *altepetl* or lineage offered a noble woman in marriage to a lower level *altepetl* or lineage, or vice versa), increasing hierarchies and territorial control until reaching the ambiguous maximum of the *huey altepetl*. Alliances and confederations allowed the evolution of systems of cumulative complexity.

In the opposite direction, one or several *altepeme* could segregate from the larger entity and forge their autonomy. The segregated units increased their hierarchy in circumscribed territorial domains, while the larger system reduced its size and territory. These dynamics, when present in an accelerated fashion in short periods, like an avalanche, is a collapse. The reiteration of these processes—the diffusion and propagation of decisions—resulted in *altepeme* of different levels of hierarchy and territorial extension or the pulverization and the return to the minimum unit of the system: the *altepetl* [16, pp. 40–41].

The *altepetl* is a complex autonomous agent, since the decisions it makes while acting on its environment can intensify unsuspected evolutionary capacities that can manifest as an increase in hierarchy and social complexity, as an indifferent response, or as a transit toward lower levels of organization or to collapse or extinction.

In the environment of each *altepetl*, there are other *altepetl* that react to the actions and decisions of their near and far neighbors, with which they compete or collaborate to obtain the maximum benefit. The result of the actions and interactions is unforeseeable but, as in an interrelated system, the *altepeme* co-evolve, they are co-dependent one from the other and, in the network of local relations and practices, at times they win, at times they lose.

The *altepetl* is an agent that has action capability: it has reasons; it strives to concur in what it can do and what it knows with its peers, other *altepeme*. The decisions can take the form of cooperation, competition or rivalry, that is, alliances, confederations, segregations, or warfare. The aggregate of interactions between the agents can produce greater social and political hierarchy or collapse, the possibility to acquire prestige goods or consumption restricted to local goods [16].

Minor autonomous or subordinate entities (lineages, *altepeme*) tend to show a layout like that of the major entity due to integration and greater social hierarchies, which, in turn, results in complex cohesive and durable units. The complex autonomous human agent *altepetl* is a reproducing system based on the structure of lineages of the conical clan.

As corporative systems, in the lineage, in the conical clan, and in the *altepetl*, the action capacity resides in the head of the hierarchies, in the rulers, who spoke for the people. Collectively or individually, the ruler's decision was reflected in the action of the *altepetl*. Consequently, the dynamics of the *altepetl* reflects circumstances, intentions, reasons, deliberation, voluntary or involuntary motions, passivity, coercion or expected results, conformed in an open network of inter-signification, where each action has significant repercussions on all the network [17].

The agent's action has a cultural horizon that establishes the limits and conditions of knowledge, of know-how, and of awareness of problems, dilemmas, solutions, and strategies to follow. What is not in the framework of their traditions, their knowledge, and of their historically determined cultural horizon cannot be done, thought, practiced, or even imagined [16, pp. 21–32].

Dynamics and fluctuations of Mesoamerican systems can be modeled by a space where N elementary agents (lineages) have K interactions with their peers. The dynamics of this NK space result in the emergence of an agent of a higher degree of complexity: the *altepetl*. The latter also interacts with peers in an NK1 space originating an even higher degree of complexity, the *hueyaltepetl*. In turn, the interactions of this agent with the ensemble of its peers in an NK2 space increase complexity until a limit in which the system collapses (**Figure 3**).

Collapses were a historical possibility in any moment of the evolution of the system in the *NK*-dimensional space of the Mesoamerican interactions. It could have a local and restricted character, or take the form of a global and generalized avalanche as is shown by the scheme elaborated by Joyce Marcus for the Maya area [1, pp. 322, Figure 11] (**Figure 4**). This was the stable form of Mesoamerican fluctuations that were present throughout their history.

http://dx.doi.org/10.5772/intechopen.68190

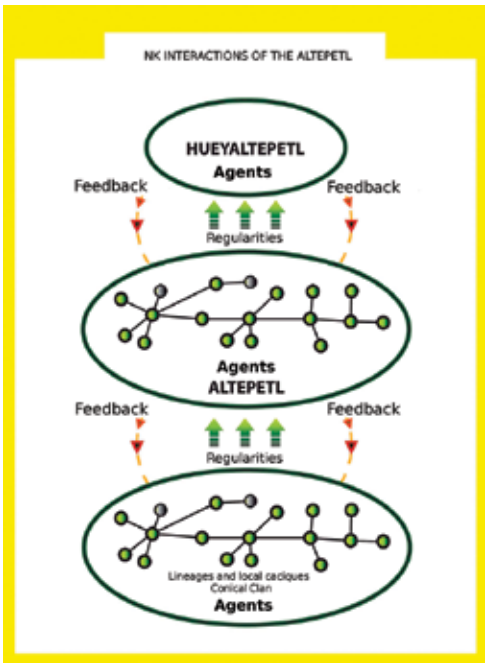

Figure 3. Space of interaction among agents and self-similar hierarchy.

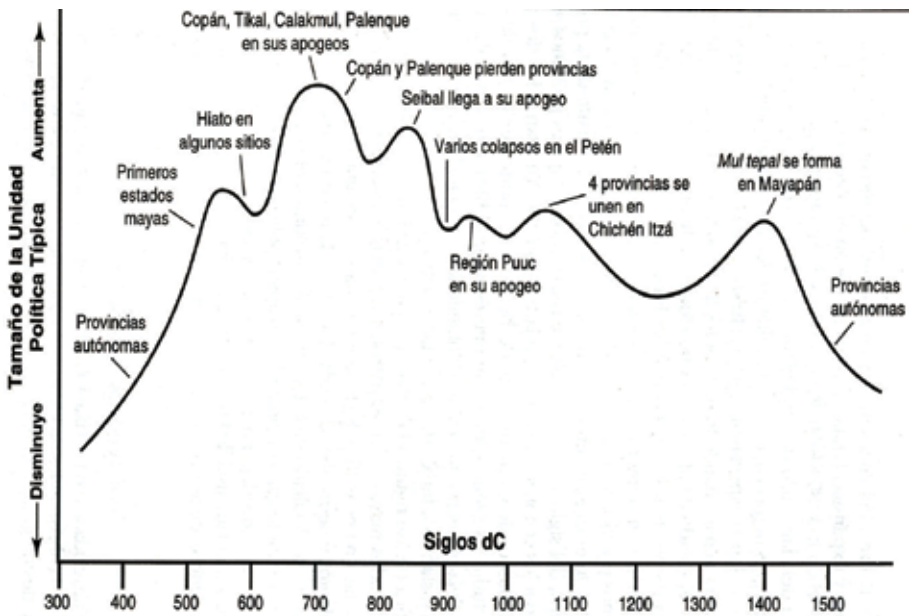

Figure 4. Oscillations of Maya collapses, taken from Ref. [1, p. 322, Figure 11].

3. Conclusions

One of the dilemmas faced by the fractal modeling of Mesoamerican pre-Hispanic societies is that the history and the evolutionary path of these cultures have been undertaken from a perspective that does not contemplate oscillations and fluctuations that characterize a dynamical complex system.

In this long-term research, we analyze the self-similar fractal properties that occur in systems that emerge from the NK space of interactions of the *altepetl* as a human agent.

The NK interactions of the *altepetl* can be considered as an example of what Kauffman called the NK landscapes that are based on the interconnections between agents: the actions of an agent are dependent on the actions of other agents.

Interconnections between agents are the basis of Kauffman's model, in which a network of N agents is constructed such that each is randomly connected to K others. The interactions between each agent and its K neighbors can be cooperative, competitive, or a mixture of both. Now, instead of all agents reacting to a few environmental variables, each agent reacts to the actions of the K other agents in its communication network. Each agent, therefore, has a unique set of conditions governing its behavior. Optimal strategies in the present moment may not be what they were before, because they depend on the previous actions of other agents. This result is a "Red Queen" effect, in that agents are forced to keep evolving (i.e., searching the fitness landscape) toward higher fitness peaks just to stay competitive [18, p. 13].

Kauffman's model [19] establishes that interactions among agents depend on the value of the interconnections among them and that they react differently when they have a moderate connection than when they are completely interconnected. In the first case, they can adapt easily and make small adjustments in their strategies to avoid greater risks, while in the other case, each agent has so many unfavorable interconnections that the favorable ones do not seem to exist, and the quest toward a decision is not better than chance [18, p. 13].

Kauffman's model was used by Kohler to analyze the Plaza people that occupied the Pajarito plateau in New Mexico toward the thirteenth century AD. Kohler focused principally on the interaction between households (N) and observed that their number increased while their interconnections (K) practically remained constant [20, p. 381].

When the NK interactions of the *altepetl* are considered in the long run, they result not only in the existence of closer interactions but also in closer organizational *altepeme*, and therefore a superior entity is formed—the *huey altepetl*— that maintains lower-level interconnections and reiterates them with neighboring *huey altepeme*, forming an NK space self-similar to that of the *altepetl*.

This characteristic was repeated until a configuration of higher hierarchy and control entities were established. In the case of Teotihuacan, up to seven hierarchical levels above the *altepetl* can be distinguished. In a self-similar fashion, they repeated the NK interactions with their close neighbors. We can put forth the hypothesis that when these interconnections reached a limit, a critical state was reached without the interference of external agents. Small local collapses ensued and, eventually, the massive cultural collapses.

The Mesoamerican attractor, characterized by three intertwined trajectories of stability, instability, and semi-stability, included the fractal self-similarity of the interaction among agents that formed its cultures, with independence of the scale of hierarchical complexity of the system.

Author details

Fernando López Aguilar

Address all correspondence to: flopez.enah@inah.com.mx

National School of Anthropology and History, Mexico City, Mexico

References

[1] Marcus J. La zona maya en el Clásico terminal. de Historia Antigua de México. Volumen II: El horizonte Clásico. México: INAH-IIA/UNAM-Porrúa; 2001. pp. 301–346.

[2] López Aguilar F, Bali Chávez G. Mesoamérica, una visión desde las teorías de la complejidad. Ludus Vitalis. 1995;**3**:83–102

[3] Maldonado CE. Exploración de una teoría general de la complejidad. de Complejidad: revolución científica y teórica. Bogotá: Universidad del Rosaio; 2009. pp. 113–143

[4] Bak P. How Nature Works: The Science of Self-Organized Criticality. New York: Copernicus Press; 1996

[5] Kauffman S. Investigaciones. Complejidad, autoorganización y nuevas leyes para una biología general. Barcelona: Tusquets; 2003

[6] Bernal García ME, García Zambrano ÁJ. El altepetl colonial y sus antecedentes prehispánicos: contexto teórico-historiográfico.de Territorialidad y paisaje en el altepetl del siglo XVI. México: Fondo de Cultura Económica-Instituto de Geografía/UNAM, 2006. pp. 31–113

[7] García Martínez B. Los pueblos de la Sierra. El poder y el espacio entre los indios del norte de Puebla hasta 1700. México: El Colegio de México; 1987

[8] Reyes García C. El altépetl, origen y desarrollo: construcción de la identidad regional náuatl. Morelia: El Colegio de Michoacán; 2000

[9] Schroeder S. Chimalpahin y los reinos de Chalco, Chalco: El Colegio Mexiquense, H. Ayuntamiento Constitucional de Chalco; 1994

[10] Kirchhoff P. The principles of clanship in human society. de Readings in Anthropology. Nueva York: Thomas Y. Crowell; 1959. pp. 259–270

[11] Sahlins MD. Las sociedades tribales. Barcelona: Labor; 1972

[12] López Aguilar F. Símbolos del Tiempo. Inestabilidad y bifurcaciones en los pueblos de indios del Valle del Mezquital. Pachuca: Consejo Estatal para la Cultura y las Artes del Estado de Hidalg; 2005

[13] López Aguilar F.Fundación y colapso. El altépetl Ixmiquilpan entre los siglos X y XVIII. de Arqueología colonial latinoamericana. Modelos de estudio. Oxford, British Archaeological Reports International Series; 2009. pp. 17–36

[14] López Aguilar F, Márquez Lago T. El colapso de un altépetl. Trayectoria de Ixmiquilpan después de la conquista de Antropología Fractal. México: D. F.: Sociedad Matemática Mexicana/CIMAT; 2007. pp. 137-158

[15] Morgan LH. La sociedad primitiva. Madrid: Ayuso; 1971

[16] López Aguilar F. El altépetl como agente autónomo. de Arqueología y complejidad social. México: ENAH-INAH-PROMEP; 2007. pp. 25–46

[17] Ricoeur P. Una semántica de la acción sin agente. México: Siglo XXI; 2003. pp. 37–74

[18] Bentley RA. An introduction to complex systems. de Complex Systems and Archaeology. Empirical and Theoretical Applications. Salt Lake City: The University of Utah Press; 2003. pp. 9–24

[19] Kauffman SA. The Origins of Order. Self-Organization and Selection in Evolution. New York: Oxford University Press; 1993

[20] Kohler, T. A., Van Pelt, M., & Yap, L. Reciprocity and its limits: Considerations for a study of the prehispanic Pueblo world. Alternative leadership strategies in the Prehispanic Southwest; 2000. pp. 180–206.

Chapter 7

Fractal Analysis Based on Hierarchical Scaling in Complex Systems

Yanguang Chen

Additional information is available at the end of the chapter

http://dx.doi.org/10.5772/intechopen.68424

Abstract

A fractal is in essence a hierarchy with cascade structure, which can be described with a set of exponential functions. From these exponential functions, a set of power laws indicative of scaling can be derived. Hierarchy structure and spatial network proved to be associated with one another. This paper is devoted to exploring the theory of fractal analysis of complex systems by means of hierarchical scaling. Two research methods are utilized to make this study, including logic analysis method and empirical analysis method. The main results are as follows. First, a fractal system such as Cantor set is described from the hierarchical angle of view; based on hierarchical structure, three approaches are proposed to estimate fractal dimension. Second, the hierarchical scaling can be generalized to describe multifractals, fractal complementary sets, and self-similar curve such as logarithmic spiral. Third, complex systems such as urban systems are demonstrated to be a self-similar hierarchy. The human settlements in Germany and the population of different languages in the world are taken as two examples to conduct empirical analyses. This study may reveal the association of fractal analysis with other types of scaling analysis of complex systems, and spatial optimization theory may be developed in future by combining the theories of fractals, allometry, and hierarchy.

Keywords: fractal, multifractals, hierarchical scaling, rank-size rule, systems of human settlements, language

1. Introduction

In recent years, the hierarchical systems with cascade structure have attracted attention of many scientists. Representing a form of organization of complex systems, hierarchy is frequently observed within the natural world and in social institutions [1]. A fractal can be treated

as a self-similar hierarchy because a fractal object bears many levels, which are systematically arranged according to scaling laws [2, 3−5]. Fractal phenomena can be described with power laws, and a power law can be decomposed into two exponential laws by means of hierarchical structure. Generally speaking, it is difficult to solve an equation based on power laws or spatial network because of dimensional problems, but it is easy to deal with the problem based on exponential models or hierarchies. Using self-similar hierarchy, we can transform fractal scaling into *a* hierarchical scaling with characteristic scales, thus many complex problems can be solved in a simple way. If we explore fractal systems such as a system of cities by means of hierarchy, we can use a pair of exponential laws to replace a power law, and the analytical process can be significantly simplified [6, 7]. A fractal is a special case of hierarchical scaling. Hierarchy suggests a new way for understanding fractal organization and exploring complex systems.

In scientific research, three factors increase the difficulty of mathematical modeling, that is, *spatial dimension*, *time lag* (response delay), and *interaction*. Economics is relatively simple because economists do not usually consider much the spatial dimension in economic systems [8]. However, all the difficult problems related to mathematical modeling, especially the spatial dimension, are encountered by geographers. If the spatial dimension is avoided, geography is not yet real geography. Geographers often study spatial structure by means of hierarchy. A discovery is that hierarchy and network structure represent two different sides of the same coin [2]. Two typical hierarchy theories are developed in human geography. One is central place theory [9, 10], and the other is rank-size distributions [11, 12]. The two theories are related to fractal ideas [2, 13−16]. Fractal theory, scaling concepts, and the related methods become much more important in geographical analysis such as urban studies [3]. As Batty (2008) once observed [17], "*an integrated theory of how cities evolve, linking urban economics and transportation behavior to developments in network science, allometric growth, and fractal geometry, is being slowly developed*." In fact, fractals, allometry, and complex network can be associated with one another in virtue of hierarchical scaling.

Hierarchical scaling suggests a new perspective to examine the simple rules hiding behind the complex systems. Many types of physical and social phenomena satisfy the well-known rank-size distribution and thus follow Zipf's law [7, 11, 18]. Today, Zipf's law has been used to describe the discrete power law probability distributions in various natural and human systems [3, 19]. However, despite a large amount of research, the underlying rationale of the Zipf distribution is not yet very clear. On the other hand, many types of data associated with Zipf's law in the physical and social sciences can be arranged in good order to form a hierarchy with cascade structure. There are lots of evidences showing that the Zipf distribution is inherently related to the self-similar hierarchical structure, but the profound mystery has not yet to be unraveled for our understanding of natural laws. The Zipf distribution is associated with fractal structure and bears an analogy with the 1/f fluctuation [6]. Fractals, 1/f noise, and the Zipf distribution represent the observation of the ubiquitous empirical patterns in nature [19]. This article provides scientists with a new way of looking at the relations between these ubiquitous empirical patterns and the complex evolution processes in physical and social systems, and thus to understand how nature works.

A scientific research actually includes two elements of methodology, namely description and understanding. Science should proceed first by describing how a system works and then by understanding why [20]. The description process is by means of mathematics and measurement, while the understanding process is by means of observation, experience, or even artificially constructed experiments [21]. This work is devoted to exploring fractal modeling and spatial analysis based on hierarchy with cascade structure. First of all, we try to describe and understand hierarchy itself; later, we try to use hierarchical scaling to describe and understand complex systems. Two research methods are utilized in this works. One is *logic analysis method*, including induction method and deduction method, and the other is *empirical analysis method*, fitting the mathematical models to observational data. The induction method is based on various regular fractals such as Cantor set, Koch snowflake curve, Vicsek box, and Sierpinski gasket, while the deduction method is mainly based on mathematical derivation. As for empirical analysis, systems of cities and population size distribution of languages can be taken as examples. Anyway, the success of natural sciences lies in their great emphasis on the interplay between quantifiable data and models [22]. The rest of the parts are organized as follows. In Section 2, a set of hierarchical models of fractals, including monofractals and multifractals, are presented. In Section 3, case studies are made by means of German systems of human settlements and world population size of different languages. In Section 4, several questions are discussed, and the hierarchical-scaling modeling is generalized. Finally, the discussion is concluded by summarizing the main points of this work.

2. Models

2.1. Three approaches to estimating fractal dimension

A regular fractal is a typical hierarchy with cascade structure. Let's take the well-known Cantor set as an example to show how to describe the hierarchical structure and how to calculate its fractal dimension (**Figure 1**). We can use two measurements, the length (L) and number (N) of fractal copies in the mth class, to characterize the self-similar hierarchy. Thus, we have two exponential functions such as

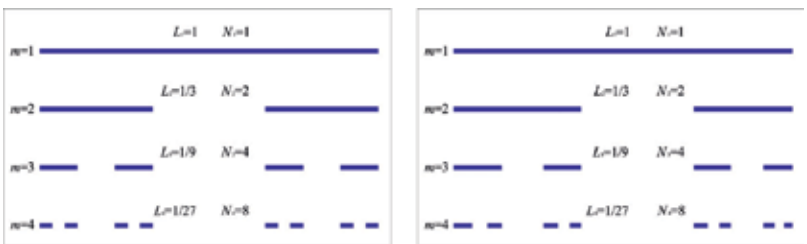

Figure 1. The Cantor set as a self-similar hierarchy with cascade structure (the first four classes). [**Note**: An analogy can be drawn between the Cantor sets and self-hierarchies of human settlements. For the multifractal Cantor set, the length of each level is the average value.]

$$N_m = N_1 r_n^{m-1} = \frac{N_1}{r_n} e^{(\ln r_n)m} = N_0 e^{\omega m}, \tag{1}$$

$$L_m = L_1 r_l^{1-m} = L_1 r_l e^{-(\ln r_l)m} = L_0 e^{-\psi m}, \tag{2}$$

where m denotes the ordinal number of class ($m = 1, 2, \ldots$), N_m is the number of the fractal copies of a given length, L_m is the length of the fractal copies in the mth class, N_1 and L_1 are the number and length of the initiator ($N_1 = 1$), respectively, r_n and r_l are the ***number ratio*** and ***length ratio*** of fractal copies, $N_0 = N_1/r_n$, $L_0 = L_1 r_l$, $\omega = \ln(r_n)$, $\psi = \ln(r_l)$. From Eqs. (1) and (2), it follows the common ratios of number and length, that is

$$r_n = \frac{N_1 r_n^m}{N_1 r_n^{m-1}} = \frac{N_{m+1}}{N_m}, \tag{3}$$

$$r_l = \frac{L_1 r_l^{1-m}}{L_1 r_l^{-m}} = \frac{L_m}{L_{m+1}}. \tag{4}$$

According to the definitions of ω and ψ, the logarithms of Eqs. (3) and (4) are

$$\omega = \ln(r_n) = \ln\left(\frac{N_{m+1}}{N_m}\right), \tag{5}$$

$$\Psi = \ln(r_l) = \ln\left(\frac{L_m}{L_{m+1}}\right). \tag{6}$$

From Eqs. (1) and (2), we can derive a power law in the form

$$N_m = k L_m^{-D}, \tag{7}$$

in which $k = N_1 {L_1}^D$ is the proportionality coefficient, and $D = \ln(r_n)/\ln(r_l)$ is the fractal dimension of the Cantor set ($k = 1$). Thus, three formulae of fractal dimension estimation can be obtained. Based on the power law, the fractal dimension can be expressed as

$$D = -\frac{\ln(N_m)}{\ln(L_m)}. \tag{8}$$

Based on the exponential models, the fractal dimension is

$$D = \frac{\omega}{\Psi}. \tag{9}$$

Based on the common ratios, the fractal dimension is

$$D = \frac{\ln r_n}{\ln r_l}. \tag{10}$$

In theory, Eqs. (8)–(10) are equivalent to one another. Actually, by recurrence, Eq. (7) can be rewritten as $N_{m+1} = {L_{m+1}}^{-D}$, and thus we have

$$\frac{N_{m+1}}{N_m} = \left(\frac{L_{m+1}}{L_m}\right)^{-D}, \tag{11}$$

Taking logarithms on both sides of Eq. (11) yields

$$D = -\frac{\ln(N_{m+1}/N_m)}{\ln(L_{m+1}/L_m)} = -\frac{\ln(N_m)}{\ln(L_m)} = \frac{\ln r_n}{\ln r_l} = \frac{\omega}{\Psi}. \tag{12}$$

For the Cantor set, $N_m = 2^{m-1}$, $L_m = 1/3^{m-1}$, $r_n = N_{m+1}/N_m = 2$, $r_l = L_m/L_{m+1} = 3$, $\omega = \ln(2)$, $\psi = \ln(3)$, thus we have

$$D = \frac{\ln(2)}{\ln(3)} \approx 0.631.$$

This suggests that, for the regular fractal hierarchy, three approaches lead to the same result. The fractal dimension can be computed by using exponential functions, power function, or common ratios, and all these values are equal to one another. However, in practice, there are subtle differences between the results from different approaches because of random noise in observational data. Certainly, the differences are not significant and thus can be negligible.

The mathematical description and fractal dimension calculation of the Cantor set can be generalized to other regular fractals such as Koch snowflake and Sierpinski gasket or even to the route from bifurcation to chaos. As a simple fractal, the Cantor set fails to follow the rank-size law. However, if we substitute the multifractal structure for the monofractal structure, the multiscaling Cantor set will comply with the rank-size rule empirically.

2.2. Multifractal characterization of hierarchies

Monofractals (unifractals) represent the scale-free systems of homogeneity, while multifractals represent the scale-free systems of heterogeneity. In fact, as Stanley and Meakin (1988) [23] pointed out, "*multifractal scaling provides a quantitative description of a broad range of heterogeneous phenomena*." In geography, multifractal geometry is a powerful tool for describing spatial heterogeneity. A multifractal hierarchy of Cantor set can be organized as follows. At the first level, the initiator is still a straight line segment of unit length, that is, $S_1 = L_1 = 1$. At the second level, the generator includes two straight line segments of different lengths. The length of one segment is a, and the other segment's length is b. Let $a = 3/8$, $b = 2/3 - a = 7/24$. The summation of the two line segments' length is 2/3, that is, $S_2 = a + b = 2/3$, and the average length of the two segments is $L_2 = S_2/2 = 1/3$. At the third level, there are four line segments, and the lengths are a^2, ab, ba, and b^2, respectively. The total length of the four line segments is 4/9, namely $S_3 = (a+b)^2 = (2/3)^2$, and the average length is $L_3 = S_3/4 = 1/3^2$. Generally speaking, the mth level consists of 2^{m-1} line segments with lengths of a^{m-1}, $a^{m-2}b$, $a^{m-3}b^2$, …, a^2b^{m-3}, ab^{m-2}, and b^{m-1}, respectively. The length summation is $S_m = (a+b)^{m-1} = (2/3)^{m-1}$, so the average length is

$$L_m = \frac{(a+b)^{m-1}}{N_m} = 3^{1-m}, \tag{13}$$

where

$$N_m = 2^{m-1}. \tag{14}$$

From Eqs. (13) and (14), it follows a scaling relation as below:

$$N_m = L_m^{-\ln(2)/\ln(3)} = \mu L_m^{-D_0}, \tag{15}$$

which is identical in form to Eq. (7), and the capacity dimension $D_0 = \ln(2)/\ln(3) \approx 0.631$ is equal to the fractal dimension of the monofractal Cantor set (**Figure 1**).

Two sets of parameters are always employed to characterize a multifractal system. One is the set of *global* parameters, and the other is the set of *local* parameters. The global parameters include the generalized correlation dimension and the mass exponent; the local parameters comprise the Lipschitz-Hölder exponent and the fractal dimension of the set supporting this exponent. For the two-scale Cantor set, the mass exponent is

$$\tau(q) = -\frac{\ln[p^q + (1-p)^q]}{\ln(3)}, \tag{16}$$

where q denotes the moment order ($-\infty < q < \infty$), $\tau(q)$ refers to the mass exponent, and p is a probability measurement. Taking the derivative of Eq. (16) with respect to q yields the Lipschitz-Hölder exponent of singularity in the form

$$\alpha(q) = \frac{\mathrm{d}\tau(q)}{\mathrm{d}q} = -\frac{1}{\ln(3)}\frac{p^q \ln p + (1-p)^q \ln(1-p)}{p^q + (1-p)^q}, \tag{17}$$

in which $\alpha(q)$ refers to the singularity exponent. Utilizing the Legendre transform, we can derive the fractal dimension of the subsets supporting the exponent of singularity such as

$$f(\alpha) = q\alpha(q) - \tau(q) = \frac{1}{\ln(3)}\left[\ln[p^q + (1-p)^q] - \frac{p^q \ln p^q + (1-p)^q \ln(1-p)^q}{p^q + (1-p)^q}\right], \tag{18}$$

where $f(\alpha)$ denotes the local dimension of the multifractal set. Furthermore, the general fractal dimension spectrum can be given in the following form:

$$D_q = \begin{cases} -\dfrac{p\ln p + (1-p)\ln(1-p)}{\ln(3)}, & q = 1 \\ \dfrac{\tau(q)}{q-1}, & q \neq 1 \end{cases}, \tag{19}$$

where D_q denotes the generalized correlation dimension. If the order moment $q \neq 1$, the general dimension can also be expressed as

$$D_q = \frac{1}{q-1}[q\alpha(q) - f(\alpha)]. \tag{20}$$

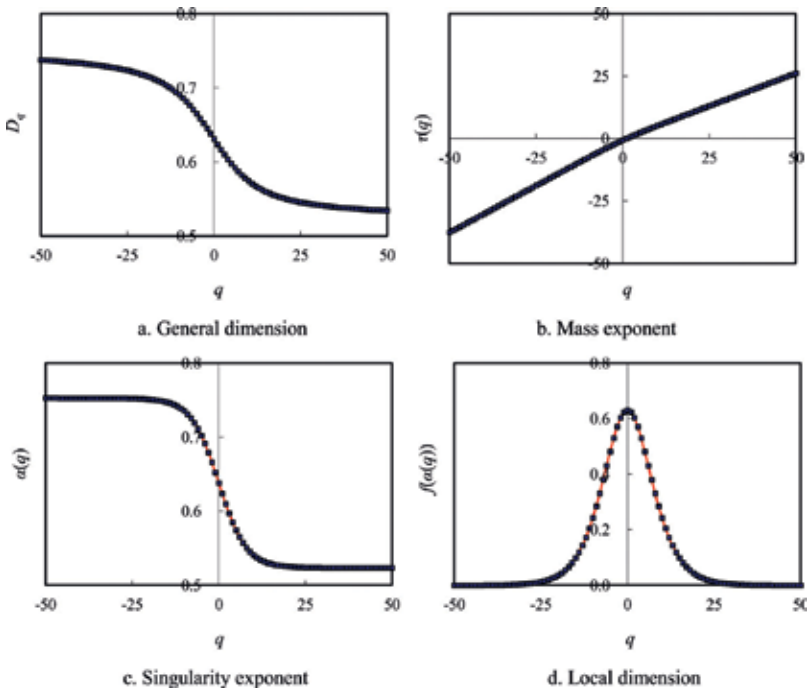

Figure 2. The dimension spectrums of multifractals Cantor set and the curves of related parameters ($p = 9/16$).

Using the above equations, we can describe multifractal Cantor set. For example, if the length of one line segment in the generator is $a = 3/8$ as assumed, then the length of another line segment is $b = 7/24$. Accordingly, the probability measures are $p = a/(2/3) = 9/16$ and $1-p = 7/16$. By means of these formulae, the multifractal dimension spectra and the related curves can be displayed in **Figures 2** and **3**. The capacity dimension is $D_0 \approx 0.631$, the information dimension is $D_1 \approx 0.624$, and the correlation dimension is $D_2 \approx 0.617$. Substituting ln(2) for ln (3) in the equations shown above, we can use the multifractal models of Cantor set to describe multiscaling rank-size distribution of cities [6, 24].

2.3. Hierarchical scaling in social systems

Fractal hierarchical scaling can be generalized to model general hierarchical systems with cascade structure. Suppose the elements (e.g., cities) in a large-scale system (e.g., a regional system) are divided into M levels in the top-down order. We can describe the hierarchical structure using a set of exponential functions as follows:

$$N_m = N_1 r_f^{m-1}, \tag{21}$$

$$P_m = P_1 r_p^{1-m}, \tag{22}$$

$$A_m = A_1 r_a^{1-m}. \tag{23}$$

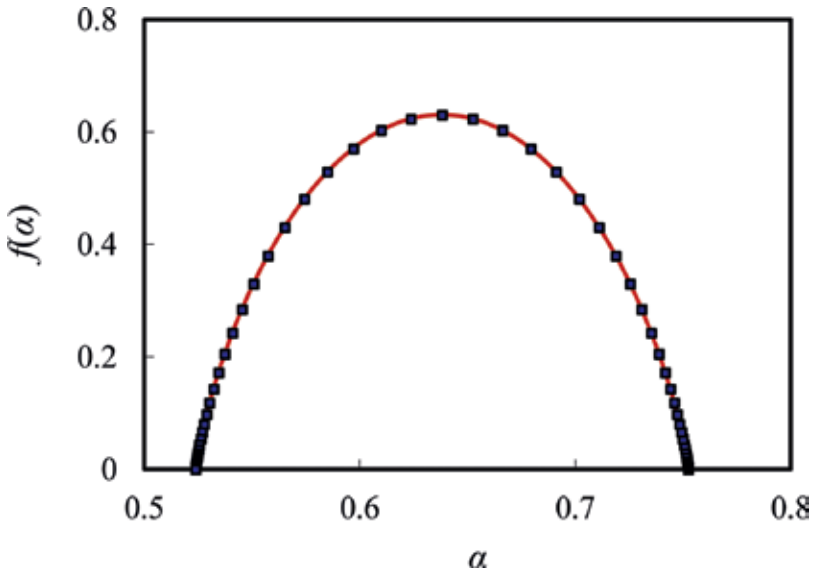

Figure 3. The $f(\alpha)$ curves of the local dimension versus the singularity exponent.

where m denotes the top-down order ($m = 1, 2, \ldots M$), N_m represents the element number in a given order, $r_n = N_{m+1}/N_m$ is actually the **number ratio**, N_1 is the number of the top-order elements. Generally speaking, we have $N_1 = 1$; P_m represents the mean size of order m, $r_p = P_m/P_{m+1}$ is the element **size ratio** of adjacent levels, P_1 is the mean size of the first-order elements, that is, the largest ones; A_m is the average area of order m, $r_a = A_m/A_{m+1}$ is the **area ratio**, and A_1 is the area of the first order. Rearranging Eq. (22) yields ${r_p}^{m-1} = P_1/P_m$, then taking logarithm to the base r_n of this equation and substituting the result into Eq. (21) yield a power function as

$$N_m = \mu P_m^{-D}, \tag{24}$$

where $\mu = N_1 {P_1}^D$, $D = \ln(r_n)/\ln(r_p)$. Eq. (24) is hereafter referred to as the "size -number law," and D proved to be the fractal para dimension of self-similar hierarchies measured by city population size. Similarly, from Eqs. (21) and (23), it follows

$$N_m = \eta A_m^{-d}, \tag{25}$$

in which $\eta = N_1 {A_1}^d$, $d = \ln(r_n)/\ln(r_a)$. Eq. (25) is what is "area-number law," and d is the fractal para dimension of self-similar hierarchies measured by urban area. Finally, we can derive the hierarchical allometric-scaling relationships between area and size from Eqs. (22) and (23), or from Eqs. (24) and (25), and the result is

$$A_m = a P_m^b, \tag{26}$$

where $a = A_1 {P_1}^{-b}$, $b = \ln r_a/\ln r_p$. This is just the generalized allometric growth law on the area-size relations. Further, a three-parameter Zipf-type model on size distribution can be derived from Eqs. (1) and (2) such as

$$P_k = C(k+\varsigma)^{-\alpha}, \tag{27}$$

where k is the rank among all elements in a given system in decreasing order of size, P_k is the size of the kth element. As the parameters, we have the constant of proportionality $C = P_1[r_n/(r_n-1)]^{1/D}$, the small parameter $\varsigma = 1/(r_n-1)$, and the power $\alpha = 1/D = \ln r_p/\ln r_f$. Where P_1 is the size of the largest element, q proved to be the reciprocal of the fractal dimension D of city-size distribution or urban hierarchies, that is, $\alpha = 1/D$ [7]. By analogy, we can derive a three-parameter Zipf-type model on area distribution from Eqs. (1) and (3), that is

$$A_k = G(k+\zeta)^{-\beta}, \tag{28}$$

where G, ζ, and β are parameters. In theory, $\beta = 1/d$. From Eqs. (27) and (28), it follows

$$\left(\frac{P_k}{C}\right)^{-1/\alpha} - \varsigma = \left(\frac{A_k}{G}\right)^{-1/\beta} - \zeta, \tag{29}$$

which suggests an approximate allometric relation. If $\zeta = \varsigma$, then we can derive a cross-sectional allometry relation between size and area from Eqs. (27) and (28) as below

$$A_k = aP_k^b, \tag{30}$$

where $a = A_1{P_1}^{-b}$, $b = \beta/\alpha$. Eq. (30) is mathematically equivalent to Eq. (26), that is, the rank-size allometric scaling is equivalent to hierarchical allometric scaling in theory. Further, if $\zeta = \varsigma = 0$, then Eqs. (27) and (28) will be reduced to the common two-parameter Zipf's models [3]. The fractal models (principal scaling laws), allometric model (the law of allometric growth), and rank-size distribution model (Zipf's law) are three basic scaling laws of hierarchical systems such as cities, and all the scaling relations can be derived from the hierarchical models expressed by exponential functions.

3. Empirical analysis

3.1. A case of Germany "natural cities"

3.1.1. Materials and data

First of all, the hierarchy of German cities is employed to illustrate hierarchical-scaling method. Recently, Bin Jiang and his coworkers have proposed a concept of "natural city" and developed a novel approach to measure objective city sizes based on street nodes or blocks and thus urban boundaries can be naturally identified [18, 25]. The street nodes are defined as street intersections and ends, while the naturally defined urban boundaries constitute the region of what is called ***natural cities***. The street nodes are significantly correlated with population of cities as well as city areal extents. The city data are extracted from massive volunteered geographic information OpenStreetMap databases through some data-intensive computing processes and three data sets on European cities, including the cities of **France**, **Germany**, and

the **United Kingdom** (UK), have been obtained. Among all these data sets, the set for German is the largest one, which encompasses the 5160 natural cities. Therefore, German cities are taken as an example to make empirical analysis. In the processing of data, the area variable is divided by 10,000 for comparability.

3.1.2. Method and results

The analytical method is based on the theoretical models shown above. For the natural cities, the population size measurement (P) should be replaced by the amount of blocks in the physical areal extent (A), which can be treated as a new size measurement of cities. It is easy to use German cities to construct a hierarchy to illustrate the equivalence relation between the rank-size law and the hierarchical scaling. Empirically, the 5160 German cities and towns follow the rank-size rule and we have

$$\hat{P}_k = 160175.044k^{-1.051}, \tag{31}$$

where k is the rank of natural cities, and P_k denotes the city size defined with urban blocks in objective boundaries. The symbol "^" implies "estimated value," "calculated value," or "predicted value." The goodness of fit is about $R^2 = 0.993$, and the scaling exponent is around $q = 1.051$, as shown in the equation (**Figure 4**). The Zipf distribution suggests a hierarchical scaling of the urban system.

The models of fractals and allometry can be built for German hierarchies of cities as follows. Taking number ratio $r_f = 2$, we can group the cities into different classes according to the 2^n rule [7, 26]. The results, including city number (N_m), total amount of urban blocks (S_m), average size by blocks (P_m), total area (T_m), and average area (A_m), in each class, are listed in **Table 1**. In a hierarchy, two classes, that is, top class and bottom class, are always special and can be considered to be exceptional

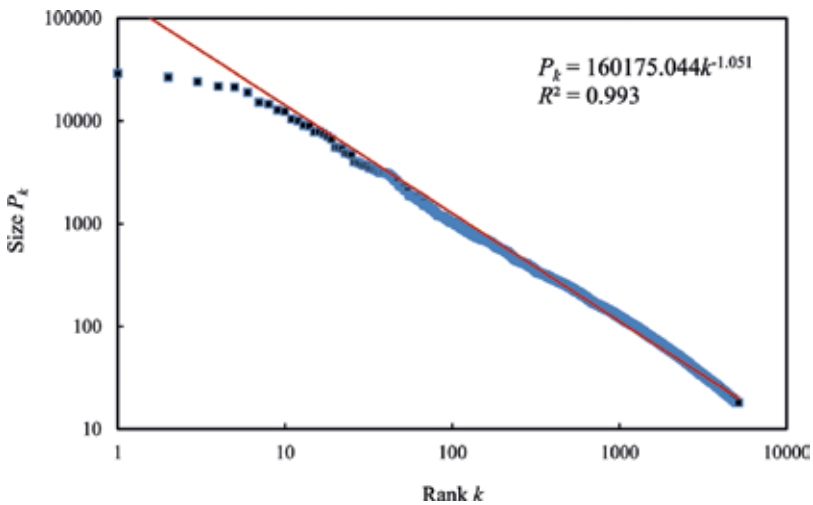

Figure 4. The rank-size pattern of Germany cities by blocks within physical extent (2010).

m	Total block (S_m)	Total area (T_m)	Average size (P_m)	Average area (A_m)	Number (N_m)
1	28,866	402657796.2	28866.0	402657796.2	1
2	50,709	731271674.1	25354.5	365635837.1	2
3	77,576	1030661786.8	19394.0	257665446.7	4
4	86,071	973558025.6	10758.9	121694753.2	8
5	82,700	999267240.9	5168.8	62454202.6	16
6	80,912	940916731.4	2528.5	29403647.9	32
7	72,397	986813213.3	1131.2	15418956.5	64
8	75,375	1070810188.5	588.9	8365704.6	128
9	79,299	1165806475.4	309.8	4553931.5	256
10	84,327	1271861134.1	164.7	2484103.8	512
11	84,599	1310854103.8	82.6	1280131.0	1024
12	75,214	1138100595.1	36.7	555713.2	2048
13	21,820	197476690.8	20.5	185424.1	1065*

Source: The original data come from Jiang (http://arxiv.org/find/all/). *__Note__: The last class of each hierarchy is a *lame-duck class* termed by Davis (1978) [26].

Table 1. The size and number for the hierarchy of German cities based on the 2^n principle.

values (**Figure 5**). In fact, the power law relations always break down if the scale is too large or too small [19]. Thus, a scaling range can be found in a log-log plot of fractal analysis on cities [3]. Two hierarchical-scaling relations can be testified by the least-squares calculation. For common ratio r_n= 2, the hierarchical-scaling relation between city size and number is

$$\hat{N}_m = 91161.315 P_m^{-1.025}. \tag{32}$$

The goodness of fit is about $R^2 = 0.996$, and the fractal dimension of the self-similar hierarchy is $D \approx 1.025$. The average size ratio within the scaling range is about r_p= 1.942, which is very close to r_n= 2. Thus, another fractal dimension estimation is $D = \ln(r_n)/\ln(r_p) \approx 1.045$. The average size follows the exponential law, that is, P_m= 133869.061*exp(−0.674m). So, the third fractal dimension estimation is $D = \omega/\psi \approx 0.693/0.674 \approx 1.028$. All these results are based on the scaling range rather than the whole classes. Similarly, the relation between urban area and city number is as below

$$\hat{N}_m = 162295.381 A_m^{-1.060}. \tag{33}$$

The goodness of fit is about $R^2 = 0.998$, and the fractal dimension of the self-similar hierarchy is $d \approx 1.060$. The average size ratio within the scaling range is about r_p= 1.927. So, another fractal dimension is estimated as $d = \ln(r_n)/\ln(r_a) \approx 1.056$. The average area complies with the exponential law, namely A_m= 157737.532*exp(−0.653m). Thereby, the third fractal dimension is estimated as $d = \omega/\psi \approx 0.693/0.653 \approx 1.061$. Further, by means of the datasets of urban size and area, an allometric-scaling model can be built as follows:

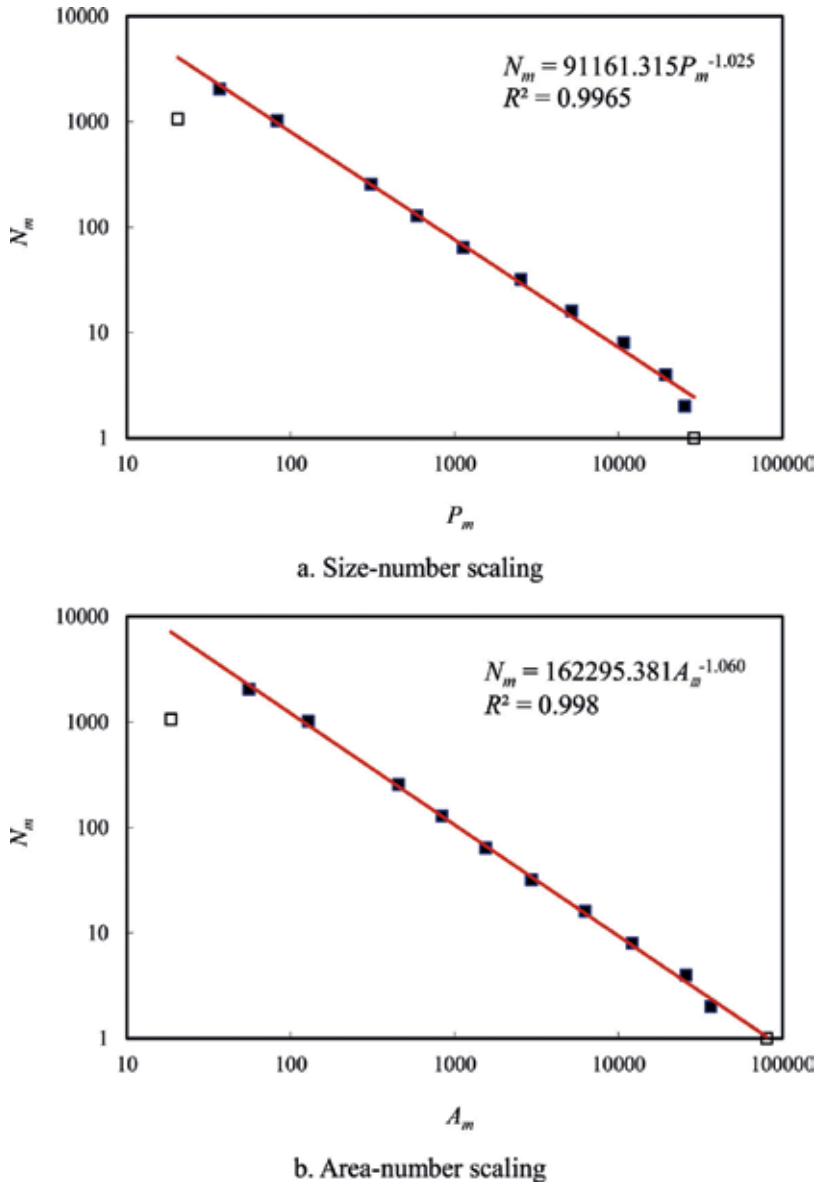

Figure 5. The scaling relations between city numbers and average sizes/areas in the hierarchies of German cities by the blocks in physical extent in 2010. [**Note**: The hollow squares represent the outliers, while the solid squares form a scaling range. For simplicity, the urban area is rescaled by dividing it using 10,000.]

$$\hat{A}_m = 1.722P_m^{0.967}. \tag{34}$$

The goodness of fit is around $R^2 = 0.999$, and the scaling exponent $b \approx 0.967$ (**Figure 6**). Another estimation of the allometric exponent is $b \approx 1.025/1.060 \approx 0.967$. The two results are close to one

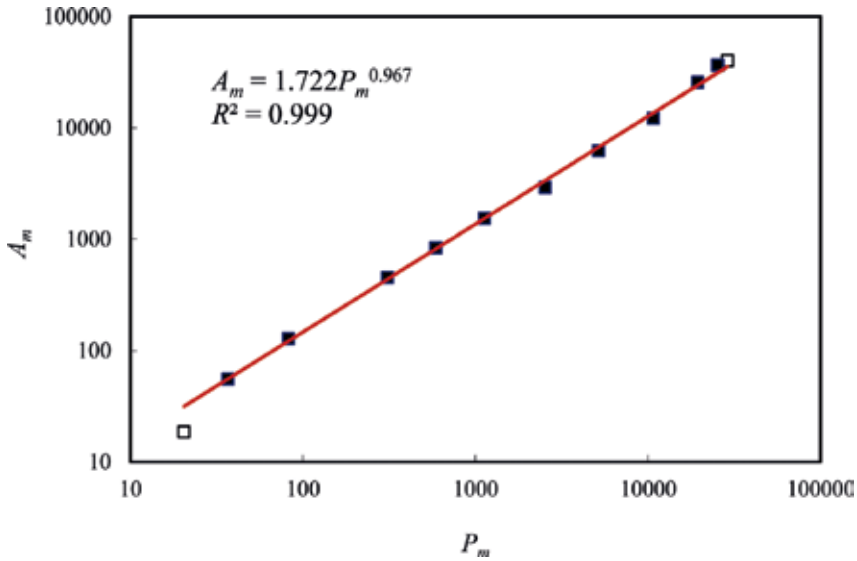

Figure 6. The allometric-scaling relations between average population sizes and urban areas in the hierarchies of Germany cities in 2010. [**Note**: The hollow square represents the outlier, while the solid squares form a scaling range. For comparability, the area measure is divided by 10,000.]

another. The natural cities of Germany lend further support to the equivalent relationship between the rank-size distribution and the self-similar hierarchy.

3.2. A case of language hierarchy in the world

The hierarchical scaling can be used to model the rank-size distribution of languages by population. Where population size is concerned, there are 107 top languages in the world such as Chinese, English, and Spanish. In data processing, the population size is rescaled by dividing it with 1,000,000 for simplicity. Gleich et al. (2000) [27] gave a list of the 15 languages by number of native speakers (**Table 2**). The rank-size model of the 107 languages is as below:

$$\hat{P}_k = 1092.160k^{-1.053}, \tag{35}$$

where k refers to rank, and P_k to the population speaking the language ranked k, the goodness of fit is about $R^2 = 0.986$ (**Figure 7**). The fractal dimension is estimated as $D \approx 0.949$.

Using the hierarchical scaling, we can estimate the fractal dimension of the size distribution of languages in the better way. According to the 2^n rule, the 107 languages fall into eight classes by size (**Table 3**). In the top level, one language, that is, Chinese, and the total of Chinese-speaking population is 885 million; in the second level, two languages, English and Spanish, with total population 654 million, and so on. The number ratio is defined as $r_n = 2$. The corresponding size ratio is around $r_p = 2.025$. Thus, the fractal dimension can be estimated as $D = \ln(r_n)/\ln(r_p) = \ln(2)/\ln(2.025) = 0.983$, which is close to the reciprocal of Zipf exponent,

Level	Number	Language and population				Total population	Average population	Size ratio
1	1	Chinese	885			885	885	
2	2	English	470	Spanish	332	802	401	2.207
3	4	Bengali	189	Portuguese	170	711	177.75	2.256
		Indic	182	Russian	170			
4	8	Japanese	125	Korean	75	657	82.125	2.164
		German	98	French	72			
		Wu-Chinese	77	Vietnamese	68			
		Javanese	76	Telugu	66			

Source: Ref. [27]. **Note**: If we use the lower limits of population size $s_1 = 520$, $s_2 = 260$, $s_3 = 130$, and $s_4 = 65$ to classify the languages in the table, the corresponding number of languages is $f_1 = 1$, $f_2 = 2$, $f_3 = 4$, and $f_4 = 8$, and the scaling exponent is just 1.
Unit: million.

Table 2. The self-similar hierarchy of the 15 top languages by population.

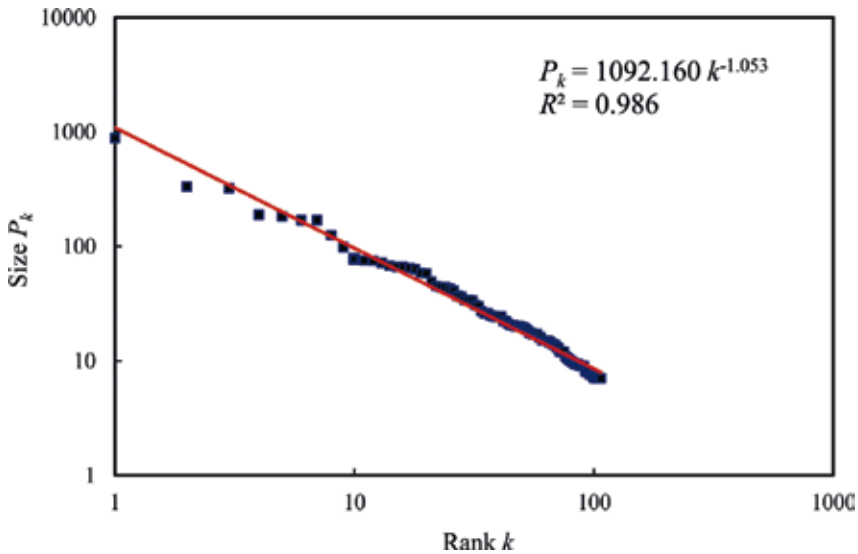

Figure 7. The rank-size pattern of the top 107 languages by population (Unit: million).

0.949. A regression analysis yields a hierarchical-scaling relation between language number, N_m, and average population size, S_m, such as

$$\hat{N}_m = 723.421 P_m^{-1.012}. \tag{36}$$

The squared correlation coefficient is $R^2 = 0.997$, and the fractal dimension is about $D = 1.012$, which is close to the above-estimated value, 0.983 (**Figure 8**). The results suggest that the languages by population and cities by population follow the same hierarchical-scaling laws.

Level (m)	Total population (S_m)	Number (N_m)	Average size (S_m)	Size ratio (r_p)
1	885,000,000	1	885000000.0	
2	654,000,000	2	327000000.0	2.706
3	711,000,000	4	177750000.0	1.840
4	656,687,800	8	82085975.0	2.165
5	751,058,000	16	46941125.0	1.749
6	668,446,000	32	20888937.5	2.247
7	433,020,412	44	9841373.0	2.123

Note: The source of the original data: http://www.nationmaster.com/. The number ratio is 2. The first class is exceptional, and the last class is a lame-duck class, which is defined by Davis (1978) [26]. By the way, there is subtle difference of English population between **Tables 2** and **3**, but this error does not influence the conclusions.

Table 3. The self-similar hierarchy of the 107 top languages by population size.

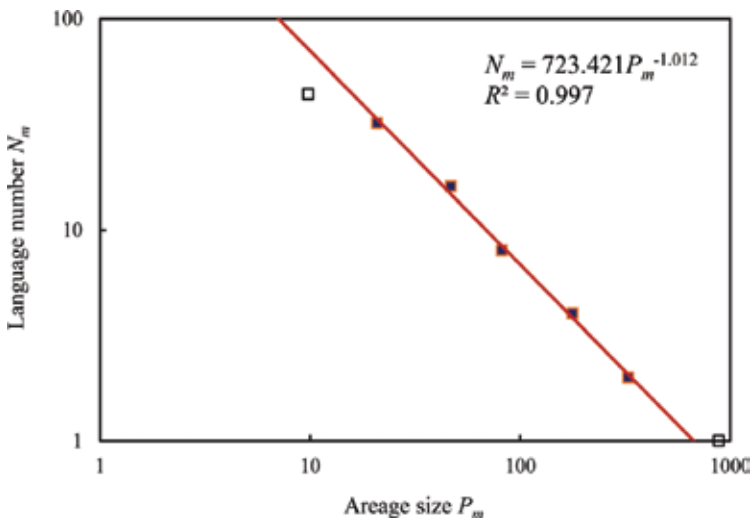

Figure 8. The hierarchical-scaling relationships between population size and number of languages (Unit: million). [**Note:** The small circles represent top classes and the lame-duck classes, respectively. Removing the first and last classes yields a scaling range. The slope based on the scaling range indicates the fractal parameters of rank-size distributions.]

4. Questions and discussion

4.1. Hierarchical scaling: a universal law

A complex system is always associated with hierarchy with cascade structure, which indicates self-similarity. A self-similar hierarchy such as cities as systems and systems of cities can be described with three types of scaling laws: *fractal laws*, *allometric law*, and *Zipf's law*. These scaling laws can be expressed from Eqs. (24) to (30). Hierarchical scaling is a universal law in nature and human society, and it can be utilized to characterize many phenomena with different levels. Besides fractals, it can be used to depict the routes from bifurcation to chaos [3]. In geomorphology, the hierarchical scaling has been employed to describe river systems [28–31].

In geology and seismology, it is employed to describe the cascade structure of earthquake energy distributions [32, 33]. In biology and anatomy, it is used to describe the geometrical morphology of coronary arteries in human bodies and dogs [34−36]. In urban geography, it is used to describe central place systems and self-organized network of cities [3, 7]. In short, where there is a rank-size distribution, there is cascade structure, and where there is cascade structure, there is hierarchical-scaling relations.

Next, hierarchical scaling is generalized to describe fractal complementary sets and quasi-fractal structure, which represent two typical cases of hierarchical description besides fractals. The basic property of fractals is self-similarity. For convenience of expression and reasoning, the concept of self-similarity point should be defined. A fractal construction starts from an initiator by way of generator. If a fractal's generator has two parts indicative of two fractal units, the fractal bears two self-similarity points; if a fractal's generator has three parts, the fractal possesses three self-similarity points, and so on. For example, Cantor set has two self-similarity points, Sierpinski gasket has three self-similarity points, Koch curve has four self-similarity points, and the box growing fractal has five self-similarity points. The number of self-similarity points is equal to the number ratio, that is, the common ratio of fractal units at different levels. A real fractal bears at least two self-similarity points, this suggests cross-similarity of a fractal besides the self-similarity. Self-similarity indicates dilation symmetry, where cross-similarity implies translation symmetry. However, if and only if a system possesses more than one self-similarity point, the system can be treated as a real fractal system, and this system can be characterized by fractal geometry. A fractal bears both dilation and translation symmetry. The systems with only one self-similarity point such as logarithmic spiral can be described with hierarchical scaling. However, it cannot be characterized by fractal geometry. In this case, we can supplement fractal analysis by means of hierarchical scaling.

4.2. Hierarchies of fractal complementary sets

A fractal set and its complementary set represent two different sides of the same coin. The dimension of a fractal is always a fractional value, coming between the topological dimension and the Euclidean dimension of its embedding space. Certainly, the similarity dimension is of exception and may be greater than its embedding dimension. The dimension of the corresponding complement, however, is equal to the Euclidean dimension of the embedding space. Anyway, the Lebesgue measure of a fractal set is zero; by contrast, the Lebesgue measure of the fractal complement is greater than zero. Let us see the following patterns. **Figure 9(a)** shows the generator (i.e., the second step) of Vicsek's growing fractal set [37], which bears an analogy with urban growth; **Figure 9(b)** illustrates the complementary set of the fractal set (the second step). It is easy to prove that the dimension of a fractal's complement is a Euclidean dimension. If we use box-counting method to measure the complement of a fractal defined in a two-dimension space, the extreme of the nonempty box number is

$$C_m = \lim_{m\to\infty}\left(r_l^{2(m-1)} - r_n^{m-1}\right) \to r_l^{2(m-1)}, \tag{37}$$

where C_m denotes the nonempty box number for fractal complement, the rest notation is the same as those in Eqs. (1) and (2). Thus, the dimension of the fractal complement set is

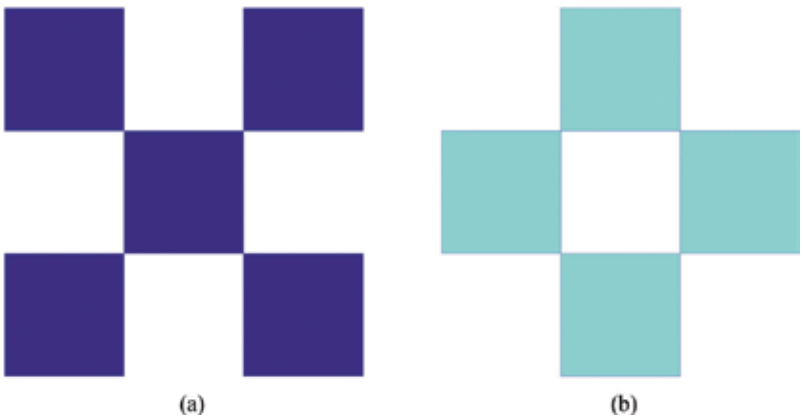

Figure 9. A schematic representation of fractal set and its complementary set (the second step). (a) Fractal set. (b) fractal complement.

$$d = -\lim_{m\to\infty}\frac{\ln C_m}{\ln L_m} = -\lim_{m\to\infty}\frac{\ln\left(r_l^{2(m-1)} - r_n^{m-1}\right)}{\ln(r_l^{1-m})} \to 2, \tag{38}$$

which is equal to the Euclidean dimension of the embedding space.

However, a fractal set and its complement are of unity of opposites. A thin fractal is characterized with the fractal parameter, and the value of a fractal dimension is determined by both the fractal set and its complement. Without fractal dimension, we will know little about a fractal; without fractal complement, a fractal will degenerate to a Euclidean geometrical object. This suggests that the fractal dimension of a fractal can be inferred by its complement by means of hierarchical scaling. For example, in fractal urban studies, an urban space includes two parts: one is fractal set and the other fractal complement. If we define a fractal city in a two-dimensional space, the form of urban growth can be represented by a built-up pattern, which comprises varied patches in a digital map. Further, if we define an urban region using a circular area or a square area, the blank space in the urban region can be treated as a fractal complement of a city. Certainly, a self-organized system such as cities in the real world is more complicated than the regular fractals in the mathematical world. The differences between fractal cities and real fractals can be reflected by the models and parameters in the computational world.

A set of exponential functions and power laws can be employed to characterize the hierarchical structure of fractal complementary sets. Suppose the number of fractal units in a generator is u, and the corresponding number of the complementary units in the generator is v. For example, for Cantor set, $u = 2$, $v = 1$ (**Figure 1**); for Koch curve, $u = 4$, $v = 1$; for Sierpinski gasket, $u = 3$, $v = 1$; for Vicsek fractal, $u = 5$, $v = 4$ (**Figure 9**); and so on. Thus, a fractal complement can be described by a pair of exponential function as below:

$$N_m = \frac{v}{u} r_n^{m-1} = v r_n^{m-2}, \tag{39}$$

$$L_m = L_1 r_l^{1-m}, \tag{40}$$

where the parameter $u = r_n$. That is, the number of fractal units in the generator is equal to the number ratio of the fractal hierarchy. Obviously, Eq. (39) is proportional to Eq. (1), while Eq. (40) is identical to Eq. (2). From Eqs. (39) and (40), it follows

$$N_m = cL_m^{-D}, \tag{41}$$

in which $c = (v/u){L_1}^D$ is the proportionality coefficient, and $D = \ln(r_n)/\ln(r_l)$ is the fractal dimension. This suggests that we can estimate the dimension value of a fractal by means of its complement. For a fractal defined in a two-dimensional embedding space, the dimension of the complementary set is $d = 2$. However, we can calculate the fractional dimension of the fractal through the scaling exponent of the complement. For instance, the exponent of the hierarchical-scaling relation between scale and number in different levels of the complement of Sierpinski gasket is $D = \ln(3)/\ln(2) = 1.585$, which is just the fractal dimension of Sierpinski gasket itself. The other fractals can be understood by analogy (**Table 4**).

Studies on fractal complement hierarchies are useful in urban and rural geography. In many cases, special land uses such as vacant land, water areas, and green belts can be attributed to a fractal complement rather than a fractal set [38]. However, this treatment is not necessary. Sometimes, we specially evaluate the fractal parameter of vacant land, water areas, green belts, and so on. In particular, the spatial state of a settlement may be reversed: the fractal structure evolves into fractal complementary structure and *vice versa*. The concepts of fractals and fractal complements can be employed to model the evolution process of a settlement. If a fractal settlement is defined in a two-dimensional space, its fractal dimension comes between 0 and 2 [2, 4, 39]. According to the spatial state and fractal dimension, the settlement evolution can be divided into four stages. The first stage is fractal growth. In this stage, the geographical space is unstinted, and settlement growth bears a large degree of freedom. Typical phenomena are the new villages and young cities. The second stage is space filling. In this stage, small fractal clusters appear in the vacant places. Typical phenomena are the mature cities, towns, and villages. The third stage is structural reverse. Settlement growth is a process of phase transition, which can be explained by space replacement dynamics. In this stage, the fractal structure of a central part in the settlement is replaced by a fractal complementary structure. The space dimension is near 2, which is a Euclidean dimension. Typical phenomena are the old cities, towns, and villages. Gradually, the central part becomes aging, degenerate, and finally has to be abandoned. Thus, the settlements become hollow cities or hollow villages, from which inhabitants move away. The fourth stage is fractal regeneration. After a period of desolation, the buffer space becomes large, and the central area is suitable for reconstruction. Thus, some people try to settle there by rebuilding houses. In this stage, the fractal structure may become more complex and should be characterized by multifractal parameters.

4.3. Logarithmic spiral and hierarchical scaling

The logarithmic spiral is also termed equiangular spiral or growth spiral, which is treated as a self-similar spiral curve in the literature and is often associated with fractal such as the Mandelbrot set. The logarithmic spiral was first described by René Descartes in 1638 and later deeply researched by Jacob Bernoulli, who was so fascinated by the *marvelous spiral* that he

Level	Cantor set			Koch curve		
	Scale (L_m)	Number (N_m)		Scale (L_m)	Number (N_m)	
		Fractal	Complement		Fractal	Complement
1	$1/3^0$	2^0	(2^{-1})	$1/3^0$	4^0	(4^{-1})
2	$1/3^1$	2^1	2^0	$1/3^1$	4^1	4^0
3	$1/3^2$	2^2	2^1	$1/3^2$	4^2	4^1
4	$1/3^3$	2^3	2^2	$1/3^3$	4^3	4^2
5	$1/3^4$	2^4	2^3	$1/3^4$	4^4	4^3
6	$1/3^5$	2^5	2^4	$1/3^5$	4^5	4^4
7	$1/3^6$	2^6	2^5	$1/3^6$	4^6	4^5
8	$1/3^7$	2^7	2^6	$1/3^7$	4^7	4^6
9	$1/3^8$	2^8	2^7	$1/3^8$	4^8	4^7
10	$1/3^9$	2^9	2^8	$1/3^9$	4^9	4^8
Level	**Sierpinski gasket**			**Vicsek snowflake**		
	Scale (L_m)	**Number (N_m)**		**Scale (L_m)**	**Number (N_m)**	
		Fractal	**Complement**		**Fractal**	**Complement**
1	$1/2^0$	3^0	(3^{-1})	$1/3^0$	5^0	(4×5^{-1})
2	$1/2^1$	3^1	3^0	$1/3^1$	5^1	4×5^0
3	$1/2^2$	3^2	3^1	$1/3^2$	5^2	4×5^1
4	$1/2^3$	3^3	3^2	$1/3^3$	5^3	4×5^2
5	$1/2^4$	3^4	3^3	$1/3^4$	5^4	4×5^3
6	$1/2^5$	3^5	3^4	$1/3^5$	5^5	4×5^4
7	$1/2^6$	3^6	3^5	$1/3^6$	5^6	4×5^5
8	$1/2^7$	3^7	3^6	$1/3^7$	5^7	4×5^6
9	$1/2^8$	3^8	3^7	$1/3^8$	5^8	4×5^7
10	$1/2^9$	3^9	3^8	$1/3^9$	5^9	4×5^8

Table 4. The relationships and differences between hierarchies of fractal sets and corresponding hierarchies of complementary sets (four typical examples).

wished it to be engraved on his tombstone. Hierarchical scaling can be employed to describe logarithmic spiral. Where geometric form is concerned, a logarithmic spiral bears an analogy with fractals, while where mathematical structure is concerned, the logarithmic spiral is similar to rank-size rule. Sometimes, the logarithmic spiral is treated as a fractal by scientists [40]. In fact, a logarithmic spiral is not a real fractal because it has only one self-similarity point. For

the section around the original point, the part of the logarithmic spiral is strictly similar to its whole. However, there is only self-similarity but there is no cross-similarity (**Figure 10**).

Though a logarithmic spiral is not a fractal, this curve bears the similar mathematical model to simple fractals. A logarithmic spiral can be expressed as below:

$$x = a^{\varphi} \sin\theta = \sin\theta e^{(\ln\alpha)\varphi} = \beta e^{\alpha\varphi}, \tag{42}$$

where x denotes the distance from the origin, ϕ is the angle from the abscissa axis, θ is a constant, and $\alpha = \ln(a)$ and $\beta = \sin(\theta)$ are two parameters. Integrating x over φ yields

$$L(\varphi) = \int_0^{m\pi} x(\varphi)\mathrm{d}\varphi = \beta\int_0^{m\pi} e^{\alpha\varphi}\mathrm{d}\varphi = \frac{\beta}{\alpha}\int_0^{m\pi} e^{\alpha\varphi}\mathrm{d}(\alpha\varphi) = \frac{\beta}{\alpha}[e^{\alpha m\pi} - 1] \to \infty, \tag{43}$$

where $L(\phi)$ refers to a cumulative length. Thus, we have

$$L_m(\varphi) = \beta\int_m^{m+1} e^{\alpha\phi}\mathrm{d}\varphi = \frac{\beta}{\alpha}[e^{\alpha\phi}]_m^{m+1} = \frac{\beta}{\alpha}(e^{\alpha} - 1)e^{\alpha m} \tag{44}$$

in which $L_m(\phi)$ denotes the length of the curve segment at the mth level. From Eqs. (42) and (44), we can derive two common ratios

$$r_l = \frac{L_{m+1}(\varphi)}{L_m(\varphi)} = e^{\alpha} \tag{45}$$

$$r_x = \frac{x_{m+1}}{x_m} = \frac{\beta e^{\alpha(m+1)}}{\beta e^{\alpha m}} = e^{\alpha}. \tag{46}$$

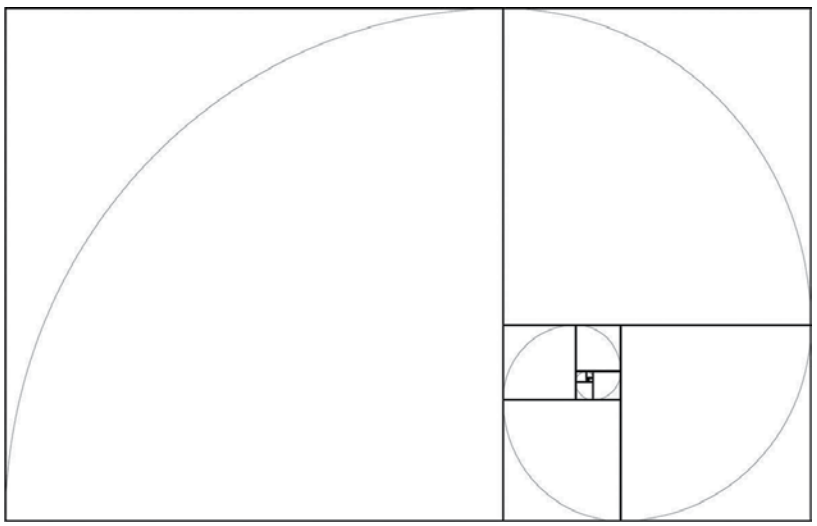

Figure 10. A sketch map of spatial hierarchy for the logarithmic spiral based on the golden rectangle. [**Note**: Using squares based on golden rectangles of different scales, we can derive a self-similar hierarchy for the logarithmic spiral, from which we can find an allometric-scaling relation.]

This suggests that the two common ratios are equal to one another, that is, $r_l = r_x$. From Eqs. (45) and (46), we can derive an allometric-scaling relation such as

$$L_m = \kappa x_m^b, \tag{47}$$

where κ refers to a proportionality coefficient, and b to the scaling exponent. The allometric-scaling relation indicates a special geometric measure relation. In fact, the allometric-scaling exponent is

$$b = \frac{\ln r_l}{\ln r_x} = \frac{\alpha}{\alpha} = 1. \tag{48}$$

This result suggests a special allometric relation between the two measurements of the logarithmic spiral. The above mathematical process shows that the logarithmic spiral as a quasi-fractal curve can be strictly described by hierarchical scaling.

In urban studies, the logarithmic spiral study is helpful for us to understand the central place theory about human settlement systems and the rank-size distribution of cities. Central place systems are composed of triangular lattice of points and regular hexagon area [9]. From the regular hexagonal networks, we can derive logarithmic spiral [41]. On the other hand, the mathematical models of hierarchical structure of the logarithmic spiral based on the systems of golden rectangles are similar to the models of urban hierarchies based on the rank-size distribution. The logarithmic spiral suggests a latent link between Zipf's law indicating hierarchical structure and Christaller's central place models indicative of both spatial and hierarchical structure. Maybe, we can find new spatial analytical approach or spatial optimization theory by exploring the hierarchical scaling in the logarithmic spiral.

5. Conclusions

The conventional mathematical modeling is based on the idea of characteristic scales. If and only if a characteristic length is found in a system, the system can be effectively described with traditional mathematical methods. However, complex systems are principally scale-free systems, and it is hard to find characteristic lengths from a complex system. Thus, mathematical modeling is often ineffectual. Fractal geometry provides a powerful tool for scaling analysis, which can be applied to exploring complexity associated with *time lag*, *spatial dimension*, and *interaction*. However, any scientific method has its limitation. Fractal description bears its sphere of application. In order to strengthen the function of fractal analysis, hierarchical-scaling theory should be developed. Fractal analytical process can be integrated into hierarchical-scaling analysis. In this work, three aspects of studies are presented. *First, hierarchical scaling is a simple approach to describing fractal structure*. Fractal scaling is used to be expressed with power laws. Based on hierarchical structure, a power law can be transformed into a pair of exponential laws, and the analytical process is significantly simplified because the spatial dimensional problems can be avoided. *Second, fractal analysis can be generalized to quasi-fractal phenomena such as logarithmic spiral*. A real fractal possesses more than one self-similarity point, while logarithmic spiral has only one self-

similarity point. Using hierarchical scaling, fractals and quasi-fractals can be modeled in its right perspective. *Third, spatial analysis can be associated with hierarchical analysis*. Spatial dimension is one of obstacles for mathematical modeling and analysis. It is more difficult to make spatial analysis than hierarchical analysis. By hierarchical scaling, a spatial network can be transformed into a hierarchy with a cascade structure, and the spatial analysis can be equivalently replaced by hierarchical analysis. According to the abovementioned ideas, we can develop an integrated theory based on fractal and hierarchical scaling to research complex systems such as cities. What is more, fractals reflect optimum structure in nature. A fractal object can occupy its space in the most efficient way. Using concepts from fractals and hierarchical scaling, we can optimize human settlement systems, including cities, towns, villages, and systems of cities and towns.

Acknowledgements

This research belongs to the Key Technology R&D Program of the National Ministry of Science and Technology of China (Grant No. 2014BAL01B02). The financial support is gratefully acknowledged.

Author details

Yanguang Chen

Address all correspondence to: chenyg@pku.edu.cn

Department of Geography, College of Urban and Environmental Sciences, Peking University, Beijing, China

References

[1] Pumain D, editor. Hierarchy in Natural and Social Sciences. Dordrecht: Springer; 2006.

[2] Batty M, Longley PA. Fractal Cities: A Geometry of Form and Function. London: Academic Press; 1994.

[3] Chen YG. Fractal Urban Systems: Scaling, Symmetry, and Spatial Complexity. Beijing: Science Press; 2008 [in Chinese].

[4] Frankhauser P. The fractal approach: A new tool for the spatial analysis of urban agglomerations. Population: An English Selection. 1998;**10**(1):205–240.

[5] Mandelbrot BB. The Fractal Geometry of Nature. New York, NY: W. H. Freeman and Company; 1983.

[6] Chen YG. Zipf's law, 1/f noise, and fractal hierarchy. Chaos, Solitons & Fractals. 2012;**45** (1):63–73.

[7] Chen YG, Zhou YX. The rank-size rule and fractal hierarchies of cities: Mathematical models and empirical analyses. Environment and Planning B: Planning and Design. 2003;**30**(6):799–818.

[8] Waldrop M. Complexity: The Emerging of Science at the Edge of Order and Chaos. NY: Simon and Schuster; 1992.

[9] Christaller W. Central Places in Southern Germany (translated by C. W. Baskin). Englewood Cliffs, NJ: Prentice Hall; 1966.

[10] Lösch A. The Economics of Location. New Haven: Yale University Press; 1954.

[11] Carroll C. National city-size distributions: What do we know after 67 years of research? Progress in Human Geography. 1982;**6**(1):1–43.

[12] Semboloni F. Hierarchy, cities size distribution and Zipf's law. The European Physical Journal B: Condensed Matter and Complex Systems. 2008;**63**(3):295–301.

[13] Arlinghaus SL. Fractals take a central place. Geografiska Annaler B. 1985;**67**(2): 83–88.

[14] Arlinghaus SL, Arlinghaus WC. The fractal theory of central place geometry: A Diophantine analysis of fractal generators for arbitrary Löschian numbers. Geographical Analysis. 1989;**21**(2):103–121.

[15] Chen YG. Fractal systems of central places based on intermittency of space-filling. Chaos, Solitons & Fractals. 2011;**44**(8):619–632.

[16] Chen YG. Multifractals of central place systems: Models, dimension spectrums, and empirical analysis. Physica A: Statistical Mechanics and its Applications. 2014;**402**:266–282.

[17] Batty M. The size, scale, and shape of cities. Science. 2008;**319**:769–771.

[18] Jiang B, Jia T. Zipf's law for all the natural cities in the United States: A geospatial perspective. International Journal of Geographical Information Science. 2011;**25**(8):1269–1281.

[19] Bak P. How Nature Works: The Science of Self-organized Criticality. New York, NY: Springer-Verlag; 1996.

[20] Gordon K. The mysteries of mass. Scientific American. 2005;**293**(1):40–46/48.

[21] Henry J. The Scientific Revolution and the Origins of Modern Science. 2nd ed. New York, NY: Palgrave; 2002.

[22] Louf R, Barthelemy M. Scaling: Lost in the smog. Environment and Planning B: Planning and Design. 2014;**41**:767–769.

[23] Stanley HE, Meakin P. Multifractal phenomena in physics and chemistry. Nature. 1988;**335**:405–409.

[24] Chen YG, Zhou YX. Multifractal measures of city-size distributions based on the three-parameter Zipf model. Chaos, Soliton & Fractals. 2004;**22**(4):793–805.

[25] Jiang B, Liu XT. Scaling of geographic space from the perspective of city and field blocks and using volunteered geographic information. International Journal of Geographical Information Science. 2012;**26**(2):215–229.

[26] Davis K. World urbanization: 1950-1970. In: Bourne IS, Simons JW, editors. Systems of Cities. New York, NY: Oxford University Press; 1978. pp. 92–100.

[27] Gleich M, Maxeiner D, Miersch M, Nicolay F. Life Counts: Cataloguing Life on Earth. Berlin: Springer; 2000.

[28] Horton RE. Erosional development of streams and their drainage basins: Hydrophysical approach to quantitative morphology. Bulletin of the Geophysical Society of America. 1945;**56**(3):275–370.

[29] Rodriguez-Iturbe I, Rinaldo A. Fractal River Basins: Chance and Self-Organization. Cambridge: Cambridge University Press; 2001.

[30] Schumm SA. Evolution of drainage systems and slopes in badlands at Perth Amboy, New Jersey. Geological Society of America Bulletin. 1956;**67**(5):597–646.

[31] Strahler AE. Hypsometric (area-altitude) analysis of erosional topography. Geological Society of American Bulletin. 1952;**63**(11):1117–1142.

[32] Gutenberg B, Richter CF. Seismicity of the Earth and Associated Phenomenon. 2nd ed. Princeton: Princeton University Press; 1954.

[33] Turcotte DL. Fractals and Chaos in Geology and Geophysics. 2nd ed. Cambridge, UK: Cambridge University Press; 1997.

[34] Chen YG. Fractals and fractal dimension of systems of blood vessels: An analogy between artery trees, river networks, and urban hierarchies. Fractal Geometry and Nonlinear Analysis in Medicine and Biology. 2015;**1**(2):26–32.

[35] Jiang ZL, He GC. Geometrical morphology of the human coronary arteries. Journal of Third Military Medical University. 1989;**11**(2):85–91 [in Chinese].

[36] Jiang ZL, He GC. Geometrical morphology of coronary arteries in dog. Chinese Journal of Anatomy. 1990;**13**(3):236–241 [in Chinese].

[37] Vicsek T. Fractal Growth Phenomena. Singapore: World Scientific Publishing; 1989.

[38] Chen YG. Exploring the fractal parameters of urban growth and form with wave-spectrum analysis. Discrete Dynamics in Nature and Society. 2010;**2010**:20, Article ID 974917.

[39] Feng J, Chen YG. Spatiotemporal evolution of urban form and land use structure in Hangzhou, China: Evidence from fractals. Environment and Planning B: Planning and Design. 2010;**37**(5):838–856.

[40] Addison PS. Fractals and Chaos: An Illustrated Course. Bristol and Philadelphia: Institute of Physics Publishing; 1997.

[41] Thompson DW. On Growth and Form. Cambridge, England: Cambridge University Press; 1966 (An abridged edition, edited by J.T. Bonner, c1961).

Chapter 8

Characterization of Cultural Traits by Means of Fractal Analysis

Sabrina Farías-Pelayo

Additional information is available at the end of the chapter

http://dx.doi.org/10.5772/67893

Abstract

Archaeology, as a science, dares to explain how extinct societies functioned. As in all sciences, knowledge is built through the classification of data. In this case, data appear as fragments of objects that human groups have left behind. Traditionally, archaeological classification systems use stylistic criteria to assign the belonging of fragments to a territory, to a moment in time, and to a culture. The underlying idea is that changes in the characteristics of objects respond to changes in cultural processes. Despite a long tradition in the analysis of archaeological material, there is still a significant subjective component in which the classification criteria should be. If the archaeologist uses one that is too broad, then fragments with very diverse characteristics can be included in the same group. Conversely, if the criterion is too narrow, fragments that are very similar to each other, but not identical, will not be considered of the same type. Conclusions that depend on the size of the tool used in the analysis do not seem to be very sound. Therefore, the limits of traditional archaeological analysis have been reached. New perspectives are required to move forward. In this chapter, it is proposed that social vestiges acquire fractal properties by the repeated iteration of culturally transmitted rules embedded in their production processes. Complex patterns emerge in a variety of cultural manifestations, but are all related to the way in which cultural practices of different groups occupy space: practices related to, for example, tool elaboration, symbolic representation or the choice of the geographic location where they settle. Fractal properties are the reflection of these cultural practices and the metrics that synthesizes the properties of each of the cultural manifestations is its fractal dimension. The fractal signature is built as a distinctive set of fractal dimensions of cultural traits of a social group. This is intended with the construction of the Xajay culture's "fractal signature." Xajay civilization flourished to the south of the northern border of Mesoamerica from around 350 AD until its collapse in 900 AD.

Keywords: cultural patterns, archaeology, fractal dimension, fractal signature, Xajay, characterization

1. Introduction

Archaeology is the science of fragments. Archaeologists excavate to obtain information from fragments of cities, buildings, tools, pottery and a great diversity of objects that when put together form complex patterns of cultural manifestations. The objective of archaeological work is the classification of the fragments to assign them to a chronological period, to a certain usage, and to a specific social group. In this process, fragments acquire meaning.

Traditional classifications are built on discrimination by region, by types of objects, of material, of forms, etc. If the groupings are meaningful, the result will be the association of the different objects to a social group and to a culture. However, in the analysis of a territory that has been occupied by different cultures and which remains fit in more than one classification, traditional methods quickly reach their limits and a different approach is necessary. The hypothesis that guides our research is that a culture can be better characterized by means of the fractal analysis of the objects it produced and has left behind for the archaeologists to find and analyze. Supporting the hypothesis is the idea that the know-how that underlies the production of every cultural manifestation is not acquired individually, but is part of a complex social transmission system. Therefore, the fabrication of the distinctive paraphernalia of a group implies the reiteration of social practices that result in patterns that can be identified by fractal analysis.

2. The elusive Xajay

Our research uses artifacts from the Xajay culture to attempt its characterization by means of fractal analysis. The Xajay culture flourished from 350 to 900 AD in a semi-desert region close to the northern border of Mesoamerica in what is now central Mexico. The most important of their ceremonial centers is Pahñu, located 180 km to the northwest of modern Mexico City. In ancient times, the Mesoamerican border divided the nomadic (barbarian, hunter and forager) groups to the north from the sedentary (civilized and agricultural) population to the south.

The frontier condition of the Xajay, as well as other of their characteristics, has challenged a precise archaeological classification of this group. At times, they have been thought of as a development associated to the northern expansion of the great city of Teotihuacan, whereas at others they were considered as isolated groups that defended the entry to the central Mexican plateau from the northern barbarians.

Among the problems that arose while trying to classify the Xajay is that their architecture has decorative elements that are like those used at the moment in Monte Albán—located almost 500 km to the southeast—, but has other elements that are similar to those used by the Aztecs more than 700 years later [1]. Another classification predicament is that the Xajay ceremonial centers are contemporary to Teotihuacan and within its potential area of control; however, the influence of the big city on their small neighbors is almost insignificant. For example, the archaeological record of Teotihuacan-controlled sites always denotes the presence of artifacts

http://dx.doi.org/10.5772/67893

knapped from green obsidian. The access to the sources of this volcanic glass was monopolized by Teotihuacan for hundreds of years [2]. In contrast, the archaeological record of the Xajay sites only yields black obsidian obtained from local sources. A final inconsistent classification topic that is worth mentioning refers to the widespread stone engraving tradition in pre-Hispanic Central Mexico. Instead, the motifs of the Xajay petroglyphs are more like those of the Bajío region, located to the west of the Xajay sites [3].

With this conflicting evidence, every attempt to classify Xajay remains with respect to a previously known culture ended in ambiguity. As more archaeological material was obtained and analyzed, the prevailing confusion only increased. Also, classifications became so detailed that they became useless.

Here is where we believe that fractal analysis can make a difference. We used fractal analysis on some elements that had been previously used to attempt the characterization of the Xajay with two basic underlying questions: how similar among themselves are the remains; and how different are these remains with respect to those of other cultures?

3. The fractal nature of archaeological objects

The first thing that had to be done was to confirm the fractal nature of archaeological objects. If the challenge was to prove the usefulness of the fractal dimension for archaeological analysis, then it was important to justify why archaeological objects have fractal properties. It makes no sense to calculate the fractal dimension of something that is not fractal.

In mathematics, fractals are complex objects that show self-similarity at all scales resulting from the repeated iteration of a simple rule. In nature, again because of the reiteration of a simple rule, certain objects show self-similarity, but only on a limited number of scales due to the limitations imposed by matter. It is said that these are statistical fractals [4]. We propose that in the cultural domain, objects acquire statistical fractal properties due to the repetition of a simple (cultural) rule. This can explain the emergence of complex patterns in cultural manifestations, in domestic aspects such as pottery, textiles, and even hair-dos, but also in more social and aggregate phenomena such as urban and settlement patterns.

This definition of a cultural fractal fits perfectly well in archaeology. The simple rules that are repeated to form cultural fractals are the traditions that are transmitted from one generation to another and manifest themselves in the specific way in which things are done within a social group. For example, these traditions have to do with the sequence and strength of gestures that result in knapping a projectile point from an obsidian core, the steps involved in engraving blocks of tuff to obtain a certain symbol or glyph, or the way in which clay is knead and shaped to form a characteristic vessel, etc. All these social practices, repeated recursively, leave traces in the archaeological record and can be subject to fractal analysis. The fractal properties of cultural manifestations are the direct consequence of cultural practices. The metric that synthesizes the properties of each of the cultural manifestations is its fractal dimension.

In brief, it can be said that the fractal dimension measures the way in which an image fills the space that contains it. In a social domain, it is straightforward to think that two cultures will use space in distinct ways; their cultural manifestations will occupy space differently. Therefore, the fractal dimension of the objects they produce can be used to identify specific cultural traits.

Then, there is the problem of how to detect the fractal nature of the objects from the images that represent them, mostly because the fractal patterns are not always visible to the naked eye.

Box-counting is the most commonly used method for calculating fractal dimension from images. Essentially, this method calculates the fractal dimension as the relation between the number of squares (boxes) needed to cover an image and the size (scale) of the squares. If this relation is stable when the size of the squares changes, then there is scale invariance, and it can be said that the image fills the space that contains it in the same manner, with independence of scale. In other words, there is also some sort of self-similarity. We can be confident then that we are in the presence of an object with fractal properties, and that it makes sense to calculate its fractal dimension.

4. Choice of tools

The first issue we had to address was the choice of a tool to calculate the fractal dimension of the archaeological images. It is amazing that despite a relatively long history of fractal analysis in archaeology[1], there is very little discussion of the results of research and even less of the methods employed. The literature we reviewed was of little help for deciding the software to use for the calculation of fractal dimension. We had access to five open-source or freely available programs[2] and to our surprise, each one gave a very different result for the fractal dimension of a same image using the same method (Box-counting).

Before going any further, it was necessary to clarify these differences and have certainty with respect to what was being calculated by each of the programs. In the end, we identified the main source of discrepancy in the way each program processed the images and converted them into binary files which are the input needed to use the box-counting method. We found other minor differences that derived from the way each program placed the grid of squares to cover the images, and from the way the size of the squares is increased in each iteration of the procedure[3]. By controlling the binary images that were used as input and by adjusting the parameters of grid placement and square size, we could obtain the same result for the fractal dimension of the same image calculated by each of the five programs.

---

[1] The earliest work that we are aware of is [12].

[2] We tested: (a) *FROG* (Fractal Researches on Geosciences) v1.0 developed by Jean-François Parrot of the Geography Institute at UNAM; (b) *Fractalyse* v2.4, developed at Université de Franche-Comté de Besançon; (c) *fractal3*, v3.4.7, developed by the National Agriculture Research Organization of Japan; (d) *HarFa*, v DEMO 5.5.30 developed at the Brno University of Technology, Czech Republic; and (e) *ImageJ* v1.46r developed by the US National Institutes of Health, and its plug-in *FracLac* v2.5, developed by A. Karperian at Charles Sturt University of Australia.

[3] For a complete description of the comparison of the five programs, see Ref. [20].

http://dx.doi.org/10.5772/67893

Having clarified the procedures of each of the programs, we decided to use *FracLac* for *Imagej* because it allowed for a finer parametrization which gives better control over the process, it calculates not only the fractal dimension but other indicators, such as lacunarity that would result useful in our analysis, and finally because it was possible to batch process large sets of images.

A crucial lesson that can be drawn from this first step of the experiment is that software should not be taken as a black-box that produces a magical number: the fractal dimension. If there is not a discussion on methods, then the results can be very interesting, but will only be relevant for isolated cases. It is important to produce results that can be comparable to others so research can build on previous works.

5. Fractal dimensions of the Xajay culture

The first issue to define is what are the traits that can be measured and allow the characterization of a culture by means of fractal analysis. Archaeological evidence suggested that at least three distinctive cultural traits of the Xajay should be used: (a) the location in a specific landscape where the group built its ceremonial centers; (b) the stone engravings that can be found throughout what has been interpreted as their sacred territory; and (c) the projectile points included in offerings as part of their funerary practices.

5.1. Location

The study of location, landscape, and territory is common in archaeological research. They are topics that have also been approached by fractal analysis. A rigorous paper on the intervention, organization, and planning of space in pre-Hispanic times is that of Oleschko et al. [5] who proposed to use fractal geometry to identify the urban master-plan of the city of Teotihuacan. In their study, they analyzed satellite imagery and aerial photography of the archaeological zone. It is worth noting that an important part of their effort was devoted to verifying the fractal nature of what was represented in the images they analyzed. In particular, they proposed that the invariant fractal dimension that was obtained from images with different scales was evidence of self-similarity. The results of their calculations for the principal buildings of Teotihuacan as well as for the archaeological site as a whole gave a fractal dimension of 1.89 with minor variations. This outcome was the same in satellite imagery as well as in aerial photographs with scales of 1:30,000 and 1:5000. With this, the authors sustain their claim that the main buildings of Teotihuacan have fractal properties. Even more, they propose that, given the visual similarity of the plan of the Ciudadela complex with the mathematical fractal known as the Sierpinski Carpet—which coincidently has a fractal dimension of 1.89—it was very possible that the urbanists and architects of Teotihuacan had in mind schemas and parameters like those that give place to the mathematical fractal.

Other examples are [6, 7] that propose a relation between the intra-site settlement pattern with kinship and between the regional distribution of sites with warfare. The argument focuses on the rank-size distribution observed in archaeological materials and in the settlement patterns to sustain their fractal properties; however, they also mention that fractal dimension

can be calculated from images. It is interesting that the authors warn explicitly that neither everything is fractal nor all dynamics are nonlinear, but that many archaeological patterns are fractal and should be described and analyzed properly.

Landscape has also been a topic in the analysis of the Xajay. The location where this group built all their ceremonial centers is peculiar. The eruption of a huge caldera about 4 million years ago formed vast tuff plains that have since suffered erosion and given place to plateaus or mesas that end abruptly on their northern side. It is precisely on the edge or these mesas that the Xajay decided to place their ceremonial centers. Because of this characteristic, the Xajay were once named the Mesas Culture [8].

We built on the assumption that if the location of the sites is peculiar, then it should have a specific fractal dimension and of course, it should be different from that of other locations. We used topography as represented by contour lines as a proxy for location to measure its fractal dimension. Contour lines are abstractions that represent points in a map with the same altitude. The more rugged the terrain, contour lines will be closer to each other and have more twists and bends: they will fill the map space in a more complete way. Consequently, it should be expected that the fractal dimension of a topographical map of a mountainous landscape should be greater than that of a flat location.

To prove this hypothesis, topographical maps were obtained for the location of the Xajay ceremonial centers and eight other archaeological sites in Mexico: Teotihuacan, Cantona, Cacaxtla, Xochicalco, Teotenango, Tula, Tenayuca, and Cerro de la Cruz. However, we were not only interested in quantifying the ruggedness of the terrain but also in sustaining that the precise location of the archaeological sites, at least for the Xajay, had a cultural meaning. Therefore, we expected that the fractal dimension of the topography of the location of the Xajay ceremonial centers would be like that of Cerro de la Cruz with whom, it is known [9], they share cultural traits—among others the placement of sites on edges of cliffs.

Contour lines were extracted from the digital elevation models provided online by the Mexican Institute of Geography (INEGI). The resolution of the digital elevation model files is 15 m per pixel and differences in altitude represented by each contour line is 10 m. The generated maps, covering approximately 10 × 15 km in a scale of 1:50,000 were stored in TIFF files of 3500 × 2480 pixels and are shown in **Table 1**.

Because different images can have very similar fractal dimensions, lacunarity was also calculated to discriminate more effectively between images. Lacunarity was proposed by Mandelbrot [10] as a complementary measure to fractal dimension. If the fractal dimension measures the way an image fills the space that contains it, lacunarity measures the holes or the lumpiness of the image, the way in which it does not fill space.

In **Figure 1**, the fractal dimensions and lacunarities of the topographical maps of the nine archaeological sites are plotted.

Even if the limited number of points in the sample do not allow for statistically significant inferences, it is relevant that the points representing the values of maps of the Xajay ceremonial centers and of Cerro de la Cruz are proximate to each other, which corresponds to what

http://dx.doi.org/10.5772/67893

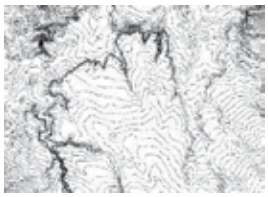 Xajay	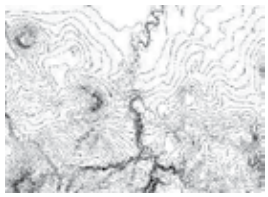 Cerro de la Cruz	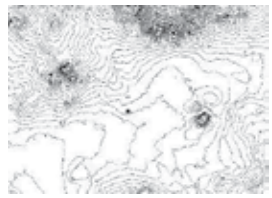 Teotihuacan
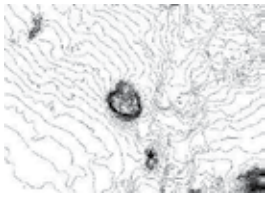 Cantona	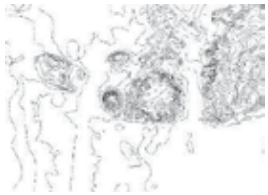 Cacaxtla	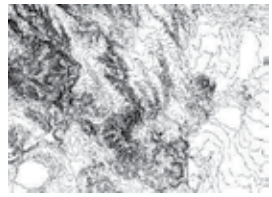 Xochicalco
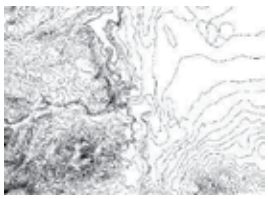 Tula	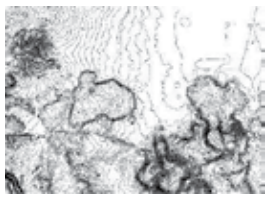 Teotenango	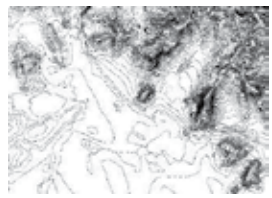 Tenayuca

Table 1. Topographical maps of archaeological sites.

was expected because of the shared cultural traits. In this case, topography has a cultural meaning. The other sites have topographies whose combination of fractal dimension and lacunarity are quite separate from the Xajay; hence, we can conclude that they do not share with them their characteristic cultural placement on the edge of cliffs.

These results confirm that the particularity of the location of the Xajay ceremonial centers is more than something perceptual: it has been measured. The placement of the sites on the edges of cliffs is now associated to specific values of fractal dimension and lacunarity of their topographies. In this way, it can be used to distinguish objectively between preferences of ancient peoples for the building of their sites.

5.2. Petroglyphs

The existence of petroglyphs in and around the ceremonial centers is another trait that has been mentioned as characteristic of the Xajay culture [8]. There are almost 200 petroglyphs registered in the five Xajay ceremonial centers[4], being Zidada the one where they have been found more abundantly. A selection of 23 images of petroglyphs from the survey records of Zidada was prepared for measuring their fractal dimension. The petroglyph motif was

[4] Apart from Pahñu, the main ceremonial center, the Xajay built Zidada, Taxangú, Cerrito, and Zethé, all of them on the northern edge of cliffs. The maximum distance between the sites (Zidada to the west and Zethé to the east) is less than 8 km.

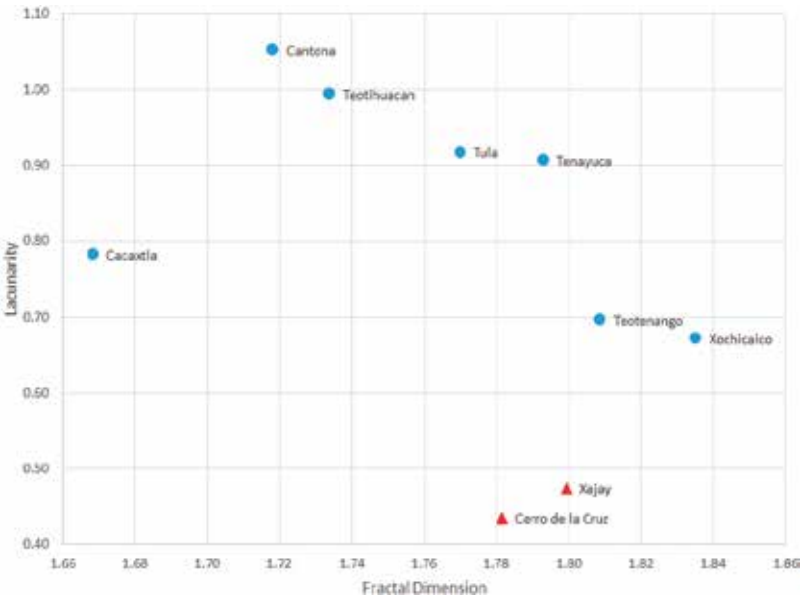

Figure 1. Fractal dimension and lacunarity of the location of archaeological sites.

retraced as a black line on the digitized original survey photographs. Then, the background photograph was erased and the file was converted to a binary format. **Table 2** illustrates this process.

The mean fractal dimension of the sample of 23 images is 1.1234 with a standard deviation of 0.0688, denoting a relatively compact grouping. This can be indicative that petroglyphs in and around the Xajay ceremonial centers are specific of this culture. The values of the fractal dimension of the Zidada petroglyphs were compared to those of three other pre-Hispanic petroglyphs from the Xajay sites of Pahñu and Taxangú and to that of a modern stone carving found near Zidada. Assuming normality in the distribution, it can be sustained that there is more than 95% probability that the pre-Hispanic petroglyphs belong to the same set as the ones from Zidada. With the same probability, we can conclude that the modern petroglyph has a motif that does not belong to the Xajay culture. Another comparison was made

Original survey photograph	Retraced motif	Binary image
		
	Zidada 11	

Table 2. Example of the extraction of petroglyph motif.

http://dx.doi.org/10.5772/67893

with two petroglyphs that functioned as astronomical markers from the site of Xihuingo [11], contemporary to Pahñu, but with a strong influence from Teotihuacan. Not surprisingly, the fractal dimension of these petroglyphs fell outside of the 95% confidence interval for the Xajay motifs.

These results support and give a numerical expression to the idea that the Xajay elaborated a specific type of petroglyphs in association with their ceremonial sites. Xajay petroglyphs are similar and this is one of their characteristic cultural traits.

5.3. Projectile points

Orton and Grace, two British archaeologists, made team with two computer specialists and conducted a pioneer research on the fractal properties of archaeological lithic material [12]. The authors confirmed their intuition that the fractal dimension would change depending on the different erosive processes that affected flint flakes, but could not meet their objective of determining the use that had been given to the artifacts by the differences in the fractal dimension of the images of microware types. Nonetheless, they set the ground for further research based on fractal analysis in archaeology.

During excavations at the Xajay site of Pahñu, a significant quantity of archaeological material was recovered. Of special interest was the material of an offering placed in a cache under the northwest corner of the main pyramid around 500 AD. Among the findings, archaeologist recovered a great diversity of projectile points, of different forms and made of different materials. These points were used to explore if, despite the diversity, some specific Xajay trait could be revealed through the fractal analysis of their images.

As with the petroglyphs, the images of the points had to be prepared for their processing. The silhouette or edge of the images of the dorsal side of 54 projectile points were extracted from the original digitized photographs and saved in a binary format. **Table 3** illustrates the process.

Fractal dimension and lacunarity were calculated for the 54 images of projectile points. In both calculations, the dispersion of values is relatively small, which can indicate a clustering of the points in terms of these characteristics.

Plotting fractal dimension against lacunarity of the images reveals what could be two groups within the Xajay projectile points. A first group formed by the points whose image has a fractal dimension less than 1.09, and the second group has fractal dimensions greater than this value.

To find an explanation for this segmentation, the data were compared to the information contained in the lithic database of the excavation project. The grouping of the data could be explained by differences in the material out of which the points were knapped. The points with a fractal dimension less than 1.09 were made from obsidian with two exceptions. The only point made from basalt belongs to this group, and there is one made from flint that requires a more detailed analysis to determine why it has such a low fractal dimension compared to the other flint points. The second group of points with a fractal dimension greater

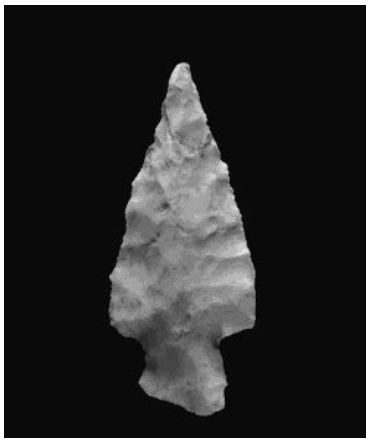

Original image

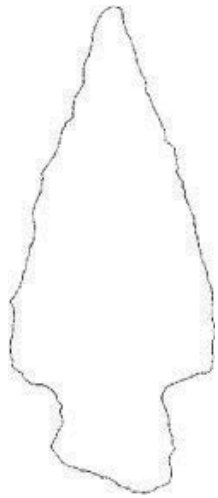

Binary image

Table 3. Example of the extraction of the silhouette of a point.

than 1.09 comprises 20 points made from flint, 5 from chalcedony, 1 from calcite, 1 from rhyolite, and 1 from obsidian. **Figure 2** shows the segmentation of the points with respect to their knapping material.

The mean fractal dimensions of these two groups of points resulted different with a confidence interval of more than 99%. Also, and this is not clearly visible to the naked eye, the mean lacunarity of the two groups is likewise different. It follows that, as a complementary measure, lacunarity is also useful to distinguish between these two groups[5].

This result could lead us to think that fractal dimensions and lacunarity are simply distinguishing some physical attributes of the raw material, and not a cultural practice, which, in the last instance, is the relevant criterion to characterize a human group. However, if the physical properties are explaining the clustering of fractal dimensions and lacunarities, then as many groups as different raw materials would be discernible, and this is not the case.

To further explore if the segmentation of fractal dimensions was due to the physical properties of the raw material, the Xajay collection was compared to the images of other points obtained from the Internet. The criteria for selecting the points were that they should not be very different in form than the Xajay so the differences could not be explained by this reason. For contrasting, four very distinct Clovis points were also chosen, which in principle should have a very different fractal dimension than the Xajay points. Most of the images were taken from the online catalogue of the American Southwest Virtual Museum [13]. The comparative set of images was composed of 15 points from Arizona, of which 2 were obsidian, 4 Clovis

[5] The value of Student's *t*-statistic for the independent sample equality of means test for fractal dimensions was 11.093, with 52 degrees of freedom. The two-tailed confidence interval is greater than 99%. For lacunarities, Student's *t*-statistic was 5.320 with the same degrees of freedom and confidence interval as for fractal dimensions.

http://dx.doi.org/10.5772/67893

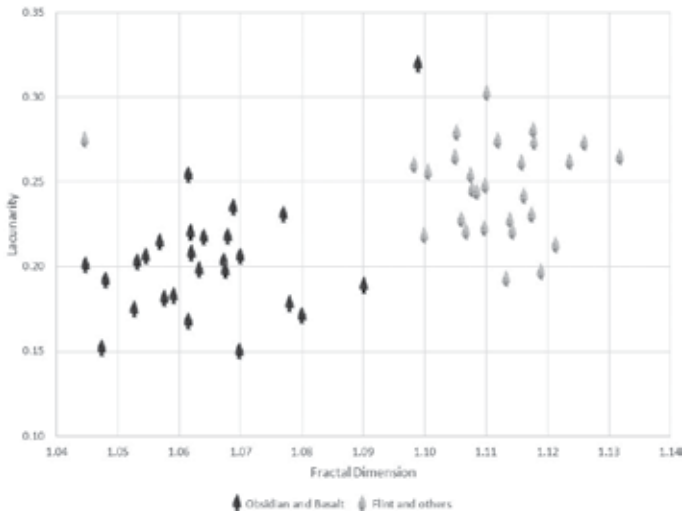

Figure 2. Fractal dimension and lacunarity of Xajay projectile points.

points from several locations in the United States, 1 point from Kansas, and 1 obsidian point from an unknown provenance in the southwest of the United States. An obsidian point from Teotihuacan and a flint point from Belize were also included in this set. **Figure 3** plots the fractal dimension and lacunarity of the ensemble of points.

The first thing that is worth noting is that the four Clovis points clearly form a distinct group with the lowest fractal dimensions of all. The number of observations is very small, and statistically significant inferences cannot be made, but once again, the potential of fractal

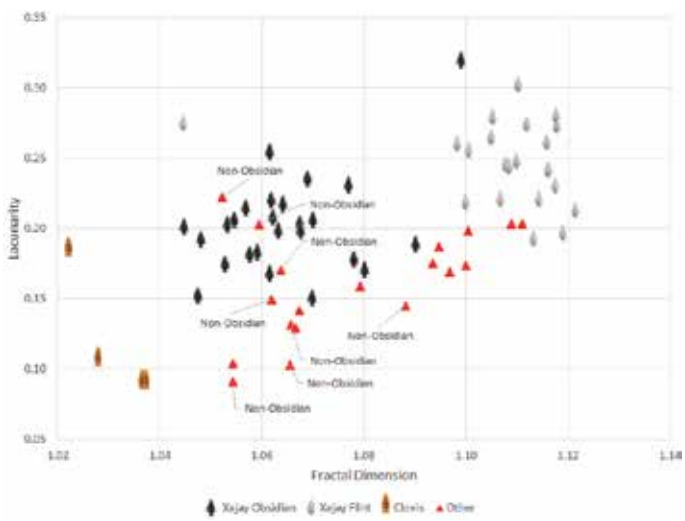

Figure 3. Fractal dimension and lacunarity of projectile points.

dimensions to distinguish among groups of objects is manifest. The Clovis points are visibly not made from obsidian but probably from a sedimentary material. The fact that their fractal dimensions are smaller than those calculated for the Xajay points in general and much smaller than those of the points made from sedimentary material gives some weight to the argument that the fractal dimension is not measuring the physical attributes of the artifacts.

As for the set of points from the American Southwest and the other isolated points, the fractal dimensions of those knapped from obsidian are all in the range of the Xajay points made from that material. Also, fractal dimensions of the points made from other material are distributed in the whole range of values of the Xajay points, independently of the raw material used in their manufacture. Once again, there is an indication that fractal dimensions are measuring something more than the simple attributes of raw materials.

Even if the differences in fractal dimensions were related to the raw material, it could be argued that it is due to the precise gestures involved in working with them, and this is cultural. Artifacts are manufactured from each raw material through a carefully thought out sequence of interrelated actions. The knowledge behind this sequence is transmitted within each human group.

6. The fractal signature

Up to this point of the research, we have obtained a handful of fractal dimensions, each one of them saying something with respect to a trait of the Xajay culture. The next step was to integrate them into a more synthetic measure that could represent the ensemble of the Xajay culture. A characteristic required of this synthetic measure was that it distinguishes the Xajay from any culture with whom it was compared. The fractal signature is a measure that complies with this condition.

Given the ambiguity with which the concepts of fractal dimension and fractal signature are used in literature, their distinction is worth a brief discussion. The lack of precision in the use of these terms is not exclusive of fractal archaeological research. At times, the distinction is solved by choosing one, or the other, or simply by making them interchangeable. See, for example, Refs. [14, 15].

It is amazing that the most precise definitions of fractal signature occur in the extremes of the observation spectrum. At a macro level, in astronomy, near galaxies are distinguished by the fractal dimension of their images at different resolutions [16]. With a method, similar to box-counting, the area of a galaxy in an image is calculated by counting the non-black pixels. The authors observed that the area of the galaxies change when the resolution of the image changes. For them, the fractal signature is the relation between the area of a galaxy calculated from different images and the resolution of the images.

In the opposite extreme of the spectrum, there are several medical science papers that use the fractal signature for the analysis of the microscopic structure of bone tissue to detect anomalies. The definition used in some of these papers is like the one used in the study of galaxies.

http://dx.doi.org/10.5772/67893

The fractal signature is the variability of fractal dimension calculated from images with a different resolution: "a fractal signature […] is simply the estimated fractal dimension as a function of scale" [17].

The problem faced by astronomers and physicians is that the fractal dimension of objects represented in the images they were using (galaxies or microscopic structure of tissue) varied as a function of the resolution of the image. In other words, the fractal dimension of an object changed depending on the "magnification" with which the image had been captured. There was thus a need for a method permitting their comparison, independently of the capture conditions.

The above-mentioned works are based on the study of Peleg et al. [18], who used mathematical morphology procedures to solve a general problem arising from the characterization of textures. The sharpness of digital images changes with their resolution, which in principle conflicts with the properties of fractal objects that should be self-similar independently of scale. The fractal signature was defined to measure the degree of detail or sharpness that is lost when the resolution of the image is reduced. "The magnitude of the fractal signature $S(\varepsilon)$ relates to the amount of detail that is lost when the size of the measuring yardstick passes ε." [18] Note that ε refers to the measurement scale or to the resolution of the image. Another way of understanding this would be that the fractal signature measures the change in the fractal dimension of objects calculated from images that represent different "levels of observation."

The usefulness of fractal signatures in research that propose to measure the detail of "texture" of tissues or galaxies from microscopic or telescopic observations is clear. In social sciences, and particularly in the research that we present, the analysis of "texture" of cultural remains is not only done through successive magnifications, but the different "levels of observation" imply seeing the archaeological context from diverse domains, opening the field of vision toward object of varied nature.

We propose that the concept of fractal signature in archaeology can be recovered if it is considered as the measure of change in fractal dimension of the different aspects of material culture. In this case, fractal dimension would not change only because of the resolution of images of a single object, but because the observations would include distinct aspects of culture. The fractal signature would not be a single number, but a set of numbers each one measuring the fractal dimension of a particularity of the archaeological context. Under the hypothesis that archaeological objects have fractal properties due to the repeated iteration of cultural rules, it is reasonable to assume that those that govern the fabrication of pottery are different than those applied to architecture and urbanism, and also different than those present in sculpture, stone engraving or any other activity that leaves traces in the archaeological context. Therefore, each aspect or element of a social group has a specific fractal dimension, and the ensemble of these dimensions is what constitutes their fractal signature.

The obvious question that arises is how many aspects of a culture should be observed to have an adequate characterization. In other words, how many elements should be measured to have an effective fractal signature. Fractal dimension can be used to measure

as many aspects of a culture as is required to build a fractal signature that characterizes adequately a human group. In principle, the inclusion of additional traits would be never ending; the number of dimensions of the cultural space would increase incessantly. Nonetheless, the same result should be expected: each group will have a unique location in that space. The way this is understood is related to the way in which groups, societies or cultures are looked at. Each one has endless components, their difference is not in the similarity or lack of the components, but in the way in which these interact and combine. In other words, what is important is to understand how the components form a dynamic system with transformation rules of its own. Considering this, we propose that the fractal signature is the representation of the systemic dynamics of the group in the *n*-dimensional space of culture.

In what follows we will present some ideas of how a prototype of the Xajay fractal signature could begin to be assembled from the set of fractal dimensions of the attributes that were measured. To facilitate presentation, the fractal signature will consider only the mean fractal dimensions of the topography of the placement of the sites, of the petroglyph motifs and of the silhouettes of the projectile points, as shown in **Table 4**.

Likewise, it can be represented in a vector notation in the three-dimensional cultural space defined by topography × petroglyphs × points.

$$\overrightarrow{\text{XajayFS}} = [\,1.7973,\quad 1.1243,\quad 1.0882\,] \tag{1}$$

This combination of fractal dimensions occupies a unique position in this space and is therefore proposed that the fractal signature expressed in this manner is a measurement of the specificity of the Xajay.

The usefulness of the fractal signature to make distinctions between groups would be given by the fact that the measurements of the attributes of the distinct groups would occupy different positions in this space.

To illustrate this, fractal dimensions of the three domains that form the prototypical cultural space were obtained for Teotihuacan and Cantona, enabling the comparison with the Xajay. This is presented in **Table 5**.

A graphical representation of these fractal signatures in the three-dimensional cultural space is shown in **Figure 4**.

The graph clearly shows how each cultural group occupies a unique position in the space determined by the fractal dimensions of their attributes.

Topography	Petroglyphs	Projectile points
1.7973	1.1243	1.0882

Table 4. Prototype of the Xajay fractal signature.

http://dx.doi.org/10.5772/67893

	Topography	Petroglyphs	Projectile points
Xajay	1.7973	1.1243	1.0882
Teotihuacan	1.7339	1.5067	1.0535
Cantona	1.7181	1.1819	1.0402

Table 5. Three attribute fractal signature of the Xajay, Teotihuacan, and Cantona.

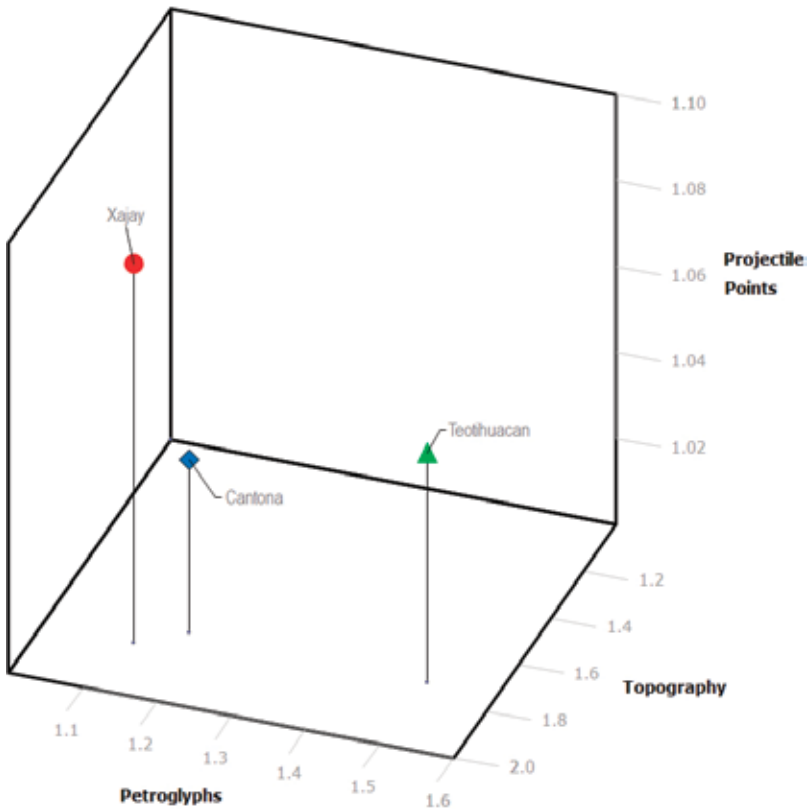

Figure 4. Fractal signature of the Xajay, Teotihuacan, and Cantona.

7. Conclusions

The driving purpose of our research was to assign quantitative measures to the classifications made by archaeologists in their day-to-day work. Classification of objects and cultural traits are made from the knowledge and experience acquired through research and are always biased in some way and have a certain dose of ambiguity. It is not our intention to demerit archaeologists. Their work has achieved the non-easy task of giving form to the history of social transformations. Moreover, when societies under study do not leave written records, research becomes even harder and the only thing archaeologists can get a grasp on to reconstruct history from are fragments of

objects. With these fragments, the functioning of societies and the relations between its elements have to be recreated. To reduce subjectiveness in archaeological work, we have proposed a model to characterize different cultures by means of their fractal dimensions. The bet is that, independently of how many elements (fractal dimensions) are considered, there will never be two groups that occupy the same location in the *n*-dimensional space of culture, given that each point in this space (each fractal signature) is the representation of one and only one social group.

Characterization of social groups by means of fractal analysis opens the door to a great variety of future research. For example, the configuration of the territory occupied in pre-Hispanic times can be represented by a cloud of points in cultural space, each one associated to a social group. The points of this cloud could get closer or move away from each other, giving place in certain moments to clusters of cultural significance. One of these clusters is probably Mesoamerica.

Another line of research, maybe much more ambitious, is related to the discovery of the "generators" of the fractal properties of cultural objects, namely the simple rules whose repetition produces fractal patterns. These are the lines developed in Ron Eglash's classic work on African fractals [19]. In this chapter, we have shown the potential of the fractal signature to characterize the Xajay from the fractal properties of different aspects of their culture, but there was no attempt to discover the cultural rules that produced them. If such rules could be determined, if their repetition could be identified as processes, an important step would be taken in the understanding of the interactions of the different components of the Xajay material culture.

Author details

Sabrina Farías-Pelayo

Address all correspondence to: sabrinafariasp@gmail.com

National School of Anthropology and History, Mexico City, Mexico

References

[1] Sandoval G. Un espacio autosimilar. El altépetl, el centro ceremonial y la ofrenda [Tesis de Licenciatura en Arqueología]. Mexico: Escuela Nacional de Antropología e Historia; 2009.

[2] Pastrana A., Domínguez S. Cambios en la estrategia de la explotación de la obsidiana de Pachuca: Teotihuacan, Tula y la triple alianza. Ancient Mesoamerica. 2009;**20–1**:129–148.

[3] Viramontes CA. La pintura rupestre como indicador territorial. Nómadas y sedentarios en la marca fronteriza del río San Juan, Querétaro. In: Viramontes Anzures C. and Crespo Oviedo A. M., editors. Expresión y memoria. Pintura rupestre y petrograbado en las sociedades del norte de México. Mexico: INAH; 1999.

[4] Mandelbrot B. How long is the coast of Britain? Statistical self-similarity and fractional dimension. Science. 1967;**156**(3775):636–638.

[5] Oleschko K, Brambila R., Brambila F, Parrot J-F, López P. Fractal analysis of teotihuacan, Mexico. Journal of Archaeological Science. 2000;**27**:1007–1016.

[6] Brown CT, Witschey WR. The fractal geometry of ancient Maya settlement. Journal of Archaeological Science. 2003;**30**:1619–1632.

[7] Brown CT, Witschey WR, Leibovitch LS. The broken past: Fractals in archaeology. Journal of Archaeological Method and Theory. 2005;**12**(1):37–78.

[8] J. Cedeño Nicolás. Cosmología y arquitectura. El caso de la Cultura de las Mesas. Dimensión Antropológica. 1998;**12**:7–48.

[9] Farías PMS. Identificación de la cultura de las mesas o Xajay [Tesis de Maestría en Arqueología]. Mexico: Escuela Nacional de Antropología e Historia; 2010.

[10] Mandelbrot B. The Fractal Geometry of Nature (Updated and augmented edition). New York: W.H. Freeman and Company; 1983.

[11] Galindo TJ, Wallrath BM, Rangel RA. Marcadores punteados como manifestación de la ideología teotihuacana respecto al cielo: el caso de Xihuingo. In Ideología y política a través de materiales, imágenes y símbolos. Memoria de la Primera Mesa Redonda de Teotihuacan. México: UNAM-INAH; 2002. pp. 255–271.

[12] Rees D, Wilkinson G, Orton C, Grace R. Fractal analysis of digital images of flint microwear. In: Rahtz S., editor. Computer and Quantitative Methods in Archaeology. Oxford: BAR; 1988. pp. 177–183.

[13] American Southwest Virtual Museum [Internet]. Available from: http://swvirtualmuseum.nau.edu/wp/index.php/artifacts/projectile-points/ [Accessed July 24, 2015].

[14] Malamou A, Pandis C, Frangos P, Stefaneas P, Karakasiliotis A, Kodokostas D. Application of the modified fractal signature method for terrain classification from synthetic aperture radar images. Elektronika ir Elektrotechnika. 2014;**20**(6):118–121.

[15] Lara GAP. Las firmas fractales en las manifestaciones rupestres de Valle del Mezquital, Hidalgo, México [Tesis Doctorado en Arqueología]. Mexico: Escuela Nacional de Antro pología e Historia; 2014.

[16] Lekshmi S, Revathy K, Prabhakaran NS. Galaxy classification using fractal signature. Astronomy & Astrophysics. 2003;**405**:1163–1167.

[17] Lynch J, Hawkes D, Buckland-Wright J. Analysis of texture in macroradiographs of osteoarthritic knees using the fractal signature. Physics in Medicine and Biology. 1991;**36** (6):709–722.

[18] Peleg S, Naor J, Hartley R, Avnir D. Multiple resolution texture analysis and classification. IEEE Transactions on Pattern Analysis and Machine Intelligence. 1984;**PAMI-6** (4):518–523.

[19] Eglash R. African Fractals: Modern Computing and Indigenous Design. New Brunswick: Rutgers University Press; 1999.

[20] Farías PS. La cultura Xajay. Los otomíes al sur de la frontera norte de Mesoamérica [Tesis de Doctorado], Mexico: Escuela Nacional de Antropología e Historia; 2015.

Section 3

Fractal Graphs and Correlation

Chapter 9

On Self-Affine and Self-Similar Graphs of Fractal Interpolation Functions Generated from Iterated Function Systems

Sean Dillon and Vasileios Drakopoulos

Additional information is available at the end of the chapter

http://dx.doi.org/10.5772/intechopen.68499

Abstract

This chapter provides a brief and coarse discussion on the theory of fractal interpolation functions and their recent developments including some of the research made by the authors. It focuses on fractal interpolation as well as on recurrent fractal interpolation in one and two dimensions. The resulting self-affine or self-similar graphs, which usually have non-integral dimension, were generated through a family of (discrete) dynamic systems, the iterated function system, by using affine transformations. Specifically, the fractal interpolation surfaces presented here were constructed over triangular as well as over polygonal lattices with triangular subdomains. A further purpose of this chapter is the exploration of the existent breakthroughs and their application to a flexible and integrated software that constructs and visualises the above-mentioned models. We intent to supply both a panoramic view of interpolating functions and a useful source of links to assist a novice as well as an expert in fractals. The ideas or findings contained in this paper are not claimed to be exhaustive, but are intended to be read before, or in parallel with, technical papers available in the literature on this subject.

Keywords: approximation, attractor, fractal, interpolating function, iterated function system, recurrent, self-affinity, self-similarity, surface construction

1. Introduction

In the mathematical field of numerical analysis, *interpolation* is a method of constructing new data points within the range of a discrete set of known data points. Interpolation by fractal (graph of) functions, as defined in Refs. [1, 2], is based on the theory of *iterated function systems*

and can be seen as an alternative to traditional interpolation techniques, aiming mainly at data which present detail at different scales, some degree of self-similarity or self-affinity. A *fractal interpolation function* can be seen as a continuous function whose graph is the attractor of an appropriately chosen iterated function system. This attractor is called a *fractal interpolation surface*, since the graph of a continuous function of two variables defined over a connected open subset of $\mathbb{R}^2$ is a *topological surface*, if the so formed graph belongs to the three-dimensional space and has *Hausdorff-Besicovitch dimension* between 2 and 3. It is called a *fractal interpolation volume* whenever the graph has dimension greater than three. The key difficulty in constructing fractal interpolation surfaces (or volumes) involves ensuring continuity. Another important element necessary in modelling complicated surfaces of this type is the existence of the *contractivity*, or *vertical scaling*, *factors*.

1.1. Historical background

Massopust introduced in Ref. [3] fractal surfaces constructed as attractors of iterated function systems. He considered the case of a triangular domain with coplanar boundary data. Later on, Geronimo and Hardin in Ref. [4] presented a slightly more general construction of such fractal surfaces. They examined the case when the domain is a polygonal region with arbitrary interpolation points but with identical contractivity factors. In Ref. [5], $\mathbb{R}^m$-valued multivariate fractal functions were investigated. The latter two constructions use the *recurrent* iterated-function-system formalism. The construction of Wittenbrink [6] either produces discontinuous surfaces (and volumes) or reduces to the case, where the contractivity factors must be constant. Zhao [7] allows the contractivity factors to become a continuous 'contraction function' and uses consistent triangulation in order to guarantee continuity. All of the previous constructions are based on triangular subdomains. As it is always possible to construct fractal surfaces as tensor products of univariate continuous fractal functions, Massopust in Ref. [8], Section 9.4 suggests a construction by taking the tensor product of two univariate fractal interpolation functions. The derived function is uniquely determined by its evaluation along a pair of adjacent sides of the rectangular domain.

Two piecewise self-affine models for representing discrete image data on rectangular lattices by using fractal surfaces are proposed in Ref. [9]. In Ref. [10], the piecewise self-affine IFS model is extended from $\mathbb{R}^3$ to $\mathbb{R}^n$ (n is an integer greater than 3), which is called the *multi-dimensional piecewise self-affine fractal interpolation model*. The same methodology is repeated in Ref. [11]. According to Ref. [12], the self-affine iterated function system model is extended from $\mathbb{R}^3$ to $\mathbb{R}^n$ (n is an integer greater than 3), which is called the *multi-dimensional self-affine fractal interpolation model*. Vijender and Chand in Ref. [13] proposed a class of affine fractal interpolation surfaces that stitch a given set of surface data arranged on a rectangular grid. The created fractal interpolation surfaces are a blend of the affine fractal interpolation functions constructed along the grid lines of a given interpolation domain.

The study of fractals is a field in science that unifies mathematics, theoretical physics, art and computer science. Therefore, it is not difficult to find applications of fractal interpolation functions in almost every scientific field wherein information available in finite number of grid points has to be modelled with a continuous function. Applications of this theory include

http://dx.doi.org/10.5772/intechopen.68499

geometric design, data visualisation, reverse engineering, physics, geology, image encoding and compression (see Ref. [14]), signal processing and wavelet theory. Fractal interpolation also provides a good representation of economic time series such as the stock market fluctuation and weather data. The reason for this variety of applications lies in the underlying complicated mathematical structure of fractal (graph of) functions, produced with simple recursive construction. It has been noted that, for certain problems, they provide better approximants than their classical non-recursive counterparts.

1.2. Clarifications and interpretations

Although, in most of the cases, the words *function*, *map* and *mapping* can be used as nouns interchangeably in several parts of mathematics, they generally do not have the same meaning. Originally, the word 'map' comes from the medieval Latin *Mappa mundi*, wherein *mappa* meant napkin or cloth and *mundi* the world. 'Mapping' as a noun is the process of making maps. In mathematics, we think of a *map* as a way of sending elements from one set to elements of another set. A *mapping* shows how the elements are paired. A *function* is a way or rule of associating elements from one set, the *domain*, to elements of another set, the *codomain*. So, a domain is where a function maps from, and a *range*, as a subset of the codomain, is where it maps to. The definition of a *function* requires that each element in the domain corresponds to one and only one element of the codomain. Moreover, a function is commonly used as a special type of mapping, namely it is used as a mapping from a set into the set of numbers, that is, into $\mathbb{R}$, or $\mathbb{C}$ or into a field $\mathbb{K}$. So, a map is slightly more general, as it allows a many-to-one situation, arbitrary sets, etc. For example, we refer to 'The open mapping theorem' and not to the 'The open function theorem', and we refer to 'The contraction mapping theorem' and so on. A mapping of a set into itself is called a *transformation*.

An *affine map* (from the Latin, *affinis*, "connected with") between two (vector) spaces consists of a *linear map* followed by a translation. Similarly, one can define an *affine transformation*. In a geometric setting, these are precisely the functions that map straight lines to straight lines. Be aware that the term *linear function* refers to two distinct but related notions. It may be a linear map or a polynomial of degree one or less, including the zero polynomial, because its graph, when there is only one independent variable, is a non-vertical straight line.

Another common error involves the incorrect use of the notions 'self-affine function' and 'self-similar function'. There is no 'self-affine' or 'self-similar' function but a function with a self-affine or self-similar graph. Therefore, an object or a set, but not a function, can be self-affine or self-similar. Each part of a *self-affine* object is an image of the whole object (either strictly or in a statistical sense) scaled differently in different directions. Self-affine sets form an important class of sets, which include self-similar sets as a particular case. A *self-similar* object is exactly or approximately similar to a part of itself (i.e. the whole has the same shape as one or more of the parts).

The aim of our paper is to review the usage of fractal interpolation functions in order to construct self-affine graphs generated by iterated function systems. Furthermore, we compare and contrast several constructions presented in Refs. [3–8] by pointing out some of their ambiguities, limitations and restrictions. Particularly, in Section 2, we briefly review the theory

of iterated function systems. In Section 3, we revisit the 1D fractal interpolation theory and state the prerequisites of the constructions. Necessary conditions for the attractor of an iterated function system to be the graph of a continuous function interpolating a given set of data are also given. In Section 4, we revisit the two-dimensional fractal interpolation theory. A comparison to existing methods and some examples of fractal interpolation surfaces constructed by them are also presented. The corresponding algorithms for constructing these surfaces are developed and illustrated through several graphic examples. Finally, Section 5 summarises our conclusions and points out areas of future work.

2. Fractal image generation

In mathematics, an *iterated map* is a map composed with itself, possibly *ad infinitum*, in a process called iteration. *Iteration* means the act of repeating a process with the aim of approaching a desired goal, target or result. More formally, let X be a set and $f\colon X\to X$ be a map. Define f^k as the k-th iterate of f, where k is a non-negative integer, by $f^0 = \mathrm{id}_X$ and $f^{k+1} = f \circ f^k$, where id_X is the identity map on X and $f \circ g$ denotes map composition.

A *contraction mapping*, or *contraction*, on a metric space (X, ρ) is a function f from X to itself, that is, a *transformation*, with the property that there is a non-negative real number $s < 1$ such that for all x and y in X, $\rho(f(x), f(y)) \le s{\cdot}\rho(x, y)$, where ρ is a *distance function* between elements of X. The smallest such value of s is called the *Lipschitz constant* or *contractivity factor* of f. If the above condition is satisfied for $s \le 1$, then the mapping is said to be *non-expansive*. A contraction mapping has at most one *fixed point*, that is, a point x^* in X such that $f(x^*) = x^*$. Moreover, the *Banach fixed point theorem*, also known as the *contraction mapping theorem* or *contraction mapping principle*, states that every contraction mapping on a non-empty, complete metric space has a unique fixed point, and that for any x in X the iterated function sequence x, $f(x)$, $f(f(x))$, $f(f(f(x)))$, … converges to this fixed point. Furthermore, this fixed point can be found as follows: Start with an arbitrary element x_0 in X and define an iterative sequence by $x_n = f(x_{n-1})$ for $n = 1, 2, 3, \ldots$. This sequence converges and its limit is x^*.

2.1. Iterated function systems

An *iterated function system*, or *IFS* for short, is defined as a collection of a complete metric space (X, ρ), for example, $(\mathbb{R}^n, \|\cdot\|)$ or a subset, together with a finite set of continuous transformations $\{w_i\colon X\to X,\ i = 1, 2, \ldots, M\}$. It is often convenient to write an IFS formally as $\{X; w_1, w_2, \ldots, w_M\}$ or, somewhat more briefly, as $\{X; w_{1-M}\}$. If w_i are contractions with respective contractivity factors s_i, $i = 1, 2, \ldots, M$, the IFS is termed *hyperbolic*.

Hutchinson in Ref. [15] showed that, for the metric space $\mathbb{R}^n$, such a (hyperbolic) system of functions has a unique *compact* (closed and bounded) *fixed set* S. One way for constructing a fixed set is to start with an initial point or set S_0 and iterate the actions of the w_i, taking S_{n+1} to be the union of the image of S_n under the w_i; then taking S to be the closure of the union of the S_n. Symbolically, the unique fixed (non-empty compact) set $S \subset \mathbb{R}$ has the property

http://dx.doi.org/10.5772/intechopen.68499

$$S = \bigcup_{i=1}^{M} w_i(S). \tag{1}$$

The set S is thus the fixed set of the *Hutchinson operator*

$$H(A) = \bigcup_{i=1}^{M} w_i(A),$$

where A is any subset of $\mathbb{R}^n$. The operator H itself is a contraction with contractivity factor $s = \max\{s_1, s_2, \ldots, s_M\}$ (Ref. [2], Theorem 7.1, p. 81 or Ref. [16]). The existence and uniqueness of S, which is called the *attractor*, or *invariant set*, of the IFS, are a consequence of the contraction mapping principle as is the fact that $\lim_{k\to\infty} H^k(A) = S \equiv \mathcal{A}_\infty$ for all A in $\mathcal{H}(\mathbb{R}^n)$, where $\mathcal{H}(X)$ is the metric space of all non-empty, compact subsets of X with respect to some metric, for example, the *Hausdorff metric*. The operator H is also called the *collage map* to alert us to the fact that $H(A)$ is formed as a union or 'collage' of sets. If X is a Euclidean space and the w_i are *similitudes*, that is, *similarity transformations*, then the attractor is called a *self-similar set*. These sets are usually fractals.

A fractal derived by an IFS is made up of the union of several copies of itself, each copy being transformed by a function (hence 'function system'). A canonical example is the Sierpiński gasket; see **Figure 1**. The functions are normally contractions which means they bring points closer together and make shapes smaller. Hence, such a shape is made up of several possibly overlapping smaller copies of itself, each of which is also made up of copies of itself, ad infinitum. This is the source of its self-similar nature. Note that this infinite process is not dependent upon the starting shape being a triangle—it is just clearer that way. The first few steps starting, for example, from a square also tend towards a Sierpiński gasket; see **Figure 2**.

Sometimes each function w_i is required to be a linear, or more generally an affine transformation, and hence represented by a matrix. Formally, a transformation w is *affine*, if it may be represented by a matrix $\mathbf{A}$ and translation $\mathbf{t}$ as $w(\mathbf{x}) = \mathbf{A}\mathbf{x} + \mathbf{t}$, or, if $X = \mathbb{R}^2$,

$$w\begin{pmatrix} x \\ y \end{pmatrix} = \begin{pmatrix} a & b \\ c & s \end{pmatrix}\begin{pmatrix} x \\ y \end{pmatrix} + \begin{pmatrix} d \\ e \end{pmatrix}. \tag{2}$$

The *code* of w is the 6-tuple (a, b, c, s, d, e) and the *code of an IFS* is a table whose rows are the codes of $w_1, w_2, \ldots, w_M$. For the three-dimensional case, this becomes

Figure 1. The evolution of the Sierpiński gasket.

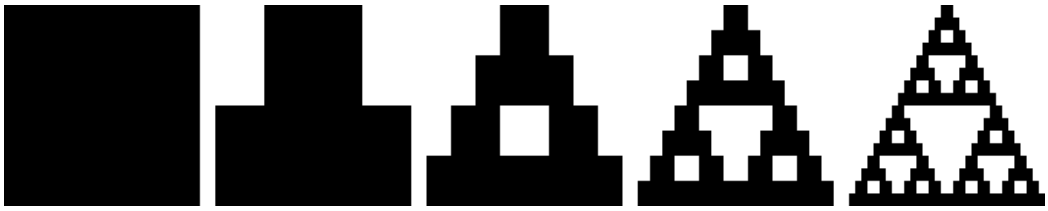

Figure 2. Iterating from a square.

$$w\begin{pmatrix} x \\ y \\ z \end{pmatrix} = \begin{pmatrix} a & b & c \\ d & e & g \\ h & k & s \end{pmatrix} \begin{pmatrix} x \\ y \\ z \end{pmatrix} + \begin{pmatrix} l \\ m \\ r \end{pmatrix}. \tag{3}$$

However, IFS's may also be built from non-linear functions, including *projections* and *Möbius transformations*.

2.2. Recurrent iterated function systems

An *IFS with probabilities*, written formally as $\{X; w_1, w_2, \ldots, w_M; p_1, p_2, \ldots, p_M\}$ or, somewhat more briefly, as $\{X; w_{1-M}; p_{1-M}\}$, gives to each transformation in H a probability or weight. If the weights of transformations differ, so do the measures on different parts of the attractor. A non-self-similar attractor, however, is more easily represented with a *recurrent iterated function system*, or *RIFS* for short. Each transformation has, instead of a single weight for the next iteration, a vector of weights for each transformation, $\{X; w_{1-M}; p_{i,j} \in [0, 1]; i, j = 1, 2, \ldots, M\}$, so that the matrix of weights is a recurrent Markov operator for the Hutchinson operator's transformation (see Ref. [17]). Therefore, the attractor of a RIFS need not exhibits the self-similarity or self-tiling properties characteristic of the attractor of an IFS, such as Eq. (1).

The most common algorithm to compute fractals derived by IFS is called the *chaos game* or *random iteration algorithm*. It consists of picking a random point in the plane, then iteratively applying one of the functions chosen at random from the function system and drawing the point. An alternative algorithm, the *deterministic iteration algorithm*, or *DIA* for short, is to generate each possible sequence of functions up to a given maximum length and then to plot the results of applying each of these sequences of functions to an initial point or shape. For a short survey on iterated function systems see Ref. [18].

3. Fractal interpolation functions in $\mathbb{R}$

Based on a theorem of Hutchinson ([15], p. 731) and using the IFS theory of Ref. [16], Barnsley introduced a class of functions (see Ref. [1]) which he called *fractal interpolation functions*. He basically worked with affine fractal interpolation functions, in the sense that they are obtained using affine transformations. Their main difference from elementary functions is their fractal character. Since their graphs usually have non-integral dimension, they can be used to approximate image components such as the profiles of mountain ranges, the tops of clouds and

horizons over forests, to name but a few. For a short survey on fractal interpolation functions see Ref. [19].

Fractal interpolation functions are suitable for data sets with points linearly ordered with respect to their abscissa. This is often sufficient, for example, when interpolating time series data. In practice, however, there are many cases where the data are suitable for fractal interpolation but define a curve rather than a function, for example, when modelling coastlines or plants. There exist methods for constructing *fractal interpolation curves* based on the theory of fractal interpolation functions. These methods use various approaches, such as generalisations to higher dimensions, use of index coordinates or application of reversible transformations.

Let the continuous function f be defined on a real closed interval $I = [x_0, x_M]$ and with codomain the metric space $(\mathbb{R}, |\cdot|)$, where $x_0 < x_1 < \cdots < x_M$. It is not assumed that these points are equidistant. The function f is called an *interpolation function* corresponding to the *generalised set of data* $\{(x_m, y_m) \in K : m = 0, 1, \ldots, M\}$, if $f(x_m) = y_m$ for all $m = 0, 1, \ldots, M$ and $K = I \times \mathbb{R}$. The points $(x_m, y_m) \in \mathbb{R}^2$ are called the *interpolation points*. We say that the function f *interpolates* the data and that (the graph of) f passes through the interpolation points. The *graph* of f is the set of points $G(f) = \{(x, f(x) : x \in X\}$.

3.1. Affine fractal interpolation

Let us represent our, real valued, set of *data points* as $\{(u_n, v_n) : n = 0, 1, \ldots, N; u_n < u_{n+1}\}$ and the interpolation points as $\{(x_m, y_m) : m = 0, 1, \ldots, M; M \le N\}$, where u_n is the sampled index and v_n the value of the given point in u_n. Let $\{\mathbb{R}^2; w_{1-M}\}$ be an IFS with affine transformations of the special form (see Eq. (2))

$$w_i\begin{pmatrix} x \\ y \end{pmatrix} = \begin{pmatrix} a_i & 0 \\ c_i & s_i \end{pmatrix}\begin{pmatrix} x \\ y \end{pmatrix} + \begin{pmatrix} d_i \\ e_i \end{pmatrix}$$

constrained to satisfy

$$w_i\begin{pmatrix} x_0 \\ y_0 \end{pmatrix} = \begin{pmatrix} x_{i-1} \\ y_{i-1} \end{pmatrix} \quad \text{and} \quad w_i\begin{pmatrix} x_M \\ y_M \end{pmatrix} = \begin{pmatrix} x_i \\ y_i \end{pmatrix} \tag{4}$$

for every $i = 1, 2, \ldots, M$. Solving the above equations results in

$$a_i = \frac{x_i - x_{i-1}}{x_M - x_0}, \quad d_i = \frac{x_M x_{i-1} - x_0 x_i}{x_M - x_0}$$

$$c_i = \frac{y_i - y_{i-1}}{x_M - x_0} - s_i\frac{y_M - y_0}{x_M - x_0}, \quad e_i = \frac{x_M y_{i-1} - x_0 y_i}{x_M - x_0} - s_i\frac{x_M y_0 - x_0 y_M}{x_M - x_0}$$

i.e., the coefficients a_i, c_i, d_i, e_i are completely determined by the interpolation points, while the s_i are free parameters satisfying $|s_i| < 1$ in order to guarantee that the IFS is hyperbolic with respect to an appropriate metric for every $i = 1, 2, \ldots, M$. The transformations w_i are *shear transformations*: line segments parallel to the y-axis are mapped to line segments parallel to the

y-axis contracted by the factor $|s_i|$. For this reason, the s_i are called *vertical scaling* (or *contractivity*) *factors*.

The IFS $\{\mathbb{R}^2; w_{1-M}\}$ has a unique attractor that is the graph of some continuous function which interpolates the data points. This function is called a *fractal interpolation function*, or *FIF* for short, because its graph usually has non-integral dimension. A *section* is defined as the function values between interpolation points. It is a function with a self-affine graph since each affine transformation w_i maps the entire (graph of the) function to its section. The above function is known as *affine FIF*, or *AFIF* for short. For example, let {(0, 0), (0.4, 0.5), (0.7, 0.2), (1, 0)} be a given set of data points. **Figure 3** shows the graph of an AFIF with $s_1 = 0.5$, $s_2 = -0.2$ and $s_3 = 0.4$. The closeness of fit of a FIF is mainly influenced by the determination of its vertical scaling factors. No direct way to find the optimum values of these factors exists, and various approaches have been proposed in the literature.

3.2. Piecewise affine fractal interpolation

The *piecewise self-affine* fractal model is a generalisation of the affine fractal interpolation model and has its mathematical roots embedded in RIFS theory. A pair of data points $\{(\tilde{x}_{i,j}, \tilde{y}_{i,j}) : i = 1, 2, \ldots, M; j = 1, 2\}$, which are called *addresses* or *address points*, is now associated with each *interpolation interval*. Each pair of addresses defines the *domain* or *address interval*. The constraints Eq. (4) become

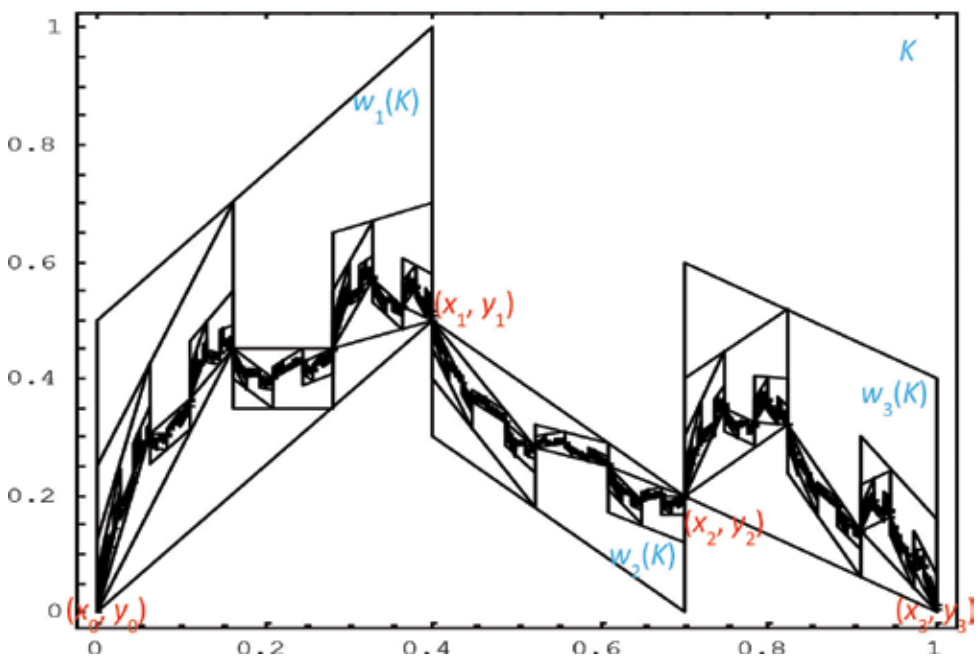

Figure 3. The construction of an affine FIF starting from the unit square and using the DIA.

$$w_i\begin{pmatrix}\tilde{x}_{i,1}\\ \tilde{y}_{i,1}\end{pmatrix}=\begin{pmatrix}x_{i-1}\\ y_{i-1}\end{pmatrix}\quad\text{and}\quad w_i\begin{pmatrix}\tilde{x}_{i,2}\\ \tilde{y}_{i,2}\end{pmatrix}=\begin{pmatrix}x_i\\ y_i\end{pmatrix}$$

subjected to $\tilde{x}_{i,2}-\tilde{x}_{i,1}>x_i-x_{i-1}$ for every $i=1, 2, \ldots, M$. Solving the above equations results in

$$a_i=\frac{x_i-x_{i-1}}{\tilde{x}_{i,2}-\tilde{x}_{i,1}},\quad d_i=\frac{\tilde{x}_{i,2}x_{i-1}-\tilde{x}_{i,1}x_i}{\tilde{x}_{i,2}-\tilde{x}_{i,1}},$$

$$c_i=\frac{y_i-y_{i-1}}{\tilde{x}_{i,2}-\tilde{x}_{i,1}}-s_i\frac{\tilde{y}_{i,2}-\tilde{y}_{i,1}}{\tilde{x}_{i,2}-\tilde{x}_{i,1}},\quad e_i=\frac{\tilde{x}_{i,2}y_{i-1}-\tilde{x}_{i,1}y_i}{\tilde{x}_{i,2}-\tilde{x}_{i,1}}-s_i\frac{\tilde{x}_{i,2}\tilde{y}_{i,1}-\tilde{x}_{i,1}\tilde{y}_{i,2}}{\tilde{x}_{i,2}-\tilde{x}_{i,1}}$$

for every $i=1, 2, \ldots, M$. The function constructed as the attractor of the above-mentioned IFS is called *recurrent fractal interpolation function*, or *RFIF* shortly, corresponding to the interpolation points. A RFIF is a piecewise self-affine function since each affine transformation w_i maps the part of the (graph of the) function defined by the corresponding address interval to each section.

4. Fractal interpolation functions in $\mathbb{R}^2$

Let the discrete data $\{(x_i, y_j, z_{i,j}=z(x_i, y_j))\in\mathbb{R}^3 : i=0, 1, \ldots, N; j=0, 1, \ldots, M\}$ be known. Each affine mapping that comprises the hyperbolic IFS $\{\mathbb{R}^3; w_{1-N,\,1-M}\}$ is given by the following special form of Eq. (3)

$$w_{n,m}\begin{pmatrix}x\\ y\\ z\end{pmatrix}=\begin{pmatrix}a_{n,m} & b_{n,m} & 0\\ c_{n,m} & d_{n,m} & 0\\ e_{n,m} & g_{n,m} & s_{n,m}\end{pmatrix}\begin{pmatrix}x\\ y\\ z\end{pmatrix}+\begin{pmatrix}h_{n,m}\\ k_{n,m}\\ l_{n,m}\end{pmatrix},$$

with $|s_{n,m}|<1$ for every $n=1, 2, \ldots, N$ and $m=1, 2, \ldots, M$. The condition

$$\left\|\begin{matrix}a_{n,m} & b_{n,m}\\ c_{n,m} & d_{n,m}\end{matrix}\right\|<1$$

ensures that

$$u_{n,m}\begin{pmatrix}x\\ y\end{pmatrix}=\begin{pmatrix}a_{n,m} & b_{n,m}\\ c_{n,m} & d_{n,m}\end{pmatrix}\begin{pmatrix}x\\ y\end{pmatrix}+\begin{pmatrix}h_{n,m}\\ k_{n,m}\end{pmatrix}$$

is a similitude and the transformed surface does not vanish or flip over.

A formal definition for the fractal interpolation surfaces, as presented in Ref. [4], with some generalisations is given below. Let D be a convex polygon in $\mathbb{R}^2$ with ℓ vertices and let $S=\{q_0, q_1, \ldots, q_{m-1}\}$ be m, with $m>\ell$, distinct points in D such that $q_0, q_1, \ldots, q_{\ell-1}$ are the vertices of D. Given real numbers $z_0, z_1, \ldots, z_{m-1}$, we wish to construct a function f such that $f(q_j)=z_j$, $j=0, 1, \ldots, m-1$ and whose graph is self-affine or self-similar. Let us denote by $C(D)$ the linear space of all real-valued continuous functions defined on D, that is,

$$C(D) = \{f: D \to \mathbb{R} \mid f \text{ continuous}\}.$$

A mapping Φ on $C(D)$ which corresponds to piecing the $G(\Phi(f))$ together using copies of parts of $G(f)$ will be defined.

4.1. Affine fractal interpolation

The basic idea is to decompose D into N non-degenerate subregions $\Delta_1, \Delta_2, \ldots, \Delta_N$ with vertices chosen from S and define affine maps $L_i: D \to \Delta_i$ and $F_i: D \times \mathbb{R} \to \mathbb{R}$, $i = 1, 2, \ldots, N$ such that Φ defined by

$$\Phi(f)(\mathbf{x}) = F_i\left(L_i^{-1}(\mathbf{x}), f\left(L_i^{-1}(\mathbf{x})\right)\right) \tag{5}$$

for $\mathbf{x} \in \Delta_i$ maps an appropriate subset of $C(D)$ onto itself. The main work is in showing that Φ is well defined and contractive on some subset of $C(D)$. If L_i is invertible, $G(f)$ is mapped onto $G\left(\Phi(f)|_{\Delta_i}\right)$ by (L_i, F_i). Henceforth, we assume that the set $\{\Delta_i\}_{i=1}^N$ consists of non-degenerate convex polygons with extreme points whose interior are non-intersecting, $L_i^{-1}(\Delta_i) = D$ and the set of vertices of $\{\Delta_i\}_{i=1}^N$ equals S. Let k: $\{1, 2, \ldots, N\} \times \{0, 1, \ldots, \ell-1\} \to \{0, 1, \ldots, m-1\}$ be such that $\{q_{k(i,j)}\}_{j=0}^{\ell-1}$ gives the vertices of $\{\Delta_i\}_{i=1}^N$.

Let $i \in \{1, 2, \ldots, N\}$. Since D and Δ_i are non-degenerate, there exists an invertible map satisfying

$$L_i(q_j) = q_{k(i,j)}, j = 0, 1, \ldots, \ell - 1. \tag{6}$$

Also, given any necessary free parameters,

$$F_i(q_j, z_j) = z_{k(i,j)}, j = 0, 1, \ldots, \ell - 1. \tag{7}$$

With these definitions for L_i and F_i, if $f \in C(D)$ and $f(q_j) = z_j$, $j = 0, 1, \ldots, \ell-1$, then $\Phi|_{\Delta_i} \in C(\Delta_i)$ and $\Phi(f)(q_{k(i,j)}) = z_{k(i,j)}$, $j = 0, 1, \ldots, \ell-1$. If Δ_i and $\Delta_{i'}$ are adjacent polygons with common edge $\overline{q_j q_{j'}}$, it remains to be determined if Φ is well defined along $\overline{q_j q_{j'}}$, that is, whether $\Phi(f)$ satisfies for all $\mathbf{x} \in \overline{q_j q_{j'}}$ the 'join-up' condition

$$F_i(L_i^{-1}(\mathbf{x}), f(L_i^{-1}(\mathbf{x}))) = F_{i'}(L_{i'}^{-1}(\mathbf{x}), f(L_{i'}^{-1}(\mathbf{x}))).$$

When there is no proof that our construction always satisfies it, the surface may be not continuous and a geometrical and visual artefact, known as 'discontinuity', appears. When a surface suffers from discontinuities, a correct visualisation should render aligned horizontal holes over the surface. A surface with discontinuities should not be considered as a fractal interpolation surface; the function f is ambiguous on the common edge points and $\Phi(f)$ is not well defined.

Let the number of extreme points of the convex region D be 3. A triangular domain is formed, and the set $\{\Delta_i\}_{i=1}^N$ contains non-degenerate triangles whose interior is non-intersecting. In

http://dx.doi.org/10.5772/intechopen.68499

what follows, we shall deal with a special class of maps, namely affine ones. For all $i = 1, 2, \ldots, N$ the invertible map $L_i: \mathbb{R}^2 \to \mathbb{R}^2$ is defined as follows

$$L_i(x, y) = (a_i x + b_i, c_i y + d_i)$$

and let the map $F_i: \mathbb{R}^3 \to \mathbb{R}$ be defined by

$$F_i(x, y, z) = e_i x + f_i y + s_i z + g_i. \tag{8}$$

Then, the corresponding IFS is of the form $\{\mathbb{R}^3; w_{1-N}\}$, where $w_i(x, y, z) = (L_i(x, y), F_i(x, y, z))$, $i = 1, 2, \ldots, N$ and can be written in a matrix form

$$w_i \begin{pmatrix} x \\ y \\ z \end{pmatrix} = \begin{pmatrix} a_i & 0 & 0 \\ 0 & c_i & 0 \\ e_i & f_i & s_i \end{pmatrix} \begin{pmatrix} x \\ y \\ z \end{pmatrix} + \begin{pmatrix} b_i \\ d_i \\ g_i \end{pmatrix}.$$

The real numbers a_i, b_i, c_i and d_i for $i = 1, 2, \ldots, N$ are chosen to ensure that Condition (6) holds, that is, $L_i(q_0) = q_{k(i,\,0)}$, $L_i(q_1) = q_{k(i,\,1)}$ and $L_i(q_2) = q_{k(i,\,2)}$. Thus, for $i = 1, 2, \ldots, N$,

$$a_i = \frac{x_{k(i,j')} - x_{k(i,j)}}{x_{j'} - x_j}, \; b_i = x_{k(i,j)} - x_j \frac{x_{k(i,j')} - x_{k(i,j)}}{x_{j'} - x_j}, \; j \neq j' \in \{0, 1, 2\}, \; x_j \neq x_{j'},$$

$$c_i = \frac{y_{k(i,j')} - y_{k(i,j)}}{y_{j'} - y_j}, \; d_i = y_{k(i,j)} - y_j \frac{y_{k(i,j')} - y_{k(i,j)}}{y_{j'} - y_j}, \; j \neq j' \in \{0, 1, 2\}, \; y_j \neq y_{j'}.$$

After selecting the scaling factors s_i with $|s_i| < 1$, the values e_i, f_i and g_i are chosen to ensure that Condition (7) holds, that is, $F_i(q_0, z_0) = z_{k(i,\,0)}$, $F_i(q_1, z_1) = z_{k(i,\,1)}$ and $F_i(q_2, z_2) = z_{k(i,\,2)}$. That is, $s_i \in (-1, 1)$ is chosen and then

$$e_i = \frac{z_{k(i,0)}(y_1 - y_2) + z_{k(i,2)}(y_0 - y_1) + z_{k(i,1)}(y_2 - y_0)}{x_0(y_1 - y_2) + x_2(y_0 - y_1) + x_1(y_2 - y_0)} + s_i \frac{z_1(y_0 - y_2) + z_0(y_2 - y_1) + z_2(y_1 - y_0)}{x_0(y_1 - y_2) + x_2(y_0 - y_1) + x_1(y_2 - y_0)},$$

$$f_i = \frac{z_{k(i,1)}(x_0 - x_2) + z_{k(i,0)}(x_2 - x_1) + z_{k(i,2)}(x_1 - x_0)}{y_1(x_0 - x_2) + y_0(x_2 - x_1) + y_2(x_1 - x_0)} + s_i \frac{z_0(x_1 - x_2) + z_2(x_0 - x_1) + z_1(x_2 - x_0)}{y_1(x_0 - x_2) + y_0(x_2 - x_1) + y_2(x_1 - x_0)},$$

$$g_i = \frac{x_0(y_1 z_{k(i,2)} - y_2 z_{k(i,1)}) + x_1(y_2 z_{k(i,0)} - y_0 z_{k(i,2)}) + x_2(y_0 z_{k(i,1)} - y_1 z_{k(i,0)})}{x_0(y_1 - y_2) + x_1(y_2 - y_0) + x_2(y_0 - y_1)} +$$

$$s_i \frac{x_0(y_2 z_1 - y_1 z_2) + x_1(y_0 z_2 - y_2 z_0) + x_2(y_1 z_0 - y_0 z_1)}{x_0(y_1 - y_2) + x_1(y_2 - y_0) + x_2(y_0 - y_1)},$$

for all $i = 1, 2, \ldots, N$. We construct the IFS of the form $\{S; w_{1-N}\}$, with the intention to produce $G(f)$ that is continuous and passes through the points (q_j, z_j), $q_j \in S$, $j = 0, 1, \ldots, m-1$ as the unique attractor $\mathcal{A}$ of the IFS. Since we consider $f \in C(D)$, we must check if the 'join-up' condition is satisfied for all possible starting points of the IFS. **Figure 4** illustrates the surface

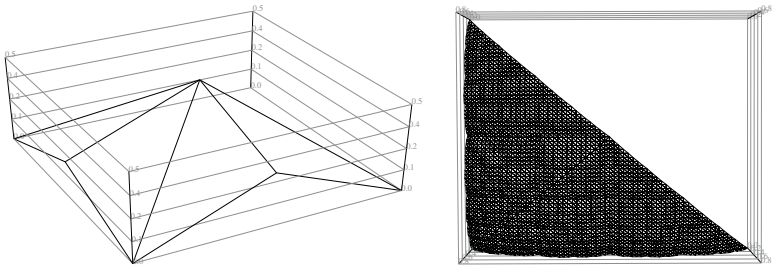

Figure 4. The generation of an affine fractal surface and its view from above.

graph (Level = 0) drawn with the original set of data {(0, 0, 0), (0.5, 0, 0.2), (1, 0, 0), (0, 0.5, 0.3), (0.5, 0.5, 0.5), (0, 1, 0)} where $s = 0.6$. See also Example 58 of Ref. [8].

4.1.1. Coplanar boundary data, arbitrary contractivity factors

If P is a non-vertical plane in $\mathbb{R}^3$, let $\hat{C}(D)$ denote the collection of continuous functions $f: D \to \mathbb{R}$ such that $(x, f(x)) \in P$ for all $x \in \partial D$.

Theorem 4.1.1. Suppose the points $\{(q_j, z_j) : q_j \in \partial D\}$ are contained in a plane $P \subset \mathbb{R}^3$. Let Φ be defined by (5), where L_i and F_i, $i = 1, 2, \ldots, N$ are defined by Eqs. (6)–(8). Then, $\Phi: \hat{C}(D) \to \hat{C}(D)$ is well defined and contractive in the sup-norm $\|\cdot\|_\infty$. Furthermore, for every $j = 0, 1, \ldots, m-1$ and $f \in \hat{C}(D)$, $\Phi(f)(q_j) = z_j$.

We call the unique attractor of the afore-mentioned IFS a *self-affine fractal interpolation surface*, or *SAFIS* for short, *with coplanar boundary data and arbitrary contractivity factors*. **Figure 5** illustrates Example 1 constructed in Ref. [4].

4.1.2. Arbitrary boundary data, identical contractivity factors

The *chromatic number* of a graph is the smallest number of colours needed to colour its vertices so that no two adjacent vertices share the same colour. Let G be the graph with S as its vertices and its edges correspond to the decomposition of D to $\{\Delta_i\}_{i=1}^N$. We assign a colour to each vertex of the graph through the labelling function $l = l(j) \in \{0, 1, 2\}$, $j = 0, 1, \ldots, m-1$; see **Figure 6**.

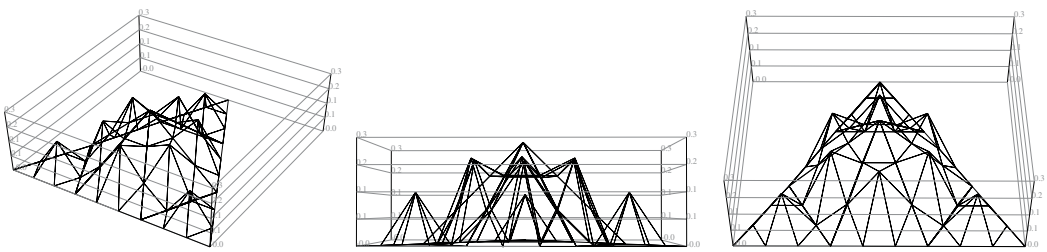

Figure 5. Three views of a SAFIS with coplanar boundary data and arbitrary contractivity factors.

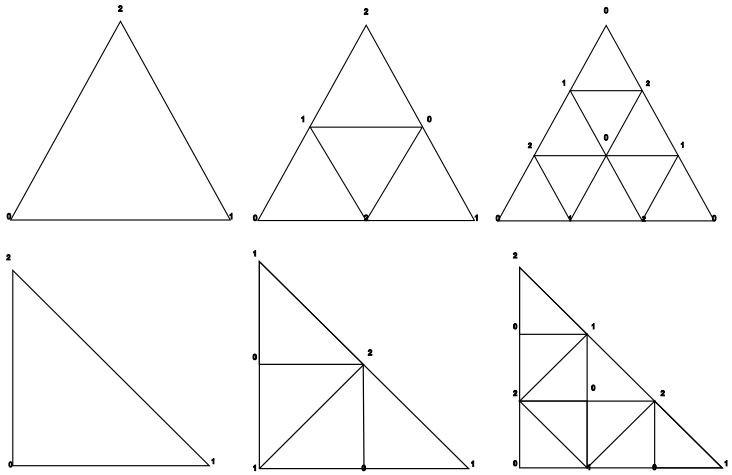

Figure 6. Domain for fractal interpolating surfaces over triangular lattice and possible subdomains.

For $i = 1, 2, \ldots, N$ and $j = 0, 1, 2$ let $k(i, j)$ be determined by the condition $k(i, l(j')) = j'$ for all vertices $q_{j'}$ of Δ_i. Then, for each of the vertices q_j of Δ_i, Eqs. (6) and (7) become

$$L_i\left(q_{l(j)}\right) = q_j \text{ and } F_i\left(q_{l(j)}, z_{l(j)}\right) = z_j. \tag{9}$$

Let $\hat{C}(D)$ denote the collection of continuous functions f such that $f(q_j) = z_j$, $q_j \in \partial D$.

Theorem 4.1.2. Suppose the graph associated with $\{\Delta_i\}_{i=1}^N$ has chromatic number 3. Let L_i and F_i, $i = 1, 2, \ldots, N$ be determined by Eqs. (8) and (9) with $s_i = s \in (-1, 1)$. Let Φ be defined by Eq. (5). Then, Φ: $\hat{C}(D) \to \hat{C}(D)$ is well defined and contractive in the sup-norm $\|\cdot\|_\infty$. Furthermore, for every $j = 0, 1, \ldots, m-1$ and $f \in \hat{C}(D)$, $\Phi(f)(q_j) = z_j$.

We call the unique attractor of the afore-mentioned IFS a *self-affine fractal interpolation surface*, or *SAFIS* for short, *with arbitrary boundary data and identical contractivity factors*. The colouring of Theorem 4.1.2 is also known as 'consistent triangulation' within the context of computational geometry. We will be using this term from now on, for simplicity. **Figure 7** illustrates Example 2 constructed in Ref. [4].

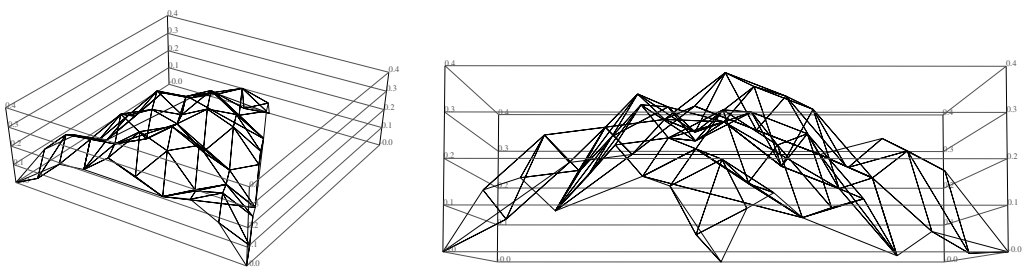

Figure 7. Two views of a SAFIS with arbitrary boundary data and identical contractivity factors.

4.1.3. Arbitrary boundary data, arbitrary contractivity factors

Zhao in Ref. [7] deploys a piecewise linear function γ over the graph G of the IFS. Let G be the graph mentioned earlier and S its vertices. We assign a value $s \in (-1, 1)$ to each vertex by defining for all $i = 1, 2, \ldots, N$ the piecewise linear function $\gamma = \gamma_i$: $\mathbb{R}^2 \rightarrow (-1, 1)$ as follows

$$\gamma_i(q) = \begin{cases} \beta_s(q_{k(i,0)}, q_{k(i,1)}, q_{k(i,2)}, q), & q \in \Delta_i \\ 0, & \text{otherwise} \end{cases},$$

where β_s is the barycentric interpolation function with the attribute s as coefficient

$$\beta_s(q_a, q_b, q_c, q) = \frac{\|(q - q_a) \times (q - q_b)\| s_c + \|(q - q_b) \times (q - q_c)\| s_a + \|(q - q_c) \times (q - q_a)\| s_b}{\|(q_a - q_b) \times (q_c - q_b)\|}.$$

Theorem 4.1.3. Consider the IFS $\{S; w_{1-N}\}$ and the corresponding graph G described above that also fulfils the conditions mentioned in Theorem 4.1.2, except for the usage of identical scaling factors over the whole surface. For each transformation w_i, we substitute the scaling factors s_i with the function γ_i described above, so the map F_i becomes for all $i = 1, 2, \ldots, N$

$$F_i(x, y, z) = e_i x + f_i y + \gamma_i(L_i(x, y))z + g_i.$$

Then, the unique attractor of the IFS mentioned previously is the graph of a continuous function f that passes though the points (q_j, z_j), $q_j \in S$, $j = 0, 1, \ldots, m-1$.

We call the unique attractor of the afore-mentioned IFS a *self-similar fractal interpolation surface*, or *SSFIS* for short, *with arbitrary boundary data and contractivity factors*. The assignment of the scaling factor value s_j, $j = 0, 1, \ldots, m-1$ to each vertex can be done either during the parameter identification process or can be inferred via a given set of vertical scaling factors $\{s_1, s_2, \ldots, s_N\}$, where each s_i corresponds to Δ_i, $i = 1, 2, \ldots, N$. The technique is identical to the calculation of the vertex normal vectors on the Gouraud and Phong shading models, where the facets of the mesh are the sub-regions Δ_i, $i = 1, 2, \ldots, N$. Compare and contrast **Figures 6** and **9** of Ref. [7] with **Figure 8**.

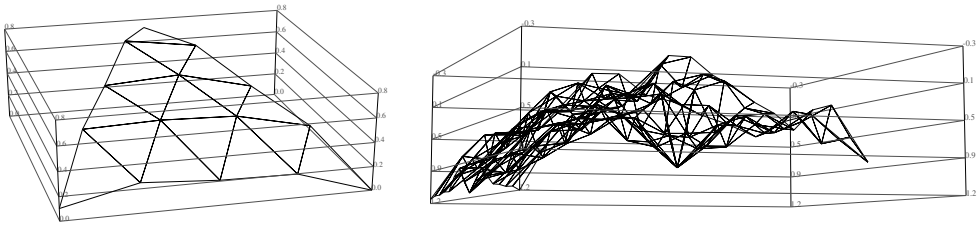

Figure 8. Two views of a SSFIS with arbitrary boundary data and contractivity factors.

4.2. Recurrent affine fractal interpolation

Let D be a polygonal domain, $\{\Delta_i\}_{i=1}^N$ a triangulation of D consisting of non-degenerate triangles with non-intersecting interiors whose union is D and $S = \{q_0, q_1, \ldots, q_{m-1}\}$ be the set of vertices of $\{\Delta_i\}_{i=1}^N$. Let $\{\delta_k\}_{k=1}^M$ be M triangles each of which is a union of some subset of

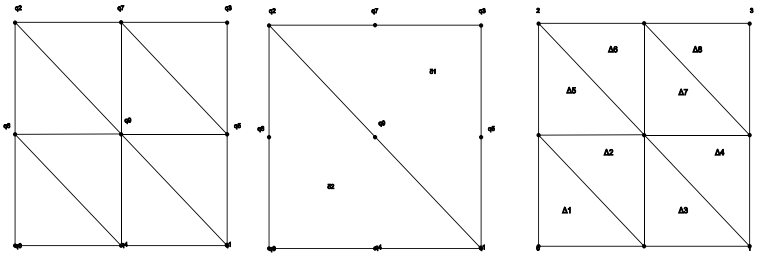

Figure 9. Domain for fractal interpolating surfaces over polygonal lattice and possible subdomains.

$\{\Delta_i\}_{i=1}^N$; see **Figure 9**. We order S so that the first n points $\{q_0, q_1, \ldots, q_{n-1}\} \subset S$ are the vertices of $\{\delta_k\}_{k=1}^M$.

4.2.1. Coplanar boundary data, arbitrary contractivity factors

We call l: {1, 2, …,N} → {1, 2, …, M} a *Δ-labelling* which associates the vertices of Δ_i with the vertices of some δ_k. If P_k are non-vertical planes in $\mathbb{R}^3$, let $\hat{C}(D)$ denote the collection of continuous functions $f_k = f|_{\Delta_i}$: $\delta_k \to \mathbb{R}$ such that $(x, f_k(x)) \in P_k$ for all $x \in \partial\delta_k$.

Theorem 4.2.1. Suppose the points $\{(q_j, z_j) : q_j \in \partial\delta_k\}$ are contained in the planes $P_k \subset \mathbb{R}^3$ for every k. Let Φ be defined by Eq. (5), where L_i and F_i, $i = 1, 2, \ldots, N$ are defined by Eqs. (6)–(8). Then, Φ: $\hat{C}(D) \to \hat{C}(D)$ is well defined and contractive in the sup-norm $\|\cdot\|_\infty$. Furthermore, for every $j = 0, 1, \ldots, m-1$ and $f \in \hat{C}(D)$, $\Phi(f)(q_j) = z_j$.

We call the unique attractor of the afore-mentioned RIFS a *recurrent self-affine fractal interpolation surface*, or *RSAFIS* for short, *with coplanar boundary data and arbitrary contractivity factors*.

4.2.2. Arbitrary boundary data, identical contractivity factors

We call l: {0, 1, …, $m-1$} → {0, 1, …, $n-1$} a *Δ-labelling* associated with $\{\delta_k\}_{k=1}^M$ and $\{\Delta_i\}_{i=1}^N$ if $\{q_{l(j)}, q_{l(j')}, q_{l(j'')}\}$ are the vertices of some δ_k whenever $\{q_j, q_{j'}, q_{j''}\}$ are the vertices of some Δ_i; see **Figure 10**.

Theorem 4.2.2. Let l be a Δ-labelling associated with the triangulations $\{\Delta_i\}_{i=1}^N$ and $\{\delta_k\}_{k=1}^M$. Let L_i: $\mathbb{R}^2 \to \mathbb{R}^2$ and F_i: $\mathbb{R}^3 \to \mathbb{R}$ be the unique affine maps satisfying (9) with $s_i = s$ ($|s| < 1$). Let Φ be defined by Eq. (5). Then, Φ: $\hat{C}(D) \to \hat{C}(D)$ is well defined and contractive in the sup-norm $\|\cdot\|_\infty$. Furthermore, for every $j = 0, 1, \ldots, m-1$ and $f \in \hat{C}(D)$, $\Phi(f)(q_j) = z_j$.

Geronimo and Hardin in Ref. [4] have showcased a two-dimensional multi-resolution analysis. Based on their work, we have created acceptable colourings of graphs with any desirable density, by solving the problem on a small instance that we call *pattern graph*. If the solution has the identity of self-similarity, the density of the graph is then enhanced by interpolating the pattern with a RIFS defined on the metric space of the undirected graphs. With the help of a geometric predicate, we unify the resulting points into a single graph that now has the desired density. The results are illustrated in **Figure 11**.

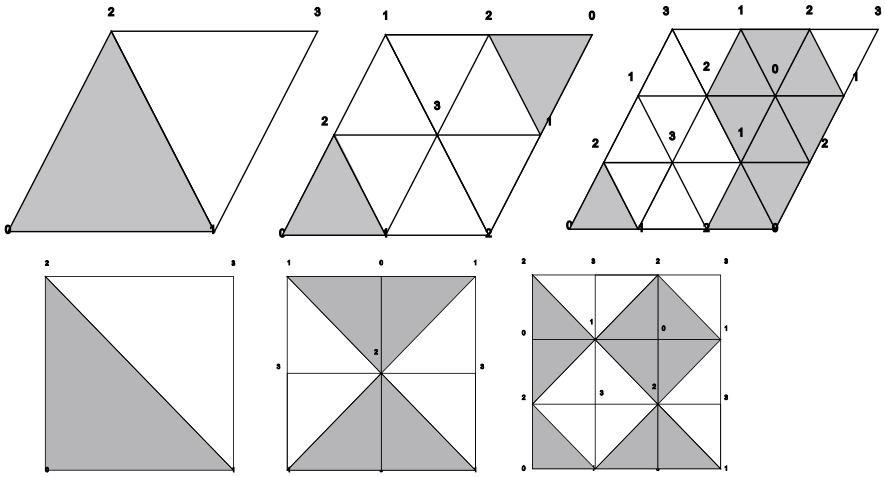

Figure 10. Domain for fractal interpolating surfaces over polygonal lattices and possible subdomains.

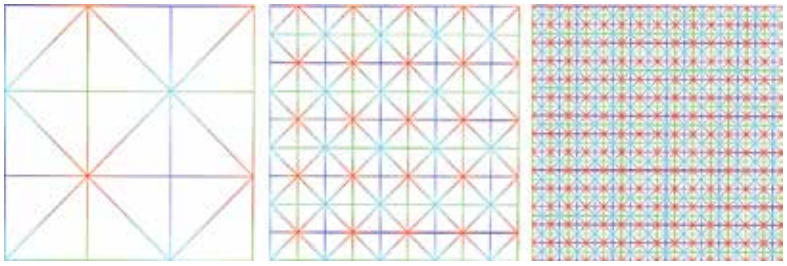

Figure 11. Examples of increasing the density of partially self-similar coloured graphs.

We call the unique attractor of the afore-mentioned RIFS a *recurrent self-affine fractal interpolation surface,* or *RSAFIS* for short, *with arbitrary boundary data and identical contractivity factors*. **Figure 12** illustrates Example 3 constructed in Ref. [4].

4.2.3. Arbitrary boundary data, arbitrary contractivity factors

The map F_i becomes for all $i = 1, 2, \ldots, N$, $F_i(x, y, z) = e_i x + f_i y + \gamma_i(L_i(x, y))z + g_i$.

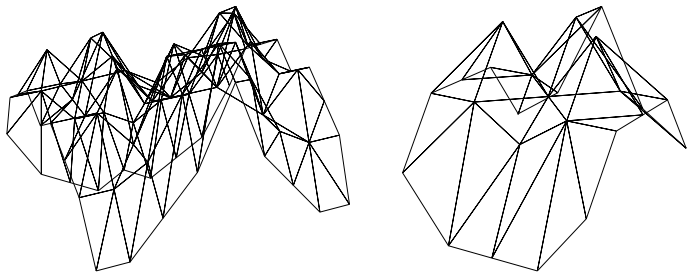

Figure 12. Two views of a RSAFIS over polygonal domain with arbitrary boundary data and identical contractivity factors.

Theorem 4.2.3. Suppose the graph associated with $\{\Delta_i\}_{i=1}^N$ has chromatic number 3. Let L_i and F_i, $i = 1, 2, \ldots, N$ are defined by Eqs. (6)–(8) and Φ be defined by Eq. (5). Then, Φ: $\hat{C}(D) \to \hat{C}(D)$ is well defined and contractive in the sup-norm $\|\cdot\|_\infty$. Furthermore, $\Phi(f)(q_j) = z_j$, $j = 0, 1, \ldots, m-1$ and $f \in \hat{C}(D)$.

We call the unique attractor of the afore-mentioned RIFS a *recurrent self-similar fractal interpolation surface*, or *RSSFIS* for short, *with arbitrary boundary data and contractivity factors*. We illustrate this construction in **Figure 13**.

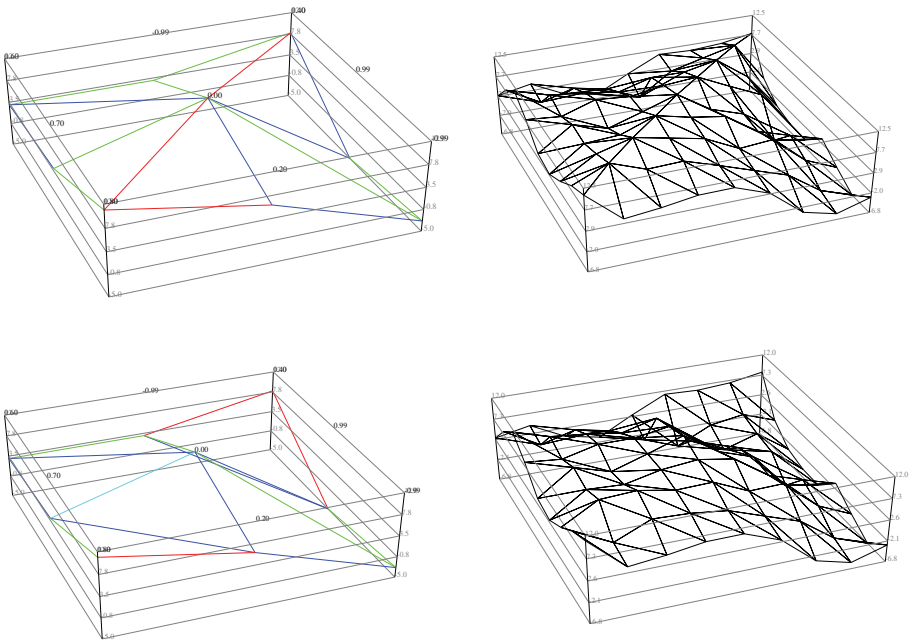

Figure 13. Two levels of a RSSFIS over different polygonal domains with arbitrary boundary data and contractivity factors.

5. Conclusions, extensions and future work

We have presented an overview of affine interpolation as well as of recurrent affine interpolation using fractal functions in one and two dimensions. The effectiveness of a self-affine fractal model is limited to the types of data: only those data that are self-affine, or nearly so, are well represented. Since most data are not self-affine, the piecewise or recurrent self-affine fractal model may be a suitable alternative tool.

Nevertheless, our future work should focus on the parameter identification of fractal interpolation surfaces. More methods must be explored, including the ones for self-affine FIS's and the vertex-based ones, while a better sampling technique for the heights is needed. For the recurrent FIS's, it is utmost important to connect the domains with the subdomains that they resemble the most instead of determining the connections through an arbitrary colouring

scheme. Therefore, a premise for future work is to find the optimal connections between domains and subdomains through a statistical analysis and then, starting from a feasible solution, to perform a heuristic local search with the intention to minimise the distance between current connections, implied by the current colouring, and those of the optimal solution. Moreover, methods to construct FIS, other than those based on the iterated function systems, exist, including the ones that use wavelets and tensor products, in which they should be also studied.

Many areas of fractal functions and their applications are yet to be explored, for instance, calculating the Hausdorff dimension of a general FIF is a challenging open problem. By believing that the field of fractal functions has bright future, the reader, in order to be able to contribute to it, should leave the idea of staying in the comfort of well-known classical approximation theory and start enjoying the benefits of the more versatile fractal approximants, to supplement the former if not to replace it.

Author details

Sean Dillon[1] and Vasileios Drakopoulos[2]*

*Address all correspondence to: vdrakop@uth.gr

1 Department of Informatics and Telecommunications, National and Kapodistrian University of Athens, Athens, Greece

2 Department of Computer Science and Biomedical Informatics, University of Thessaly, Lamia, Greece

References

[1] Barnsley MF. Fractal functions and interpolation. Constructive Approximation. 1986;**2** (1):303–329. DOI: 10.1007/BF01893434

[2] Barnsley MF. Fractals Everywhere. 2nd ed. San Diego: Academic Press Professional; 1993

[3] Massopust PR. Fractal surfaces. Journal of Mathematical Analysis and Applications. 1990;**151**(1):275–290. DOI: 10.1016/0022-247X(90)90257-G

[4] Geronimo JS, Hardin D. Fractal interpolation surfaces and a related 2-D multiresolution analysis. Journal of Mathematical Analysis and Applications. 1993;**176**(2):561–586. DOI: 10.1006/jmaa.1993.1232

[5] Hardin DP, Massopust PR. Fractal interpolation functions from $\mathbb{R}^n$ into $\mathbb{R}^m$ and their projections. Zeitschrift für Analysis und ihre Anwendungen. 1993;**12**(3):535–548. DOI: 10.4171/ZAA/549

[6] Wittenbrink CM. IFS fractal interpolation for 2D and 3D visualization. In: VIS '95 Proceedings of the 6th Conference on Visualization '95; 29 October–03 November 1995; Atlanta, GA. IEEE; 1995. pp. 77–84. DOI: 10.1109/VISUAL.1995.480798

[7] Zhao N. Construction and application of fractal interpolation surfaces. The Visual Computer. 1996;**12**(3):132–146. DOI: 10.1007/BF01725101

[8] Massopust PR. Fractal Functions, Fractal Surfaces and Wavelets. 2nd ed. San Diego: Academic Press; 2016.

[9] Drakopoulos V, Bouboulis P, Theodoridis S. Image compression using affine fractal interpolation on rectangular lattices. Fractals. 2006;**14**(4):259–269. DOI: 10.1142/S0218348X06003271

[10] Zhang T, Liu J, Zhuang Z. Multi-dimensional piece-wise self-affine fractal interpolation model in tensor form. Advances in Complex Systems. 2006;**9**(3):287–293. DOI: 10.1142/S0219525906000756

[11] Zhang T, Zhuang Z. Multi-dimensional self-affine fractal interpolation model. Tsinghua Science and Technology. 2007;**12**(3):244–251. DOI: 10.1016/S1007-0214(07)70036-6

[12] Zhang T, Liu J, Zhuang Z. Multi-dimensional piece-wise self-affine fractal interpolation model in tensor form. Nonlinear Dynamics. 2008;**52**(1):83–87. DOI: 10.1007/s11071-007-9259-5

[13] Vijender N, Chand AKB. Shape preserving affine fractal interpolation surfaces. Nonlinear Studies. 2014;**21**(2):175–190

[14] Drakopoulos V. Fractal-based image encoding and compression techniques. Communications-Scientific Letters of the University of Zilina. 2013;**15**(3):48–55

[15] Hutchinson JE. Fractals and self similarity. Indiana University Mathematics Journal. 1981;**30**(5):713–747. DOI: 10.1512/iumj.1981.30.30055

[16] Barnsley MF, Demko S. Iterated function systems and the global construction of fractals. Proceedings of the Royal Society of London. Series A, Mathematical and Physical Sciences. 1985;**399**(1817):243–275. DOI: 10.1098/rspa.1985.0057

[17] Barnsley MF, Elton JH, Hardin DP. Recurrent iterated function systems. Constructive Approximation. 1989;**5**(1):3–31. DOI: 10.1007/BF01889596

[18] Hoggar S.G., Mathematics for computer graphics. Cambridge: Cambridge Univ. Press; 1992

[19] Navascués MA, Chand AKB, Veedu VP, Sebastián MV. Fractal interpolation functions: A short survey. Applied Mathematics. 2014;**5**(12):1834–1841. DOI: 10.4236/am.2014.512176

Chapter 10

Pair-Pair Angular Correlation Function

Filipe Leoncio Braga and
Alexandre Barbosa de Souza

Additional information is available at the end of the chapter

http://dx.doi.org/10.5772/67940

Abstract

In addition to the Hausdorff dimension used as fractal characterization parameter, in general, correlation functions can also be employed for this purpose. Given the approximately pure random spatial dispersion of big part of natural fractals, with respect to the center of a reference frame, the most common use of the pair-to-pair correlation function has as main variable the radial distance between two elements of the fractal. Such an approach is extremely practical, since the fractal basic structure statistically presents some kind of isotropy. For the cases where the fractal growth is not isotropic, the use of a pair-to-pair angular correlation function can detect a fractal pattern may be worthy. This will be the topic that is going to be discussed in this chapter, how to implement, discuss and visualize a pair-to-pair angular correlation function.

Keywords: characterization, correlation functions, fractal growth

1. Introduction

Several fractal structures show morphological properties that can be mapped and studied by means of a great amount of geometric parameters. Such definitions generally seek to directly and precisely evidence some physical and structural properties of the object. The Hausdorff dimension [1], recognized as the fractal dimension of a given object, represents a characteristically stationary information of the fractals, that is, it returns an image about the morphology after its formation. In general, this type of parameter becomes very effective in the characterization of several fractal types or different samples, where the process of formation of the same is well-known, such as the case for the deterministic fractals.

However, the most interesting fractals to be analyzed are those found in nature where the growth processes are not well known. In order to investigate and determine the main

phenomena involved in the formation of these fractals, it is vitally important to characterize the growth process of these objects. In this context, we can introduce the pair-pair correlation functions [2].

Statistically speaking, the pair-pair correlation functions return probabilistic information related to the dispersion of the constituent parts, taken as fractal singularity elements, to be found by a given characteristic separation. This statistical tool has applications within the analysis of fractal structures and is also commonly used in studies of Molecular Physics, in the analysis and interpretation of simulations of classical molecular dynamics (CMD). Using the taxonomy appropriate to this large area of knowledge, this function is called radial distribution function (RDF) [2]. As structurally CMD simulations require radial information, the most relevant spatial data retrieval takes into account that the dispersion of the particles to be investigated follows a spherical symmetry, hence only analyzing the radial dispersion of the particles.

In fractals with dendritic structures, such as diffusion limited aggregation (DLA) [1], which is a good representation of several physical and biological phenomena in nature, such as crystal growth, formation of polymers, sedimentation processes, among others or deterministic fractals of the group of Julia [3], this type of analysis, through the functions of pair-pair correlation, can elucidate the process of branching for the obtained structures.

Knowing how this process develops can helps the scientists to predict the behavior of the Hausdorff dimension of the fractals analyzed, and the fractal morphologies. In the next session, we will present the basic definition of a DLA fractal in a 2D (two dimensional) perspective, which will be the basic archetype for the formal presentation of radial and angular correlation analysis, which will have a basic explanation of the implementation and subsequent analysis of the results obtained.

2. DLA and radial correlation function

Formally, the diffusion limited aggregation (DLA) was initially studied by Witten and Sander in 1970 [4], and consists of a process of simple aggregate formation that emulates processes of dendritic structures that grow through diffusion, as is the case with of electrodeposition phenomena of solid materials in homogeneous solutions or polymerization process. From a computational modeling point of view, DLA aggregates can be obtained on-lattice and off-lattice, two dimensions (2D) and in three dimensions (3D) both initialized with a single deposited particle, called the seed. Given the diffusive characteristics of the system, all particles are taken as identical and run random walks, until they come into contact with the aggregate when they stop moving and are permanently added to it.

There are several variants of the DLA model, and several ways to obtain a DLA-type aggregate [5]. However, given the statistical properties of the random walk, the simplest way to perform such a simulation is to individually draw each particle and perform several steps of a random walk until one of two events may occur: First, if the particle comes into contact with some particle of the aggregate, the path is terminated and another particle is thrown at a fixed

http://dx.doi.org/10.5772/67940

distance from the seed, called the radius of launch R_{lau}, or second, particle reaches a position far from the seed, this distance called death ray R_{kill}, the probability of the particle to return by means of a random-walk and contact with the aggregate becomes very low, hence the walk is finished and another particle is thrown. In general, the launching radius is equal to the sum of the radius of the aggregate R_{agg} with a sufficiently large distance, to avoid a trend in aggregate growth. Since the particles are all identical, the rays of the particles are taken to be the basic unit (arbitrary unit). In general, $R_{kill} \gg R_{lan}$. The position of the walking particle launched is determined randomly at the launch circle. A schematic diagram of the basic structure of a DLA can be seen in **Figure 1**.

The most delicate part of a DLA simulation is the aggregation test. In the on-lattice cases, the test consists of the investigation of the elements of a regular network in the surroundings of the aggregated particles, if any element in the vicinity of the walking particle is occupied, it means that the particle has reached the aggregate and must be glued to it, see **Figure 2**. In the off-lattice cases, the aggregation is more complicate, since it must be checked at every step if the distance from the center of the walking particle to the center of all the aggregated particles is not less than twice the radius of the particles, if this occurs, the aggregation must be performed. However, double caution must be taken because in these configurations the overlap of particles must be avoided, see **Figure 2(b)**. Several works in the literature have explored algorithms that talk about this problem [6, 7].

As observed by the dendritic growth exposed at **Figure 2(a)** and **(b)**, the on-lattice simulations have typical different features when compared to the off-lattice simulations, and one special form to quantify this difference is the angular pair-pair correlation function that is discussed in Section 3.

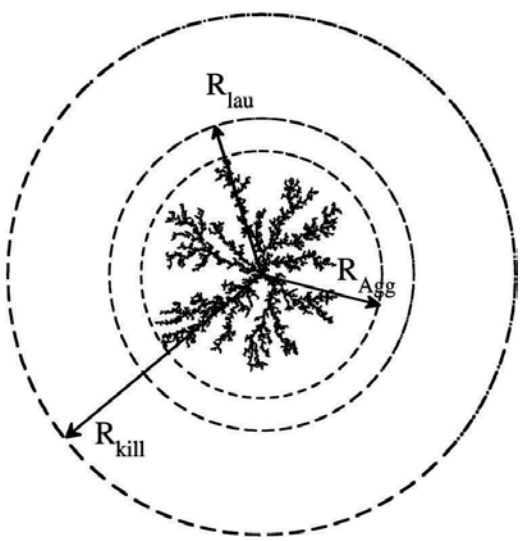

Figure 1. 2D DLA off-lattice containing 10^3 identical particles, showing the respective radii of the aggregates used during the simulation.

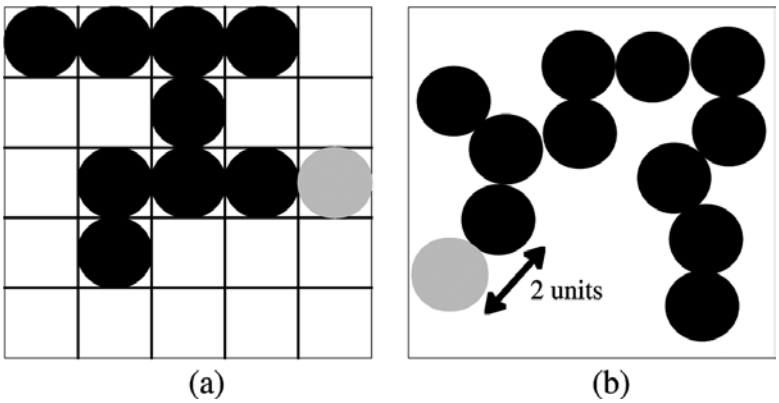

Figure 2. (a) Aggregation test in a 2D on-lattice DLA, white sites represent empty space, black sites represents spaces occupied by aggregate particles and gray site represents the walking particle. (b) DLA 2D off-lattice aggregation test, black circles are aggregate particles and the gray circle is the walking particle.

There are some types of DLAs that, instead of using a radial configuration for the launch of particles, they use a line (2D) or a plane (3D) and limitate the walk of the particles between the launching line/plane and parallel line/plane that contains the seed particle. see **Figure 3**. Although visually the two DLAs, planar-based growth and radial growth, are very different, both typically have a fractal dimension of approximately 1.71 for 2D cases [7].

The typical pair-pair correlation function c (r) directly measures the probability of finding two particles separated by a given radial distance. In classical molecular dynamics simulations, this type of function is called radial distribution function $g(r)$ [2], and may characterize, among other things, the formation of micelles, clusters, and in some cases chemical bonds.

Mathematically, in the case of fractals, this radial function can be calculated as

$$c(r) = \frac{1}{N} \sum \sum \left(\vec{r} - \left| \vec{r}_i - \vec{r}_j \right| \right) \tag{1}$$

where $\delta\left(\vec{r} - \left| \vec{r}_j - \vec{r}_i \right| \right)$ is equal to the unit for the case of particles separated by a given radial separation r and zero otherwise. N is exactly the total number of particles added.

The radial feature of this distribution does not prevent it from being used in fractals that do not present radial symmetry, as is the case of planar-based DLA, but its analysis must be performed with more cautious. From the computational point of view, it is very rare for the particles to be perfectly separated by the distance r. Effectively, an average histogram-like calculation is made for the above summation as follows: every aggregate particle is taken as the center of a spherical/circular shell/ring in the surroundings of this particle. The thickness of this shell/ring is δr. It is counted how many particles have their centers within this ring of radius r and thickness δr, - see **Figure 4**. At the end of the calculation, the summation is divided the value by N.

When this calculation is performed for different values of r, going from 1 unit to R_{Agg} which is the characteristic size of the aggregate, we can determine a continuous curve, and to denote characteristics of probability distribution to this function. In general, this function is normalized

http://dx.doi.org/10.5772/67940

Figure 3. (a) DLA 2D with 10^3 particles deposited on-lattice for the case where the seed is deposited in a plane and the particles are thrown on top a plane.

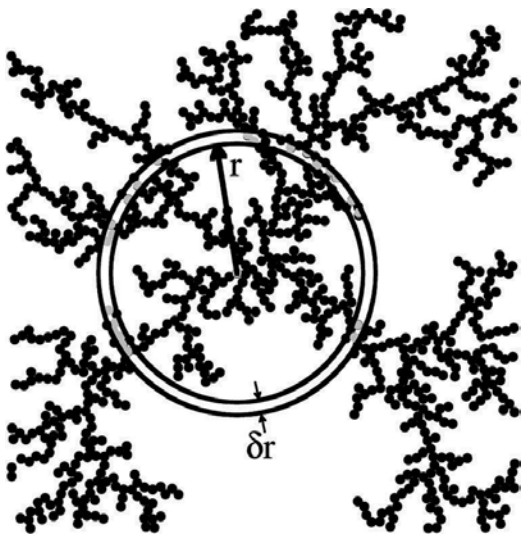

Figure 4. Schematic diagram of the calculation of c(r) by accounting for a histogram of the radial correlation function for a 2D DLA particle. Black circles are aggregate circles, the centered gray circle is the center of the circular ring, and gray circles are the circles accounted due to their centers are within the circular ring of thickness δr.

with the integral of the function obtained in the domain of the function, or it is rescaled based on the maximum value Max($c(r)$) of the function.

In the case of a typical DLA, $c(r)$ behaves similarly to that shown in **Figure 5**. Note that there is a global maximum and no other intermediate peaks. This value of r for which $c(r)$ reaches

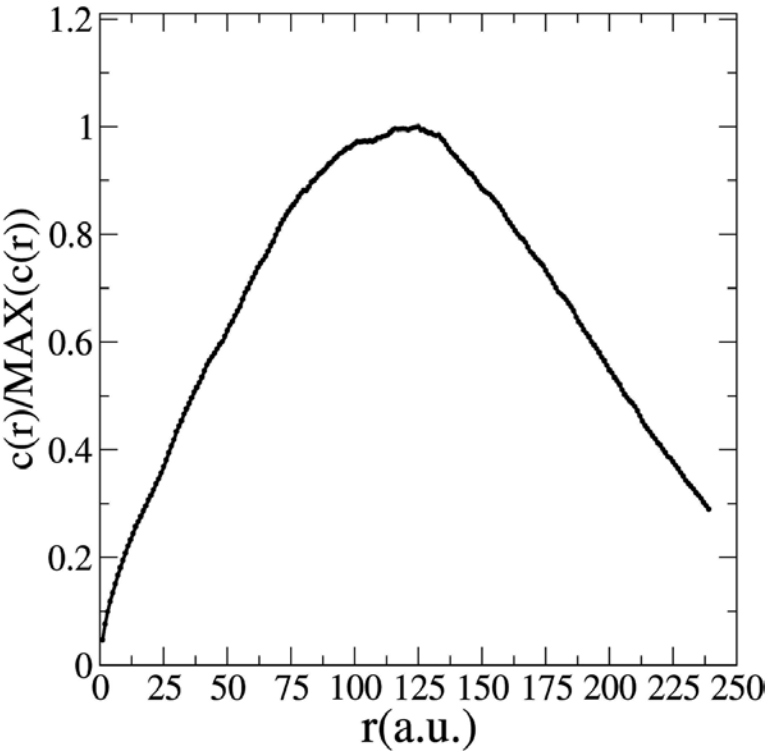

Figure 5. Radial distribution function for the 2D off-lattice DLA containing 10^4 particles of **Figure 1**.

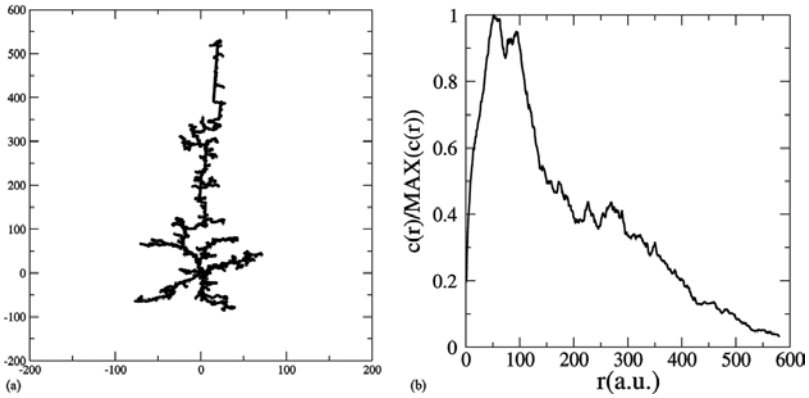

Figure 6. (a) DLA 2D off-lattice containing 2×10^3 particles containing one of the branches more developed than the other branches and (b) pair-pair radial distribution function referring to DLA of item (a) of this figure.

a maximum value means the most likely average separation between the particles. As there is only this peak, the aggregate is expected to exhibit isotropy in its morphology, or there is no trend in aggregate growth. In cases where the aggregate has one of the branches more

developed than the others, there is a change in this distance, and one of the peaks ends up becoming a peaked function, see **Figure 6**. The maximum of the function is shifted from its original position, making evident that exist an anisotropy at the aggregate, but cannot be the finally proven to be a signature of the anomalous growth of the fractal.

3. Angular pair-pair correlation function

The manner in which the dendrites of a DLA-type aggregate or other branched fractal are formed may be extremely relevant in their characterization. One way to characterize such branching is by calculating the angular pair correlation function $c(\theta)$.

Using the primitive ideas of $c(r)$, the pair-pair angular correlation function is nothing more than a probabilistic measure that we can find two aggregated particles, or two infinitesimal parts of the fractal, separated by an angular aperture (θ) one of the others. That is, we indirectly measure which angles of openings are more or less likely to be of branch bifurcations.

Mathematically, the correlation function $c(\theta)$ is

$$c(\theta) = \frac{1}{N} \sum \sum \delta\left(\theta - \left|\theta_i - \theta_j\right|\right) \tag{2}$$

where $\delta\left(\theta - \left|\theta_i - \theta_j\right|\right)$ is equal to unity since particles i and j are separated by an angular separation θ. N remains the total number of particles added to the aggregate.

Computationally speaking, it is also very complicated to determine θ angle, for this, we again perform the calculation of c (θ) by means of a histogram, which is executed as follows: all aggregated particles are taken as the center of of circular sectors with angular opening $\delta(\theta)$, centered on (θ), with (θ) being calculated as the angle based on the polar axis created on the particle analyzed, see **Figure 7**.

The aggregate particles that have their center inside the circular sector are accounted for in the histogram. After the calculation is performed for all aggregated particles, the sum is divided by the total number of particles added.

Similarly to the case of $c(r)$, one can normalize the function $c(\theta)$ or simply rescale it with its maximum value for a better visualization of it.

In the case of a typical 2D DLA, such a function can be seen in **Figure 8**. Note that again DLA growth isotropy returns us a function that is periodic with respect to the angle π and all dendrites grew at a periodic aperture, with multiple peaked angles at this interval. In cases where $c(\theta)$ presents more than one direction of growth, such a phenomenon may be associated with some anisotropy in fractal growth, similar to that presented in Ref. [8]. In general, these anisotropies are associated with symmetry breaks in the process of aggregate formation [8]. And such a mathematical tool is extremely useful and effective in the process of quantification of this phenomenology. As can be obser ved on the $c(\theta)$ function shown in **Figure 9**, for

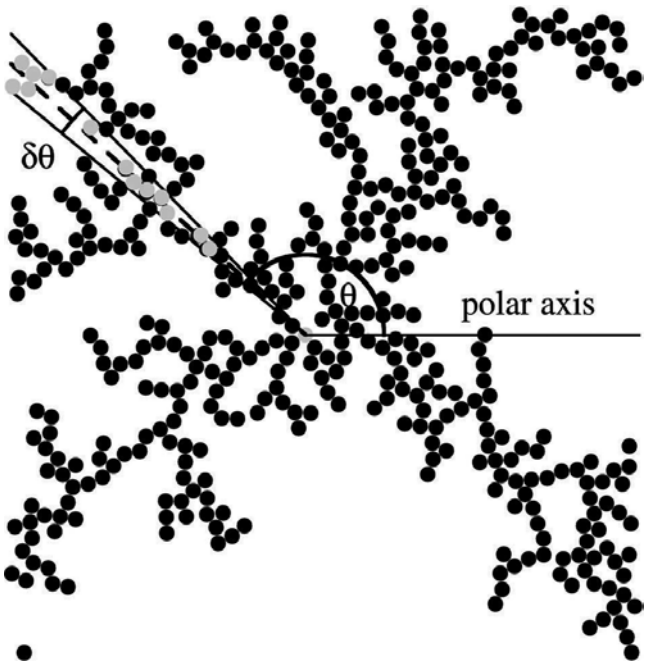

Figure 7. Schematic diagram of c(θ) calculation, for the 2D case the centered gray is the particle selected to be the center of the circular sector, the black circles are the aggregate particles and the gray circles are the particles that will be accounted for in the histogram. The black filled line is the polar axis associated with the selected particle, the black dotted lines is the centerline of the circular sector with opening $\delta\theta$ centered in angular position (θ).

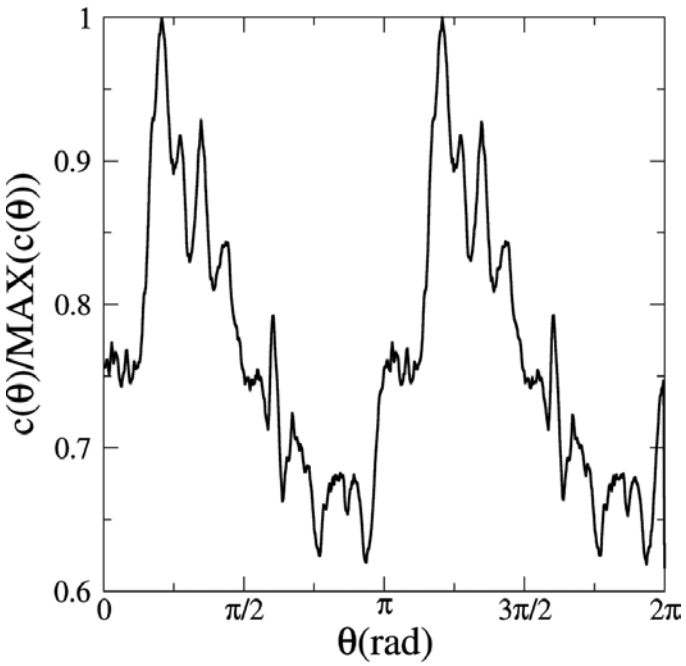

Figure 8. Rescaled $c(\theta)$ for the typical 2D DLA shown in **Figure 1** performed as described in Section 3.

http://dx.doi.org/10.5772/67940

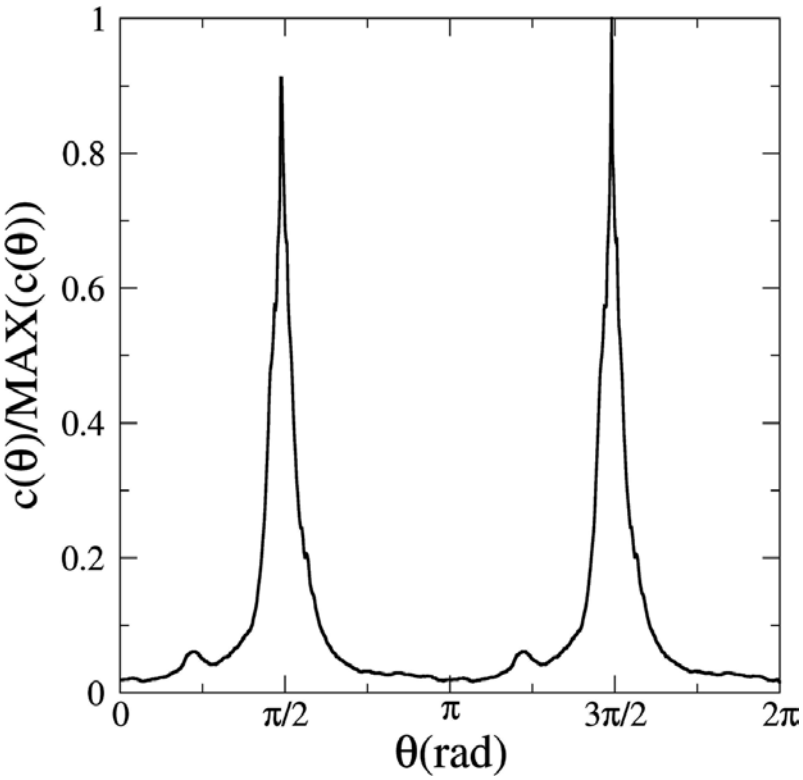

Figure 9. Rescaled $c(\theta)$ for the typical 2D DLA shown in **Figure 6(a)** performed as described in Section 3.

the anisotropic DLA, presented in **Figure 6(a)**, is visible that the peaked functions at the specific angle of approximately $\{\pi/2, 3\pi/2\}$ radians are associated with the anomalous branches that grew bigger than the rest of the aggregate.

Obviously, the Hausdorff dimension of these anisotropic structures also change, but meanwhile, the calculations of $c(r)$ and $c(\theta)$ end up corroborating the morphological changes advocated by a primary fractal dimension calculation.

There are cases in which the constituent species of the fractal/aggregate end up being different from each other, as was discussed in the paper [9]. In this case, it was necessary to create a correlation function for each of the species of particles involved in the aggregation growth process. This example proves the malleability of this type of function in the determination of morphological characteristics of the aggregates.

4. Conclusion

As observed throughout this chapter, the determination of the main characteristics associated with the morphological structures of two-dimensional fractals, especially those with dendritic properties and radial dispersion, involves the determination of angular correlation functions

c(θ) that may be useful at the capture of this characteristics. Investigations associated with diffusive processes such as crystal growth, neuronal formation, some types of tumoral growth, polymerization processes, deposition of materials, electric discharges, the formation of percolation networks among others are some of the examples that can be approached quantitatively by this mathematical tool.

Author details

Filipe Leoncio Braga[1]* and Alexandre Barbosa de Souza[2]

*Address all correspondence to: leonciob@ifi.unicamp.br

1 Department of Physics, Insitute of Education, Science and Techonolgy of Espirito Santo – Cariacica Campus, Espirito Santo, Brazil

2 Information Technology Department, Insitute of Education, Science and Techonolgy of Espirito Santo – Reitoria, Vitória, Espirito Santo, Brazil

References

[1] Vicksek, T., Fractal Growth Phenomena, World Scientific, Singapore, 1992.

[2] Egami, T. and Billinge, S.J.L., Underneath the Bragg Peaks: Structural Analysis of Complex Materials, Pergamon, San Diego, 2003.

[3] Mandelbrot, B., Jones, P.W., Evertsz, C.J.G. and Gutzwiller, M.C., Fractals and Chaos: The Mandelbrot Set and Beyond, Springer, New York, 2013.

[4] Witten, T. A. and Sander, L. M., Diffusion-Limited Aggregation, a Kinetic Critical Pheno menon, Physical Review Letters, 47, 19, 1400–1403, 1981.

[5] Pietronero, L. and Tosatti, E. (eds.), Fractals in Physics, Elsevier Science, Netherlands, 1986.

[6] Alves, S. G., Ferreira, Jr. S. C. and Martins, M. L., Strategies for optimize off-lattice aggregate simulations. Brazilian Journal of Physics, 38, 1, 81–86, 2008.

[7] Braga, F.L. and Ribeiro, M.S., Diffusion Limited Aggregation: Algorithm optimization revisited, Computer Physics Communications, 182, 8, 1602–1605, 2011.

[8] Alves, S. G., Braga, F. L. and Martins, M. L., Symmetry break in ferromagnetic electrocrystallization: The interplay between dipolar interactions and Laplacian growth, Journal of Statistical Mechanics: Theory and Experiment, 10, P10015, 2007.

[9] Braga, F. L. Mattos, O. A., Amorin, V. S. and Souza, A. B., Diffusion limited aggregation of particles with different sizes: Fractal dimension change by anisotropic, Physica A: Statistical Mechanics and its Applications, 429, 28–34, 2015.

Edited by Fernando Brambila

Fractal analysis has entered a new era. The applications to different areas of knowledge have been surprising. Benoit Mandelbrot, creator of fractal geometry, would have been surprised by the use of fractal analysis presented in this book. Here we present the use of fractal geometry, in particular, fractal analysis in two sciences: health sciences and social sciences and humanities. Part 1 is Health Science. In it, we present the latest advances in cardiovascular signs, kidney images to determine cancer growth, EEG signals, magnetoencephalography signals, and photosensitive epilepsy. We show how it is possible to produce ultrasonic lenses or even sound focusing. In Part 2, we present the use of fractal analysis in social sciences and humanities. It includes anthropology, hierarchical scaling, human settlements, language, fractal dimension of different cultures, cultural traits, and Mesoamerican complexity. And in Part 3, we present a few useful tools for fractal analysis, such as graphs and correlation, self-affine and self-similar graphs, and correlation function. It is impossible to picture today's research without fractal geometry.

ISBN 978-953-51-4721-3

Photo by sakkmesterke / iStock

IntechOpen